STUDY OF THE COULOMB NUCLEAR INTERFERENCE OF ^{23}Al BREAKUP REACTION WITH DIFFERENT TARGETS

 Surender[*], Ravinder Kumar

Deenbandhu Chhotu Ram University of Science and Technology, Murthal(Sonipat), 131039, Haryana, India
*Corresponding Author e-mail: surender.schphy@dcrustm.org

The impact of Coulomb-diffraction interference on the one-proton removal breakup cross-section and the width of the longitudinal momentum distribution (LMD) has been investigated for the breakup reaction of the ^{23}Al nucleus with different light to the heavy target for energy 40-100MeV/nucleon. Sensitivity to the target size and incident energy was analyzed through calculations that incorporate Coulomb interactions to all orders, including the full multipole expansion and nuclear diffraction using the eikonal approximation in the Glouber model. The results indicate that both constructive and destructive interferences significantly impact the observables, with the effects being more pronounced for medium-mass targets than light or heavy targets.

Keywords: *Coulomb nuclear interference; Proton halo; LMD; Proton breakup; One proton-removal cross-section*

PACS: 25.60.Gc

1. INTRODUCTION

After the discovery of halo nuclei in 1985 [1, 2], extensive experimental and theoretical research has been conducted to explore their unique nuclear structures and their significant role in nucleosynthesis reactions [3–15]. Advancements in accelerator facilities have greatly accelerated this field of research, leading to the discovery of numerous exotic nuclei near the neutron or proton drip lines. Breakup reactions have been one of the most frequently used methods to investigate these nuclei [16–20]. While the breakup mechanisms of loosely bound neutron-rich nuclei are well understood, those of loosely bound proton-rich nuclei present a more complex situation. In such cases, both the core of the projectile and the valence proton experience Coulomb interactions with the target, complicating the analysis, particularly when studying the Coulomb breakup mechanism exclusively [15, 16, 21]. Recent theoretical studies have demonstrated that this complexity affects observables such as breakup cross sections, the width of longitudinal momentum distributions, and angular distributions. Additionally, interference between diffraction and Coulomb breakup mechanisms has been reported to significantly influence these observables, depending on the size of the participating nuclei and the incident energies [22–27].

The study of single proton breakup from proton-rich nuclei via the Coulomb breakup mechanism is directly linked to astrophysical proton capture reactions through the detailed balance theorem [28, 29]. Precise values of Coulomb breakup observables are crucial inputs for estimating the reaction rates of proton capture reactions [13, 15, 30]. Therefore, it is essential to gain a deeper understanding of the Coulomb breakup mechanism and its interference with nuclear diffraction mechanisms to accurately derive astrophysical information.

In this study, we investigate the interference between Coulomb and diffraction mechanisms in the breakup of ^{23}Al at beam energies of 60 and 100 MeV/nucleon for various target cases, extending our previous work [31] to explore the trend of interference effects across a beam energy range of 40-100 MeV/nucleon. We analyze the impact of interference on single proton breakup cross-sections and the full width at half maximum (FWHM) of core longitudinal momentum distributions (LMD) for different targets and examine the sensitivity of these observables to the incident energies. The calculations account for Coulomb interactions to all orders, including full multipole expansion, and treat nuclear diffraction within the eikonal approximation [23, 27]. The calculations are performed in the absence and presence of each mechanism, allowing us to clearly identify the role of interference between the breakup mechanisms.

The ^{23}Al nucleus is chosen for this investigation because it is a proton-rich nucleus located near the proton drip line, with a very low proton separation energy of $S_p = 141.11(43)$ keV [15], and its significant astrophysical implications as noted in [21, 32, 33]. In a recent experimental study [15], the measurement of core fragment momentum distribution and breakup cross-section was used to extract spectroscopic factors and asymptotic normalization coefficients (ANCs) [32, 34–36], which were subsequently employed to determine the stellar reaction rate for the direct radiative proton capture reaction $^{22}Mg(p, \gamma)^{23}Al$ [15].

Given the important role of ^{23}Al in the $^{22}Mg(p, \gamma)^{23}Al$ direct capture reaction, it is intriguing to investigate the interference between Coulomb and nuclear diffraction breakup mechanisms in the ^{23}Al breakup reaction, as these interferences may either enhance or suppress the single proton breakup cross-section and the LMD width, as reported in [26, 27]. This study has been conducted in light of previous works [26, 27]. The effect of uncertainty in the one-proton

separation energy (S_p = 141.11(43) keV) on breakup observables was found to be less than 5% for both light [37] and heavy targets.

2. THEORETICAL FORMALISM

We followed the theoretical formalism of ref. [23, 27], where the Coulomb potential between projectile and target is taken as

$$V(\vec{r}, \vec{R}) = \frac{V_c}{|\vec{R} - \beta_1\vec{r}|} + \frac{V_v}{|\vec{R} + \beta_2\vec{r}|} - \frac{V_0}{\vec{R}} \tag{1}$$

where $V_c = Z_c Z_t e^2$, $V_v = Z_v Z_t e^2$, and $V_0 = (Z_v + Z_c) Z_t e^2$. β_1 and β_2 are the mass ratios of proton and core, respectively, to that of projectile. Z_c, Z_t and Z_v are the core, target and valence proton charges, respectively. Also $\vec{r}$ and $\vec{R}$ are the position vectors of core to proton and target to projectile, fig. 1 in ref. [26]. So the perturbed Coulomb phase for the whole projectile (core plus valence proton) is

$$\chi^p = \frac{2}{\hbar v}\left(V_c e^{i\beta_1\omega z/v}K_0\left(\omega b_c/v\right) - V_0 K_0\left(\omega R_\perp/v\right) + V_v e^{-i\beta_2\omega z/v}K_0\left(\omega b_v/v\right)\right), \tag{2}$$

where $\omega = \left(\varepsilon_f - \varepsilon_0\right)/\hbar$ and ε_0 is the valence nucleon binding energy while ε_f is the final nucleon-core continuum energy. The Coulomb potential for the entire projectile (V_0) can be expressed as the sum of the core (V_c) and valence proton (V_v) Coulomb potentials with respect to the target, i.e., $V_0 = V_c + V_v$. Consequently, the perturbed Coulomb phase for the entire projectile can be written as:

$$\chi^p = \chi\left(\beta_1, V_c\right) + \chi\left(-\beta_2, V_v\right) \tag{3}$$

where

$$\chi(\beta_1, V_c) = \frac{2V_c}{\hbar v}\left(e^{i\beta_1\omega z/v}K_0(\omega b_c/v) - K_0\left(\omega R_\perp/v\right)\right) \tag{4}$$

$$\chi(-\beta_2, V_v) = \frac{2V_v}{\hbar v}\left(e^{-i\beta_2\omega z/v}K_0(\omega b_v/v) - K_0\left(\omega R_\perp/v\right)\right) \tag{5}$$

corresponds to core- target Coulomb phase and valence proton-target Coulomb phase respectively. As series of work have stressed the importance of inclusion of Coulomb mechanism to all orders specially in proton halo breakup reactions [22–27]. Therefore, we have also treated the Coulomb interaction to all orders in sudden formalism for both core-target (called recoil interaction) and valence proton-target (called direct interactions), as discussed in detail in ref. [22–25], and respective Coulomb phases can be written as

$$g^{rec}(b_c) = \int d\vec{r}e^{-i\vec{k}\cdot\vec{r}}\phi_i(\vec{r})\left(e^{i\frac{2V_c}{\hbar v}\log\frac{b_c}{R_\perp}} - 1 - i\frac{2V_c}{\hbar v}\log\frac{b_c}{R_\perp} + i\chi(\beta_1, V_c)\right) \tag{6}$$

$$g^{dir}(b_v) = \int d\vec{r}e^{-i\vec{k}\cdot\vec{r}}\phi_i(\vec{r})\left(e^{i\frac{2V_v}{\hbar v}\log\frac{b_v}{R_\perp}} - 1 - i\frac{2V_v}{\hbar v}\log\frac{b_v}{R_\perp} + i\chi(-\beta_2, V_v)\right) \tag{7}$$

and nuclear diffraction dissociation amplitude is calculated in eikonal approximation as

$$g^{diff} = \int d\vec{r}e^{-i\vec{k}\cdot\vec{r}}\phi_i(\vec{r})\left(e^{i\chi_{nt}(b_v)} - 1\right) \tag{8}$$

So the core fragment momentum distribution can be written as

$$\frac{d\sigma}{d\vec{k}} = \frac{1}{8\pi^3}\int d\vec{b}_c|S_{ct}(b_c)|^2|g^{rec} + g^{dir} + g^{diff}|^2 \tag{9}$$

and breakup cross section may be obtained by integrating the core fragment momentum distribution over the transverse component of momentum. Here, $S_{ct}(b_c)$ and $e^{i\chi_{nt}(b_v)}$ represent the core-target and proton-target S matrices, which are calculated using the $t\rho\rho$ formalism through the standard MOMDIS code [38]. We employed Hartree-Fock nuclear density forms [39] for both the core and the targets. The projectile wave function, $\phi_i(\vec{r})$, was computed by numerically solving the Schrödinger equation for the Woods-Saxon nuclear potential with fixed geometry parameters: radius ($r_0 = 1.25$ fm), diffuseness ($a_0 = 0.7$ fm) [15], and spin-orbit coupling potential $V_{ls} = -20.72$ MeV [40], for the $[0^+ \otimes 1d_{5/2}]$ bound state configuration. The depth of the nuclear potentials was adjusted to reproduce the binding energy of the valence proton, $S_p = 0.141$ MeV.

The sensitivity of the breakup cross-section and longitudinal momentum distribution (LMD) width to the Woods-Saxon potential parameters (r_0 and a_0) was also evaluated for the 40 MeV/nucleon case. We found that the cross-section increased by approximately 20% as r_0 changed from 1.15 fm to 1.3 fm, while the FWHM of the LMD increased by less than 2-3%. Similarly, an increase in the cross-section of less than 10% was observed when a_0 was varied from 0.6 fm to 0.7 fm, with the LMD width increasing by less than 2-3%. This sensitivity is consistent with the results reported in [41]. Additional theoretical details of the formalism can be found in [22–25].

3. RESULTS AND DISCUSSION

The single proton breakup cross-section and core fragment momentum distribution were calculated for the ^{23}Al nucleus with ^{12}C, ^{58}Ni, and ^{208}Pb targets, in the beam energy range of 40-100 MeV/nucleon. The ^{23}Al nucleus is treated as a two-body system, consisting of a $[0^+ \otimes 1d_{5/2}]$ core plus a proton in a bound state configuration, resulting in $J^\pi = 5/2^+$. In this analysis, only the $1d_{5/2}$ state of the valence proton is considered, as predicted by the shell model and widely reported in the literature [15].

For the present calculations, we focused on 60 and 100 MeV/nucleon beam energies, as the 40 and 80 MeV/nucleon data had already been published in our previous work [31], though the table includes all energies from 40-100 MeV/nucleon. The objective was to examine how the breakup cross-section and FWHM of the parallel momentum distribution change with different beam energies and targets. The calculations were performed separately for nuclear diffraction breakup and Coulomb breakup mechanisms, as well as for the combined effect of both mechanisms, to observe the interference effects.

Table 1. Calculated one-proton removal breakup cross-section and FWHM of LMD for ^{12}C target at different incident beam energies corresponding to nuclear diffraction, pure Coulomb, nuclear diffraction with Coulomb mechanisms and percentage change in observables values

Beam energy(MeV/nucleon)	40		60		80		100	
	σ_{-p} (mb)	FWHM (MeV/c)	σ_{-p} (mb)	FWHM (MeV/c)	σ_{-p} (mb)	FWHM (MeV/c)	σ_{-p} (mb)	FWHM (MeV/c)
Diff.	10.37	164.24	16.45	178.30	13.65	177.59	9.46	178.50
Coul.(total)	5.27	121.33	4.30	128.76	3.92	135.40	3.50	139.14
Coul+Diff.(simple sum)	15.64	145.64	20.75	163.07	17.57	164.65	12.96	164.71
Coul+Diff. (Cal. together)	16.42	144.54	20.01	160.64	16.20	162.20	11.59	161.97
% change	+4.99	-0.75	-3.57	-1.49	-7.80	-1.48	-10.57	-1.66

Table 2. Calculated one-proton removal breakup cross-section and FWHM of LMD for ^{58}Ni target at different incident beam energies corresponding to nuclear diffraction, pure Coulomb, nuclear diffraction with Coulomb mechanisms and percentage change in observables values

| Beam energy (MeV/nucleon)	40		60		80		100	
	σ_{-p} (mb)	FWHM (MeV/c)	σ_{-p} (mb)	FWHM (MeV/c)	σ_{-p} (mb)	FWHM (MeV/c)	σ_{-p} (mb)	FWHM (MeV/c)
Diff.	14.96	156.54	20.04	168.59	22.55	167.08	15.77	162.57
Coul.(total)	115.09	114.16	81.25	116.98	66.92	120.44	57.85	123.13
Coul+Diff. (simple sum)	130.05	117.83	103.81	124.20	86.96	127.72	73.62	129.31
Coul+Diff. (Cal. together)	156.90	125.43	127.49	130.24	105.04	132.23	87.82	132.75
% change	+20.65	+6.44	+22.81	+4.86	+20.79	+3.53	+19.28	+0.79

Calculated one-proton removal breakup cross-section and FWHM widths of the longitudinal momentum distribution (LMD) are presented in Tables 1-3. These results are shown exclusively for nuclear diffraction ($diff$), total Coulomb (recoil + direct) ($Coul$), the simple algebraic sum of total Coulomb and diffraction ($Coul + diff$ (simple sum)), and the total Coulomb and diffraction mechanisms calculated together ($Coul + diff$ (calculated together)). The rows correspond to the ^{12}C, ^{58}Ni, and ^{208}Pb targets for Tables 1, 2, and 3, respectively. The respective LMD results are illustrated in Figures 1-3, where the percentage change is calculated using the formula:

$$\frac{X^{(Coul+diff)} - (X^{Coul} + X^{diff})}{(X^{Coul} + X^{diff})} \times 100\%,$$

where X represents either the cross-section or the FWHM of the LMD. For simplicity, the spectroscopic factor is taken as unity throughout the calculations.

Table 1 shows the results for the ^{12}C target at 40, 60, 80, and 100 MeV/nucleon beam energies. At 40 MeV/nucleon, the Coulomb and diffraction mechanisms (calculated together) result in a cross-section increase of +5% compared to their simple sum, indicating constructive interference between the Coulomb and diffraction breakup mechanisms. However, at higher beam energies (60, 80, and 100 MeV/nucleon), destructive interference occurs, reducing the cross-section by -3.5% to -10.5%, with the magnitude of the reduction increasing as the beam energy increases. The interference effect on the FWHM of the LMD shows a slight destructive trend for all incident energies, reducing the width by -0.7% to -1.66%, with this variation mildly depending on the beam energy. In contrast, for the ^{12}C target, except at 40 MeV/nucleon (Fig. 1(a)),

the black solid curve appears lower than the green dash-dotted curve, indicating destructive interference, which reduces the cross-section. However, at 40 MeV/nucleon, the interference is constructive.
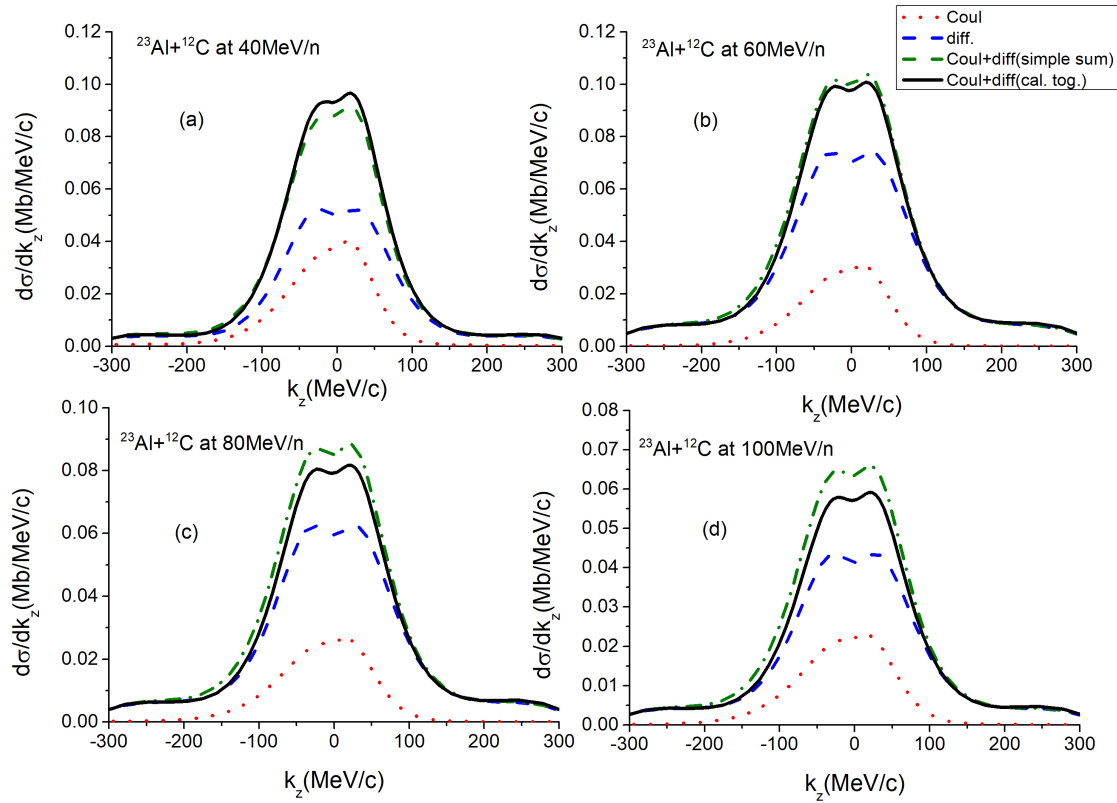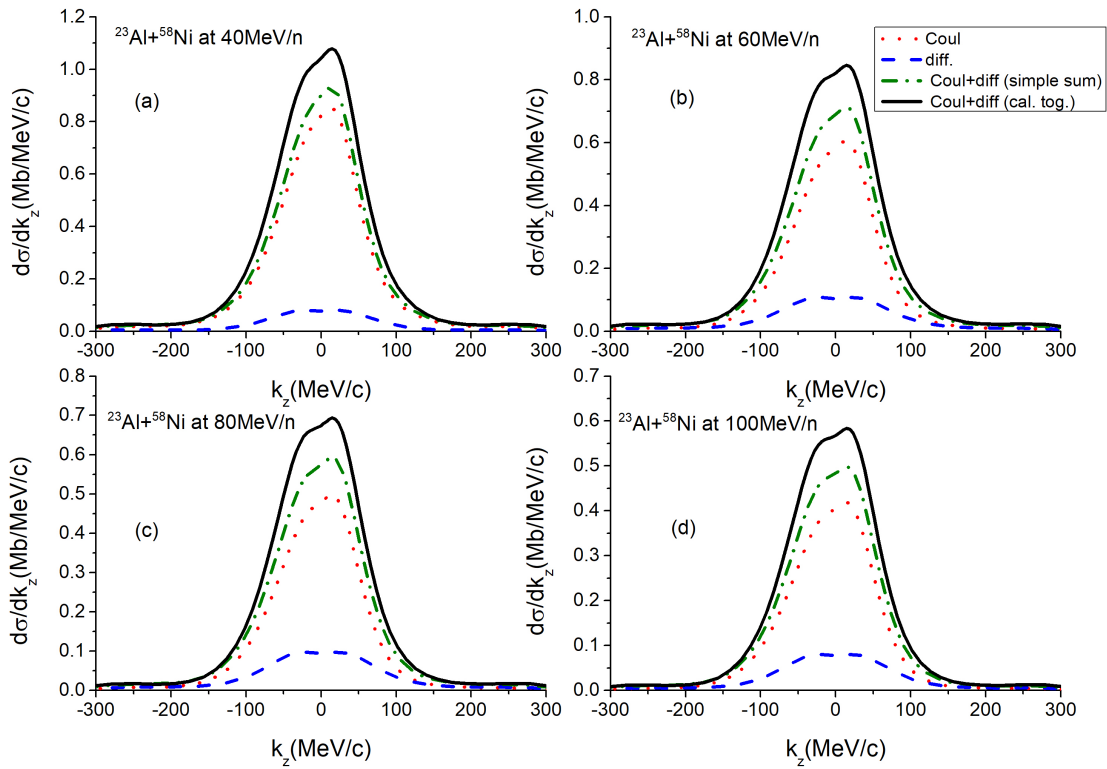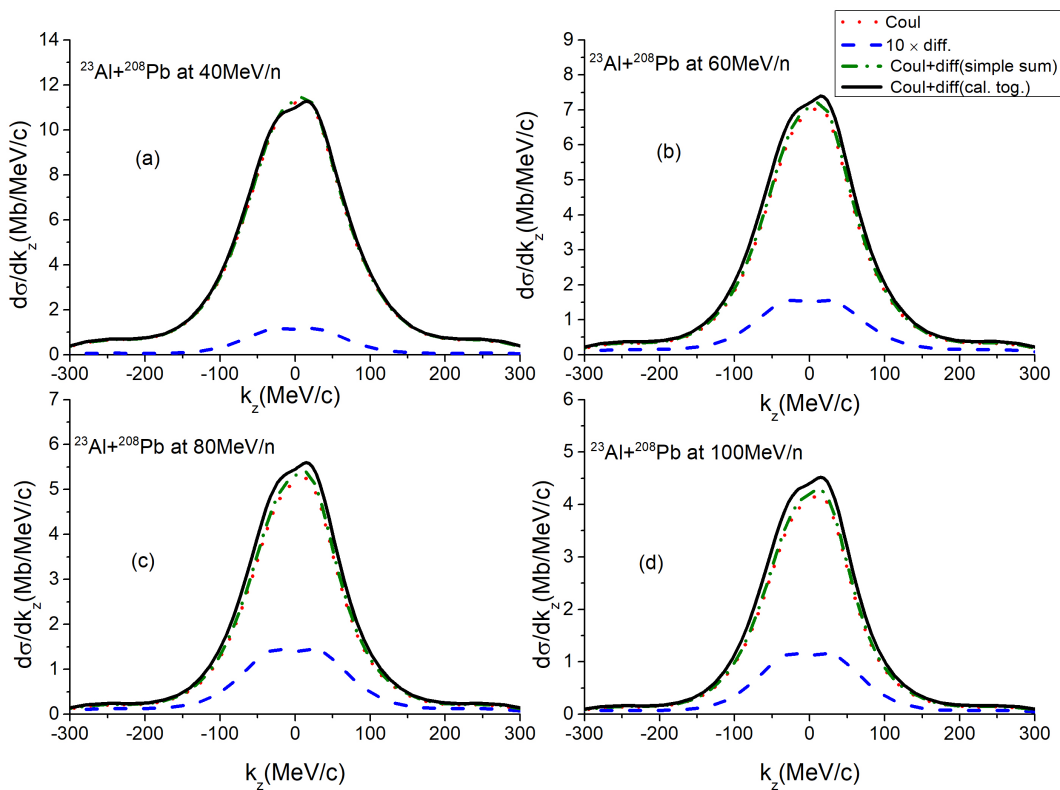

Figure 1. (Color online) Longitudinal Momentum Distribution for $^{12}C(^{23}Al, ^{22}Mg)X$ at 40-100 MeV/nucleon beam energies.

Table 3. Calculated one-proton removal breakup cross-section and FWHM of LMD for ^{208}Pb target at different incident beam energies corresponding to nuclear diffraction, pure Coulomb, nuclear diffraction with Coulomb mechanisms and percentage change in observables values

Beam energy (MeV/nucleon)	40		60		80		100	
	σ_{-p} (mb)	FWHM (MeV/c)	σ_{-p} (mb)	FWHM (MeV/c)	σ_{-p} (mb)	FWHM (MeV/c)	σ_{-p} (mb)	FWHM (MeV/c)
Diff.	21.45	153.73	32.32	166.13	29.26	163.91	21.94	157.98
Coul.(total)	2029.37	146.23	1162.78	134.62	821.72	129.78	638.78	127.64
Coul+Diff. (simple sum)	2050.81	146.34	1195.11	135.44	850.98	130.80	660.72	128.52
Coul+Diff. (Cal. together)	2077.99	152.13	1277.35	142.65	927.91	138.19	725.65	135.23
% change	+1.32	+3.96	+6.88	+5.32	+9.04	+5.65	+9.82	+5.22

For the ^{58}Ni target (Table 2), constructive interference is consistently observed across all incident energies, resulting in an enhancement of the breakup cross-section by approximately +20%. Additionally, the FWHM of the LMD increases from +6.4% to +0.79% as the incident energy increases, in comparison to the algebraic sum of the Coulomb and diffraction components calculated independently.

In the case of the ^{208}Pb target, as shown in Table 3, the breakup cross-section exhibits an increase ranging from +1.3% to +9.8% with increasing incident energy, while the FWHM of the LMD broadens by +3.96% to +5.22%. This behavior again indicates the presence of constructive interference between the Coulomb and nuclear breakup mechanisms.

Figure 2. (Color online) Longitudinal Momentum Distribution for ^{58}Ni(^{23}Al, ^{22}Mg)X at 40-100 MeV/nucleon beam energies.

Figure 3. (Color online) Longitudinal Momentum Distribution for ^{208}Pb(^{23}Al, ^{22}Mg)X at 40-100 MeV/nucleon beam energies.
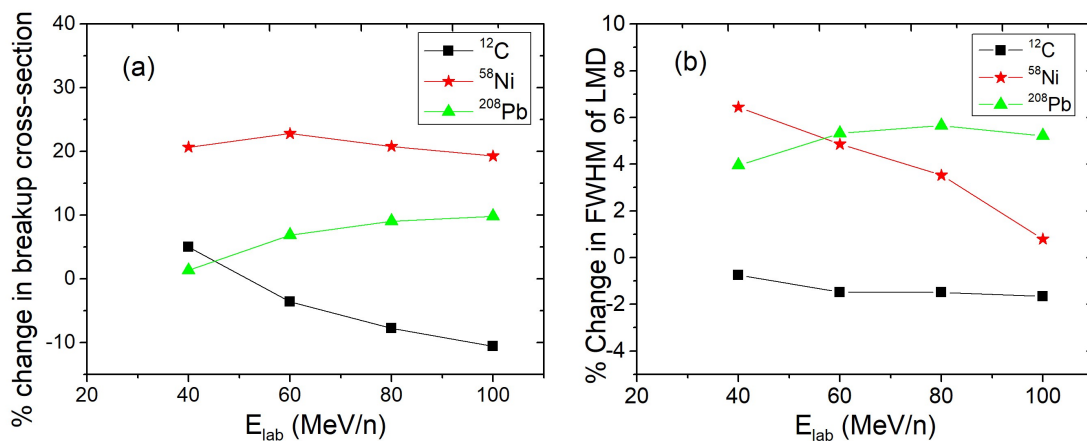
Figure 4. (Color online) (a) Variation of Percentage change in single proton breakup cross-section due to Coulomb diffraction interference with incident energy, (b) Variation of Percentage change in FWHM of LMD due to Coulomb diffraction interference with incident energy, in case of different target.

For enhanced clarity, Figures 1-3 present the LMD results for all target cases, where the diffraction component is represented by a blue dashed curve, the Coulomb component by a red dotted curve, their simple algebraic sum by a green dash-dotted curve, and the combined Coulomb and diffraction calculation by a black solid curve. For the ^{58}Ni and ^{208}Pb targets, the black solid curve (representing Coulomb and diffraction calculated together) consistently exceeds the green dash-dotted curve (representing the algebraic sum), thereby reflecting the constructive interference between the two breakup mechanisms, which leads to an enhancement in both the breakup cross-section and the LMD width. In our previous paper [31], we investigated the interference effects between recoil and direct breakup reactions, which were consistently found to be destructive for all target and beam energies. Therefore, in this paper, we do not provide the LMD or cross-sections; instead, the Coulomb calculations presented here reflect the result of the interference effect between recoil and direct breakup.

Figures 4(a) and 4(b) further illustrate the percentage variations in the single-proton breakup cross-section and the FWHM of the LMD as a function of incident energy for all targets. It is evident from these figures that the trend of percentage variations differs between targets, exhibiting behavior consistent with the results reported in Ref. [24]. Thus, we observed that for medium-mass targets such as ^{58}Ni, the magnitude of constructive interference is greater compared to ^{12}C and ^{208}Pb. This can be attributed to the fact that, for smaller targets, the dominant reaction mechanism causing the breakup is nuclear interaction, with Coulomb interaction being relatively insignificant. In contrast, for heavier targets, the Coulomb interaction tends to dominate over the nuclear interaction, driving the breakup process. For medium-mass targets, both Coulomb and nuclear interactions play significant roles during the interaction between the projectile and target, making the interference between Coulomb and nuclear mechanisms more pronounced and significantly affecting the breakup observables. This observation suggests that when designing experiments with proton-rich nuclei, it may be beneficial to choose either light or heavy targets to minimize the impact of interference on the breakup observables. However, further detailed investigation is needed to fully understand the complex interference mechanisms in breakup reactions.

4. CONCLUSIONS

The investigation examines the Coulomb-diffraction interference present during the single-proton breakup reaction of the ^{23}Al nucleus. The study analyzes the interference effects on the single-proton breakup cross-section and the full-width at half maximum (FWHM) of the longitudinal momentum distribution (LMD) of core fragments for targets ^{12}C, ^{58}Ni, and ^{208}Pb. Sensitivity to target size and incident energy was systematically assessed by performing calculations at commonly used incident beam energies - 40, 60, 80, and 100 MeV/nucleon for each target.

The results indicate that Coulomb-diffraction interference can be either constructive or destructive, leading to significant variations in the observable values. The magnitude of these variations is sensitive to both target size and incident energy, with the effect being most enhancement in breakup cross-section for medium-mass targets compared to light or heavy targets. This finding highlight the need for careful consideration when dealing with reactions involving medium-mass targets. For greater clarity, we will further explore our breakup formalism in the upcoming studies by examining the angular distribution. This study represents a step towards a quantitative understanding of Coulomb-diffraction interference in ^{23}Al breakup reactions. It aims to aid in the planning of future breakup experiments, helping to either minimize or avoid interference effects to obtain clearer and more accurate information.

Data Availability Statement: This manuscript has no associated data or the data will not be deposited.

ORCID

🔳 **Surender**, https://orcid.org/0000-0002-5306-3115; 🔳 **Ravinder Kumar**, https://orcid.org/0000-0002-4992-2394

REFERENCES

[1] I. Tanihata, et al., Phys. Rev. Lett. **55**, 2676 (1985). https://doi.org/10.1103/PhysRevLett.55.2676

[2] I. Tanihata, et al., Physics Letters B, **160**(6), 380, (1985). https://doi.org/10.1016/0370-2693(85)90005-X

[3] T. Nakamura, et al., Physical Review C, **79**(3), 035805 (2009). https://doi.org/10.1103/PhysRevC.79.035805

[4] G. Baur, et al., Progress in Particle and Nuclear Physics, **51**(2), 487 (2003). http://dx.doi.org/10.1016/S0146-6410(03)90006-8

[5] G. Baur, et al., Progress in particle and nuclear physics, **59**(1), 122 (2007). https://doi.org/10.1016/j.ppnp.2006.12.002

[6] L.V. Grigorenko, et al., Physics Letters B, **641**(3-4), 254 (2006). https://doi.org/10.1016/j.physletb.2006.08.054

[7] C.A. Bertulani, et al., Physics Reports, **485**(6), 1959 (2010). https://doi.org/10.1016/j.physrep.2009.09.002

[8] L. Trache, et al., Physical review letters, **87**(27), 271102 (2001). https://doi.org/10.1103/PhysRevLett.87.271102

[9] L.Trache et al., Physical Review C, **66**(3), 035801 (2002). https://doi.org/10.1103/PhysRevC.66.035801

[10] V.E. Iacob, et al., Physical Review C, **74**(4), 045810 (2006). https://doi.org/10.1103/PhysRevC.74.045810

[11] S.S. Chandel, et al., Physical Review C, **68**(5), 054320 (2003). https://doi.org/10.1103/PhysRevC.68.054320

[12] M.M. Khansari, et al., New Astronomy, **57**, 76 (2017). https://doi.org/10.1016/j.newast.2017.06.013

[13] T.L. Belyaeva, et al., Physical Review C, **80**(6), 064617 (2009). https://doi.org/10.1103/PhysRevC.80.064617

[14] V.S. Melezhik, et al., Physical Review C, **64**(5), 054612 (2001). https://doi.org/10.1103/PhysRevC.64.054612

[15] A. Banu, et al., Physical Review C, **84**(1), 015803 (2011). https://doi.org/10.1103/PhysRevC.84.015803

[16] K. Hencken, et al., Physical Review C, **54**(6), 3043 (1996). https://doi.org/10.1103/PhysRevC.54.3043

[17] V.S. Melezhik, et al., Physical Review C, **59**(6), 3232 (1999). https://doi.org/10.1103/PhysRevC.59.3232

[18] N. Fukuda, et al., Physical Review C, **70**(5), 054606 (2004). https://doi.org/10.1103/PhysRevC.70.054606

[19] S. Typel, et al., Physical Review C, **64**(2), 024605 (2001). https://doi.org/10.1103/PhysRevC.64.024605

[20] R. Chatterjee, et al., Nuclear Physics A, **675**(3-4), 477 (2000). https://doi.org/10.1016/S0375-9474(00)00179-2

[21] T. Gomi, et al., Journal of Physics G: Nuclear and Particle Physics, **31**(10), S1517 (2005). https://doi.org/10.1088/0954-3899/31/10/023

[22] A. Garcia-Camacho, et al., Nuclear Physics A, **776**(3-4), 118 (2006). https://doi.org/10.1016/j.nuclphysa.2006.07.033

[23] A. García-Camacho, et al., Physical Review C, **76**(1), 014607 (2007). https://doi.org/10.1103/PhysRevC.76.014607

[24] J. Margueron, et al., Nuclear Physics A, **703**(1-2), 105 (2002). https://doi.org/10.1016/S0375-9474(01)01336-7

[25] J. Margueron, et al., Nuclear Physics A, **720**(3-4), 337 (2003). https://doi.org/10.1016/S0375-9474(03)01092-3

[26] R. Kumar, and A. Bonaccorso, Physical Review C, **84**(1), 014613 (2011). https://doi.org/10.1103/PhysRevC.84.014613

[27] R. Kumar, and A. Bonaccorso, Physical Review C, **86**(6), 061601 (2012). https://doi.org/10.1103/PhysRevC.86.061601

[28] G. Baur, et al., Nuclear Physics A, **458**(1), 188 (1986). https://doi.org/10.1016/0375-9474(86)90290-3

[29] H. Rebel, in: Nuclear Astrophysics: Proceedings of a Workshop,FRG, (Springer, 1987), pp. 38-53.

[30] F. Schümann, et al., Physical Review C - Nuclear Physics, **73**(1), 015806 (2006). https://doi.org/10.1103/PhysRevC.73.015806

[31] Surender, and R. Kumar, Acta Physica Polonica B, **54**(9), (2023). https://doi.org/10.5506/APhysPolB.54.9-A1

[32] X.Y. Li, et al., Chinese Physics C, **44**(7), 074001 (2020). https://doi.org/10.1088/1674-1137/44/7/074001

[33] R.N. Panda, et al., Physics of Atomic Nuclei, **81**(4), 417 (2018). https://doi.org/10.1134/S1063778818040154

[34] F. De-Qing, et al., Chinese Physics Letters, **22**(3), 572 (2005). https://doi.org/10.1088/0256-307X/22/3/015

[35] D.Q. Fang, et al., Physical Review C, **76**(3), 031601 (2007). https://doi.org/10.1103/PhysRevC.76.031601

[36] Y.-L. Zhao, et al., Chinese physics letters, **20**(1), 53 (2003). https://doi.org/10.1088/0256-307X/20/1/316

[37] Surender, and R. Kumar, DAE Symp. Nucl. Phys. **66**, 691 (2023). https://www.sympnp.org/proceedings/66/B174.pdf

[38] C.A. Bertulani, and A. Gade, Computer Physics Communications, **175**(5), 372 (2006). https://doi.org/10.1016/j.cpc.2006.04.006

[39] Experimental Nuclear Reaction Data. National nuclear data center. Brookhaven National Laboratory (http://www. nndc. bnl. gov/exfor/exfor00. htm) and International Atomic Energy Agency, Nuclear Data Services, (http://www-nds. iaea. org/exfor/exfor. htm), 2000.

[40] W. Horiuchi, et al., Physical Review C, **81**(2), 024606 (2010). https://doi.org/10.1103/PhysRevC.81.024606

[41] X.Y. Zhao, et al., Physical Review C, **100**(4), 044609 (2019). https://doi.org/10.1103/PhysRevC.100.044609

ДОСЛІДЖЕННЯ КУЛОНОВСЬКОЇ ЯДЕРНОЇ ІНТЕРФЕНЦІЇ РЕАКЦІЇ РОЗПАДУ ^{23}Al З РІЗНИМИ МІШЕНЯМИ

Сурендер, Равіндер Кумар

[a] Департамент математики, Відья Бхараті Махавідьяля, Кемп, Амраваті, 444601, Індія

Вплив інтерференції кулонівської дифракції на поперечний переріз розпаду відриву одного протона та ширину розподілу поздовжнього імпульсу (LMD) було досліджено для реакції розпаду ядра ^{23}Al з різним світлом від важка мішень на енергію 40-100 МеВ/нуклон. Чутливість до розміру мішені та енергії падіння аналізувалася за допомогою розрахунків, які включають кулонівські взаємодії для всіх порядків, включаючи повне мультипольне розширення та ядерну дифракцію з використанням наближення ейконала в моделі Глоубера. Результати показують, що як конструктивні, так і деструктивні перешкоди суттєво впливають на спостережувані, причому ефекти більш виражені для цілей середньої маси, ніж для легких або важких цілей.

Ключові слова: *кулонівська ядерна інтерференція; протонне гало; LMD; розпад протона; поперечний переріз видалення одного протона*

EFFECT OF SINTERING TEMPERATURE ON MICROSTRUCTURE AND PROPERTIES OF ZIRCONIA CERAMICS FOR THE NEEDS OF NUCLEAR ENERGY

I.O. Chernov[a], K.V. Lobach[a]*, S.Yu. Sayenko[a], I.V. Kolodiy[a], S.V. Lytovchenko[b], O.V. Pylypenko[a], H.O. Kholomieiev[a], B.O. Mazilin[b]

[a]National Science Center "Kharkiv Institute of Physics and Technology" 1, Akademichna St., 61108, Kharkiv, Ukraine
[b]V.N. Karazin Kharkiv National University, 4, Svoboda Sq., Kharkiv, 61022, Ukraine
*Corresponding Author e-mail: lobach0709@gmail.com

The paper provides experimental results of obtaining high-density $ZrO_2+3\%Y_2O_3$ ceramics, which is promising for use as a matrix for immobilization of HLW. The effect of sintering temperature in the range of 1100...1650 °C on the microstructure of the sintered tablets was studied. Phase composition and microstructure of experimental samples were characterized by XRD and SEM. Grain size distribution analysis was carried out using the "Thixomet" image analyzer. Microhardness was determined using a metallographic complex LECO (USA), an inverted microscope IM-3MET and a hardness tester UIT HVB-30. It was established that increase in the sintering temperature leads to a significant increase in the average grain size (from 85 nm to 1000 nm) and increase in the density of the sintered tablets. Sintering temperature should be at least 1550...1650ºC to produce high-dense ceramics (97...98 % of theoretical value). Obtained ceramics is characterized by high values of microhardness HV > 12 GPa and crack resistance of 5.5...6.3 MPa·m$^{1/2}$.
Keywords: *Zirconium oxide; Sintering; Microstructure; Microhardness; Crack resistance*
PACS: 62.25.-g; 81.07.Wx; 81.20.Ev; 61.05.C-; 81.40.Gh

INTRODUCTION

Zirconia-based materials (for example, $ZrO_2+Y_2O_3$, $Zr_2Gd_2O_7$) are widely used as matrices for high-level waste (HLW) due to their high radiation resistance and ability to bind in the crystal lattice (incorporation) of such elements as Pu, Am, Np and Ln in spent nuclear fuel (SNF) [1-3].

Recently, there is a considerable interest in obtaining and studying the characteristics of nanostructured ZrO_2-based ceramics with a grain size of less than 100 nm [4-6]. Thus, a number of works revealed that this material with a grain size of 25 nm and 38 nm has the ability to resist amorphization under Krypton ions irradiation (Kr^+, 400 keV) up to a fluence of $5.36 \cdot 10^{16}$ ion/cm^2 (129 dpa), and also has enhanced radiation resistance [7, 8].

In addition, nanosized zirconia-based powders are used for the manufacturing of oxide dispersion-strengthened (ODS) materials [9, 10] – a promising class of structural materials for the next-generation nuclear reactors [11]. Exactly, the presence of such nanooxide precipitates with a uniform distribution into the matrix improves the radiation resistance of materials, as well as their mechanical and corrosion properties, especially at elevated temperatures.

Another field of ZrO_2 materials application is the structural and refractory ceramics [12, 13]. Also, ZrO_2 is widely used in medicine due to its high biocompatibility [14]. In order to achieve the highest operational characteristics, methods for manufacturing of ZrO_2 nanopowders, as well as methods of their compaction and sintering to obtain products with a fine-grained structure, are actively developed [15-17].

The methods aimed on compacting of the raw powders and obtaining oxide ceramics in relation to its usage as both HLW matrices and structural ceramics are traditionally developed at NSC KIPT [18-20].

The goal of this work is to study the possibility of obtaining experimental samples from nanosized yttria-partially stabilized zirconia (Y-PSZ) powder by cold-pressing at different modes and subsequent sintering in air into dense ceramics with a fine-grained structure. Also, research of physical and mechanical characteristics of obtained ceramics is focused too.

MATERIALS AND METHODS

The powder of partially-stabilized zirconia PSZ-5.3YB manufactured by "Stanford Materials Corporation" (USA) was used as the raw material. According to the manufacturer, the powder was obtained the chemical co-precipitation of zirconium and yttrium salts solutions, followed by filtration, drying and calcination. PSZ-5.3YB powder is characterized by the good ability for pressing, as it contains an organic binder based on polyvinyl alcohol, which was introduced into the material at the stage of spray drying. This powder consists of micro-spherical granules size of 70...100 μm (Figure 1a), and the size of the particles of which the granules are composed is 30...40 nm (Figure 1b). Chemical composition of material according to the manufacturer: $Zr(Hf)O_2$ -94.5%; Y_2O_3 -5.2 ± 0.2%wt.

Compacting powders in the form of tablets (Ø10 mm and height 6-7 mm) was carried out by the method of uniaxial bilateral cold pressing (CP) in a steel mold at a pressure of 200 MPa. The density of samples after CP was 2.84±0.02 g/cm^3 (46 % of theoretical).

a   b
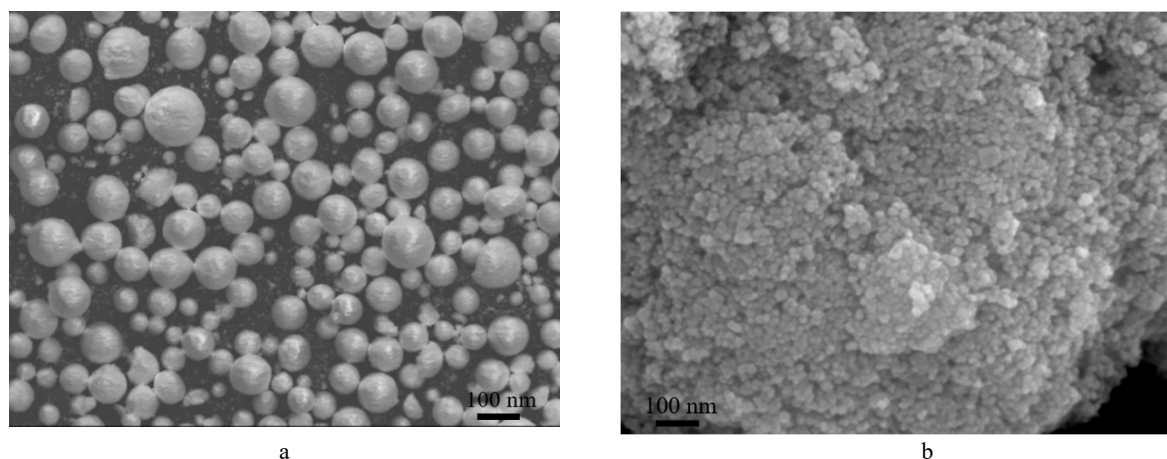
Figure 1. SEM micrographs of the PSZ-5.3YB powder (ZrO$_2$+3mol%Y$_2$O$_3$)

Tablets were sintered in the temperature range of 1100...1650ºC for 3 hours in an air atmosphere. The rate of reaching the isothermal holding temperature was 5ºC/min.

Density and open porosity of sintered ceramics were determined by hydrostatic weighing in distilled water.

XRD measurements were conducted using DRON-4-07 diffractometer in a filtered Cu-Kα radiation (λ = 0.154187 nm). Phase composition and lattice parameters were determined by the Rietveld method (MAUD software). Microstructural characteristics of the samples (size of coherent scattering domains CSD) were estimated by the Williamson-Hall technique (integral breadth analysis).

Microhardness of the sintered samples was determined using a metallographic complex LECO (USA), an inverted microscope IM-3MET and a hardness tester UIT HVB-30. Final surface polishing was performed using diamond paste with a particles size of 1 μm.

Microstructure studies of the samples were carried out using JSM-7001F scanning electron microscope (JEOL, Japan). The average grain size was determined by the method of random secants; the number of analyzed chords for each microstructure image was 18 [21]. Calculation of the grains diameter, based on their area, as well as grain size distribution analysis was carried out using the "Thixomet" image analysis system.

The stress intensity factor K$_{1C}$ (crack resistance) of ceramics was determined by the indentation method using Vickers diamond pyramid under the load of 10 kg and holding time of 15 s. Calculation of K$_{1C}$ [MPa·m$^{1/2}$] was carried out according to the Niihara approach [22, 23]:

$$K_{1C} = 0.203(c/a)^{-3/2} \cdot H \cdot a^{1/2} \tag{1}$$

where, a – half value of the indentation diagonal, μm; c – crack length, μm; H – microhardness, MPa. For each sample 7 indentations were made and analyzed.

RESULTS AND DISCUSSION

XRD analysis revealed that the raw powder ZrO$_2$+3mol%Y$_2$O$_3$ consists of two zirconia polymorphs. The content of monoclinic zirconia ZrO$_2$-m is 54.9wt%, and content of tetragonal ZrO$_2$-t - 45.1wt%. Estimated CSD size for the ZrO$_2$-m and ZrO$_2$-t phases are 36.6 nm and 40.6 nm, respectively.

It was established that increase in the sintering temperature from 1100ºC to 1650ºC leads to an increase in the density of the sintered samples. Thus, the density of the samples at T = 1450ºC was 5.6...5.7 g/cm^3, and the open porosity was 1.0...1.5%. Increasing the sintering temperatures to T = 1550ºC and T = 1650ºC results in obtaining a denser ceramic (5.9...6.03 g/cm^3) with a linear shrinkage of 14...15%, which is characterized by the absence of open porosity. The characteristics of the sintered samples are given in Table 1.

Table 1. Characteristics of ZrO$_2$ +3mol%Y$_2$O$_3$ samples

Sample No	Sintering temperature, °C	Density, g/cm^3	Total porosity, %	Open porosity, %
T-11	1100	3.6	42	40
T-14	1450	5.7	6.6	1.5
T-15	1550	5.9	3.3	~0
T-16	1650	6	1.6	

Analysis of the grain size evaluation revealed that with the increase in the sintering temperature significant increase in the grain size occurs. Average grain size of samples sintered at 1450ºC, 1550ºC and 1650ºC was 309±23 nm, 563±52 nm and 1000±74 nm, respectively.

It should be noted that after sintering at temperature of 1100ºC the material is still nanocrystalline, since the average grain size is 85±10 nm (Figure 2).
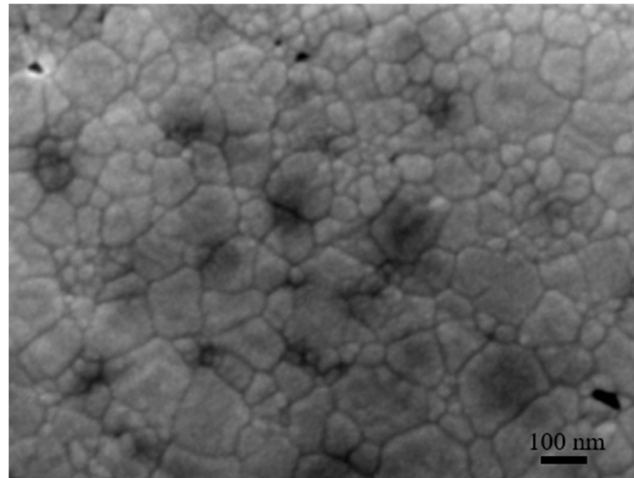

Figure 2. Microstructure of the sample sintered at 1100ºC, 3 hours

Ceramics obtained under these conditions is low-density (3.6 g/cm^3) and remains two-phase: it still consists of both monoclinic ZrO_2-m and tetragonal ZrO_2-t modifications of zirconia, although the content of ZrO_2-t phase increases up to 94.2wt%. Lattice parameters of the ZrO_2-t modification are: a = 0.3607 nm; c = 0.5173 nm and the crystallite size reaches the value of D = 121.7 nm.

In works [5, 6] comparative studies of sintered nanoceramics from partially stabilized zirconia with a similar composition of brands TZ3Y-SE, TZ-3YB (Tosoh, Japan) and Z3Y (BUT, Czech Republic) were carried out. The authors established that low-temperature sintering of ceramics up to 99 % of the theoretical density can be realized for the Z3Y powder at a temperature of 1100ºC/4 hours. At the same time, obtained ceramics remains in nanocrystalline state (grain size is less than 80 nm). However, the sintering of zirconium dioxide nanopowder of the Japanese manufacturer TZ3Y-SE or TZ-3YB at this temperature is insignificant; and increase in temperature to 1460ºC is required to obtain a density of 99 % of the theoretical one. However, the average grain size was already 200 nm [5].

In our case, the difference in the average grain size obtained by the secant method (85 nm) and according to XRD data (121.7 nm) can be explained by the fact that in the secant method the image is analyzed in plane (2D size of grains), while XRD analyzes data in a certain volume of the sample (3D grain size). In [25] similar aspects regarding the average grain size in UO_2 tablets were discussed, and the authors suggested introducing a correction factor of 1.22 to reconcile the measurement results. In addition, the ASTM E112-96 standard introduces a scaling factor of 1.5 for calculating the spatial diameter (3D grain size) [21].

The grain size values, obtained in present study at different sintering temperatures of ZrO_2+3mol%Y_2O_3 ceramics, are shown in Figure 3.
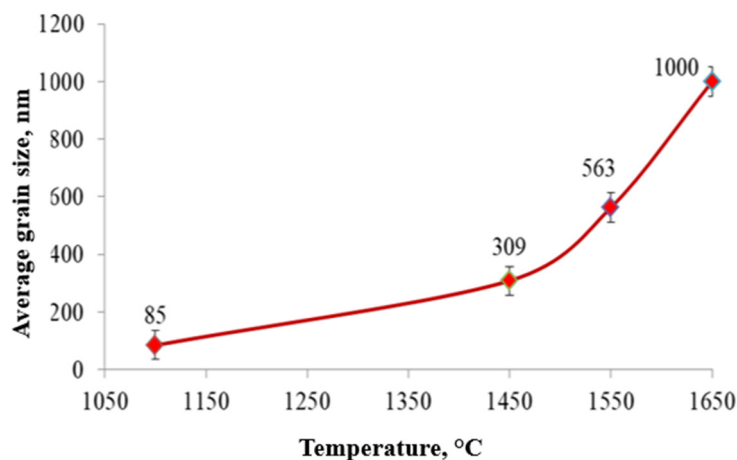
Figure 3. Average grain size values at different sintering temperatures of ZrO_2+3mol%Y_2O_3

As the sintering temperature increases, an active recrystallization process and growth of individual grains occurs, the number of which is small. Thus, sample T-14 is characterized by a fine-grained structure (d$_{90}$ < 500 nm) and the presence of closed pores up to 5 μm in size. The microstructure of sample T-16 is characterized by the predominant grain size d$_{90}$ < 1800 nm, while the maximum grain size is 3.4 μm. The microstructure of these samples is shown in Figure 4.
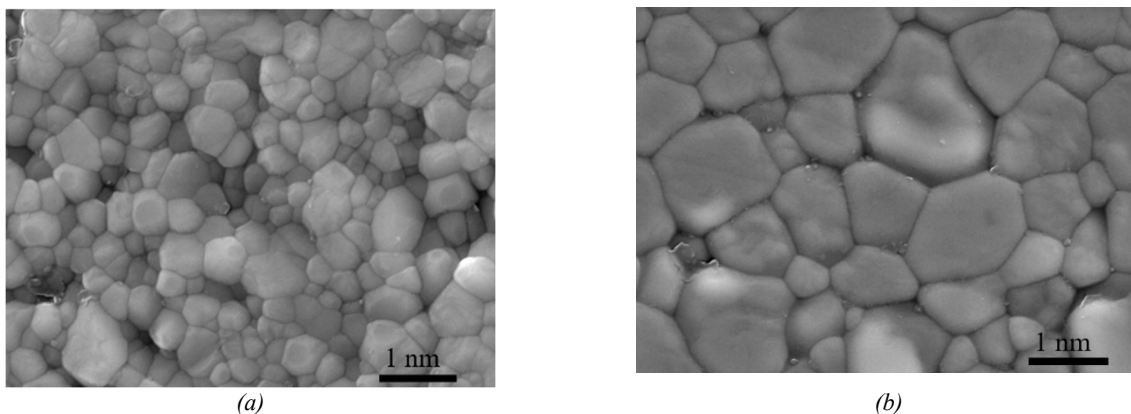
(a)   *(b)*

Figure 4. Microstructure of samples sintered at 1450ºC (a) and 1650ºC (b)

Digital image processing of the T-15 sample microstructure by the graphic analyzer "Thixomet" is presented in Figure 5, and the grain size distribution is shown in Figure 6. The average grain size in this sample is 563 nm, and the maximum grain size is 1.8 μm.
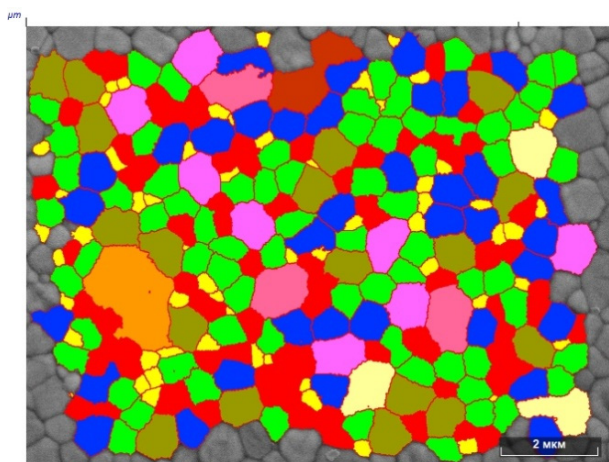

Figure 5. Microstructure of the sample T-15, processed by the Thixomet image analyzer
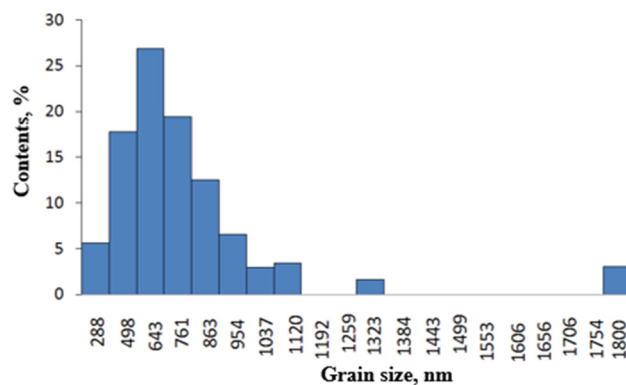
Figure 6. Grain size distribution in the sample T-15 sintered at 1550ºC (calculated by the Thixomet image analyzer)

XRD analysis revealed that samples sintered in the temperature range of 1450...1650°C have an equilibrium structural-phase state: they mostly consist of tetragonal ZrO_2-t modification (85...88)wt%, which is typical for Y-PSZ ceramics [26]. Representative diffraction pattern of samples sintered at temperatures of 1450-1650°C is shown in Figure 7.
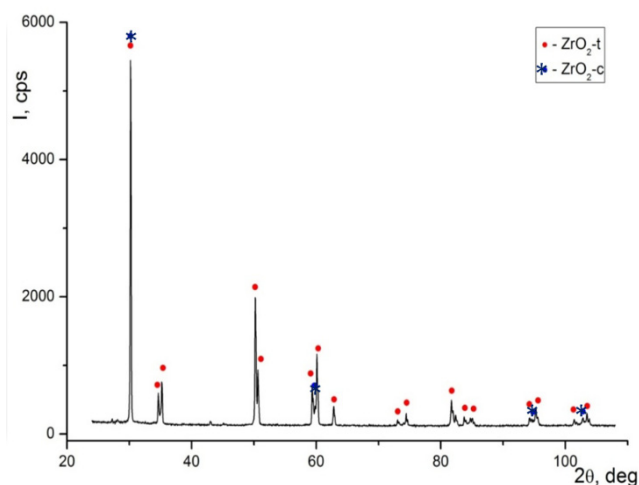

Figure 7. Representative diffraction pattern of samples sintered at 1450...1650 °C

The study of the effect of density and microstructure on some mechanical characteristics of the obtained ceramics consists in determining the critical intensity stress factor (crack resistance K_{1C}) using a technique based on the study of

the characteristics of indentations and cracks, formed by the Vickers diamond pyramid. This technique is characterized by the simplicity of sample preparation and experiment [24-26, 29, 30]. It is known that while loading the surface of ceramic materials with a Vickers indenter, only two types of cracks can be realized: Palmqvist cracks and half-disc (median) cracks [22, 27, 28]. In this regard, a number of researchers propose to use the *c/a* ratio (*c* is the crack length from the center of the indent to the crack tip, and *a* is the half value of the indentation diagonal) to establish the crack type and empirical dependence of processing results. If *c/a* < 2.5, then the cracks are the Palmqvist type, otherwise - median cracks [22]. Another well-known technique of determining the cracks type is to study the cracks after re-polishing the surface of the sample [28, 30]. Interruption of the crack near the indentation corner confirms the presence of Palmqvist-type cracks. In present study, exactly this type of cracks was observed after applied indentation load of 10 kg. The characteristics of the diamond pyramid indentations and cracks for the high-density samples are shown in Table 2.

**Table 2.** Characteristics of $ZrO_2+3mol\%Y_2O_3$ tablets and cracks

Sample No	Density, g/cm^3	a, μm	c, μm	c/a	HV, GPa	K_{1C}, MPa·m$^{1/2}$
T-14	5.7	65.9 (1.2)	141.6 (2.6)	2.15	11.6 (1.3)	5.52 (0.11)
T-15	5.9	62.0 (0.9)	140.0 (2.9)	2.26	12.8 (0.6)	5.56 (0.13)
T-16	6	62.1 (0.7)	128.9(1.5)	2.08	12.2 (0.6)	6.29 (0.11)

in brackets () the mean square deviation is given

It can be seen that with an increase in the density of the samples, there is an increase in microhardness and crack resistance, which is in good agreement with the results in [30]. Obtained ratio *c/a* < 2.5 also indicates the presence of Palmqvist-type cracks and the correctness of the chosen calculating model for K_{1C}. In a number of works [23, 28] it is shown that the calculated value of K_{1C} using various empirical dependencies (Antists, Casellas, Palmqvist, Niihara models) can be very different. In addition, the value of the applied load on the indenter also significantly affects the resulting value of K_{1C}.

It was found that for samples with a close value of density (5.9...6.0 g/cm^3) and an average grain size that differs by a factor 2 (563 nm and 1000 nm, sintered at T = 1550 °C and 1650 °C, respectively), K_{1C} factor is higher for material with a larger grain size. Obtained results are in good agreement with the published data [24], according to which ceramics with the maximum grain size have higher crack resistance. In above work, a sample of ceramics sintered at 1650 °C/10 hours from the partially stabilized zirconium dioxide powder of brand TZ-3YB (Tosoh, Japan) with a close value of density and grain size (6.08 g/cm^3 and 990 nm, respectively) had the value of K_{1C} = 6.4 MPa·m$^{1/2}$ at applied load of 10 kg; with the increase in the indenter load the value of K_{1C} decreased [24].

Study of the nature of the crack's propagation, coming from the indentation corners, revealed the following. For the sample with an average grain size of 562 nm (sintered at 1550 °C) crack propagation has both intercrystalline and transcrystalline nature (Figure 9a).

(a)   (b)
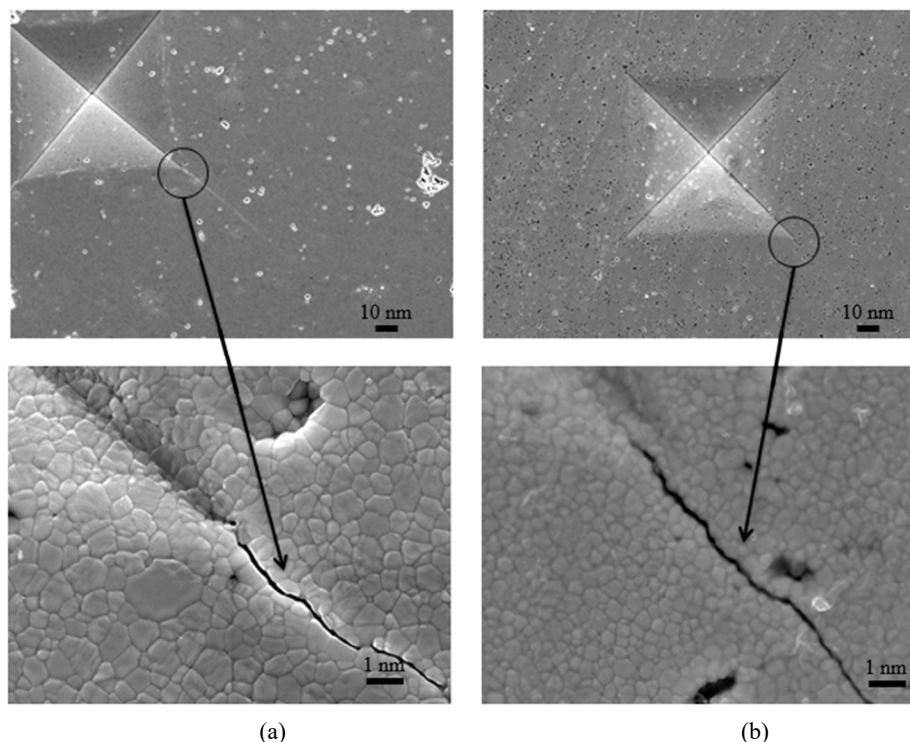
Figure 9. Character of crack propagation in the indentation area of samples with an average grain size of 563 nm (a) and 309 nm (b).

The crack has no significant deviation from its direction. When a large grain is encountered, the latter is destroyed. For the sample with an average grain size of 309 nm (sintering temperature 1450 °C, density 5.7 g/cm^3) the nature of the crack propagation is intercrystalline, since we did not find destroyed grains, which is typical for fine-grained materials in general (Figure 9b).

Thus, the conducted studies showed the possibility of obtaining fine-grained ceramics based on nanosized Y-PSZ powder (ZrO_2+3mol%Y_2O_3) with high physical and mechanical characteristics. Obtained ceramics meet the requirements for the manufacturing of matrices for the incorporation of HLW, as well as for medical and structural purposes.

CONCLUSIONS

Research results showed the possibility of obtaining fine-grained zirconia-based ceramics by cold-pressing and sintering of nanosized Y-PSZ powder (ZrO_2+3mol%Y_2O_3).

The influence of the sintering temperature in the range of 1100...1650 °C on the microstructure of ceramics (ZrO_2+3mol%Y_2O_3) was studied. An increase in the sintering temperature leads to significant increase in the average grain size (from 85 nm to 1000 nm), increase in the density and decrease in the porosity of the samples.

Sintering temperature should be at least 1550...1650ºC to produce dense ceramics (97...98 % of theoretical value). Obtained ceramics is characterized by rather high values of microhardness HV > 12 GPa and crack resistance of 5.5...6.3 MPa·m$^{1/2}$.

ORCID

Igor O. Chernov, https://orcid.org/0000-0003-1424-4471; **Kostiantyn V. Lobach,** https://orcid.org/0000-0002-9838-2259
Sergey Yu. Sayenko, https://orcid.org/0000-0002-2598-3598; **Igor V. Kolodiy,** https://orcid.org/0000-0001-8598-9732
Serhiy V. Lytovchenko, https://orcid.org/0000-0002-3292-5468; **Olexandr V. Pylypenko,** https://orcid.org/0000-0001-7243-2505
Hennadii O. Kholomieiev, https://orcid.org/0000-0003-1779-9050; **Bohdan O. Mazilin,** https://orcid.org/0000-0003-1576-0590

REFERENCES

[1] R. Heimann, T. Vandergraaf, "Cubic Zirconia as a Candidate Waste Form for Actinides Dispositions Studies," J. Mater. Sci. Lett. **7**, 583-586 (1988). https://doi.org/10.1007/BF01730301

[2] S.S. Khin, *Immobilization of actinide wastes in ceramics for long-term disposal*, (Publikations server der RWTH Aachen University, 2006). http://publications.rwth-aachen.de/record/51927/files/Soe_Khin.pdf

[3] S. Saienko, G. Kholomieiev, Zh. Azhazha, L. Ledovskaia, and A. Pilipenko, "Assessing Efficiency of Radioactive Waste Isolation in Containers of Different Materials," Nuclear and Radiation Safety, **3**, 36-42 (2015). https://doi.org/10.32918/nrs.2015.3(67).07 (in Russian)

[4] S.Yu. Sayenko, M.M. Belash, E.S. Gevorkyan, T.E. Konstantinova, O.E. Surkov, V.A. Chishkala, I.A. Danylenko, and F.V. Belkin, "Production of nanoceramics based on zirconium dioxide by hot vacuum pressing," Fizika I tehnika vysokih davleniy, **18**(1), 47-52 (2008). (in Russian)

[5] K. Maca, M. Trunec, P. Dobsak, and J. Svejcar, "Sintering of Bulk Zirconia Nanoceramics," Rev. Adv. Sci. **5**, 183-186 (2003). https://www.ipme.ru/e-journals/RAMS/no_3503/maca/maca.pdf

[6] K. Maca, M. Trunec, and P. Dobsak, "Bulk Zirconia Nanoceramics Prepared by Cold Isostatic Pressing and Presureless Sintering," Rev. Adv. Sci. **10**, 84-88 (2005). https://www.ipme.ru/e-journals/RAMS/no_11005/maca.pdf

[7] D. Sanchita, J.W. Drazin, W. Yongqiang, *et al*., "Radiation Tolerance of Nanocrystalline Ceramics: Insight from Yttria Stabilized Zirconia," Scientific Reports, **5**, 7746 (2015). https://doi.org/10.1038/srep07746

[8] D**.** Sanchita, J. Mardinly, W**.** Yongqiang, *et al*., "Irradiation-induced grain growth and defect evolution in nonocrystalline zirconia with doped grain boundaries," Phys. Chem, Chem. Phys. **18**, 16921-16929 (2016). https://doi.org/10.1039/C6CP01763K

[9] A.N. Velikodnyi, V.N. Voyevodin, M.A. Tихonovsky, V.V. Bryk, A.S. Kalchenko, S.V. Starostenko, I.V. Kolodiy, *et al*., "Structure and properties of austenitic ODS steel 08Cr18Ni10Ti," PAST, 4, 94-102, (2014). https://vant.kipt.kharkov.ua/TABFRAME1.html

[10] I.V. Kolodiy, O.M. Velikodnyi, M.A. Tikhonovsky, V.N. Voyevodin, O.S. Kalchenko, R.L. Vasilenko, and V.S. Okovit, "Microstructure and mechanical properties of oxide dispersion strengthened high-entropy alloys CoCrFeMnNi and CrFe$_2$MnNi," PAST, 2(132), 87-94 (2021), https://doi.org/10.46813/2021-132-087

[11] S. Ukai, and M. Fujiwara, "Perspective of ODS alloys application in nuclear environments," J. Nucl. Mater. **307-311**, 749-757 (2002). https://doi.org/10.1016/S0022-3115(02)01043-7

[12] M. Lubszczyk, J. Wyrwa, K. Wojteczko, *et al*., "Electrical and Mechanical Properties of ZrO2-Y2O3-Al2O3 Composite Solid Electrolytes," J. Electron. Mater. **50**, 5933–5945 (2021). https://doi.org/10.1007/s11664-021-09125-x

[13] R. Parveen, P. Kalita, R. Shukla, *et al*., "Investigation of radiation tolerance of yttria stabilized zirconia in the ballistic collision regime: Effect of grain size and environmental temperature," **551**, 165344 (2024). https://doi.org/10.1016/j.nimb.2024.165344

[14] M.H. Ghaemi, S. Reichert, A. Krupa, M. Sawczak, A. Zykova, S. Sayenko, K. Lobach, and Y. Svitlychnyi, "Zirconia ceramics with additions of Alumina for advanced tribological and biomedical applications," Ceramic International, **43**(13), 9746–9752 (2017). https://doi.org/10.1016/j.ceramint.2017.04.150

[15] A.V. Shevchenko, V.V. Lashneva, E.V. Dudnyk, A.K. Ruban, L.I. Podzorova, "Synthesis and physicochemical properties of ceramics from nanocrystalline zirconium dioxide powder," Nanosystems, Nanomaterials, Nanotechnologies, **9**(4), 881-893 (2011). https://www.imp.kiev.ua/nanosys/media/pdf/2011/4/nano_vol9_iss4_p0881p0893_2011.pdf (in Russian)

[16] A.V. Shevchenko, V.V. Lashneva, E.V. Dudnyk, A.K. Ruban, V.P. Redko, V.V. Tsukrenko, D.G. Verbylo, N.N. Brychevsky, "Manufacturing technology and physicochemical properties of ceramics based on nanocrystalline powder of zirconium dioxide composite," Nanosystems, Nanomaterials, Nanotechnologies, **12**(2), 333-345 (2014). https://www.imp.kiev.ua/nanosys/media/pdf/2014/2/nano_vol12_iss2_p0333p0345_2014.pdf (in Russian)

[17] W. Li, A. Armani, M.C. Leu, *et al*., "Properties of partially stabilized zirconia components fabricated by the ceramic on-demand extrusion process," in: *Proceedings of the 27th Annual International Solid Freeform Fabrication Symposium – An Additive Manufacturing Conference Reviewed Paper*, (2016). https://www.researchgate.net/publication/313158956

[18] S.Yu. Sayenko, "Isolation of radioactive waste using hot isostatic pressing," Nuclear and Radiation Safety, **1**(65), 41-48 (2015). https://doi.org/10.32918/nrs.2015.1(65).10

[19] K.V. Lobach, S.Yu. Sayenko, E.O. Svitlichnyi, and O.E. Surkov, "Application of the electroconsolidation method for obtaining ceramics on the basis $ZrO_2-3\%Y_2O_3$," PAST, 76(6), 99-102, (2011). https://vant.kipt.kharkov.ua/ARTICLE/VANT_2011_6/article_2011_6_99.pdf (in Russian)

[20] E.O. Svitlychnyi, "Preparation of $ZrO_2-3\%Y_2O_3$ ceramics from nanoscale powder and study of its properties," Zbirnyk naukovyh prats PAT "UkrNDIvognetryviv im. A.S. Berezhnogo," **113**, 53-57 (2013). http://nbuv.gov.ua/UJRN/vognetryv_2013_113_9 (in Russian)

[21] ASTM E 112-96 Standard Test Method for Determination Average Grain Size.

[22] K. Niihara, R. Morena, and D.P.H. Hasselman, "Evaluation of K_{1C} of brittle solids by the indentation method with low crack-to-indent ratios," J. Mater. Sci. Lett. **1**, 13-16 (1982). https://doi.org/10.1007/BF00724706

[23] K. Harada, A. Shinya, D. Yokokama, and A. Shinya, "Effect of loading conditions on the fracture toughness of zirconia," Journal of Prosthodomic Research, **57**, 82-87 (2013). https://doi.org/10.1016/j.jpor.2013.01.005

[24] M. Trurnec, "Effect of grain size on mechanical properties of 3Y-TZP ceramics," Ceramics – Silicaty, **52**(3), 165-171 (2008). https://www.ceramics-silikaty.cz/2008/pdf/2008_03_165.pdf

[25] M. Yinbin, M. Kun, M. Laura, *et al*., *Experimental studies of Micro- and Nano-grained UO₂: Grain Growth Behavior, Surface Morphology, and Fracture Toughness ANL/NE-16/12/*, (Nuclear Engineering Division, Argonne National Laboratory, 2016). https://publications.anl.gov/anlpubs/2016/10/130669.pdf

[26] R. Ruh, K.S. Mazdiyasni, P.G. Valentine, and H.O. Bielstein, "Phase relations in the system $ZrO_2-Y_2O_3$ at low Y_2O_3 contents," J. Am. Ceram. Soc. **67**, 190-192 (1984). https://doi.org/10.1111/j.1151-2916.1984.tb19618.x

[27] G.A. Gogotsy, and A.V. Bashta, "Investigation of ceramics by Vickers diamond pyramid," Problemy prochnosti, **9**, 49-54 (1990). https://dspace.nuft.edu.ua/handle/123456789/9764 (in Russian)

[28] D. Coric, R.M. Manic, L. Curkovic, and I. Zmak, "Indentation fracture toughness of Y-TZP dental ceramics," in: *16th International Conference on New Trends in Fatigue and Fracture (NT2F16)*, (Dubrovnic, Croatia, 2016). https://core.ac.uk/download/pdf/79433762.pdf

[29] A.G. Evans, and E.A. Charles, "Fracture Toughness Determination by Indentation," J. Am. Ceram. **59**, 371-372 (1976). https://doi.org/10.1111/j.1151-2916.1976.tb10991.x

[30]   J.-D. Lin, and J.-G. Duh, "Fracture toughness and hardness of ceria and yttria-doped tetragonal zirconia ceramics," Mater. Chem. Phys. **78**, 253–261 (2002). https://doi.org/10.1016/S0254-0584(02)00327-9

ВПЛИВ ТЕМПЕРАТУРИ СПІКАННЯ НА МІКРОСТРУКТУРУ ТА ВЛАСТИВОСТІ КЕРАМІКИ З ОКСИДУ ЦИРКОНІЮ ДЛЯ ПОТРЕБ ЯДЕРНОЇ ЕНЕРГЕТИКИ

І.О. Чернов[a], К.В. Лобач[a], С.Ю. Саєнко[a], І.В. Колодій[a], С.В. Литовченко[b], О.В. Пилипенко[a], Г.О. Холомєєв[a], Б.О. Мазілін[b]

[a]Національний науковий центр "Харківський фізико-технічний інститут", вул. Академічна, 1, 61108, Харків, Україна
[b]Харківський національний університет ім. В.Н. Каразіна, майдан Свободи, 4, 61022, Харків, Україна

У статті наведено експериментальні результати отримання високощільної кераміки на основі ($ZrO_2+3\%Y_2O_3$), яка є перспективною для використання як матриця зберігання високоактивних відходів. Досліджено вплив температури спікання в діапазоні 1100…1650 °C на мікроструктуру спечених таблеток. Фазовий склад і мікроструктуру дослідних зразків було охарактеризовано за допомогою рентгенівської дифрактометрії (РСА) та сканувальної електронної мікроскопії (SEM). Аналіз розподілу зерен за розмірами проводили з використанням аналізатора зображень "Thixomet". Мікротвердість зразків визначали з використанням металографічного комплексу LECO (США), інвертованого мікроскопа IM-3MET і стаціонарного твердоміра UIT HVB-30. Встановлено, що підвищення температури спікання призводить до суттєвого збільшення середнього розміру зерен (від 85 нм до 1000 нм) і підвищення щільності спечених таблеток. Для отримання щільної кераміки (щільність 97...98% від теор.) температури спікання становили 1550…1650ºC, отримані значеннями мікротвердості склали > 12 ГПа та тріщиностійкості 5,5…6,3 МПа·м$^{1/2}$.

Ключові слова: *оксид цирконію; спікання; мікроструктура; мікротвердість; тріщиностійкість*

OPERATION EXPERIENCE OF WESTINGHOUSE NUCLEAR FUEL AT UKRAINIAN NPPs

ⓘ**Valeriy Zuyok***, ⓘ**Roman Rud**, ⓘ**Mykhaylo Tretyakov, Yana Kushtym, Vadym Hrudnytskyy**

"Nuclear Fuel Cycle" Science and Technology Establishment of National Science Center "Kharkiv Institute of Physics and Technology", Kharkiv, Ukraine
*Corresponding Author e-mail: valeriyz@kipt.kharkov.ua

To ensure compatibility with the more robust design of TVSA manufactured by TVEL JSC, a modification of the Westinghouse FA, referred to as RWFA, was announced in 2013, which was designed to be more robust. Since 2015, RWFAs has been in pilot operation and since 2019 in commercial operation in Ukraine. The supply of Westinghouse FAs to Ukraine was under constant supervision and integrity control at all stages of operation and after its end. From the very beginning of the implementation of the WFAs, specialists of SE "NNEGC "Energoatom" and Westinghouse Company with the scientific support of NFC STE NSC KIPT carried out the annual inspections of the fuel assemblies. Based on the inspection results of 86 WFAs/RWFAs after 1-3 years of operation, it was concluded that the obtained values of the parameters characterizing the integrity of WFAs/RWFAs did not exceed the limits set during the FA design and safety substantiation of the core loading where those FAs were operated. All FAs that were subjected to scheduled inspections were loaded in the subsequent fuel cycles.

Keywords: *VVER-1000; Bow; Inspection; Growth; Twist; Fuel Inspection and Repair Equipment; Fuel assembly; Nuclear fuel*
PACS: 28.41.Bm, 28.41.Qb, 28.41.Vx

INTRODUCTION

Modernization and improvement of FA and fuel rod design, optimization of their operation modes is a complex task that includes a large set of design and experimental works. An important place among these works is taken by the examination of fuel assemblies and fuel rods during and after operation in the reactor core. At present, trends in nuclear fuel examination are largely focused on the need to promptly obtain statistically significant data on its condition after operation in a particular fuel cycle, while minimizing the time and cost of such examination. The efficient application of the results of post-irradiation examination depends on the completeness and reliability of the information on the technical condition and performance of the fuel, which in turn depends on the methodological and technical support of the examinations.

Obtaining actual information on the condition of fuel assemblies during and after operation is becoming increasingly important due to the requirement to introduce new fuel cycles with higher burnup and extended lifetime, to ensure the reliability of Rod Cluster Control Assembly (RCCA) operation, to control the quality of fuel assembly manufacturing, and to repair leaking assemblies. For these purposes, foreign countries have experience of using inspection and repair equipment at operating NPPs to monitor and repair leaking fuel assemblies for further use [1-3].

The FIRE (Fuel Inspection and Repair Equipment) for Ukrainian NPPs was designed and manufactured by Westinghouse company to control the technical condition of nuclear fuel, which was provided by the RWFA Licensing Program during its implementation at Ukrainian NPPs since 2014. In that year, a conceptual technical solution was developed for the implementation of advanced design of fuel assemblies (RWFA) at SUNPP Unit 3, and in 2015 the first reloading batch of RWFAs was loaded into the core in the pilot operation mode. The RWFAs are the result of the modernization of the WFAs, which were first loaded in 2010 and also had a more robust design compared to the first trial batch of 6 Lead Test Assemblies (LTAs) loaded in 2005 [4].

It should be noted that fresh nuclear fuel (hereinafter referred to as FNF) for VVER-1000 power units of Ukrainian NPPs was supplied under long-term commercial contracts with TVEL JSC and Westinghouse company. At present, due to the armed aggression of the Russian Federation against the people of Ukraine, the supply of fuel produced by TVEL JSC has been cancelled, but the operation and loading of the already supplied FAs will continue for some NPP units. Thus, RWFAs and WFAs produced by Westinghouse company are gradually replacing TVSAs produced by TVEL JSC at Ukrainian NPPs with VVER-1000 V-320 reactors (units capable of installing FIRE) [5].

The authorized organization for the implementation and operation of the FIRE, including the full range of activities for its development, nuclear fuel inspection and repair at all Ukrainian NPPs, is the SS Atomremontservis (SS ARS) of SE "NNEGC "Energoatom" [5]. The personnel of SS ARS, trained and certified by Westinghouse, carried out nuclear fuel inspections under the supervision of Westinghouse specialists in 2015-2016. Since 2017, the personnel of the SS ARS independently carried out nuclear fuel inspections. Since 2018, the NFC STE NSC KIPT has been processing the nuclear fuel inspection results using independently developed alternative and verified methods that were approved by SE "NNEGC "Energoatom" and Westinghouse company.

The results obtained during fuel inspections by means of the FIRE equipment are necessary to assess the technical condition of the fuel assembly components and to provide additional information to confirm compliance with the

mechanical (strength, deformation), thermal, physical and corrosion design criteria for fuel rods and FAs, which determine their integrity [6-9]. From the scientific point of view, the results obtained by means of the FIRE equipment can be applied to understand the processes occurring in fuel rod and FA materials under irradiation conditions in VVER-1000 core, to assess the stability of geometric parameters of fuel rods and FAs, to predict their further performance, and to substantiate the safe operation of FAs in the next fuel cycles [10].

1. EXPERIENCE Of WESTINGHOUSE FUEL ASSEMBLY IMPLEMENTATION AT Ukrainian NPPs

Westinghouse company designed, developed and manufactured 6 LTAs, which have been operating as part of a mixed core of the South Ukraine Unit 3 since 2005, in order to diversify the nuclear fuel supply for the Ukrainian VVER-1000 type reactors. After the successful completion of the LTAs trial operation, the pilot operation was started and the first full refueling batch of 42 WFAs was loaded into the core of the South Ukraine Unit 3 in 2010.

A more robust design of Westinghouse fuel assemblies, referred to as RWFA, was announced in 2013 to ensure compatibility with the competitor TVSAs, with higher level of structural stiffness, manufactured by TVEL JSC. RWFA has been in operation at Ukrainian NPPs since 2015 in pilot mode and since 2019 in commercial mode. Since that timeWestinghouse enterprises produce only a modified design of RWFA for the needs of Ukrainian NPPs.

Here are the main chronological stages of Westinghouse nuclear fuel implementation at Ukrainian NPPs:
- 2005 – loading of the first 6 Lead Test Assemblies (LTA-1) as part of the mixed core of SUNPP Unit 3;
- 2010 – pilot operation of 42 modernized WFAs started in the core of SUNPP Unit 3;
- 2011 – pilot operation of 42 modernized WFAs started in the core of SUNPP Unit 2;
- 2012 – difficulties in testing WFAs in a mixed core with TVSA fuel assemblies;
- 2013 – announced a more robust design of Westinghouse fuel assemblies (RWFA) compatible with TVSAs in the mixed core;
- 2014 – approval of the Conceptual technical decision on the implementation of RWFA fuel assemblies with improved design at the SUNPP Unit 3;
- 2015 – pilot operation of the first refueling batch of RWFAs in the core of the SUNPP Unit 3 started.

Main key dates of Westinghouse nuclear fuel implementation at Ukrainian NPPs:
- In 2018, SUNPP Unit 3 was the first in Ukraine to fully switch to Westinghouse nuclear fuel after the fourth refueling batch of RWFAs;
- Since December 2019, SUNPP Unit 3 has become the first to receive SNRIU's permission for commercial operation of nuclear fuel from an alternative supplier, Westinghouse company;
- No sooner had the pilot operation of RWFAs been completed than the "Conceptual technical decision "On expansion of pilot operation of RWFAs of advanced design at Ukrainian NPP power units with VVER-1000 reactors (type V-320, V-338)" (KTR-M.13.18-244.15) was approved;
- In accordance with the Conceptual technical decision KTR-M.13.18-244.15, RWFAs have been operating at ZNPP Units 1, 3, 4, 5 since 2016;
- 42 RWFAs started operating at RNPP Unit 3 in 2022.

7 out of 13 VVER-1000 power units operate with Westinghouse nuclear fuel as of 2023, and six power units have already been fully switched to this manufacturer's nuclear fuel.

Table 1. Main periods of Westinghouse fuel implementation at Ukrainian NPPs

No.	Power Unit	First loading of WFA/RWFA*, year	Switch to Westinghouse fuel, year
1	SUNPP-2	2011	2020
2	SUNPP-3	2005	2018
3	ZNPP-1	2017	2021
4	ZNPP-3	2017	2021
5	ZNPP-4	2017	2021
6	ZNPP-5	2016	2020
7	RNPP-3	2022	2025
8	RNPP-4	2024	2027
9	KhNPP-1	2024	2027
*WFAs operated only on SUNPP-2 and SUNPP-3			

2. MAIN DESIGN DIFFERENCES BETWEEN RWFA AND WFA

The design of RWFA is almost similar to that of the WFA, but with higher robustness. Below is a list of designe changes that have been made to the spacer grids (SGs), the lower part of the top and the bottom nozzles [11].
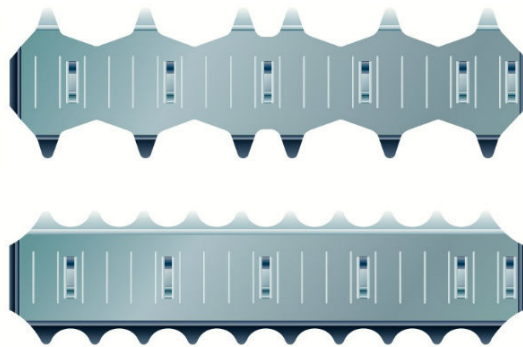
Changes in the SG design:
- SG outer strap tabs were modified to increase stiffness and the number of tabs was increased (every fuel rod location);

- The shape of the outer strap was changed, the thickness of the outer strap and its width in the corners were increased, and a beading along the length of the outer strap was added;
- The material of the midgrids was changed to Inconel (Alloy 718);
- 8 inner straps were added, which were absent in previous design of the midgrids and the top grid.
- Grid width envelope was reduced by 0.25 mm.

Changes in the top nozzle design:
- Sharp edges on legs were smoothed out;
- The top of the adapter plate includes six guiding side plates (Figure 2b) or deflectors (Figure 2c) located along the perimeter to eliminate axial interaction of the top nozzle with the bottom nozzle of an adjacent FA being loaded.


Figure 1. SG outer straps of the WFA (top) and the RWFA (bottom) [11]

| *a* | *b* | *c* |
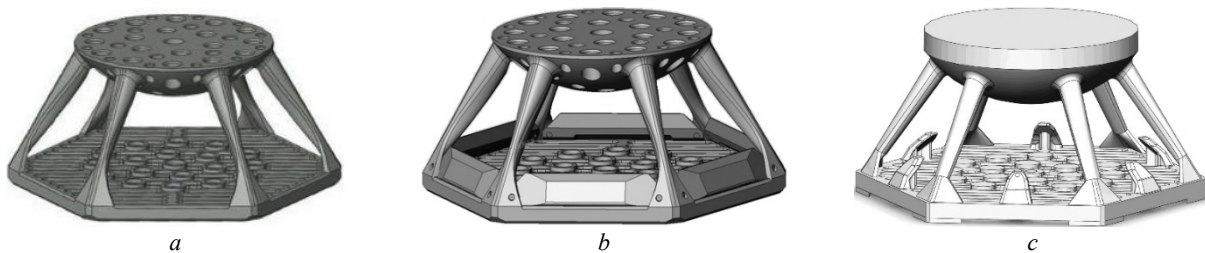
Figure 2. Lower casting machined part of the WFA top nozzle (a) and the modified RWFA (b, c) [11]

Changes in the bottom nozzle design:
- Flat chamfers were tapered on all 6 faces at the hexagonal plane transition to a hemispherical surface to exclude the formation of local loads in the central part of the SG straps in the case of hard contact interaction of the FA with the surrounding FAs under core loading;
- Edges and corners were chamfered.

a)   *Tapered chamfers*   b)   *Chamfered eges*
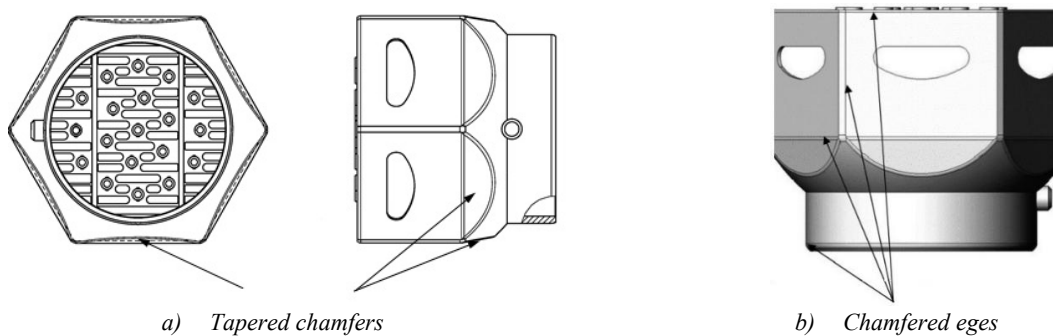
Figure 3. Changes of RWFA bottom nozzle [11]

Fuel rods, guide thimbles, and the barrel assembly of the FA top nozzle remained unchanged. The changes made by the developer increase the robustness of the FAs and facilitate their contact with FAs of other designs during vertical moving, which facilitates transportation and technological operations with FAs. This aspect is very important when loading the core, since the gap between fuel assemblies is only ~ 1 mm.

3. POST-IRRADIATION EXAMINATION OF FAS

From the very beginning of WFA implementation at all stages of its operation and after its completion, specialists of the SE "NNEGC "Energoatom" and Westinghouse company with scientific support of NFC STE NSC KIPT carried

out annual examinations and inspections of irradiated FAs. Also, the process of manufacturing, transportation and receiving inspection of fresh fuel assemblies was carried out at Ukrainian NPP sites under constant supervision of Energoatom specialists and representatives of Westinghouse.

In most cases, only measuring systems are used during scheduled inspections, which are specified in the Nuclear Fuel Inspection Schedule and do not involve FAs disassembling. Further processing of the data obtained by means of these systems allows obtaining values of parameters characterizing the technical condition of FAs (the list of parameters is given in Table 2). In accordance with the technical specification, the measuring systems of the FIRE provide measurement of the main parameters of FAs with an error not exceeding the values given in Table 2.

Table 2. FIRE measuring systems error [5]

No	Parameter, unit	Measuring error
1	FA length, mm	± 0.127
2	FA bow, mm	± 2.54
3	FA twist, deg	± 1.25
4	RCCA drag force, kgf	± 0.5
5	Axial gap, mm	± 1.0
6	Fuel rod growth, mm	± 1.0
7	Fuel rod to rod gap, %	± 10
8	Oxide film thickness on fuel rod cladding, μm	± 5
9	Spacer grid width, mm	± 0.127
10	Diameter of fuel rod cladding, mm	± 0.0051

NFC STE NSC KIPT specialists developed and verified methods for processing measurement results to obtain parameters characterizing the technical condition of fuel rods and FAs. These methods are alternative to the methods used by Westinghouse specialists in their calculations. The error in processing the inspection results does not exceed the error specified in Table 2. This allowed the inspection of nuclear fuel with subsequent processing of the results without involving Westinghouse specialists.

4. MAIN SUMMARIZED RESULTS OF FUEL INSPECTIONS

Starting from 2018, Ukrainian specialists have inspected 56 W/RWFAs at SUNPP Unit 3, ZNPP Units 3 and 5 since the time of systematization of the material and writing this article. At the same time, the Ukrainian specialists processed the results obtained during the fuel inspection at ZNPP Unit 5 in 2017. Thus, the total number of fuel assemblies inspected in the FIRE is 64, and taking into account the inspections performed by Westinghouse specialists during the 2013-2017 refueling outages, it is more than 86 FAs.

Each measurement, the results of which are shown in the graphs, was carried out in the appropriate order during the refueling outage after the end of a particular fuel cycle.

4.1. Visual assessment of FA components condition

Visual assessment of the general FAs condition is carried out on the basis of an assessment of the following FA components appearance:
- spacer grids;
- peripheral rows of fuel rods on six faces along the entire height of FA;
- top and bottom nozzles.

Criteria for visual assessment of FAs are developed by fuel manufacturers and presented in technical specifications, fuel design documentation, substantiation of safe operation, developed and summarized within the framework of scientific and technical support and given in the Methodological Guidelines for Nuclear Fuel Control for NPPs and the Proprietary standard of the SE "NNEGC "Energoatom" [12].

Visual assessment of the FA condition is carried out by visual inspection of the half-width or full width of the assembly face along the entire length. In the process of such an assessment, the fuel assembly is inspected from the top to the bottom nozzle with video recording of the image obtained. Next, the data obtained is processed and their compliance with the design and operational criteria is determined to assess the condition of FA components. The video recording materials are used to monitor the general condition of FAs, in particular, the SG outer straps, the presence of deposits and abnormal corrosion on the surface of fuel rod claddings, debris, and mechanical damage of FA structural components.

A visual inspection of the cladding surface of six fuel rods after four years of operation, removed from different rows of RWFA at SUNPP Unit 3, was performed with the support of the NFC STE specialists. The visual inspection of fuel rods is performed to obtain data to confirm the presence and nonexceedance of the design value of fretting wear in the places of contact of SG dimples and SG springs with fuel rod claddings. The cladding surface condition was analyzed to detect cladding defects that appear during operation in the VVER-1000 core.

The visual inspection results of six fuel rods revealed that after four fuel cycles, traces of interaction in the form of narrow elongated oval-shaped dark-colored strips 0.5-0.7 mm wide and 4-6 mm long located along the fuel rod axial line were observed in the upper part of all fuel rods that were inspected.

Interaction traces the "fuel rod - SG cell" are clearly visible at the levels of SG12-SG16 (Figure 4). Starting from SG8, it was rather difficult to determine the exact location of the "fuel rod - SG cell" contact. In the lower part of the fuel rod (including the area of the bottom end plug), it was almost impossible to identify the area of contact "fuel rod - SG cell".

No fuel rod cladding damage, corrosion damage (pitting, debris, fretting), or deposits of structural materials corrosion products of the primary circuit on the surface of fuel rod claddings were detected during the entire period of scheduled fuel inspections. The spacer grid outer straps surface was free of deformation, mechanical and corrosion damage. Some SGs had single and numerous longitudinal scratches formed as a result of transportation and technological operations with FAs.

No debris was found stuck between SGs and fuel rods or between fuel rods. Some FA top and bottom nozzles had single longitudinal minor scratches. No significant inhomogeneity of the surface of all inspected FA top and bottom nozzles was detected.
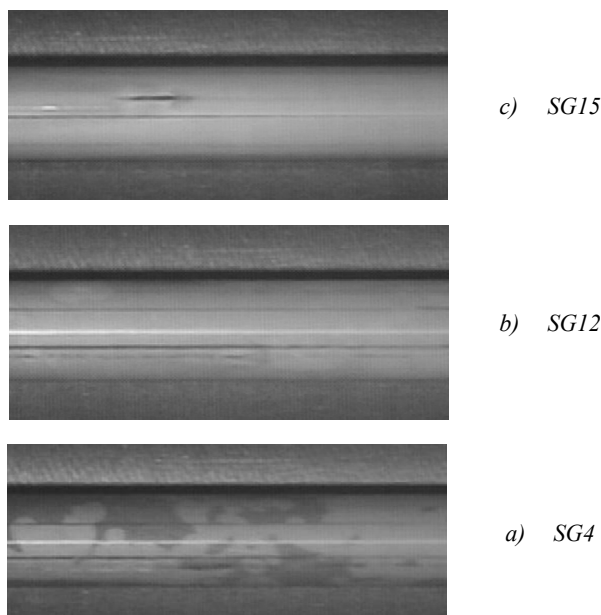

c)   SG15

b)   SG12

a)   SG4

Figure 4. Segments of fuel rods in areas of contact with SGs [5]

4.2. FA growth

When operating in the core, as a result of intense neutron irradiation, WFAs/RWFAs are being subject to the combined effects of radiation growth and radiation-thermal creep, which manifest themselves in the form of an increasing length of guide thimbles made of zirconium alloys. The length change of the guide thimbles also depends on the axial loads acting from the FA top nozzle springs. Figure 5 shows the dependence of the change in the nominal length on the average burnup of all FAs inspected by means of the FIRE.
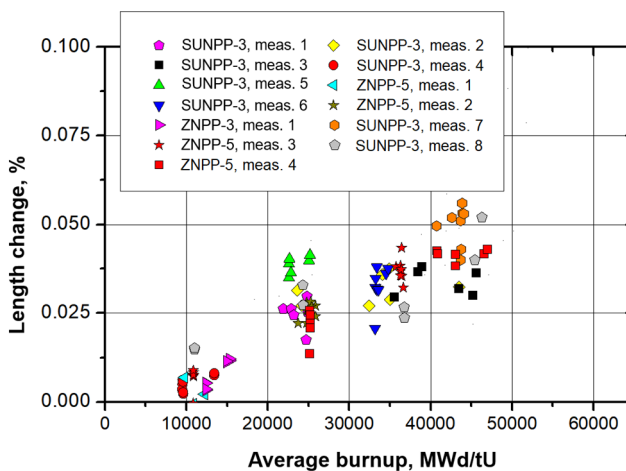

Figure 5. Generalized dependence of the nominal length change on the average burnup of WFAs/RWFAs [5]

According to the data obtained, there is a quasi-linear increase in fuel rod length throughout the entire period of operation. For FAs with a maximum burnup of ~ 46 GW·day/tU (after four years of operation), the average elongation is

0.05%. The growth rate of WFAs/RWFAs is comparable to the growth rate of FAs of other designs with ZIRLO® guide thimbles.

These measurements made it possible to confirm that the growth of the WFA/RWFA guide thimbles is below the expected value and does not exceed the design limit used in the safety analysis to calculate the stress-strain state of the guide thimbles and the FA top nozzle springs.

4.3. FA bow and twist

The deformation and bow of FAs in the core depend on the transverse stiffness of FA, the strength of its skeleton, and operating conditions. The bow deformation and bow shape of FAs with the same design and the same service life may differ significantly. Such differences are mainly due to the following factors: thermal load, location in the core, and design of the adjacent FAs.

Bow and twist are among the most important parameters that affect the reliable and safe operation of a particular FA design. These parameters also affect the drag force of RCCAs in FA guide thimbles and the drag force when inserting/removing FAs in/from the core.
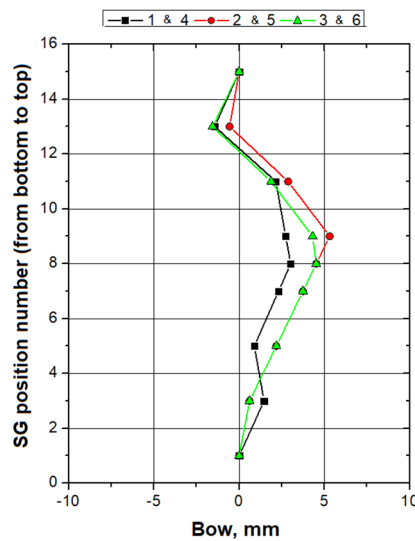

Figure 6. The RWFA bow measurement results [5]

The FIRE equipment and developed methods make it possible to obtain the values of the FA bow with regard to the top and bottom nozzle of the FA along three faces and with visualization (graphical representation) of the bow depending on the height of the FA assembly (see Fig. 6) [13].

The bow of Westinghouse FAs, as well as TVEL FAs, is characterized by a "C" or "S" shape. FAs can simultaneously have both "C" and "S" bow shapes in the core.

When designing the FA and substantiating its safe operation, the maximum bowing parameter (≤ 30 mm) and the maximum twist angle (≤ 5 degrees) were used, which guarantees the movement of the RCCA in the guide thimbles and the insertion of FA in the core with forces that do not exceed the design value.
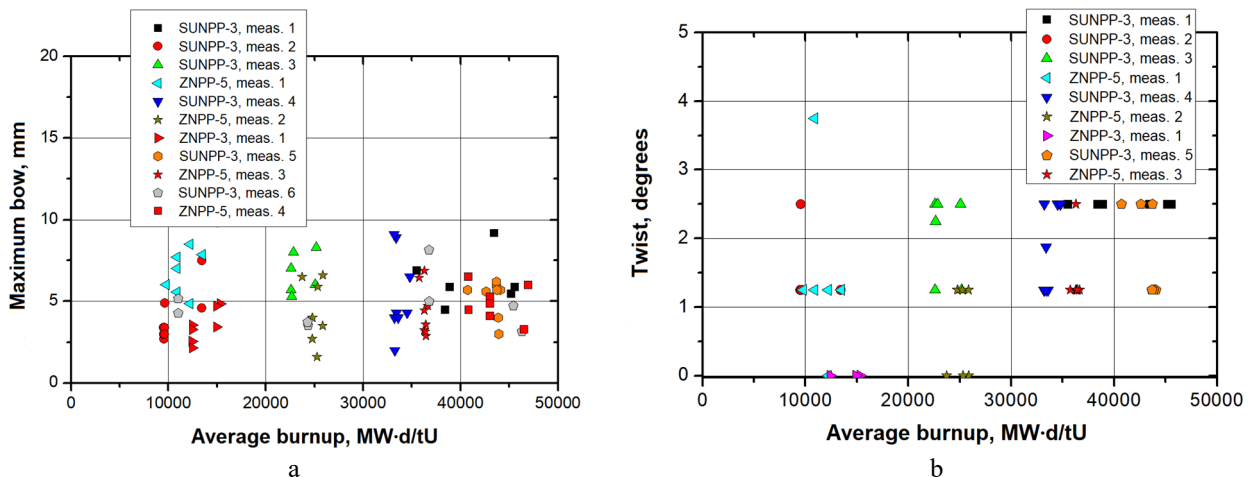

a   b

Figure 7. Generalized dependence of the change in maximum bow (a) and twist angle (b) on the RWFAs average burnup that have been inspected by means of FIRE [5]

Figure 7 shows the dependence of the change in maximum bow (a) and twist angle (b) on the average burnup of RWFAs that were inspected by means of FIRE.

Based on the results of measuring the WFAs/RWFAs geometric parameters, it was found that the deformation (bow and twist) of FAs does not depend on burnup (see Fig. 7) and is dependent on the stiffness of the FA skeleton. According to Figure 7, the bow of WFAs/RWFAs within the burnup range of 9000-46000 MW·day/tU remains constant and varies from 1.6 mm to 9.86 mm, and the twist angle averages 2.5 degrees.

4.4. RCCA drag force when loading/unloading into/from the FA

The RCCA drag force in guide thimbles is a characteristic of the stability of FA geometric parameters. The maximum RCCA drag force in FA is established and substantiated by the fuel manufacturer based on operational experience, while meeting the regulatory requirements for the RCCA fall time. This value should not exceed 8 kgf for WFAs and 14.7 kgf for RWFAs. Exceeding the design limit of the RCCA drag force may result from FA deformation (large bow or twist, complex bow shape) and, when the emergency protection is tripped, may lead to an increase in the RCCA insertion time, incomplete insertion, and even jamming in guide thimbles.

The RCCA drag force is measured when the RCCA simulator is dragged along almost the entire height of the FA guide thimbles [13]. The drag force has a different value at different FA heights with a maximum at the bottom part of FA (the RCCA is inserted along the entire length of FA). Also, the drag force differs when the RCCA moves up and down. For FAs that have been inspected, the RCCA drag force is higher when inserting the into the guide thimbles than when withdrawing it.
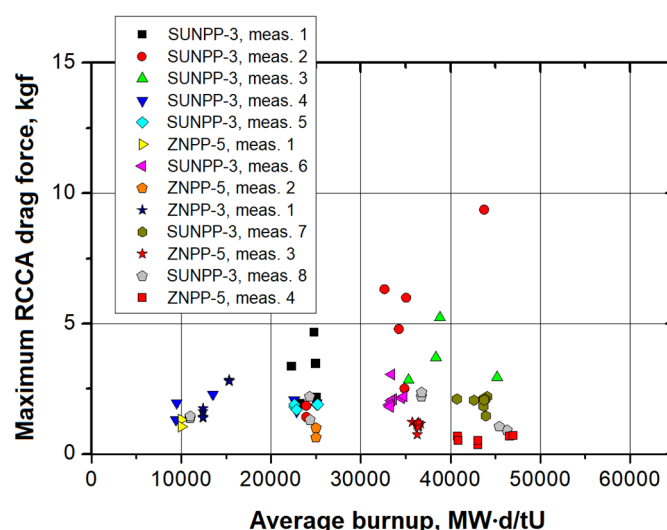

Figure 8. Generalized dependence of the RCCA maximum drag force in the guide thimbles on the WFAs/RWFAs average burnup [5]

The dependence of the RCCA maximum drag force in the guide thimbles on the average WFAs/RWFAs burnup based on the data obtained by means of the FIRE is shown in Figure 8.

The maximum drag force when the RCCA being inserted into the WFA/RWFA guide thimbles is in the range from 1 kgf to 7 kgf, which is significantly lower than the maximum design limit (14.9 kgf) [12]. In most cases, the drop time of the RCCA does not exceed 1.5 s.

4.5. Axial gap between fuel rod end plugs and the adapter plate of top nozzle and the top plate of bottom nozzle

The axial gap in WFAs/RWFAs is the total gap between the fuel rod end plugs and the adapter plate of top nozzle and the top plate of bottom nozzle. The size of the gap depends on the change in the length of the FA guide thimbles and the change in the fuel rod length due to radiation-thermal creep and radiation growth. For all designs of FAs, the axial gap should be maintained within the limits that exclude jamming, further bow and damage of fuel rods during the entire service life and fuel storage (or other fuel operations). The design limit specifies that during a four-year fuel cycle, radiation and thermal growth of WFA/RWFA components (guide thimbles, fuel rods/burnable absorber rods) should not result in a decrease in the axial gap of less than 20.5 mm.

The FIRE systems are designed to estimate the axial gap for all fuel rods/burnable absorber rods and measure it for the peripheral row [13]. Figure 9 shows the dependence of the average axial gap between fuel rods and the adapter plate of top nozzle and the top plate of bottom nozzle on the WFA/RWFA average burnup. As the burnup increases, the axial gap decreases linearly.

The data obtained during the inspections indicate that the minimum axial gap for fuel WFAs/RWFAs is at least 34-37 mm, which is significantly higher than the design limit set for a 4-year fuel cycle (20.5 mm) [13]. This measurement allowed to confirm that for all FAs that were inspected, the axial gap will remain within the limits that exclude jamming, further bow and damage to the fuel rods throughout their entire service life.
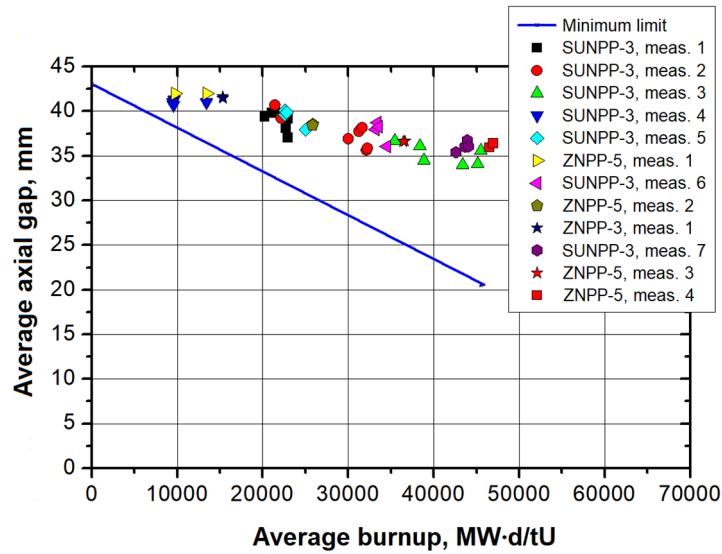
Figure 9. Dependence of the average axial gap between fuel rod end plugs and the adapter plate of top nozzle and the top plate of bottom nozzle on the WFAs/RWFAs average burnup [5]

4.6. Fuel rod growth over 6 faces of FAs

An important aspect under operation is the deformation of zirconium alloy components, which determines the performance of the entire core. Fuel rod growth is caused by radiation effects, which occur as radiation-thermal creep and radiation growth. Therefore, when licensing fuel, one of the criteria is deformation, which sets the limit values for the diameter change and fuel rod/burnable absorber rod growth. With this purpose, the diameter change and fuel rod cladding length are calculated at the design stage, and measurements performed by means of FIRE should confirm the correctness of the calculations. The limit value of the cladding deformation for the stationary fuel rod operation at the end of the fuel cycle should be less than 1%.
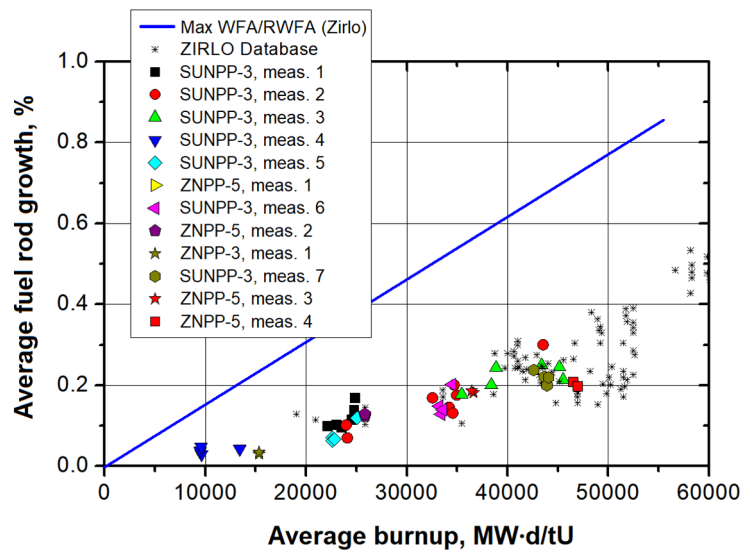

Figure 10. Dependence of the average fuel rod growth in WFAs/RWFAs on the average burnup [5]

The FIRE systems allow estimating the growth of all fuel rods/bunable absorber rods and measuring it for the peripheral row [13]. Figure 10 shows the dependence of the average peripheral row fuel rod growth on the average FA burnup in comparison with the values of the Westinghouse database. According to the data presented (see Fig. 10), in the burnup range of 9000-46000 MW·day/tU, a linear increase in fuel rod length occurs with an increase in burnup. Based on published information, when burnup is reached, above which there is a tight contact of the fuel pellet with the cladding, this fuel rod deformation trend may change [6, 7].

According to the accumulated experience of nuclear fuel inspections at Ukrainian NPPs, the average fuel rod growth in WFAs/RWFAs with a burnup of ~46 GW·day/tU is within 0.21...0.30%. Such growth does not lead to a decrease in the axial gap below the expected value for a given burnup depth (~ 34...37 mm) and, accordingly, is below the safety limit for FAs operation.

The use of the FIRE made it possible to confirm that the maximum value of cladding deformation for the standard operating mode of fuel rods at the end of the fuel cycle does not exceed the safe operation limit for each FA type operating at Ukrainian NPPs.

4.7. Profilometry of RWFA fuel rod claddings
Under reactor core irradiation, an increase in the burnup is accompanied by a decrease in the fuel rod cladding diameter due to radiation and thermal creep. Upon reaching a certain burnup depth, when the cladding-fuel pellet gap disappears, the cladding diameter begins to increase again due to fuel pellet swelling.
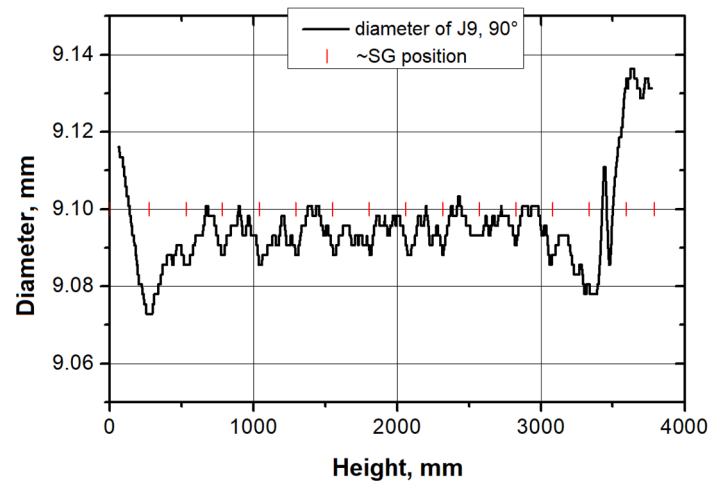
Figure 11. Distribution of the cladding diameter in mutually perpendicular directions along the height of the fuel rod J9 [5]

Measurements of the diameter of a single fuel rod are performed with the fuel assembly disassembled and the fuel rod removed. In most cases, to substantiate the fuel rod operability, it is necessary to determine not the diameter of the fuel rod at a certain height, but the change in diameter along the entire length of the fuel rod (profilometry). The profilometer head is equipped with two linear variable differential transformers (LVDTs). The fuel rod is placed between the tips of the LVDTs and the roller guides opposite the LVDTs. The outer diameter of the fuel rod causes the relative displacement of the linear transformer and generates a voltage corresponding to the size of the fuel rod with an accuracy of 5 μm (see Table 2). At the time of this article writing, profilometric measurements were performed only for 6 fuel rods/burnable absorber rods of one RWFA after the fourth year of operation.

The diameter of fuel rod/burnable absorber rod claddings in RWFAs before irradiation in the core is 9.144 mm and may differ from the specified size by +0.037/-0.038 mm. The tolerance for fuel rod/burnable absorber rod ovality is 0.025 mm.

In all cases, for the inspected FAs, the maximum change in the cladding diameter did not exceed 0.66% (see Fig. 11), which is below the design limit of 1% [13]. The maximum ovality is 0.020 mm and almost coincides with the design value, but is below the design limit obtained during the substantiation of the operation of these FAs (> 0.050 mm).

The FIRE provided a confirmation that the maximum value of the fuel rod cladding diameter changes at the end of the fourth fuel cycle did not exceed the safe operation limit.

4.8. Fuel rod to rod gap on 6 faces along the entire height of FA
The results of the fuel rod to rod gap estimation are necessary to confirm compliance with the thermophysical criteria and to prevent overheating of fuel rods. The maximum value of the reduction of the rod-to-rod gap should not exceed 50% for WFAs/RWFAs. If the value exceeds the maximum value, overheating of fuel rod cladding or localized power increase may occur.

The FIRE systems provide the capability to estimate the rod-to-rod gap on 15 spans between the SGs [13], but only for the visible (11 rods) rods of the peripheral row along all 6 faces.

According to the accumulated experience of fuel assemblies' inspection at Ukrainian NPPs, the maximum value of the rod-to-rod gap reduction for all designs of FAs operated at Ukrainian NPPs does not exceed 13-15%. In one case, a 33.7% reduction of the rod-to-rod gap was detected for WFA with a burnup of ~ 46 GW·day/tU. At the same time, no dependence of the rod-to-rod gap on the burnup was observed. The obtained values made it possible to confirm the meeting of this criterion.

### 4.9. Oxide film distribution on the fuel rod cladding along the height
For Westinghouse fuel rod claddings made of ZIRLO, the meeting of thermophysical and mechanical criteria is ensured at an oxide film thickness not exceeding 101.5 μm within the design life [12]. The local thickness of the oxide film on the fuel rod cladding, calculated for a unilateral confidence level of 99%, should not exceed 152.4 μm.

The FIRE oxide film thickness measurement system provides measurements on the fuel rod section between successive SGs along the entire FA height [13]. Figure 12 shows the dependence of the oxide film thickness on the cladding surface of the six inspected fuel rods after the fourth year of operation on the height coordinate of the fuel assembly. As can be seen from the dependence, the thickness of the oxide film varies with the height coordinate of fuel rods. The maximum oxide thickness is observed in the upper part of FAs.
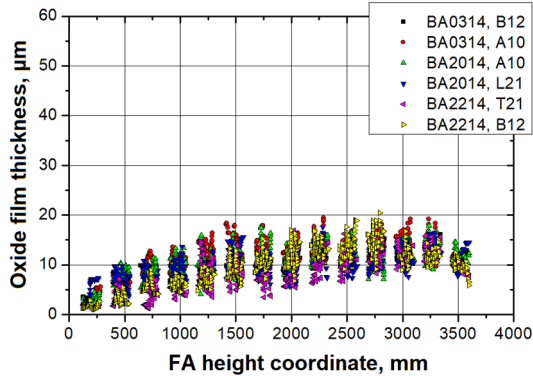
Figure 12. Distribution of oxide film thickness along the height of six inspected fuel rods of different FAs after four years of operation [5]
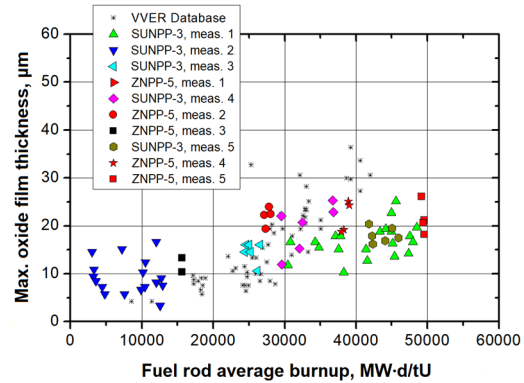
Figure 13. Dependence of the maximum oxide film thickness on the average burnup of fuel rods [5]

Figure 13 demonstrates the dependence of the maximum oxide film thickness on the average fuel rod burnup. The maximum oxide thickness on the fuel rod claddings after the fourth year of operation is in the range of 13...25 μm. Oxide film was dense, without cracks and delaminations, and exhibited good reflectivity at all height coordinates. The color of the cladding surface varies from dark gray in the lower part to light gray in the upper part of the fuel rod. Also oxide spots and contours of varying contrast and size are observed.

The obtained results of thickness measurements on the fuel rod surface are significantly lower than the maximum design limit (< 101.5 μm) set at the design stage and when obtaining a license for fuel operation in the core. Accordingly, the use of FIRE allowed to confirm the meeting of this criterion.

4.10. Spacer grid width

The change of the spacer grid width, caused mainly by radiation growth, depends on the neutron fluence, irradiation exposure time, FA position in the core, and the material of the spacer grid (zirconium alloy, Inconel). For SGs made of zirconium alloys, the width increase is caused by two mechanisms: radiation growth and volume increase as a result of hydrogenation. The maximum increase of SG width is limited by the gap between the adjacent FAs. For WFA/RWFA, the maximum grid width should not exceed 235.1 mm. Two modifications of FAs manufactured by Westinghouse are in operation at Ukrainian NPPs:

   - up to 2015, WFAs with SGs made of Zircaloy-4 and Alloy 718 (Inconel 718);
   - after 2015, RWFAs with SGs made of Alloy 718;
   - starting from 2019, the operation of two designs of Westinghouse FAs with two types of SGs continued at SUNPP Unit 3.

The FIRE [13] and the methodology for calculating the growth hexagonal SGs allow obtaining the minimum, maximum, average, and absolute values of SG width. The SG width is calculated between two parallel faces of the SG. Figure 14 shows the width of each of the SGs of one RWFA (a) after four years of operation and one RWFA (b) after three years of operation.

a

b
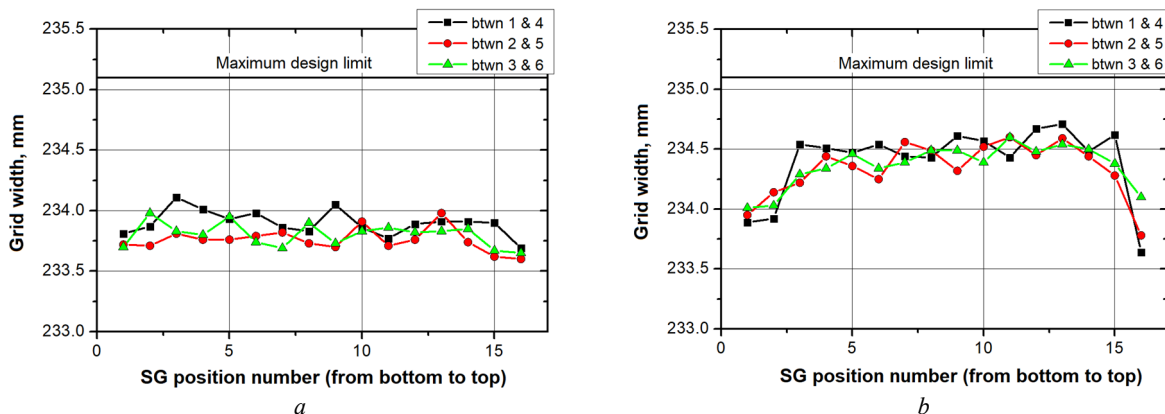
Figure 14. Dependence of the average SG width for mutually parallel faces on the height position of RWFA (a) and WFA (b) after four and three years of operation, respectively [5]

As expected, there is almost no change in the width of RWFA SGs made of Alloy 718 under irradiation. Grid width measurements of four FAs were performed for four years. The dependence of 16 SGs width change of one of these FAs on the burnup is shown in Figure 16. The results obtained during the inspection period are within the measurement accuracy of the ultrasonic inspection system and reveal that the SGs made of Alloy 718 do not change their width under the influence of irradiation during four fuel cycles.
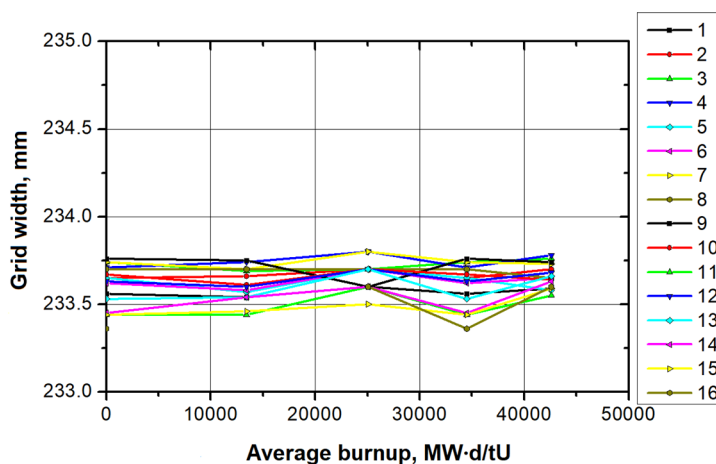
Figure 15. Dependence of the change in the average spacer grid width on the average burnup for one of the inspected RWFAs [5]

For WFAs, after three years of operation, the distribution of width for SGs made of zirconium alloy along the height of the fuel assembly (see Fig. 14.b) shows a maximum in the upper part of FA. The change of grid width is comparable to the FA burnup profile, which indicates the influence of radiation growth on the change of SG dimensions. At the time of systematization of this material, there is no data on the width of the above mentioned SGs after four years of operation, which does not allow to plot the dependence of SG width on the WFA average burnup similar to that shown in Figure 15.

During the inspection, the results of the grid width measurements confirmed that the SG width of both RWFAs and WFAs is below the design limit of safe operation (235.1 mm) [12], which was established at the design stage and when obtaining a license for fuel operation in the VVER-1000 core.

CONCLUSIONS

1. As of 2023, 7 out of 13 VVER-1000 power units operate Westinghouse nuclear fuel. Six power units have already been fully implemented the nuclear fuel from this manufacturer, and RNPP Unit 3 started operating with RWFAs in 2022.

2. The main differences between RWFAs and WFAs that were introduced in the modification are as follows: spacer grids (the shape and thickness of the outer strap were changed, 8 inner straps were added, and the material of the middle grids was replaced with Alloy 718); top nozzle (chamfers were made on sharp edges and guiding side plates or deflectors were added); bottom nozzle (pyramidal tapers were added on all 6 faces, sharp edges were chamfered). These changes increase the stiffness of the fuel assemblies and facilitate interaction with FAs of other designs during their vertical movement, which facilitates transport and technological operations with FAs.

3. The supply of Westinghouse nuclear fuel to Ukrainian NPPs was performed under constant supervision and inspection of its condition during operation and after its completion. From the very beginning of WFA implementation, annual inspections of FAs were carried out by SE "NNEGC "Energoatom" and Westinghouse specialists with scientific support of NFC STE NSC KIPT.

4. The results of nuclear fuel inspections during the 2017-2021 refueling outages at ZNPP Units 3 and 5 and SUNPP Unit 3 were accumulated and systematized. The values of parameters characterizing the technical condition of more than 86 WFAs/RWFAs with a burnup of up to 46 GW·day/tU were calculated.

5. The obtained values of the parameters characterizing the technical condition of WFAs/RWFAs are demonstrated to not exceed the limits set when designing the fuel and substantiating the safety of the fuel loading. All fuel assemblies inspected after 1-3 years of operation were loaded in subsequent fuel cycles. The values of the parameters characterizing the technical condition of WFAs/RWFAs after four fuel cycles indicate that the nuclear fuel did not exhaust its resource and has a sufficient margin of controlled parameters to achieve higher burnups.

6. Based on the results presented in the paper, the main conclusion was made that the technical condition of WFAs/RWFAs manufactured by Westinghouse and operated in Ukrainian VVER-1000 reactors fully meets the safety requirements that were set out in its design and substantiation of safe operation. In the case of damage or leakage of fuel rods in the Westinghouse fuel assemblies, they can be repaired due to their removable design and repair tool such as the FIRE, and are much more maintainable than TVSAs manufactured by TVEL JSC.

ORCID

Valeriy Zuyok, https://orcid.org/0000-0003-4256-1714; **Roman Rud,** https://orcid.org/0009-0000-8430-7015
Mykhaylo Tretyakov, https://orcid.org/0000-0003-0062-8984

REFERENCES

[1] IAEA-TECDOC-1050. Poolside Inspection, Repair and Reconstitution of LWR Fuel Elements, in: *Technical Committee Meeting*, *IAEA,* (1998). https://www-pub.iaea.org/MTCD/Publications/PDF/te_1050_prn.pdf

[2] Examination of Fuel Assembly for Water Cooled Power Reactor, in: *Specialists Meeting, Tokyo*, Japan 9-13 November 1981. (IAEA, Vienna, 1982).

[3] N.A. Ivanov, D.V. Bromirskij, D.V. Surov, L.A. Pervushin, A.N. Tishkov, A.V. Sementsov, S.V. Pavlov, and S.V. Amosov, "Fuel assembly inspection and repair stand for AES-2006 project," Tyazheloye Mashinostroyeniye, 25-28, (2017). https://sosny.ru/files/publications/TM_%204_2017.pdf

[4] A. Abdullayev, Y. Aleshin, G. Kulish, P. Lashevich, R. Latorre, O. Slyeptsov, S. Slyeptsov, *et al*., "Westinghouse Fuel Assemblies Performance after Operation in South-Ukraine NPP Mixed Core," in: *10th International Conference on WWER Fuel Performance, Modelling and Experimental Support*, (Sandanski, Bulgaria, 2013).

[5] V. Zuyok, V. Krasnorutskyy, V. Grytsyna, R. Rud, M. Tretyakov, Y. Kyshtym, V. Hrudnytskyy, *et al*., "Experience of Irradiated Nuclear Fuel Examination at Ukrainian NPPs Using Fuel Inspection and Repair Equipment," Nuclear and Radiation Safety, **95**(3), 48-63 (2022). https://doi.org/10.32918/nrs.2022.3(95).05

[6] S.V. Pavlov, "Methods and Means of VVER FAs Research for Experimental Support of New Fuel Implementation at NPPs," Dr.Sci. Thesis, Dimitrovgrad, 2015.

[7] D.V. Markov, "Main regularities of changes in properties and characteristics of new-generation VVER and RBMK fuel during operation based on the results of complex post-irradiation studies," Dr.Sci. Thesis, Moscow, 2017.

[8] E.A. Zvir, V.B. Ionov, S.V. Pavlov, *et al*., *Post-irradiation condition of VVER fuel rods and FAs*, (Atlas, 2013).

[9] J.W. Roddy, H.C. Claiborne, R.C. Ashline, P.J. Johnson, and B.T. Rhyne, *Physical and decay characteristics of commercial LWR spent fuel*, in: *ORNL/TM-959 l/Vl and Rl*, (Oak Ridgenational Lab, 1986).

[10] I.D. Sokolova, "Experience of fuel operation in PWR reactor," Atomnaya tehnika za rubezhom, **6**, 3-11 (2010).

[11] M. Dye, and H. Shah, "Enhanced Westinghouse WWER-1000 Fuel Design for Ukraine Reactors," in: *Proceedings of 11th International Conference on WWER Fuel Performance, Modelling and Experimental Support*, (Bulgaria, 2015).

[12] State enterprise standard of SE "NNEGC "Energoatom" 170:2019 "Nuclear Fuel Handling. Nuclear fuel control by means of fuel inspection and repair equipment", 2019.

[13] IE-I.61.001-15, Instructions for operation of FIRE and measurement systems included in it. State Enterprise "National Nuclear Energy Generating Company "Energoatom", Separate subdivision "Atomremonservis" SS ARS of SE "NNEGC "Energoatom".

ДОСВІД ЕКСПЛУАТАЦІЇ ЯДЕРНОГО ПАЛИВА ВЕСТІНГХАУЗ НА АЕС УКРАЇНИ

Валерій А. Зуйок, Роман А. Рудь, Михайло В. Трет'яков, Яна О. Куштим, Вадим В. Грудницький
Науково-технічний заклад «Ядерний паливний цикл» Національного наукового центру
«Харківський фізико-технічний інститут», Харків, Україна

Для забезпечення сумісності з більш жорсткою конструкцією ТВЗА компанії АТ "ТВЕЛ" у 2013 році було анонсовано модифікацію ТВЗ компанії Westinghouse під назвою ТВЗ-WR також з більш жорсткої конструкції. ТВЗ-WR експлуатується в Україні з 2015 року в режимі дослідно-промислової експлуатації, а з 2019 року – в промисловій експлуатації. Підприємства компанії Westinghouse виробляють тільки ТВЗ-WR для потреб АЕС України. Постачання ТВЗ Westinghouse для України відбувалося під постійним наглядом та контролем на всіх етапах експлуатації та після її завершення. З самого початку впровадження ТВЗ-W, спеціалістами ДП «НАЕК «Енергоатом» та компанії Westinghouse при науковій підтримці НТК ЯПЦ ННЦ ХФТІ, проводились щорічні обстеження паливних збірок. За результатами обстежень близько 86 ТВЗ-W/WR компанії Westinghouse після 1-3 років експлуатації було зроблено висновок, що отримані значення параметрів, які характеризують технічний стан ТВЗ-W/WR, не перевищують межі, закладені при проєктуванні палива та обгрунтуванні безпеки паливних завантажень, в яких експлуатувалися зазначені ТВЗ. Всі ТВЗ, планова інспекція яких проводилася після 1-3 років експлуатації, використовувалися у наступних паливних завантаженнях.

Ключові слова: *ВВЕР-1000; вигин; інспекція; подовження; скручування; стенд інспекції і ремонту палива; тепловидільна збірка; ядерне паливо*

ELASTIC PROPERTIES OF C-TYPE LANTHANIDE SESQUIOXIDES

Pooja Yadav[a], Dheerendra Singh Yadav[b], Dharmvir Singh[a], Pravesh Singh[c], Ajay Singh Verma[d,e,*]

[a]Department of Physics, Agra College, Agra 282002, India
[b]Department of Physics, Ch. Charan Singh P G College Heonra (Saifai) Etawah 206001, India
[c]Department of Electronics and Communication Engineering, KIET Groups of Institutions, Ghaziabad 201206, India
[d]Division of Research & Innovation, School of Applied and Life Sciences, Uttaranchal University,
Uttarakhand, Dehradun 248007, India
[e]University Centre for Research & Development, Department of Physics, Chandigarh University,
Mohali, Punjab 140413, India
*Corresponding Author e-mail: ajay_phy@rediffmail.com
Received August 8, 2024; revised November 5, 2024; accepted November 7, 2024

In this study, we have presented the solid-state theory of plasma oscillations to investigate the anisotropic elastic properties such as three independent static elastic stiffness constants (C_{ij}: C_{11}, C_{12} & C_{44}) of C-type Ln_2O_3 lanthanide solids. The calculated values of the static elastic stiffness constants of Ln_2O_3 are in excellent agreement with the theoretical results obtained by using ab-initio techniques. The values of elastic stiffness constants (C_{ij}) exhibit a linear relationship when plotted against their plasma energies and lie on a straight line. To further examine the validity of the present estimations on elastic moduli and other parameters of these materials. The mechanical moduli such as bulk modulus (B), shear modulus (G), Young modulus (E), Poisson's ratio (ν), shear wave constant (C_s), Cauchy pressure (C^*), Lame's coefficient (λ and μ), Kleinman parameter (ξ) Grunesien parameter (γ), Zener anisotropic constant (Z) and Pugh ratio (G/B) of lanthanide solids have also been investigated. For the lanthanide sesquioxide materials, the values of static elastic stiffness constants C_{ij} and elastic moduli were presented for the first time. Unfortunately, in the current study, for many parameters of these materials, experimental results were not found for a comparison with our theoretical predictions. Our estimations agree well with the available experimental data and other theoretical reports.
Keywords: *Elastic properties; Plasmon energy; Ln₂O₃*
PACS: 71.20.-b; 71.20.Eh; 71.20.Nr; 62.20.de

1. INTRODUCTION

Sesquioxide of lanthanide metals are very important technological inorganic materials due to their outstanding thermo-physical and thermo-chemical properties. Lanthanides sesquioxide in cubic structure with general formula Ln_2O_3 (Ln = La, Ce, Pr, Nd, Pm, Sm, Eu, Gd, Tb, Dy, Ho, Er, Tm, Yb, Lu) are the subject of theoretical and chemical research extensively due to their interesting structural, semiconducting, elastic, mechanical, thermal properties and wide industrial applications such as industrial catalysis, Biomedical applications, Solis-State lighting, permanent magnets, hydrogen storage and nuclear energy fuels, lasers, optical display, Solid state fuel cells and neutron absorber for nuclear control etc. [1-7]. Lanthanide sesquioxide metals are n-type wide band gap semiconductors with low carrier mobility and very high refractive index [8, 9]. It is well known for below the temperature 2000℃, the structure of sesquioxide crystals exists in three phases; (i) A-type, Hexagonal in space P3mI (ii) B-type, monoclinic in space group (C2/m) (iii) C-type, Cubic in space group (Ia3) [10] and above the temperature, these materials appearance in X-phase and H-phase have been reported [11]. The unit cell of cubic structured Ln_2O_3 can be built up of 8-unit cells of fluorite structure (Fm3m) by removing 25% O-atom and ordering the remaining oxygen in remaining way. In particular, Ln-atoms are surrounded by 6 O-atoms is surrounded by 4-lanthanide atoms [12]. Since, in the sesquioxide form of lanthanide compounds, these atoms are in trivalent oxidation state and show the three electrons in conduction band partially filled p-orbital of oxygen atoms "4f" electrons are strongly localized on the rare earth atoms [13]. Hirosaki et al. [14] have focused the first principles pseudo potential calculation of the equilibrium crystal lattice dimension for most lanthanide oxides Ln_2O_3 using Vienna Ab-initio simulation package (VASP). Prokofiev et al [15] have studied the optical band gap on single crystals of the Ln_2O_3 series. The electronic and optical properties of Ln_2O_3 series analyzed by Singh et al [16] and employing the FPLAP method with in Local Spin Density Approximation [LSDA] and Coulomb Corrected Local Density Approximation [LSDA+U] as implemented in the WIEN2K code. The equilibrium volume and bulk modulus of hexagonal and cubic structured RE_2O_3 investigated within the CSM approach [12].

Recently, Pathak et al [17] have been calculated the structural, elastic and mechanical properties of Ln_2O_3 via Ab-initio study. Important details of the electronic, optical, mechanical and structural properties of Re_2O_3 and Re_2S_3 crystals are revealed by many workers [18-24]. The density functional theory is to be limited on optical, electronic and structural properties of rare earth sesquioxides. For such materials the theoretical and experimental details of elastic properties of lanthanide sesquioxides are very rarer so far. Shafiq and coworker [25] have been investigates the elastic properties of lanthanide mono-oxides using DFT calculations. Rare earth oxides have increasingly turned into the focus of first principle studies due to their importance in fundamental research and practical applications [14, 15, 26]. To the best in

our current knowledge, anisotropic elastic properties of lanthanide sesquioxide series have not been investigated experimentally due to the various difficulties to found accurate results of such materials. Pathak et al [17] have been lead to fill-up this gap by the calculation of elastic properties for only six Ln_2O_3 (Ln = Pm, Sm, Eu, Gd, Tb, Dy) employing ab-initio study. In many cases their results are slightly differ and, in few cases, no satisfactory results are thus found. It is very difficult problem to associate with experimental method and their high cost, as well as difficulties to obtained accuracy in results of their physical properties, due to this, researchers turned to studying the elastic, optical, thermal and structural properties of solids state materials through different theoretical techniques. Due to a large process and the complicated computational methods employing a series of approximations, such a process has always been complicated [27-31]. In the recent past few years, on the basis of semi-empirical models the theoretical calculations have become an essential part of the material research. Since empirical formulae do not give highly accurate results for each material in many cases but they can still be very useful. An empirical concept such as valence electron concentrations, empirical radii, iconicity and Plasmon energy are then useful [32-34]. Recently, Yadav and coworkers [35-40] have been studied the structural, optical, electronic, mechanical and thermal properties of binary, ternary chalcopyrite semiconductors and rare earth chalcogenides employing the plasma energy of solids as a key parameter, which depends on the number of valence electrons and it is changed when a metal forms the compound. Although various theoretical predictions for different types of the material using plasma oscillation theory of solids are obtained in literature [31-34], to the best of my knowledge, there are no theoretical investigations on structural, optical, mechanical and elastic properties of C-type lanthanide sesquioxides employing the plasma oscillation theory of solids up to date. Therefore, in this work, we propose a semi-empirical model based on plasma oscillation theory of solids for investigation of anisotropic elastic properties of cubic structured Ln_2O_3 lanthanide series.

2. THEORETICAL INFORMATION AND COMPUTATIONAL TECHNIQUES FOR STATIC ELASTIC CONSTANTS

Static elastic constants (C_{ij}) are very important parameters which define anisotropic elastic properties of the material that undergoes stress, deform and recovers after returning to its original shape and size. For various type of crystal structure of solids, the no. of independent static elastic constants is different. In case of C-type structured sesquioxide crystals, there are three independent static-elastic constant (C_{ij}: C_{11}, C_{12} & C_{44}). Based on semi-empirical linear relations, a number of theoretical linear expressions for static-elastic constant [41] for binary solids and mechanical properties [42] of ternary chalcopyrite structured semiconductors in term of the melting temperature (T_m), Boltzmann's constant (K_B), atomic volume (Ω) and product of ionic charge. Almost in many linear empirical relations [33,40] we have observed that bulk modulus (B) for various type of crystals is related to the product of ionic charge and bond length of a compound as follows -

$$B = A(Z_1 Z_2)d^{-3} \tag{1}$$

Recently, Verma [41] has developed a linear regression relation for elastic stiffness constant C_{ij} for ZB- structured binary solids in term of product of ionic charge and bond length of a compound as -

$$C_{ij} = \delta_{ij} + \gamma_{ij}(Z_1 Z_2)^{\mu_{ij}} d^{-3} \tag{2}$$

Here γ_{ij}, μ_{ij} and δ_{ij} are numerical constant for binary solids. Further, Frost and Ashby [42] have developed an empirical model for the elastic moduli of binary solids in terms of ($K_B T_m/\Omega$) as given as-

$$E = 100 K_B T_m / \Omega \tag{3}$$

$$G = 44 K_B T_m / \Omega \tag{4}$$

Similarly, Verma [43] has developed an empirical relation for elastic stiffness constant (C_{ij}) of tetragonal structured chalcopyrite crystals using ionic charge theory of solids and defined as-

$$C_{ij} = A_{ij}(K_B T_m / (Z_1 Z_2 Z_3)\Omega)^{0.15} \tag{5}$$

Here A_{ij} is the proportionality constant for C_{ij} of $A^I B^{III} C^V_2$ and $A^{II} B^{IV} C^V_2$ chalcopyrite semiconductors. Recently, Kumar et al [44] have proposed polynomial relations for the estimations of electronic, elastic and optical properties of divalent and trivalent rare earth mono-chalcogenide materials in term of their Plasmon energy as a key parameter. According to them-

$$B = K_1 + K_2(\hbar\omega_p) + K_3(\hbar\omega_p)^2 \tag{6}$$

$$E_c = K_4 \exp[K_5(\hbar\omega_p)] \tag{7}$$

In these relations K_1, K_2, K_3, K_4, and K_5 are numerical constants. According to above theoretical information's, it is very clear that static elastic constants (C_{ij}) are also depends upon the plasma energy of the materials. To get better agreement between the available experimental and theoretical data for C-type lanthanide sesquioxide crystals, based on above discussion, we may extend the relations (2) and (5) employing the plasma oscillation theory [32, 35-38] with minor modifications and can be written in the following form as-

$$C_{ij} = D_{ij}(\hbar\omega_p)^s \tag{8}$$

In this relation (9), the numerical value of the proportionality constant depends on the crystal structure. For cubic structured lanthanide series, the value of D_{ij} equal to 0.717, 0.320 and 0.298 for C_{11}, C_{12} and C_{44} respectively and exponent S = 2.0 for all C_{ij} of the materials. Using empirical relation (8), elastic constants (C_{11}, C_{12}, C_{44}) and elastic compliance $S_{ij} = C_{ij}^{-1}$ of Ln_2O_3 are calculated and presented in Table-1 with available theoretical literature [16] for a comparative study. An excellent agreement has been found between them.

The present investigations of C_{ij} for cubic sesquioxides satisfy the mechanical stability conditions defined by Born [45] as

$$(C_{11}\text{-}C_{12}) > 0,\ C_{44} > 0,\ C_{11} > 0,\ C_{12} > 0,\ (C_{11}+2C_{12}) > 0 \text{ and } C_{11} > B > C_{12}$$

These results indicate that the lanthanide sesquioxide crystals are mechanically stable against elastic deformations. For cubic structure crystals, the static elastic constants C_{ij} play an important role to determining the elastic constants such as isotropic bulk modulus (B), compressibility (K=1/B), shear modulus (G) using Voigt-Reuss-Hill (VRH) approximations, Young's modulus (E), Poisson's ratio (v), Zener anisotropy factor (Z), shear wave constant (C_s), Cauchy Pressure (C^*) and Kleinman internal displacement parameter (ξ) of these materials. The expressions of above parameters are defined in terms of C_{ij} as follows-

$$B = (C_{11} + 2C_{12})/3 \tag{9}$$

Voigt shear modulus,

$$G_v = (C_{11} - C_{12} + 3C_{44})/5$$

Reuss shear modulus,

$$G_R = 5C_{44}(C_{11} - C_{12})/[4C_{44} + 3(C_{11} - C_{12})$$

$$G_H = (G_V + G_R)/2 \tag{10}$$

Young's modulus,

$$E = (C_{11} + 2C_{12})(C_{11} - C_{12})/(C_{11} + C_{12}) \tag{11}$$

Poisson's ratio,

$$v = C_{12}/(C_{11} + C_{12}) \tag{12}$$

Zener anisotropic factor,

$$Z = 2C_{44}/(C_{11} - C_{12}) \tag{13}$$

Kleinman parameter,

$$\xi = (C_{11} + 8C_{12})/(7C_{11} + 2C_{12}) \tag{14}$$

Shear wave constant,

$$C_s = (C_{11} + C_{12})/2 \tag{15}$$

Cauchy pressure,

$$C^* = C_{12} - C_{44}) \tag{16}$$

Grüneisen Parameter,

$$\gamma = 3(C_{11} + 2C_{12}) / 2(2C_{11} - C_{12}) = 1.5(1+v) / (2-3v) \qquad (17)$$

Based on elastic moduli E and ν, Lame's coefficients (λ & μ) are computed by the following relations as

$$\lambda = Ev / (1+v)(1-2v) \quad \text{and} \quad \mu = E / 2(1+v) \qquad (18)$$

On the basis of above relations, the investigated values of static elastic constants and mechanical moduli of the cubic structure lanthanide sesquioxides are presented in the respective Tables along with the available experimental data and other such theoretical reports. We found a good agreement between them. The values of Pugh ratio is equal to 0.556 for all sesquioxides and indicate the information about covalent and ionic behavior of the materials on the basis of their brittle and ductile nature in these solids. The upper limits of Pugh ratio is 1.1 for brittle and 0.60 for ductile nature. It is clear that, if (G/B) ≤ 0.60, the materials are ionic (ductile), otherwise covalent (brittle) in nature.

3. RESULTS AND DISCUSSION

The static elastic constants (C_{11}, C_{12}, C_{44}) and mechanical/elastic moduli are reflecting the important anisotropic elastic properties of cubic structured (with space group Ia3, 206) lanthanide sesquioxides. We have employed an empirical relation for the calculation of C_{ij} of these compounds in term of their Plasmon energy, which play an important role as key parameter. In the present work, the calculated values of C_{ij} employed to the relations (9)-(18) straight forwardly and the values of elastic moduli (B, G, E, K, ν, G/B, $S_{ij}=1/C_{ij}$,) and other parameters (Z, C_s, C^*, λ, μ, ξ, γ) of these compounds are also investigated. We note that the calculated values of C_{ij} from our proposed model are cited in Table-1and are very close to theoretical reports [17] and elastic compliances S_{ij} are also presented in such Table. The static elastic constants (C_{ij}: C_{11}, C_{12}, C_{44}) of these sesquioxides exhibit a linear relationship when plotted on log-log scale against their plasma energy. Bulk modulus is the key parameter of solid-state materials. The values of B computed by well-known relation in term of C_{11} and C_{12} and are cited in Tale-2 with the current theoretical and experimental report [17, 46]. An excellent agreement has been found between them. Voigt-Reuss-Hill approximation is average of the two bounds as lower bound of Voigt and upper bound by Reuss, which yields good estimations for shear modulus (G) and are provided in Table-2 with current theoretical literature. One of them, Young's modulus (E) is a mechanical parameter, which is used to measure the stiffness or hardness of the materials. If the value of E is very high, then the material is stiffer and for low values of E, the material is least stiff to them. Thus, it is very clear from Table-2 that in a series of Ln_2O_3, La_2O_3 is least stiff as compared to all of them, while Lu_2O_3 is much stiffer in them. Poisson's ratio is the constant which is used to differentiate the nature of the materials that it is ductile or brittle. The critical value of Poisson's ratio is 0.33 proposed by Frantsevich [52]. If ν<0.33, the material is brittle and for ν>0.33 the material in ductile nature. The calculated values of Poisson ratio for these compounds are equal to 0.2604 and displays in the Table 3, which show that the brittle nature of studied materials. In this Table, the calculated values of Kleinman parameter (ξ), Lame's coefficient (λ & μ) and Zener anisotropy factor (Z) for cubic sesquioxides are presented here. Zener anisotropy factor (Z) is used to measure the degree of anisotropy in the solid-state structure. For Z=1, the material is completely isotropic, and if Z ≠ 1 the materials are elastically anisotropic in nature. In Table-3 the positive values of the Cauchy pressure for all cubic lanthanide series indicates that the materials are ductile in nature rather than brittle [53].

Table 1. Calculated values of elastic stiffness constants of cubic structured lanthanide sesquioxides

Ln_2O_3	$\hbar\omega_p$ (eV)	Elastic Stiffness Constant C_{ij} (GPa)						Elastic Compliance S_{ij} (×10⁻³ TPa)		
		C_{11}		C_{12}		C_{44}				
		Calc.	Ref.*	Calc.	Ref.*	Calc.	Ref.*	S_{11}	S_{12}	S_{44}
La	16.403	192.91		86.09		80.18		7.2	2.2	12.5
Ce	16.612	197.86		88.30		82.23		7.0	2.2	12.2
Pr	16.818	202.80		90.51		84.28		6.8	2.1	11.9
Nd	17.021	207.72		92.71		86.33		6.6	2.1	11.6
Pm	17.222	212.66	206.9	94.91	94.0	88.38	86.0	6.5	2.0	11.3
Sm	17.422	217.63	213.8	97.12	95.8	90.45	88.6	6.3	2.0	11.1
Eu	17.617	222.52	222.6	99.31	98.4	92.48	92.8	6.2	1.9	10.8
Gd	17.812	227.48	228.7	101.53	98.9	94.54	94.6	6.1	1.9	10.6
Tb	18.004	232.41	235.1	103.73	100.3	96.59	97.1	5.9	1.8	10.4
Dy	18.194	237.34	241.2	105.93	101.4	98.64	99.6	5.8	1.8	10.1
Ho	18.382	242.27		108.13		100.69		5.7	1.8	9.9
Er	18.568	247.20		110.33		102.74		5.6	1.7	9.7
Tm	18.753	252.15		112.54		104.80		5.5	1.7	9.5
Yb	18.935	257.07		114.73		106.84		5.4	1.7	9.4
Lu	19.116	262.00		116.93		108.90		5.3	1.6	9.2

*Ref.[16]

Table-2. Values of the elastic moduli of cubic structured lanthanide sesquioxides with available theoretical and experimental data

Ln2O3	Bulk Modulus (B)			Shear Modulus (G) (in GPa)						Young's Modulus (E)		Pugh's ratio (G/B)	Gruneisen Const. γ
	Calc.	Reported#	Expt#	GVCalc	Ref*	GRCalc.	Ref*	GHCalc	Ref*	Calc	Reported*		
La	121.69	124.4, 125.6, 133.9	-----	69.47	-----	66.78	-----	68.13	-----	175.10		0.559	1.550
Ce	124.82	135.5, 135.8, 148.5	-----	71.25	-----	68.49	-----	69.87	-----	179.59		0.559	1.550
Pr	127.94	137.0, 148.2, 157.9	-----	73.02	-----	70.20	-----	71.61	-----	184.07		0.559	1.550
Nd	131.04	122.0, 136.9, 150.5	-----	74.80	-----	71.91	-----	73.35	-----	188.54		0.559	1.550
Pm	134.16	131.6*, 129.0, 136.0, 153.8	116, 142, 149	76.57	74.2	73.62	71.1	75.09	72.6	193.02	187.4	0.559	1.550
Sm	137.29	135.1*, 136.5, 138.3, 153.4	-----	78.37	76.8	75.34	73.8	76.85	75.3	197.53	193.6	0.559	1.550
Eu	140.38	139.8*, 143.1, 137.0, 156.1	115	80.13	80.5	77.03	77.5	78.58	79.0	201.97	202.7	0.559	1.550
Gd	143.51	142.2*, 144.7, 139.7, 158.3	-----	81.91	82.7	78.75	80.0	80.33	81.3	206.47	207.9	0.559	1.550
Tb	146.62	145.2*, 139.0, 143.7, 158.6	134, 125, 188	83.69	85.2	80.45	82.5	82.07	83.9	210.94	213.8	0.559	1.550
Dy	149.73	148.0*, 148.9, 145.3, 159.9	150, 191	85.46	87.7	82.16	85.1	83.81	86.4	215.42	219.8	0.559	1.550
Ho	152.84	152.0, 145.7, 161.6	134, 178, 206	87.24	-----	83.87	-----	85.55	-----	219.90		0.559	1.550
Er	155.95	157.2, 146.1, 161.2	155, 140, 200	89.02	-----	85.58	-----	87.29	-----	224.37		0.559	1.550
Tm	159.07	157.7, 161.6, 146.6	-----	90.80	-----	87.29	-----	89.04	-----	228.86		0.559	1.550
Yb	162.17		-----	92.57	-----	88.99	-----	90.78	-----	233.33		0.559	1.550
Lu	165.28		-----	94.35	-----	90.70	-----	92.53	-----	237.81		0.559	1.550

*Ref.[17], #Ref.[18]

Table 3. In this Table, we present the values of Shear constant (C$_s$), Cauchy Pressure (C'), Lame's coefficients (λ and μ), Kleinman Parameter (ξ), Zener Anisotropy (Z) and Poisson ratio (ν) of C-type lanthanide sesquioxides and compared with Ab-initio study

Ln2O3	Shear Constant C$_s$		Cauchy Pressure C'		Lame's Coefficients λ		μ		Kleinman Parameter ξ		Zener Anisotropy Z		Poisson Ratio ν	
	Calc	Ref.*	Calc	Ref.*	Calc	Ref.*	Calc	Ref.*	Calc	Ref.*	Calc	Ref.*	Calc	Ref.*
La	53.408	-----	5.919	-----	75.390	-----	69.471	-----	0.749	-----	1.501	-----	0.2602	-----
Ce	54.778	-----	6.071	-----	77.324	-----	71.252	-----	0.749	-----	1.501	-----	0.2602	-----
Pr	56.145	-----	6.224	-----	79.253	-----	73.031	-----	0.748	-----	1.501	-----	0.2602	-----
Nd	57.508	-----	6.375	-----	81.178	-----	74.804	-----	0.748	-----	1.501	-----	0.2602	-----
Pm	58.875	56.5	6.527	8.0	83.108	82.2	76.581	74.2	0.749	0.76	1.501	1.52	0.2602	0.26
Sm	60.250	59.0	6.677	7.2	85.045	84.0	78.370	76.8	0.749	0.75	1.501	1.50	0.2602	0.26
Eu	61.606	62.1	6.827	5.6	86.963	86.1	80.135	80.5	0.749	0.74	1.501	1.49	0.2602	0.26
Gd	62.978	64.9	6.979	4.3	88.898	87.0	81.918	82.7	0.749	0.73	1.501	1.46	0.2602	0.26
Tb	64.343	67.4	7.131	3.2	90.825	88.4	83.694	85.2	0.749	0.72	1.501	1.44	0.2602	0.26
Dy	65.706	69.9	7.282	1.8	92.752	89.7	85.470	87.7	0.749	0.71	1.501	1.42	0.2602	0.26
Ho	67.073	-----	7.434	-----	94.679	-----	87.245	-----	0.748	-----	1.501	-----	0.2602	-----
Er	68.437	-----	7.585	-----	96.605	-----	89.020	-----	0.749	-----	1.501	-----	0.2602	-----
Tm	69.807	-----	7.736	-----	98.539	-----	90.802	-----	0.749	-----	1.501	-----	0.2602	-----
Yb	71.179	-----	7.889	-----	100.460	-----	92.572	-----	0.748	-----	1.501	-----	0.2602	-----
Lu	72.538	-----	8.039	-----	102.330	-----	94.352	-----	0.749	-----	1.501	-----	0.2602	-----

*Ref.[16]

Hence, the calculate results indicate that proposed empirical model is quite simple and give us soundness in results for these cubic structure lanthanide sesquioxides and predicts the anisotropic elastic properties of Ln_2O_3 compounds successfully. We have plotted a graph between static elastic constant (C_{ij}; in GPa) and Plasmon energy of the materials shown in Fig.-1. It is clear that C_{ij} trends in these compounds increases on increasing their plasma energy.
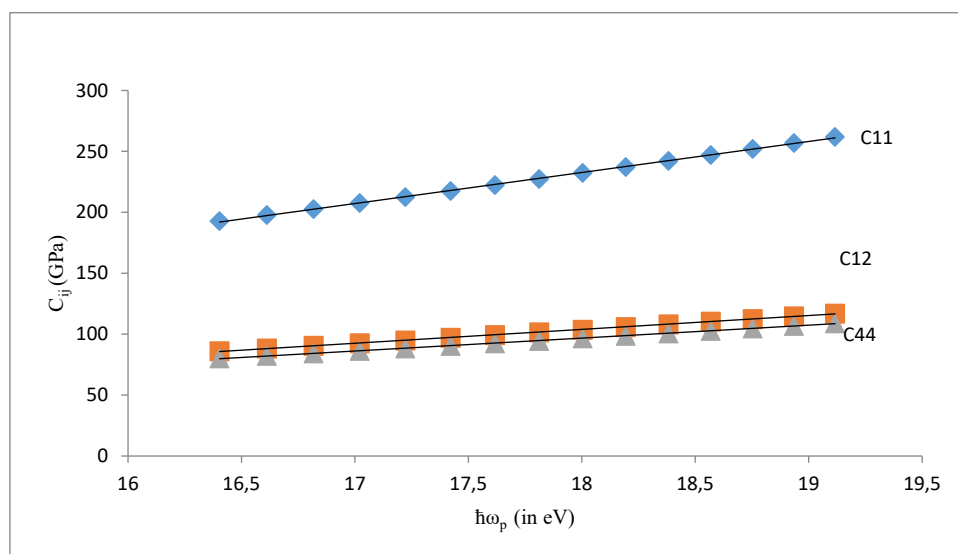

Figure 1. Plot of C_{ij} versus plasmon energy for Ln_2O_3.

4. CONCLUSIONS

On the basis of solid-state theory of plasma oscillations, the anisotropic elastic properties of lanthanide sesquioxides are investigated using the proposed empirical model. From above results and discussions, we have concluded that Plasmon energy of cubic structure sesquioxides is very important parameter which leads to determining three independent elastic stiffness constants (C_{ij}: C_{11}, C_{12}, C_{44}). Elastic moduli of these materials increase on increasing the plasma energy as from $La_2O_3 \rightarrow Lu_2O_3$. In our studied materials, La_2O_3 is least stiff and Lu_2O_3 is stiffer in Ln_2O_3 series. The elastic properties of these compounds allowed us to conclude that the considered materials are elastically anisotropic. In addition, the values of the elastic constants of these materials shows that the cubic structured lanthanide sesquioxides are mechanically stable. Here, the predictions were found to be in good agreement with the available experimental data and theoretical findings. But, unfortunately for many compounds, some predicted values could not be compared due to lacking of availability of experimental results to make a comparison. Finally, it may be seen that the proposed empirical model can easily be extended to cubic sesquioxide crystals for which the work is in progress and will be appearing in forthcoming paper.

ORCID

Ajay Singh Verma, https://orcid.org/0000-0001-8223-7658; **Dheerendra Singh Yadav,** https://orcid.org/0000-0001-8315-9743

REFERENCES
[1]   K.A. Gschneidner, and L. Erying, *Handbook on the Physics and Chemistry of Rare Earths*, Vol. **1-40**, 202 (1978-2010).
[2]   S. Jiang, J. Liu, X.-D. Li, Y.-C. Li, S.-M. He, and J.-C. Zhang, Chin. Phys. Lett. **36**(4), 046103 (2019). https://doi.org/10.1088/0256-307X/36/4/046103
[3]   J. Łazewski, M. Sternik, P.T. Jochym, J. Kalt, S. Stankov, A.I. Chumakov, J. Göttlicher, *et al.*, Inorg. Chem. **60**(13), 9571 (2021). https://doi.org/10.1021 /acs.inorgchem.1c00708
[4]   J. Ibanez, J.A. Sans, V. Cuenca-Gotor, R. Oliva, O. Gomis, P. Rodriguez-Hernandez, A. Munoz, *et al.*, Inorg. Chem. **59**(14), 9648 (2020). https://dx.doi.org/10.1021/acs.inorgchem.0c00834
[5]   S. Jiang, J. Zhang, L. Wang, C. Lin, S. Yan, J. Liu, A. Li, and R. Tai, AIP Advances, **13**, 095018 (2023). https://doi.org/10.1063/5.0164684
[6]   S. Jiang, J. Zhang, and S. Yan, AIP Advances, **13**, 055308 (2023). https://doi.org/10.1063/5.0140946
[7]   Y. He, M. Chen, Y. Jiang, L. Tang, J. Yu, Y. Chen, M. Fu, *et al.*, J. Alloys Compd. **903**, 163806 (2022). https://doi.org/10.1016/j.jallcom.2022.163806
[8]   L. Erying, *Handbook on the Physics and Chemistry of Rare Earths*, **3**, 337-339 (1997).
[9]   V.P. Zhuze, and A.I. Shelykh, Sov. Phys. Semicond. **23**, 245 (1989).
[10] H.R. Hoekstra, and K.A. Gingerich, Science, **146**, 1163 (1964). https://doi.org/10.1126/science. 146.3648.1163
[11] G. Adachi, and N. Imanaka, Chemical Reviews, **98**, 1479 (1998). https://doi.org/10.1021/cr940055h
[12] M. Rahm, and N.V. Skorodumova, Phys. Rev. **B80**, 104105 (2009). https://doi.org/10.1103 /PhysRevB.80.104105
[13] L. Petit, A. Svane, Z. Szotek, and W.M. Temmerman, Phys. Rev. B, **72**, 205118 (2005). https://doi.org/10.1103/PhysRevB.72.205118
[14] N. Hirosaki, S. Ogata, and C. Kocer, J. Alloys Compds. **351**, 31 (2003). https://doi.org /10.1016 /S0925-8388(02)01043-5
[15] A. Prokofiev, A.I. Shelykh, and B.T. Melekh, J. Alloys Compds. **242**, 41 (1996). https://doi.org/10. 1016/0925-8388(96)02293-1
[16] N. Singh, S.M. Saini, T. Nautiyal, and S. Auluck, J. Appl. Phys. **100**, 083525 (2006). https://doi.org /10.1063/1.2353267
[17] A.K. Pathak, and T. Vazhappilly, Phys. Stat. Sol. (b) **255**, 1700668 (2018). https://doi.org /10.1002 /pssb.201700668

[18] D. Rechard, E.L. Munoz, M. Renteria, L.A. Errico, A. Svane, and N.E. Christensen, Phys. Rev. B, **88**, 165206 (2013). https://doi.org/10.1103/PhysRevB.88.165206

[19] J. Sheng, B.L. Gang, L. Jing, X.W. Sheng, L.X. Dong, L.Y. Chun, T.L. Yun, *et al*., Chin. Phys. Lett. **26**, 076101 (2009). https://doi.org/10.1088/0256-307X/26/7/076101

[20] K.A. Irshad, P. Anees, R. Rajitha, T.R. Ravindran, V. Srihari, S. Kalavathi, and N.V. Chandra Shekar, Journal of Alloys and Compounds **822**, 153657 (2020). https://doi.org/10.1016/j.jallcom.2020.153657

[21] A.F. Andreeva, and I.Y. Gilman, Zh. Prikl. Spectrosk, **28**, 895 (1978). Ref. no. – AIX-10-431358, EDB-79-100351

[22] M.V. Avrashev, N.D. Todorov, and J. Geshev, J. Appl. Phys. **116,** 103508 (2014). https://doi.org/10.1063/1.4894775

[23] S. Jiang, J. Liu, C. Lin, L. Bai, Y. Zhangb, X. Li, Y. Li, *et al*., Solid State Communications **169**, 37 (2013). https://doi.org/10.1016/j.ssc.2013.06.027

[24] V.I. Marchenko, Electronic Structure and Physico Chemical Properties of Refractory Compounds and alloys, **193**, (1980).

[25] M. Shafiq, S. Arif, I. Ahmad, S.J. Asadabadi, M. Maqbool, and H.A.R. Aliabad, J. Alloys Compds. **618**, 292 (2015). https://doi.org/10.1016/j.jallcom.2014.08.171

[26] H. Jiang, P. Rinke, and M. Scheffler, Phys. Rev. B, **86**, 125115 (2012). https://doi.org/10.1103/ PhysRevB.86. 125115

[27] A.S. Verma, Solid State Communication, **149**, 1236 (2009). https://doi.org/10.1016/j.ssc.2009.04.011

[28] D.S. Yadav, and S. P. Singh, Phys. Scr. **82**, 065705 (2010). https://doi.org/10.1088/0031-8949/82/06/065705

[29] D.S. Yadav and A.S. Verma, Int. J. Mod. Phys. B, **26**, 1250020 (2012). https://doi.org/10.1142/ S02179792 12500208

[30] A. S. Verma, S. Sharma, and V.K. Jindal, Mod. Phys. Lett. B, **24**, 2511 (2010). https://doi.org /10.1142/ S0217984910024821

[31] R. Bhati, D.S. Yadav, R.C. Gupta, A.S. Verma, Materials Physics and Mechanics, **51**(5), 90 (2023). http://dx.doi.org/10.18149/MPM.5152023-9

[32] V. K. Srivastava, Phys. Rev. B, **29**(12), 6993 (1984). https://doi.org/10.1103/PhysRevB.29.6993

[33] A.S. Verma, Phys. Scr. **79**, 045703 (2009). https://doi.org/10.1088/0031-8949/79/04/045703; A.S. Verma, N. Pal, B.K. Sarkar, R. Bhandari, and V.K. Jindal, Phys. Scr. **85**, 015705 (2012). https://doi.org/10.1088/0031-8949/85/01/015705

[34] S.K. Gorai, and P. Mahto, Indian J. Phys., **86(4)**, 273 (2012). https://doi.org/10.1007/s12648-012-0053-y

[35] D. S. Yadav and D.V. Singh, Phys. Scr., **85**, 015701 (2012). https://doi.org/10.1088/0031-8949/85/01/015701

[36] D.S. Yadav, J. Alloy. Compds. **507**, 250 (2012). https://doi.org/10.1016/j.jallcom.2012.05.016

[37] D.S. Yadav, J. Mater. Chem. Phys, **3**, 6 (2015). https://doi.org/10.12691/jmpc-3-1-2

[38] R. Bhatti, D.S. Yadav, P. Vershney, R.C. Gupta, A.S. Verma, East European Journal of Physics **1,** 222 (2023). https://doi.org/10.26565/2312-4334-2023-1-29

[39] D.S. Yadav, and A.S. Verma, Int. J. Mod. Phys. B, **26**, 1250020 (2012). https://doi.org/10.1142 /S0217979212500208

[40] N. Yadav, D.S. Yadav, P. Varshney, R.C. Gupta, American Journal of Physics and Applications **11(4),** 80 (2023). https://doi.org/10.11648/j.ajpa.20231104.11

[41] A.S. Verma, Materials Science in Semiconductor Processing, **29**, 2 (2015). https://doi.org/10.1016 /j.mssp .2014.05.033

[42] H.J. Frost, and M.F. Ashby, *Deformation-Mechanism Maps*, (Pergamon, Oxford, (1982).

[43] A.S. Verma, S. Sharma, R. Bhandari, K. Sarkar, and V.K. Jindal, Mater. Chem. Phys., **132**, 416 (2012). https://doi.org/10.1016/j.matchemphys.2011.11.047

[44] V. Kumar, S. Chandra, and J.K. Singh, Indian J. Phys. **3**, 0983 (2017). https://doi.org/10.1007/s12648-017-0983-5

[45] M. Born, and K. Hung, *Dynamics Theory of Crystal Lattices*, (Oxford University Press, Oxford, (954).

[46] D. Richard, L.A. Errico, and M. Rentira, J. Alloys Compds. **664**, 580 (2016). https://doi.org/10.1016 /j.jallcom.2015.12.236

[47] W. Voiget, and Teubner, Lehrbuch Der Kristallphysik Leipzig, Germany, 962 (1928).

[48] A. Reyss, and Z. Angew, Math Mech. **8**, 55 (1929).

[49] R. Hill, Proc. Phys. Soc. A, **65**, 349 (1952). https://doi.org/10.1088/0370-1298/65/5/307

[50] D.G. Pettifor, Mater. Sci. Technol. **8**, 345 (1992). https://doi.org/10.1179/mst.1992.8.4.345

[51] L. Kleinman, Phys. Rev. B, **128**, 2614 (1962). https://doi.org/10.1103/PhysRev.128.2614

[52] I.N. Frantsevich, F.F. Voronov, and S.A. Bokuta, *Handbook in Elastic Constants and Elastic Moduli of Metals and Insulators*, (Naukova Dumka, Kiev, 1982). (in Russian)

[53] Y.F. Li, B. Xiao, Y.M. Sun, L. Gao, S.Q. Ma, and D.W. Yi, J. Phys. Chem. Solids, **103**, 49 (2017). https://doi.org/10.1016/j.jpcs.2016.12.001

ПРУЖНІ ВЛАСТИВОСТІ СЕСКВІОКСИДІВ ЛАНТАНІДУ С-ТИПУ
Пуджа Ядав[a], Дірендра Сінгх Ядав[b], Дхармвір Сінгх[a], Правеш Сінгх[c], Аджай Сінгх Верма[d,e]
[a]Департамент фізики, коледж Агра, Агра 282002, Індія
[b]Кафедра фізики, Чаран Сінгх PG коледж Хеонра (Сайфай) Етавах 206001, Індія
[c]Департамент електроніки та комунікаційної техніки, групи установ KIET, Газіабад 201206, Індія
[d]Відділ досліджень та інновацій, Школа прикладних наук та наук про життя, Університет Уттаранчал,
Уттаракханд, Дехрадун 248007, Індія
[e]Університетський центр досліджень і розвитку, факультет фізики, Університет Чандігарха,
Мохалі, Пенджаб 140413, Індія

У цьому дослідженні ми представили твердотільну теорію плазмових коливань для дослідження анізотропних пружних властивостей, таких як три незалежні статичні константи пружної жорсткості (Cij: C11, C12 і C44) твердих тіл лантаноїдів Ln2O3 типу С. Розраховані значення статичних констант пружної жорсткості Ln2O3 чудово узгоджуються з теоретичними результатами, отриманими за допомогою методів ab-initio. Значення констант пружної жорсткості (Cij) виявляють лінійну залежність, якщо їх нанести на графік відносно їхніх плазмових енергій і лежать на прямій лінії. Для подальшого вивчення достовірності наявних оцінок модулів пружності та інших параметрів цих матеріалів. Механічні модулі, такі як об'ємний модуль (B), модуль зсуву (G), модуль Юнга (E), коефіцієнт Пуассона (ν), постійна хвилі зсуву (Cs), тиск Коші (C*), коефіцієнт Ламе (λ і μ) , параметр Клейнмана (ξ), параметр Грюнезієна (γ), анізотропна константа Зенера (Z) і співвідношення П'ю (G/B) твердих речовин лантаноїдів також були досліджені. Для полусквіоксидних матеріалів лантаноїдів вперше наведено значення статичних констант пружної жорсткості Сij та модулів пружності. На жаль, у поточному дослідженні для багатьох параметрів цих матеріалів не було знайдено експериментальних результатів для порівняння з нашими теоретичними прогнозами. Отримані оцінки добре узгоджуються з наявними експериментальними даними та іншими теоретичними повідомленнями.
Ключові слова: *пружні властивості; плазмонна енергія; Ln2O3*

ELECTRONIC, STRUCTURAL, OPTICAL AND MECHANICAL PROPERTIES
OF CUBIC STRUCTURED Ln₂X₃ (Ln = La→Lu & X=O,S): AN EMPIRICAL INVESTIGATION

Pooja Yadav[a], ⓘDheerendra Singh Yadav[b], Dharmvir Singh[a], Pravesh Singh[c], ⓘAjay Singh Verma[d,e]

[a]Department of Physics, Agra College, Agra 282002, India
[b]Department of Physics, Ch. Charan Singh P G College Heonra (Saifai) Etawah 206001, India
[c]Department of Electronics and Communication Engineering, KIET Groups of Institutions, Ghaziabad 201206, India
[d]Division of Research & Innovation, School of Applied and Life Sciences, Uttaranchal University,
Uttarakhand, Dehradun 248007, India
[e]University Centre for Research & Development, Department of Physics, Chandigarh University, Mohali, Punjab 140413, India
Corresponding Author e-mail: ajay_phy@rediffmail.com
Received August 8, 2024; revised November 9,2024; accepted November 18, 2024

In this publication, we have examined the structural, optical, and mechanical features of cubic structured lanthanide Ln_2X_3 (Ln = La→ Lu and X = O, S) series using the valence electron plasma oscillation theory of solids. Using the Chemical bond theory of solids, which was created by Phillips and Van-Vechten, we have further confirmed our findings. Unfortunately, it has been discovered that the Phillips and Van-Vechten (PVV) dielectric description is applicable exclusively to semiconductors and insulators. It is shown that an empirical relationship previously presented by Yadav and Bhati [D.S. Yadav, J. Alloys and Comp. 537, 250 (2012); D.S. Yadav, and D.V. Singh, Phys. Scr. 85, 015701 (2012); D.S. Yadav, J. Mater. Phys. Chem. 3(1), 6-10 (2015); R. Bhati, et al., Mater. Phys. Mech. 51, 90 (2023); R. Bhati, et al., East Eur. J. Phys. (1), 222 (2023).] relating the plasmon energy of complex structured solids, rock salt, and zinc-blende to their electronic, mechanical, static, and dynamical properties which can be applied to the cubic structured lanthanide $(Ln_2S_3$ & $Ln_2O_3)$ series with only minor modifications. Considering the well-known theory of dielectric for solids, an alternative technique has been devised to evaluate the electronic, structural, mechanical, and optical properties of these materials, including their band gap (ΔE_g in eV), optical dielectric constant, homopolar and heteropolar gaps, average energy gaps, chemical bond ionicity, and bulk muduli. An estimate was computed based on the almost inverse relationship between the plasmon energy of these compounds and their optical, mechanical, structural, and electrical characteristics. For these substances, the expected values of the aforementioned parameters form a straight line when plotted on a log-log scale against the plasmon energy ($\hbar\omega_p$). We examined the C-type Ln_2X_3 compounds using the recommended methods, and the values we estimated are in good agreement with the values obtained from modified PVV theory and other comparable experimental and theoretical data that is currently available.
Keywords: *Electronic Properties; Optical Properties; Structural Properties; Mechanical Properties; Ln_2O_3; Ln_2S_3; Plasma Energy*
**PACS:** 71.20.-b; 71.20.Eh; 71.20.Nr; 62.20.de

1. INTRODUCTION

Because of their numerous practical applications, lanthanide sesquioxides and sesquisulphides, which have cubic structures in Ln_2O_3 and Th_3P_4 in Ln_2S_3, respectively, have drawn physicists' interest. Because of their significant technological value in a variety of fields, including solid state lasers, electroluminescence, cathode-luminescence sources, crystals for chemical and organic reactions, high-K gate dielectrics, optical components of high power lasers, generation of ultra-short laser pulses, scintillating materials, radiation detectors, transistor application and electronic industries, oxygen ion conducting electrolyte in solid oxide fuel cells, and materials with strongly hydrophobic surfaces, numerous attempts have been made in the last few years to comprehend the electronic and optical properties of C-type Ln_2O_3 and Ln_2S_3 [1-4]. Semi-core *4f* levels which are mostly concentrated on Ln-atoms and typically do not participate in bonding or electronic conduction, govern many features of lanthanide oxides. However, *4f*-shell electrons can establish strong magnetic order and be available for optical absorption. Any O and S compound containing a rare earth atom is solid at room temperature. An atom's size and electrical arrangement in relation to O and S determine most of its solid state physics. When electrons are introduced to the 4f-orbitals in the lanthanide series of elements, the outer valence electrons ($5d^1$ and $6S^2$ electrons) are effectively protected from the growing nuclear charge. For every lanthanide in the series, this leads to a trivalent state whose energy varies gradually. Oxides related to each other in relatively predictable ways are produced when the atom's size contracts gradually with oxygen throughout the series. The oxides of lanthanides are among the most thermally stable compounds known to science because of the combination of their size and electrical structure. With a very high refractive index and low carrier mobility, lanthanide sesquioxides and sesquisulphides are n-type wide gap semiconductors [5, 6]. It is generally known that below 2000^{0C}, the sesquioxide crystal structure exists in three polymorphic forms: Hexagonal A-type (P3m1), Monoclinic B-type (C2/m), and Cubic C-type (Ia3) [7]. Reports have indicated that X and H phases arise above this temperature [8] Using the Vienna ab-initio simulation package (VASP), Hirosaki et al. [9] calculated the equilibrium crystal lattice dimension for most Ln_2O_3 (Ln = La→Lu) using first principles pseudo potential. Measurements of the optical band gap on Ln_2O_3 series single crystals were made by Prokofiev et al. [10]. Using the full potential linearized augmented plane wave [FPLAP] method with in local spin density

approximation [LSDA] and Coulomb corrected local density approximation [LSDA+U], as implemented in the WIEN2K code, Singh et al. [11] reported the electronic structure and optical properties of rare earth sesquioxides. Rahm et al.'s CSM technique computed the equilibrium volume and bulk modulus of hexagonal and cubic structured RE_2O_3 [12]. Significant information about the electrical, optical, mechanical, and structural characteristics of RE_2O_3 and RE_2S_3 has been made public by numerous workers [4, 13–18]. The unit cell of the C-type structure (Figure 1) can be obtained by combining eight unit-cells of the fluorite structure (Fm3m) with 25% of the oxygen atoms removed and arranging the remaining oxygen in a specific way.

Over the past few decades, experimental and theoretical research has been conducted on the cohesive energy, heat of formation, bulk modulus, optical dielectric constant, and energy band gap of these materials. Thanks to a sophisticated computer technique, the structural, mechanical, and optical properties of a wide range of molecules and materials can now be investigated in great detail. Applying empirical concepts such as valence, empirical radii, ionicity, electronegativity, and plasmon energy is therefore beneficial [19–24]. To the best of our knowledge, no one has investigated the mechanical, structural, electrical, and optical properties of C-type Ln2O3 and Ln₂S₃ using solid state plasma oscillation theory. Literature contains references to them. Since these ideas are closely related to the nature of chemical bonds, they offer a way to categorize and explain a wide range of fundamental characteristics of molecules and solids. Consequently, we believe it would be interesting to provide a different explanation for the C-type Ln_2X_3 series' homopolar gap, heteropolar gap, average gap, bond ionicity, optical dielectric constant, and band gap. In this work, we suggest a method for calculating the electrical, structural, optical, and mechanical properties of these materials that is based on the plasma oscillation theory of solids.

2. THEORY, RESULTS AND DISCUSSION

Modified Phillips and Van-Vechten dielectric theory of solids [25–29] states that the average energy gap (E_g) between bonding and anti-bonding (sp^3) hybridized orbitals can be broken down into contributions from symmetric and anti-symmetric parts by the potential inside the unit cell.
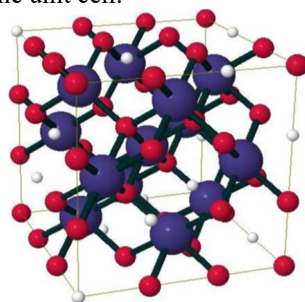
Figure 1. The unit cells of cubic C-type Ln_2O_3 and the RE atoms are shown in blue (dark gray) and oxygen are in red (light gray), vacancy positions are indicated by white spheres.

This is because the average energy gap (E_g) can be broken down into a heteropolar or part (E_c) and homopolar or covalent part (E_h). These contributions take the following form: E_c represents the heteropolar or ionic contribution, while E_h represents the homopolar or covalent contribution as-

$$E_p^2 = E_h^2 + E_c^2 . \tag{1}$$

The following is how the covalent portion E_h is dependent on the nearest neighbor separation d_{AB} -

$$E_h = A d_{AB}^{-K_1} . \tag{2}$$

where A = 40.468 eV(A°)$^{2.5}$ and the exponent K_1 = 2.5 are the constants, i.e., remain unchanged in different crystals. A = 39.74 and K_1 = 2.48 were the comparable values found by Phillips and Van-Vechten [28]. The following relation can be used to determine the ionic contribution:

$$E_c = K_2 d_0^{-1} . e^{-k_s . d_0} , \tag{3}$$

where the valence states of atoms A and B are denoted by Z_A and Z_B, respectively, and b is an adjustable quantity that is dependent upon the co-ordination number surrounding the cation [29], that is, b = 0.089 N_c^2. N_c is the average coordination number, K_s is the Thomas Fermi Screening Parameter (TFSP), and d_0=(d/2) (d-the nearest-neighboring distance) are the values of b for C-type RE_2O_3 and Th_3P_4 type RE_2S_3 respectively.

The effective number of free electrons in the valence band is correlated with both this screening factor and the bond length. As a result, the bond length and quantity exiting the cations determine the values of E_h and E_c. Ten electrons per molecule (four for RE and six for O & S) was taken into consideration while determining the value of ks, which is defined as:

$$k_s = 2 a_B^{-0.5} (3N / \pi V)^{0.167} . \tag{4}$$

Here $-a_B$ is Bohr radius. The ionicity of the chemical bond is defined as

$$f_i = \frac{E_c^2}{E_g^2} \ . \tag{5}$$

We have determined the values of E_P, E_c, and E_h for these materials based on the relations (1) through (4) above. The values of E_h^* and E_p^* can also be determined from the Phillips and Penn model[26–27] with the use of Eqns. (4)–(7). The optical and static dielectric constants, $\varepsilon\infty$ and $\varepsilon 0$, in these relations, are derived from several sources [6, 30-33]. For Ln_2O_3, the adjustable parameter $S_0 = 0.78$, and for Ln_2S_3, 0.80. The ionic contribution (E_c) to the average energy gap (E_g), ionicity (f_i), dielectric constant (ε_∞), band gap (ΔE_g), and plasmon energy of a chemical bond must therefore be correlated in some way with the physical process. The electronic, structural, optical and mechanical properties of these materials exhibit a linear relationship when plotted on log-log scale against ($\hbar\omega_p$) of the compounds, which are presented in the Figures 2-5.
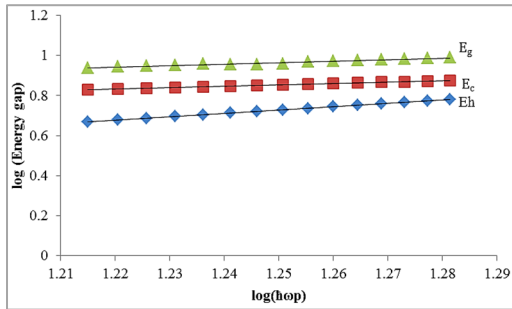
Figure 2. Plot of Energy gaps versus plasmon energy of C-type Ln_2O_3
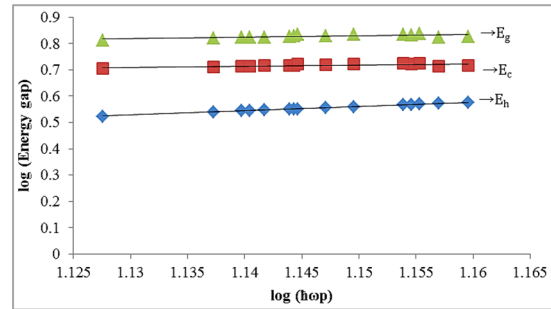
Figure 3. Plot of Energy gaps versus plasmon energy of Ln_2S_3.
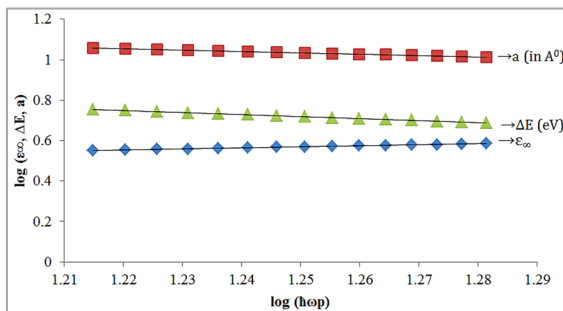
Figure 4. Plot of Dielectric constant, Optical band gap and lattice constant versus plasmon energy of C-type Ln_2O_3
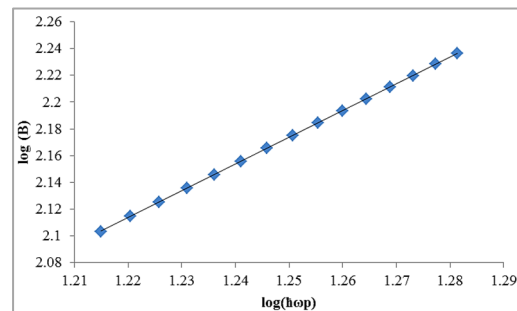
Figure 5. Plot of bulk modulus versus plasmon energy of C-type Ln_2O_3

We observe that in the plot of E_h, E_c, E_g, f_i, ε_∞, ΔE_g and lattice constant (a), versus ($\hbar\omega_p$); the lanthanide sesquioxides and sesquisulphides lies on the straight line. From Figures 2-5, it is clear that homopolar gap, heteropolar gap, average energy gap, lattice constant and optical dielectric constant trends in these materials increases with increasing plasmon energy and bond ionicity and band gap decreases on increasing this energy. We have provided empirical relations for the mechanical and electrical properties of rare earth chalcogenides and binary semiconductors in our earlier work [20–23]. Consequently, we believed it would be interesting to provide a different explanation for the optical, structural, and electrical characteristics of C-type Ln_2O_3 as follows:

$$E_h = A(\hbar\omega_p)^{1.666} \ . \tag{6}$$

$$E_c = B(\hbar\omega_p)^{0.666} \ . \tag{7}$$

$$E_g = C(\hbar\omega_p)^{0.746} \ . \tag{8}$$

$$f_i = D(\hbar\omega_p)^{-1.6} \ . \tag{9}$$

$$\varepsilon_\infty = E(\hbar\omega_p)^{0.508} \ . \tag{10}$$

$$\Delta E = F(\hbar\omega_p)^{-1.016} \ . \tag{11}$$

$$a = G(\hbar\omega_p)^{-0.666} \ . \tag{12}$$

$$B = H(\hbar\omega_p)^{2.0} \ . \tag{13}$$

The empirical constants A, B, C, D, E, F, G, and H in the aforementioned relations are listed in Table 1 and depend on the type of chemical bonds that exist between the different types of atoms. The electrical, structural, optical, and mechanical properties of these compounds have all been briefly reviewed before [2, 4, 6, 9, 25, 26–32], thus they won't be covered in length here. The values of the lattice constant (a), homopolar gap (E_h), heteropolar gap (E_c), average energy gap (E_g), bond ionicity (f_i), bulk modulus (B), optical

dielectric constant (ε_∞), and band gap (ΔE) of these materials have been studied and are shown in Tables 2-4, respectively, using the proposed empirical relations (6) through (13). In this study, we have shown excellent agreement with values derived from modified PVV theory with available theoretical findings [34, 35] and experimental data. The plasmon energy is the only input parameter used in the current empirical model to estimate the electrical, structural, mechanical, and optical properties of these materials

Table 1. Values of the constants using in relations (6-12).

Constants	A	B	C	D	E	F	G	H
Ln$_2$O$_3$	0.0442	1.051	1.079	1.054	0.859	97.576	73.593	0.472
Ln$_2$S$_3$	0.0442	0.899	0.939	0.999	---	39.030	---	

Table 2. Electronic and mechanical properties of lanthanide sesquioxides (Ln$_2$O$_3$)

Ln$_2$O$_3$	$\hbar\omega_P$ (eV)	Energy gaps (in eV)								Bond ionicity		Bulk modulus	
		Homopolar gap (E$_h$)			Ionic gap (E$_c$)		Penn gap (E$_p$)			f$_i$		B (in GPa)	
		Calc. Eq. (6)	PVV Eq. (2)	Philips model	Calc. Eq. (7)	PVV Eq. (3)	Calc. Eq.(8)	PVV Eq.(1)	Penn model	Calc. Eq. (9)	Phillips Eq. (5)	Calc. Eq.(13)	Ref. [12, 34, 35]
La$_2$O$_3$	16.403	4.672	4.442	4.435	6.772	6.434	8.697	7.819	7.861	0.67	0.67	126.9	125.6, 123.5
Ce$_2$O$_3$	16.612	4.771	4.535	4.579	6.829	6.478	8.779	7.908	7.999	0.67	0.67	130.2	129.9, 135.8
Pr$_2$O$_3$	16.818	4.870	4.631	4.608	6.886	6.685	8.860	8.133	7.908	0.67	0.67	133.5	134.3, 137.0
Nd$_2$O$_3$	17.021	4.978	4.631	4.658	6.941	6.617	8.940	8.076	8.076	0.67	0.67	136.7	139.2, 136.9
Pm$_2$O$_3$	17.222	5.067	4.703	4.732	6.995	6.735	9.078	8.214	8.198	0.67	0.67	139.9	144.3, 136.0
Sm$_2$O$_3$	17.422	5.164	4.781	4.844	7.049	6.818	9.046	8.327	8.231	0.67	0.67	143.2	146.7, 142.3
Eu$_2$O$_3$	17.617	5.262	4.989	4.919	7.102	7.215	9.012	8.772	8.084	0.66	0.67	146.4	145.0, 143.1
Gd$_2$O$_3$	17.812	5.359	5.044	4.992	7.154	7.288	9.098	8.863	8.172	0.66	0.68	149.7	154.9, 144.7
Tb$_2$O$_3$	18.004	5.456	5.329	5.014	7.205	7.822	9.322	9.465	8.158	0.66	0.67	152.9	150.0, 158.6
Dy$_2$O$_3$	18.194	5.552	5.329	5.178	7.256	7.762	9.395	9.415	8.376	0.66	0.67	156.2	159.9, 150.0
Ho$_2$O$_3$	18.382	5.648	5.329	5.246	7.306	7.702	9.468	9.366	8.444	0.66	0.67	159.4	161.6, 178.0
Er$_2$O$_3$	18.568	5.744	5.389	5.321	7.355	7.774	9.539	9.459	8.528	0.65	0.65	162.7	161.2, 155.0
Tm$_2$O$_3$	18.753	5.839	4.989	5.406	7.404	6.865	9.610	8.446	8.642	0.66	0.65	165.9	161.6, 162.0
Yb$_2$O$_3$	18.935	5.934	4.989	5.487	7.451	6.816	9.679	8.447	8.757	0.66	0.66	169.2	161.6, 181.0
Lu$_2$O$_3$	19.116	6.028	5.574	5.557	7.499	6.779	9.748	8.776	8.878	0.66	0.67	172.4	175.3, 179.4

Table 3. Electronic properties of lanthanide sesquisulphides (Ln$_2$S$_3$)

Ln$_2$S$_3$	$\hbar\omega_P$	Energy gaps (in eV)								Bond ionicity		Dielectric constant	
		E$_h$			E$_c$		E$_p$			f$_i$		ε_∞	
		Calc. Eq. (6)	PVV Eq. (2)	Philips model	Calc. Eq. (7)	PVV Eq. (3)	Calc. Eq. (8)	PVV Eq. (1)	Penn model	Calc. Eq. (9)	Phillips Eq. (5)	Calc. Eq. (11)	Ref. [10]
La$_2$S$_3$	13.414	3.341	3.347	3.244	5.066	4.865	6.513	5.958	6.039	0.66	0.66	2.78	2.8
Ce$_2$S$_3$	13.717	3.468	3.474	3.072	5.142	4.844	6.623	5.961	5.688	0.66	0.66	2.72	2.7
Pr$_2$S$_3$	13.795	3.501	3.507	3.611	5.162	5.138	6.651	6.221	5.714	0.65	0.68	2.71	2.6
Nd$_2$S$_3$	13.818	3.511	3.517	3.429	5.167	5.072	6.659	6.166	6.666	0.65	0.67	2.70	2.4
Pm$_2$S$_3$	13.859	3.540	3.564	---	5.195	5.155	6.669	6.259	---	0.65	0.67	2.69	---
Sm$_2$S$_3$	13.929	3.558	3.574	3.275	5.201	5.160	6.707	6.277	6.956	0.65	0.67	2.68	---
Eu$_2$S$_3$	13.941	3.563	3.608	---	5.221	5.212	6.736	6.225	---	0.65	0.67	2.68	---
Gd$_2$S$_3$	13.953	3.568	3.713	3.510	5.281	5.197	6.823	6.269	5.525	0.65	0.67	2.67	---
Tb$_2$S$_3$	14.032	3.601	3.642	3.552	5.240	5.128	6.764	6.484	5.706	0.65	0.67	2.66	---
Dy$_2$S$_3$	14.275	3.706	3.704	3.461	5.275	5.317	6.815	6.346	5.709	0.65	0.67	2.61	---
Ho$_2$S$_3$	14.111	3.635	3.723	3.725	5.286	5.196	6.831	6.346	6.652	0.65	0.67	2.64	---
Er$_2$S$_3$	14.252	3.696	3.747	3.741	5.300	5.294	6.851	6.466	5.734	0.65	0.67	2.62	---
Tm$_2$S$_3$	14.299	3.716	3.785	3.754	5.321	5.513	6.882	6.646	6.724	0.65	0.68	2.61	---
Yb$_2$S$_3$	14.354	3.740	3.540	3.754	5.185	5.362	6.684	6.541	5.805	0.65	0.67	2.60	---
Lu$_2$S$_3$	14.441	3.778	3.563	4.077	5.198	5.423	6.703	6.613	5.831	0.65	0.67	2.58	---

Table 4. Values of Optical dielectric constant (ε_∞), Optical band gap (ΔE_g, in eV) and lattice parameter (a in A^0) of C-type lanthanide (Ln$_2$O$_3$) sesquioxides.

Ln$_2$O$_3$	$\hbar\omega_P$	ε_∞		Optical band gap (ΔE_g)					Lattice constant (a)		
		Calc.	Expt[#]	Calc.	Theo[‡]	GW$_0$[$]	G$_0$W$_0$[$]	Expt[$]	Calc.	Expt[†].	Theo[±]
La$_2$O$_3$	16.403	3.557	3.667	5.68	5.60	5.24	4.95	5.55, 5.34, 5.30	11.42	11.38	11.39
Ce$_2$O$_3$	16.612	3.580	3.712	5.61	--	1.29	1.50	2.40	11.32	11.16	11.41
Pr$_2$O$_3$	16.818	3.603	3.775	5.54	5.56	2.82	2.86	3.90, 3.50	11.23	11.14	11.28
Nd$_2$O$_3$	17.021	3.625	3.686	5.47	4.00	4.70	4.50	4.70, 4.80	11.14	11.07	11.17
Pm$_2$O$_3$	17.222	3.646	--	5.41	--	5.41	5.25	--	11.05	10.99	11.06
Sm$_2$O$_3$	17.422	3.668	3.725	5.35	5.04	5.22	4.38	5.00	10.97	10.90	10.99
Eu$_2$O$_3$	17.617	3.689	3.877	5.28	4.48	3.48	2.77	4.40	10.89	10.82	10.81
Gd$_2$O$_3$	17.812	3.709	3.861	5.23	5.45	5.30	4.89	5.40	10.81	10.79	--
Tb$_2$O$_3$	18.004	3.730	3.857	5.17	4.77	3.74	3.81	3.80	10.73	10.73	10.66
Dy$_2$O$_3$	18.194	3.750	3.853	5.11	4.86	4.24	4.41	4.90	10.66	10.67	10.60
Ho$_2$O$_3$	18.382	3.769	3.842	5.06	5.27	5.12	4.68	5.30	10.59	10.60	10.54
Er$_2$O$_3$	18.568	3.789	3.826	5.01	5.21	5.22	4.78	5.30, 5.49	10.51	10.55	10.54
Tm$_2$O$_3$	18.753	3.808	3.803	4.96	5.25	5.15	4.73	5.40, 5.48	10.44	10.48	10.47
Yb$_2$O$_3$	18.935	3.826	3.771	4.91	5.30	4.70	3.23	4.90, 5.05	10.38	10.42	--
Lu$_2$O$_3$	19.116	3.845	3.725	4.86	5.52	4.99	4.66	4.89, 5.79, 5.50	10.31	10.38	10.35

[$]Ref. [2], [#]Ref. [6], [†]Ref. [4], [‡]Ref. [9], [‡]Ref. [15]

3. CONCLUSIONS

Investigations into the electrical, structural, optical, and mechanical characteristics of C-type Ln_2X_3 compounds have been conducted using the suggested empirical method. Based on the findings, we draw the conclusion that a compound's plasmon energy is a crucial factor to consider when determining the electrical, structural, and optical characteristics of these materials. Notably, the values are in excellent agreement with published experimental data compared to numerous academics' theoretical findings, and the suggested approach is straightforward and broadly applicable. The current study presents empirical relationships between the valence electron plasmon energy of cubic-structured Ln_2X_3 compounds and their electrical, optical, mechanical, and structural characteristics. Using the plasmon energy ($\hbar\omega_p$ in eV) as an input parameter, this can be successfully used to estimate the electric, structural, mechanical, and optical properties of these compounds. These findings demonstrate the reasonableness of our existing method and provide us with a helpful manual for estimating and forecasting the electrical, optical, and structural characteristics of these materials. Our theoretically computed data can be used to anticipate future research and wait for upcoming experimental validations.

ORCID

Dheerendra Singh Yadav, https://orcid.org/0000-0001-8315-9743; **Ajay Singh Verma,** https://orcid.org/0000-0001-8223-7658

REFERENCES

[1] V. Corumlu, I. Ermis, S.D. Acer, T. Cifci, Y. Dagdemir, and M. Ari, "The phase stability and conductivity of $Ho_2O_3 – Gd_2O_3$ co-doped electrolyte for solid oxide fuel cell," J. Materials Science: Materials in Electronics, **27**, 5839 (2016). https://doi.org/10.1007/s10854-016-4500-y

[2] H. Jiang, P. Rinke, and M. Scheffler, "Electronic properties of lanthanide oxides from the GW perspective," Physical Review B, **86**, 125115 (2012). https://doi.org/10.1103/PhysRevB.86.125115

[3] Jiang H., Gomez-bal, Rinke P., Scheffler M., Localized and Itinerant states in lanthanide oxides united by GW @ LDA + U, Physical Review letters 102 (2009) 126403. https://doi.org/10.1103/PhysRevLett.102.126403

[4] D. Richard, E.L. Munoz, M. Renteria, L.A. Errico, A. Svane, and N.E. Christensen, "Ab initio LSDA and LSDA+U Study of pure and Cd-doped cubic lanthanide sesquioxides," Physical Review B, **88**, 165206 (2016). https://doi.org/10.1103/PhysRevB.88.165206

[5] L.R. Eyring, K.A. Gschneidner, and G.H. Lander, editors, *Handbook on the Physics and Chemistry of Rare Earths*, **3**, (Elsevier, 1997). pp. 337.

[6] V.P. Zhuze, and A.I. Shelykh, "Optical properties and electron - structure of rare earth sesquisulfides and sesquioxides," Soviet Physics semiconductors, **23**, 245 (1989). (in Russian)

[7] H.R. Hoekstra, and K.A. Gingerich, "High-pressure B-type polymorphs of some rare-earth sesquioxides," Science **146**, (1964). 1163. https://doi.org/10.1126/Science.146.3648.1163

[8] G. Adachi, and N. Imanaka, "The Binary Rare Earth Oxides," Chemical Reviews, **98**, 1479-1514 (1998). https://doi.org/10.1021/cr940055h.

[9] N. Hirosaki, S. Ogata, and C. Kocer, "Ab initio calculation of the crystal structure of the lanthanide Ln_2O_3 sesquioxides," Journal of alloys and compounds, **351**, 31 (2003). https://doi.org/10.1016/S0925-8388(02)01043-5

[10] A.V. Prokofiev, A.I. Shelykh, and B.T. Melekh, "Periodicity in the band gap variation of Ln_2X_3 (X=O, S, Se) in the lanthanide series," Journal of alloys and compounds, **242**, 41 (1996). https://doi.org/10.1016/0925-8388(96)02293-1

[11] N. Singh, S.M. Saini, T. Nautiyal, and S. Anluck, "Electronic structure and optical properties of rare earth sesquioxides (R_2O_3, R= La, Pr & Nd)," Journal of applied Physics, **100**, 255 (2006). https://doi.org/10.1063/1.2353267

[12] M. Rahm, and N.V. Skorodumova, "Phase stability of the rare-earth sesquioxides under pressure," Phys. Rev. B, **80**, 104105 (2009). https://doi.org/10.1103/PhysRevB.80.104105

[13] Jiang Seng, Bai Li-Gang, Lin J., Xiao Wan-Sheng, Li Xiao-Dong, Li Yan-Chun, Tang Ling-Yun, Zhang Yu-Feng, Zhang De-Chun, Zheng Li-Rong, The phase transition of Eu_2O_3 under high pressures, Chinese Physics Letters, **26**, 076101 (2009). https://doi.org/10.1088/0256-307X/26/7/076101

[14] K.A. Irshad, N.V. Chandra Shekar, T.R. Ravindran, V. Srihari, and K.K. Pandey, "X-Ray diffraction and Raman studies on Ho: Eu_2O_3," J. Molecular Structure, **1128**, 325 (2017). https://doi.org/10.1016/j.molstruc.2016.08.077

[15] A.F. Andreeva, and I.Ya. Gilman, "Some optical properties of films of rare earth oxides," Zh. Prikl. Spektrosk. **28**(5), 895 (1978). (in Russian)

[16] M.V. Abrashev, N.D. Todorov, and J. Geshev, "Raman spectra of R_2O_3 (R= Rare earth) sesquioxides with c – type bixbyite crystal structure: A comparative study," J. Applied Physics, **116**, 10 (2014). http://dx.doi.org/10.1063/1.4894775

[17] S.J. Liu, J. Lin, B. Ligang, Y. Zhang, X. Li, Y. Li, L. Tang, and H. Wang, "Structural transformations in cubic Dy_2O_3 at high pressures," Solid State Communications, **169**, 37 (2013). https://doi.org/10.1016/j.ssc.2013.06.027

[18] V.I. Marchenko, Electronic Structure and Physico Chemical Properties of Refractory Compounds and Alloys (1980) 193

[19] A.S. Verma, and S.R. Bharadwaj, "Electronic and optical properties of zinc blende and complex crystal structured solids," Phys. State Solidi B, **243**, 4025 (2006). https://doi.org/10.1002/pssb.200844072

[20] D.S. Yadav, "Electronic and mechanical properties of rare earth monochalcogenides," J. Alloys and Comp. **537**, 250 (2012). https://doi.org/10.1016/j.jallcom.2012.05.016

[21] D.S. Yadav, and D.V. Singh, "Static and dynamical properties of II-VI and III-V group binary solids," Phys. Scr. **85**, 015701 (2012). https://doi.org/10.1088/0031-8949/85/01/015701

[22] D.S. Yadav, "Electronic Properties of Bonds in AIBIIICVI2 Chalcopyrite Semiconductors," Journal of Materials Physics and Chemistry, **3**(1), 6-10 (2015). https://doi.org/10.12691/jmpc-3-1-2

[23] R. Bhati, D.S. Yadav, R.C. Gupta, and A.S. Verma, "Simplistic model for the investigation of mechanical stability parameters of pyrochlore structured solids," Materials Physics and Mechanics, **51**, 90 (2023). http://dx.doi.org/10.18149/MPM.5152023-9

[24] R. Bhati, D.S. Yadav, P. Varshney, R.C. Gupta, and A.S. Verma, "Semi – Empirical predictions for hardness of rare earth pyrochlores; high permittivity dielectrics and thermal barrier coating materials," East European J. Physics, (1), 222 (2023). https://doi.org/10.26565/2312-4334-2023-1-29

[25] N. Yadav, D.S. Yadav, P. Varshney, and R.C. Gupta, "Electronic and mechanical properties of chemical bonds (A-O and B-O) in cubic phase A+2B+4O3 perovskite oxides," American J. Physics and Applications, **11**, 80 (2023). https://doi.org/10.11648/j.ajpa.20231104.11

[26] A.S. Verma, R.K. Singh, and S.K. Rathi, "An empirical model for dielectric constant and electronic polarizability of binary (ANB8-N) and ternary (ANB2+NC27-N) tetrahedral semiconductors," J. Alloys and compound, **486**, 795 (2009). https://doi.org/10.1016/j.jallcom.2009.07.067

[27] A.S. Verma, "Electronic and optical properties of rare earth chalcogenides and pnictides," Afr. Phys. Rev. **3**, 0003(2009). http://lamp.ictp.it/index.php/aphysrev/article/viewFile/248/151

[28] D.V. Singh, and V.P. Gupta, "Bulk moduli of Sm, Eu and Yb monochalcogenides," Physica Status Solidi (B), **171**, K71 (1992). https://doi.org/10.1002/pssb.2221710225

[29] D.S. Yadav, and A.S. Verma, "Electronic, optical and mechanical properties of AIIBVI semiconductors," International J. Modern Physics B, **26**, 1250020 (2012). https://doi.org/10.1142/S0217979212500208

[30] D.S. Yadav, and S.P. Singh, "Electronic properties of aluminium, gallium and indium pinictides," Physica Scripta, **82**, 065705 (2010). https://doi.org/10.1088/0031-8949/82/06/065705

[31] J.C. Phillips, and J.A. Van Vechten, "Spectroscopic analysis of cohesive energies and heats of formation of tetrahedrally co-ordinated semiconductors," Physical Review B, **2**, 2147 (1970). https://doi.org/10.1103/PhysRevB.2.2147.

[32] B.F. Levine, "d – electron effects on bond susceptibilities and ionicities," Physical Review B, **7**, 2591 (1973). https://doi.org/10.1103/PhysRevB.7.2591

[33] Moss T S, Relations between the refractive index and energy gap of semiconductors, Physica Status Solidi (b) 131 (1985) 415. https://doi.org/10.1002/pssb.2221310202

[34] A.K. Pathak, and T. Vazhappilly, "Ab initio study on structure, elastic and mechanical properties of lanthanide sesquioxides," Physica Status Solidi (b), **255**, 1700668 (2018). https://doi.org/10.1002/pssb.201700668

[35] D. Richard, L.E. Errico, and M. Renteria, "Structural properties and the pressure-induced C→A phase transition of lanthanide sesquioxides from DFT and DFT+ U calculations," Journal of Alloys and Compounds, **664**, 580-589 (2016). https://doi.org/10.1016/j.jallcom.2015.12.236

ЕЛЕКТРОННІ, СТРУКТУРНІ, ОПТИЧНІ ТА МЕХАНІЧНІ ВЛАСТИВОСТІ
КУБІЧНОГО СТРУКТУРОВАНОГО Ln₂X₃ (Ln = La→Lu & X=O,S): ЕМПІРИЧНЕ ДОСЛІДЖЕННЯ

Пуджа Ядав[a], Дірендра Сінгх Ядав[b], Дхармвір Сінгх[a], Правеш Сінгх[c], Аджай Сінгх Верма[d,e]
[a]Департамент фізики, коледж Агра, Агра, Індія
[b]Департамент фізики, Чаран Сінгх PG коледже Хеонра (Сайфай) Етавах, Індія
[c]Департамент електроніки та комунікаційної техніки, Групи установ KIET, Газіабад, Індія
[d]Відділ досліджень та інновацій, Школа прикладних наук та наук про життя, Університет Уттаранчал, Уттаракханд, Дехрадун, Індія
[e]Університетський центр досліджень і розвитку, факультет фізики, Університет Чандігарха, Мохалі, Пенджаб, Індія

У цій публікації ми розглянули структурні, оптичні та механічні характеристики серії лантаноїдів Ln₂X₃ з кубічною структурою (Ln = La→ Lu та X = O, S) за допомогою теорії коливань плазми валентних електронів твердих тіл. Використовуючи теорію хімічного зв'язку твердих тіл, яку створили Філліпс і Ван-Вехтен, ми додатково підтвердили наші висновки. На жаль, було виявлено, що опис діелектрика Філіпса та Ван-Вехтена (PVV) застосовний виключно до напівпровідників та ізоляторів. Показано, що емпіричний зв'язок, представлений раніше Ядавом і Бхаті [D.S. Yadav, J. Alloys and Comp. 537, 250 (2012); D.S. Yadav, and D.V. Singh, Phys. Scr. 85, 015701 (2012); D.S. Yadav, J. Mater. Phys. Chem. 3(1), 6-10 (2015); R. Bhati, et al., Mater. Phys. Mech. 51, 90 (2023); R. Bhati, et al., East Eur. J. Phys. (1), 222 (2023).], пов'язує плазмонну енергію твердих тіл зі складною структурою, кам'яної солі та цинкової обманки з їхніми електронними, механічними, статичними та динамічними властивостями, які можна застосувати до кубічна структурована серія лантаноїдів (Ln₂S₃ & Ln₂O₃) лише з незначними модифікаціями. Враховуючи добре відому теорію діелектрика для твердих тіл, була розроблена альтернативна методика для оцінки електронних, структурних, механічних і оптичних властивостей цих матеріалів, включаючи їх ширину забороненої зони (ΔEg в eB), оптичну діелектричну проникність, гомополярність і гетерополярні щілини, середні енергетичні щілини, іонність хімічного зв'язку та об'ємні мудулі. Оцінка була розрахована на основі майже зворотного зв'язку між енергією плазмону цих сполук та їхніми оптичними, механічними, структурними та електричними характеристиками. Для цих речовин очікувані значення вищезазначених параметрів утворюють пряму лінію, якщо їх відобразити в логарифмічному масштабі від енергії плазмону (ħωp). Ми перевірили сполуки типу C Ln₂X₃ за допомогою рекомендованих методів, і оцінені нами значення добре узгоджуються зі значеннями, отриманими на основі модифікованої теорії PVV та інших порівнянних експериментальних і теоретичних даних, доступних на даний момент.
Ключові слова: *електронні властивості; оптичні властивості; структурні властивості; механічні властивості; Ln₂O₃; Ln₂S₃; енергія плазми*

CHANGES IN THE STRUCTURE AND PROPERTIES OF SILICON DURING YTTERBIUM DOPING: THE RESULTS OF A COMPREHENSIVE ANALYSIS

Khodjakbar S. Daliev, Sharifa B. Utamuradova, Jonibek J. Khamdamov*,
Mansur B. Bekmuratov, Shahriyor B. Norkulov, Ulugbek M. Yuldoshev

Institute of Semiconductor Physics and Microelectronics at the National University of Uzbekistan,
20 Yangi Almazar st., Tashkent, 100057, Uzbekistan
*Corresponding Author e-mail: jonibek.uzmu@gmail.com
Received September 13, 2024; revised October 20, 2024; accepted October 20, 2024

In this work, a comprehensive study of the structural, chemical and electrophysical properties of monocrystalline silicon (Si) doped with ytterbium (Yb) has been carried out. The alloying was carried out by thermal diffusion at a temperature of 1473 K in high vacuum conditions followed by rapid cooling. Atomic force microscopy (AFM), infrared Fourier spectroscopy (FTIR), deep level spectroscopy (DLTS) and Raman spectroscopy (RAMAN) were used to analyze the samples obtained. AFM images of the surface of the doped samples demonstrated significant changes in topography. The RMS surface roughness increased from less than 10 nm to 60-80 nm, and the maximum height of the irregularities reached 325 nm. These changes are explained by the formation of nanostructures caused by the uneven distribution of ytterbium atoms in the silicon crystal lattice, as well as the occurrence of internal stresses. "IR-Fourier spectroscopy showed a significant decrease in the concentration of optically active oxygen (N_O^{opt}) by 30-40% after doping. This effect is associated with the interaction of ytterbium atoms with silicon and a change in the chemical composition of the material. The RAMAN spectra revealed the formation of new phases and nanocrystallites in the doped samples. Peak shifts and changes in their intensity were detected, indicating a rearrangement of the crystal lattice caused by the introduction of ytterbium. It was calculated that the diffusion coefficient of ytterbium in silicon is 1.9×10^{-15} cm^2/s, which indicates a slow diffusion process characteristic of rare earth metals. Electrical measurements carried out on the MDS-structures showed a shift in the volt-farad characteristics towards positive bias voltages, which is associated with a decrease in the density of surface states at the Si-SiO$_2$ interface and the appearance of deep levels with an ionization energy of E_c-0.32 eV.

Keywords: *Monocrystalline silicon, Ytterbium doping, Atomic force microscopy, Raman spectroscopy, Surface roughness, Nanostructures, Electrical properties, MDS-structures, Si-SiO$_2$ interface*
PACS: 68.37.Ps, 33.20.Fb

INTRODUCTION

The development and improvement of materials for semiconductor electronics remain key directions in modern science and technology [1-5]. Silicon, which is the main material for semiconductor devices, has unique properties [2-8]. However, in order to further improve it, it is necessary to use various alloying methods. The introduction of atoms of other elements into the silicon crystal lattice makes it possible to significantly change its properties and open up new possibilities for creating highly efficient electronic devices.

Special attention is given to rare earth elements (REE) such as yttrium, dysprosium, and ytterbium, which can significantly affect the structural and physical properties of silicon. Doping silicon with ytterbium (Yb) is a particularly interesting area of research since this element possesses unique physicochemical properties, including low chemical activity and a divalent state, making it a promising candidate for the creation of new semiconductor materials. As a rare earth element, ytterbium is not well-studied in terms of its effect on the crystal structure of silicon. However, preliminary studies indicate that doping silicon with ytterbium may lead to significant changes in its microstructure, including the formation of defects, nanocrystals, and changes in the material's phase composition. These structural transformations play an important role in determining the physical properties of silicon, such as conductivity and resistance to radiation exposure.

To study these structural changes in detail, atomic force microscopy (AFM) was used in this research. AFM allows for the visualization of material surfaces at the nanoscale, making it possible to detect changes in topography and surface structure caused by ytterbium doping [9-10]. The obtained data showed that doping leads to significant surface irregularities in silicon, with a maximum height of up to 325 nm, indicating a complex microstructure formed due to the uneven distribution of ytterbium atoms in the crystal lattice. In addition to AFM data, the study used methods of infrared Fourier spectroscopy (FTIR) and Raman spectroscopy (RAMAN) to study phase changes and the distribution of impurities in silicon. These methods revealed a reduction in the concentration of optically active oxygen, the formation of new phases and nanocrystals, as well as the evaluation of internal stress in the crystal lattice.

Thus, this study is aimed at deepening knowledge about structural changes in ytterbium-doped silicon and their effect on the physico-chemical properties of the material. The use of AFM in combination with other spectroscopic methods provides a more complete understanding of the processes occurring in doped silicon, which can become the basis for further developments in the field of semiconductor electronics and optoelectronics [11-18].

MATERIALS AND METHODS

For the experiment, samples of monocrystalline silicon with an initial resistivity ranging from 2.5 to 10 Om·cm were selected. The samples underwent thorough chemical cleaning to remove contaminants and oxide layers from the surface. This was done using an acid-peroxide wash, followed by treatment in hydrofluoric acid (HF), which ensured the complete removal of oxides and provided a clean silicon surface for subsequent doping.

After cleaning, high-purity ytterbium (Yb) films (99.999%) were deposited on the silicon surface. The deposition was carried out by vacuum sputtering under high vacuum conditions (10^{-6} Torr) using an oil-free vacuum system, which ensured uniform distribution of ytterbium atoms on the silicon surface. The doping process was performed using the thermal diffusion method. Prepared n-Si samples were placed in vacuum-sealed quartz ampoules and subjected to diffusion annealing at 1473 K (1200°C) for 15 hours. The samples were then rapidly cooled to prevent the formation of large defects and to ensure the uniform distribution of ytterbium within the silicon crystal lattice. Rapid cooling also promoted the creation of internal stresses in the samples, which could affect the formation of nanocrystals and other structural changes. After thermal diffusion, the surface layer of the samples, approximately 2 μm thick, was removed for the investigation of the doped deeper layers. This was achieved using mechanical treatment and chemical etching, allowing the study of structural changes at various depth levels.

To study the surface topography of the samples after ytterbium doping, atomic force microscopy (AFM) was used. AFM provides nanometer-resolution imaging, making it an indispensable tool for analyzing structural changes in materials. The studies were conducted on a Nanaview-2000 series microscope, which ensured high-precision measurements. Measurements were performed in several modes, including contact and semi-contact modes, to obtain information about the height of surface irregularities, the distribution of structural defects, and phase heterogeneities. 3D surface maps obtained using AFM allowed the evaluation of the maximum heights of structural elements (up to 325 nm) and revealed the distribution characteristics of ytterbium in silicon.

For chemical composition analysis and the study of molecular vibrations in the doped samples, Infrared Fourier spectroscopy (FTIR) was employed. FTIR absorption spectra were obtained using the FSM 2201 infrared Fourier spectrometer, operating in the range from 380 to 7800 cm^{-1}. The FTIR method allowed the determination of the concentration of optically active oxygen (NO$_{opt}$) in silicon and the identification of ytterbium's effect on the chemical composition and structure of the samples. Spectral analysis showed that ytterbium doping reduced the concentration of NO$_{opt}$ by 30-40%, depending on the concentration of the introduced impurities.

Raman spectroscopy was used to investigate structural changes and phase composition. Raman spectra were obtained using an Ocean Insight Raman spectrometer with laser radiation at a wavelength of 780 nm. Raman spectroscopy revealed the formation of nanocrystals in the ytterbium-doped silicon samples. Three bands were identified, corresponding to Si–Si, Si–Yb, and Yb–Yb bond vibrations. The intensity and position of these bands varied depending on the composition and thermal treatment conditions. The internal stress in the crystallites, which could reach up to 3 GPa, was also studied.

For processing and analyzing the obtained spectra, FSpec software was used for FTIR spectroscopy, and OriginPro was used for Raman data analysis. Data processing included baseline subtraction, spectrum normalization, and the calculation of crystallite sizes from Raman peaks. The analysis results allowed for the evaluation of ytterbium's influence on the structural properties of silicon and the identification of key doping features, such as defect formation, changes in phase composition, and internal stress in the crystals.

RESULTS AND DISCUSSION

Analysis of AFM images revealed significant changes in the surface topography of silicon after ytterbium doping (Fig. 1). Prior to doping, the silicon surface was relatively smooth, with minimal irregularities and defects. The root-mean-square (RMS) roughness of the control sample was less than 10 nm, and the maximum height of the irregularities did not exceed 78.1 nm (Fig. 1a). After ytterbium doping, a sharp increase in the maximum height of surface irregularities up to 325 nm was observed in the near-surface layer, representing a substantial change (Fig. 1c). Doping with rare earth metals, such as ytterbium, induces local changes in the crystalline structure of silicon. Ytterbium has a larger atomic radius compared to silicon, which leads to distortions in the crystal lattice and the formation of internal stresses. These stresses can cause the formation of microdefects and recrystallization at grain boundaries, contributing to the increase in surface roughness.
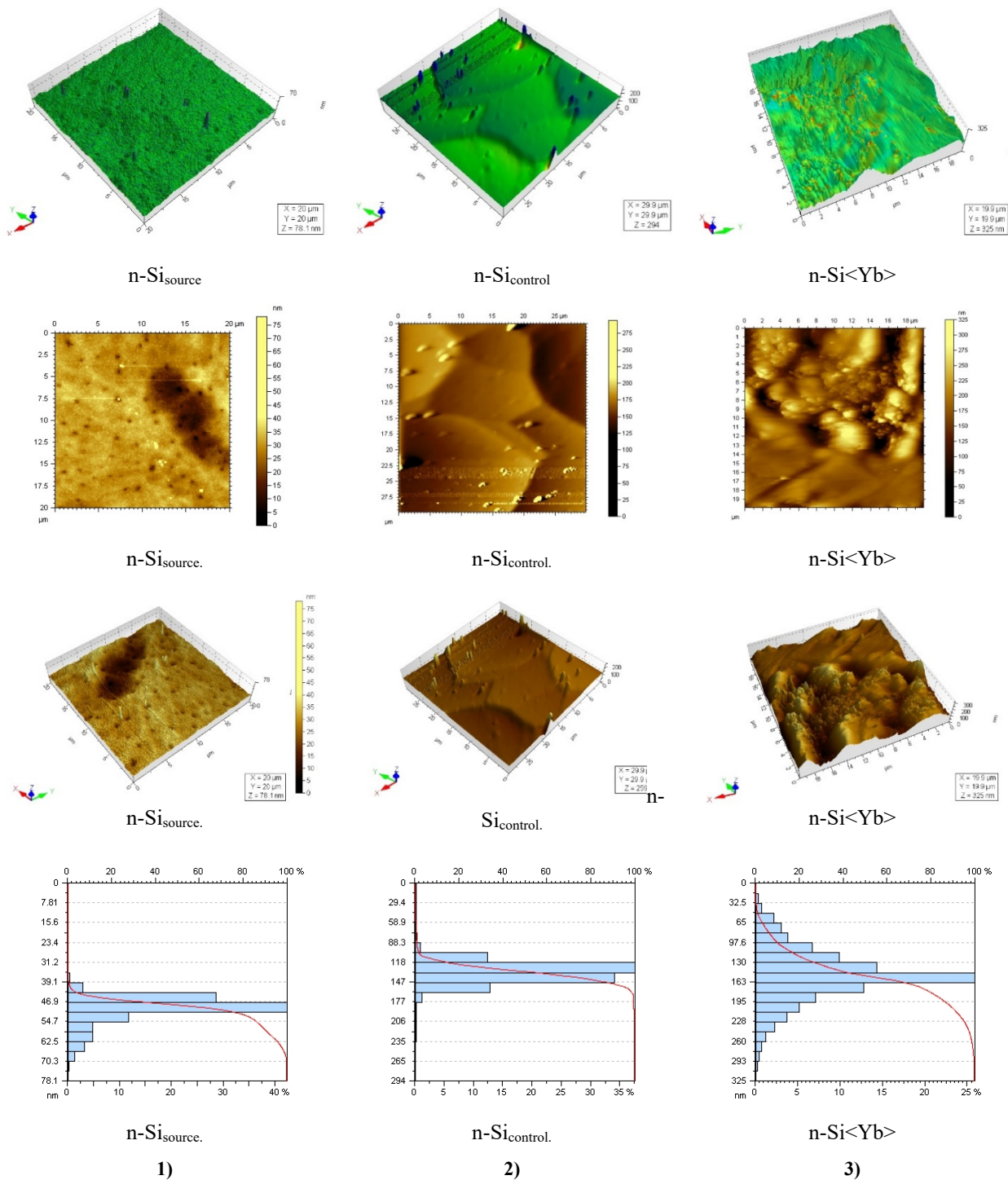
According to Gibbs' theory, surface energy depends on crystallographic orientation and the presence of impurities. The introduction of ytterbium atoms increases the free surface energy, driving the system to reduce this energy by forming structures with higher roughness. The RMS roughness of the ytterbium-doped silicon surface is 60-80 nm in the near-surface layer, which is significantly higher than that of the control sample. This increase in roughness is associated with the formation of nanostructures or clusters of ytterbium on the surface.

To assess the change in surface energy, Gibbs' expression for surface energy can be used:

$$\gamma = \frac{dW}{dA},\qquad(1)$$

where γ is the surface energy, W is the work to change the surface, A is the surface area.

As the surface roughness increases, the surface area A also increases, which leads to an increase in the surface energy γ. An increase in surface energy may also explain the tendency of the material to form larger structures on the surface.

n-Si$_{source}$ n-Si$_{control}$ n-Si<Yb>

n-Si$_{source.}$ n-Si$_{control.}$ n-Si<Yb>

n-Si$_{source.}$ Si$_{control.}$ n-Si<Yb>

n-Si$_{source.}$ n-Si$_{control.}$ n-Si<Yb>

1)   2)   3)

Figure 1. Atomic Force Microscopy (AFM) Images:
1) n-Si original sample; 2) n-Si control sample; 3) n-Si doped with ytterbium, with a 2 µm layer removed by grinding after doping

Phase analysis shows the presence of inhomogeneities, which are associated with the uneven distribution of ytterbium in the silicon structure. In the near-surface layer, the phases are distributed unevenly, indicating ytterbium agglomeration and the formation of new phases on the silicon surface.

Let's consider the changes in phase composition through the analysis of phase thermodynamic stability. Doping can cause the formation of ytterbium-containing phases, such as $YbSi_2$, which stabilize under certain conditions. The calculation of the change in Gibbs free energy during the formation of such phases can be expressed by:

$$\Delta G = \Delta H - T\Delta S, \tag{2}$$

where ΔG is the change in Gibbs free energy, ΔH is the enthalpy of formation, ΔS is the change in entropy, T is the temperature.

If G < 0, the phase is stable and can form on the surface. In this case, during high-temperature annealing and subsequent rapid cooling, the formation of thermodynamically stable ytterbium phases is likely, which explains the phase inhomogeneities on the surface.

n-Si<Yb>

n-Si<Yb>

n-Si<Yb>

n-Si<Yb>

n-Si<Yb>
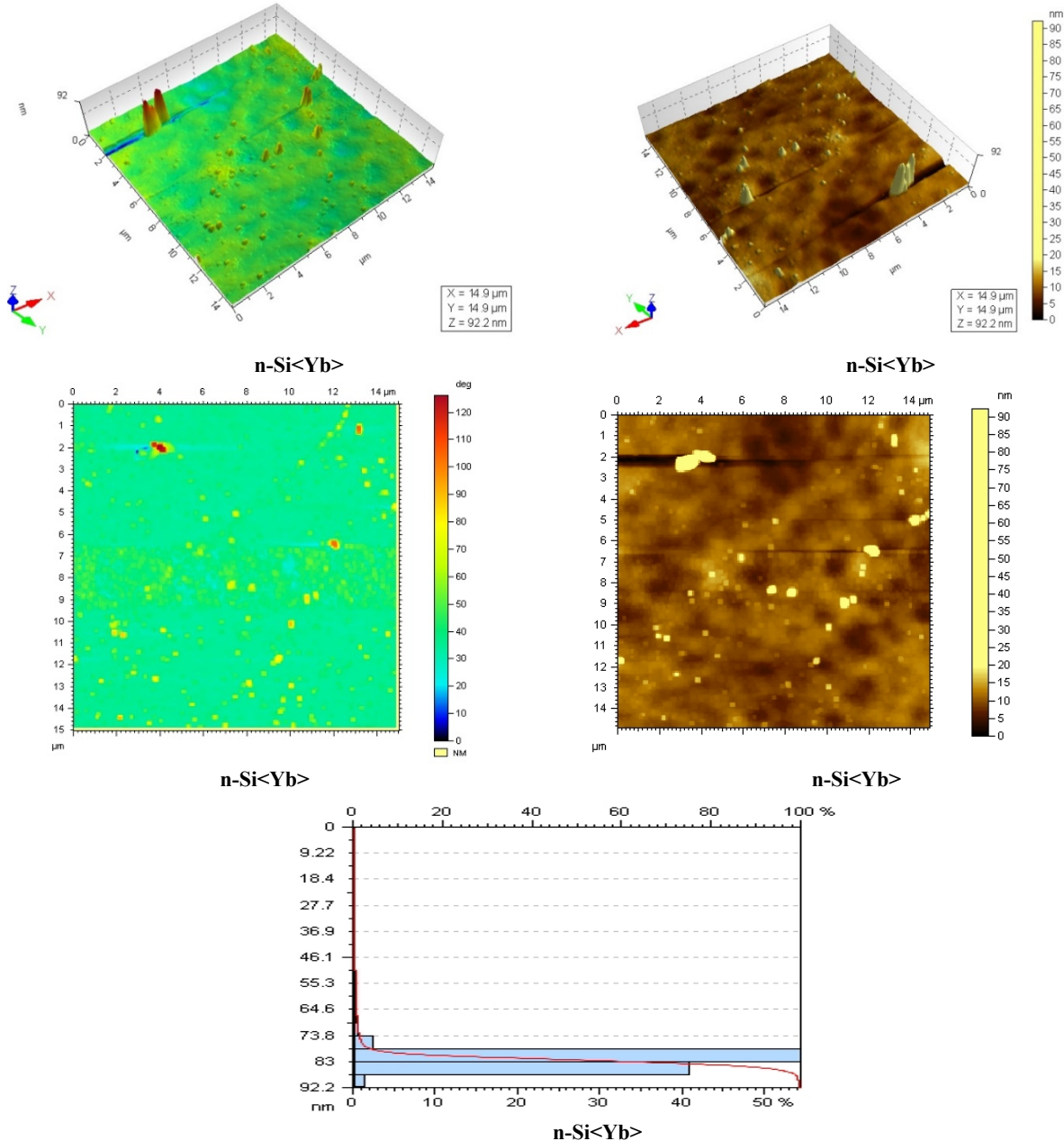
Figure 2. Profile distribution of ytterbium atoms in n-Si doped with ytterbium, obtained by AFM. The image shows the distribution of ytterbium atoms on the surface perpendicular to the sputtered layer

Based on the AFM image presented (Fig. 2), which shows the profile distribution of ytterbium atoms in n-Si doped with ytterbium, an analysis and evaluation of the diffusion coefficient can be conducted. To do this, changes in the structure and surface topography at various depths, as shown in the image, need to be analyzed. The image shows variations in topography and phase contrast, which may indicate the distribution of ytterbium within the silicon. The maximum changes are observed at a depth of approximately 2.36 µm, which can be used as an indicator for the calculation.

To evaluate the diffusion coefficient, we will use Fick's second law for non-stationary diffusion:

$$C(x,t) = \frac{C_o}{\sqrt{4\pi Dt}} exp\left(-\frac{x^2}{4Dt}\right), \tag{3}$$

where:

C(x,t) is the concentration of atoms at depth x at time t,

C_0 is the initial concentration of atoms on the surface,

D is the diffusion coefficient,

t is the diffusion time.

From the image in Fig. 2, it can be assumed that the changes in topography associated with ytterbium diffusion reach a depth of approximately 2.36 μm. The diffusion time t = 15 hours (54,000 seconds), and the depth x = 2.36 μm. The ytterbium concentration at a depth of 2.36 μm is about 10% of the initial surface concentration.

Solving the equation for D:

$$ln\left(\frac{C(x,t)}{C_0}\right) = -\frac{x^2}{4Dt}. \tag{4}$$

Substituting the values:

$$\ln(0,1) = \frac{(2.36 \times 10^{-4})^2}{4 \times D \times 54000}$$

$$D = \frac{(2.36 \times 10^{-4})^2}{4 \times 54000 \times ln(10)} \approx 1.9 \times 10^{-15} \; cm^2/_c$$

The calculated diffusion coefficient of ytterbium in silicon is approximately $\approx 1.9 \times 10^{-15} \; cm^2/_c$. This value indicates a relatively slow diffusion process, which is typical for rare earth metals such as ytterbium.

Infrared analysis showed that the comparison of the obtained data indicates a significant reduction in the concentration of optically active oxygen N_O^{opt} after ytterbium diffusion (see Fig. 3). Ytterbium doping reduces the concentration of optically active oxygen by 30-40%, depending on the concentration of the added element.
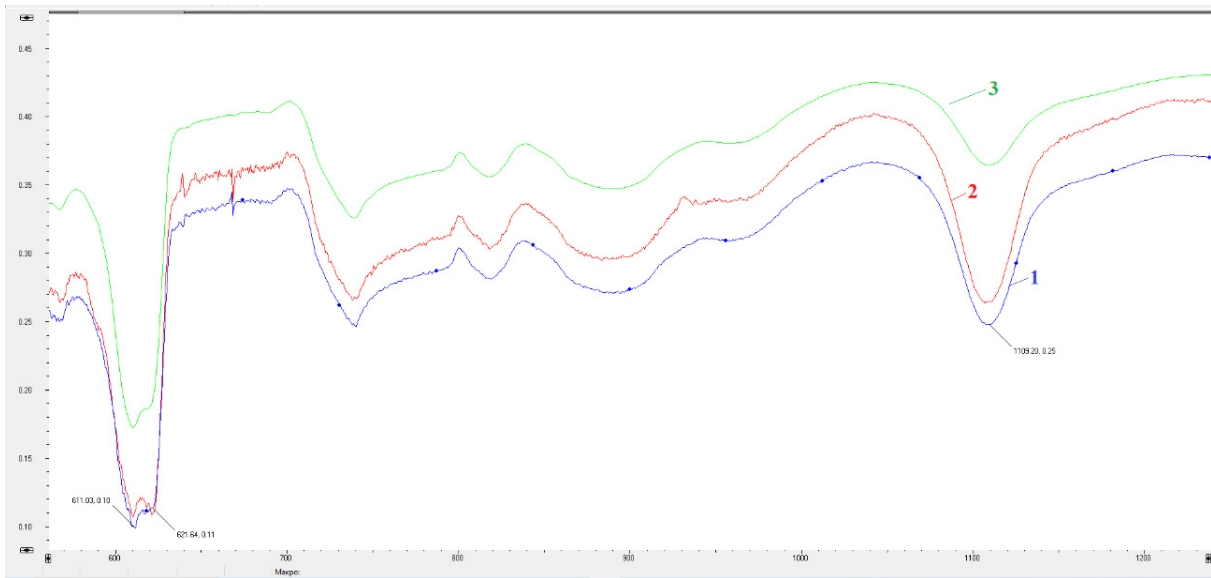
Figure 3. Infrared spectrum of n-type silicon doped with Yb impurities:
1. IR spectrum of control samples (Si_control); 2. IR spectrum of original silicon (Si_original); 3. IR spectrum of n-Si<Yb> samples.

The absorption spectra were recorded in the range from 380 to 7800 cm⁻¹. The concentrations of oxygen and carbon were determined by the intensity of the corresponding peaks in the IR spectra: 1106 cm⁻¹ for oxygen and 605 cm⁻¹ for carbon. In original silicon, compared to the control sample, an increase in the peak intensity at 1106 cm⁻¹ by 5.74% was observed, indicating a slight increase in oxygen concentration. Meanwhile, ytterbium-doped silicon showed a 42.64% reduction in the peak intensity compared to control silicon, indicating a significant decrease in oxygen concentration after doping. Comparing ytterbium-doped silicon with original silicon also revealed a 34.90% reduction in peak intensity, further confirming the decrease in oxygen concentration due to doping. Compared to the control sample, original silicon showed a slight 2.66% increase in peak intensity at 605 cm⁻¹, indicating a small rise in carbon concentration. However, ytterbium-doped silicon demonstrated a 32.45% reduction in the carbon peak intensity, signifying a substantial decrease in carbon concentration after doping. Comparing doped silicon with the original sample also showed a 29.01% decrease in peak intensity, confirming further reduction in carbon concentration due to doping.

Research shows that the capacitance-voltage characteristics of MDS structures based on ytterbium-doped silicon exhibit a shift toward positive bias voltages. This shift is associated with a reduction in surface state density at the Si-SiO₂ interface, indicating changes in the electrical properties of the structure.

The analysis also shows that the effect of ytterbium doping significantly depends on the method of its introduction into the substrate. In the case of diffusion, the capacitance-voltage shift is more pronounced compared to doping during growth, indicating that the diffusion method allows for more efficient penetration of ytterbium into the silicon structure.

Additionally, capacitance-DLTS spectra show the presence of a deep level with an ionization energy of $E_c-0.32$ eV, whose concentration is determined by diffusion conditions. This result is important for understanding defect formation mechanisms in MOS structures and could serve as a basis for optimizing technological processes in semiconductor device production.

The Raman spectra of the original Si<P> sample are shown in Fig. 4. The spectrum exhibits a high peak in the region of 521 cm^{-1} with a width at half maximum of 8–12 cm^{-1}. The intensity of the first-order scattering at 521 cm^{-1} is due to transverse (TO) and longitudinal (LO) optical phonons. In contrast to the main peak, scattering by second-order acoustic phonons at 303 cm^{-1} (TA) can be observed. Some authors suggest that this peak corresponds to the LA modes [5-18], but there is no exact confirmation of this fact. Probably, we observe a superposition of transverse and longitudinal acoustic modes. There is also a broad peak between 920–1000 cm^{-1}, which is due to the scattering of several transverse optical phonons ~2TO phonons. To date, there is no consensus on the origin of the broad peak. Some authors claim that this peak is formed by a superposition of two or more optical modes [19-23].
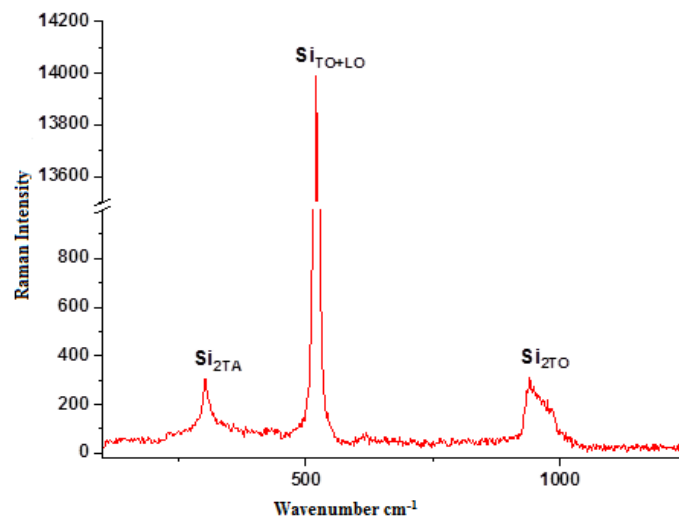
Figure 4. The Raman spectrum of the initial silicon. Oscillatory modes: Si_{2TA} – 303 cm^{-1}, Si_{TO+LO} – 521 cm^{-1}, Si_{2TO} – 920-1000 cm^{-1}

As can be seen from the figure in Fig. 5, further doping of n-Si single crystals with ytterbium impurity atoms leads to some change in the Raman spectra. The results obtained demonstrate that doping silicon with ytterbium leads to significant changes in its structural properties, which is manifested in the form of an increase in the intensity of peaks in the Raman spectra, as well as shifts of these peaks. This graph (Fig. 5) shows the Raman spectra for various ytterbium-doped silicon samples, as well as control samples.
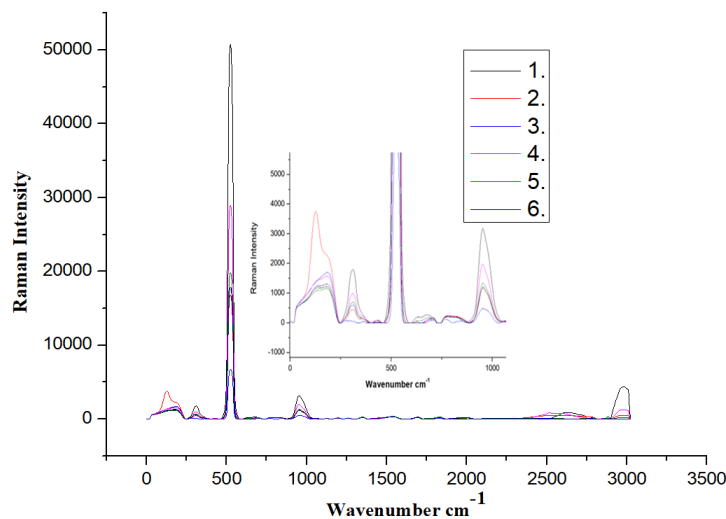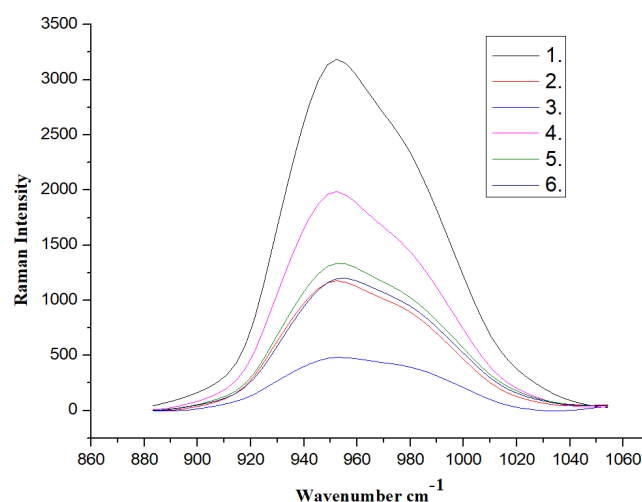

Figure 5. Raman spectra:
1. p-Si original; **2.** p-Si<Yb> (thermal diffusion in the gas phase); **3.** p-Si<Yb> (thermal diffusion in the gas phase), after diffusion 2 μm of the surface were removed; **4.** p-Si<Yb> (Solid-phase thermal diffusion); **5.** p-Si<Yb> (Solid-phase thermal diffusion) after diffusion 2 μm of the surface were removed; **6.** Si control

In ytterbium-doped samples (red line), a significant increase in peak intensity in the range of 200 to 300 cm⁻¹ is observed compared to control samples (black line). This may indicate structural changes due to doping, such as an increase in the number of defects or the formation of new phases in the material. It can also be noted that the ytterbium-doped samples exhibit peak shifts compared to control samples. This phenomenon may be related to changes in interatomic distances and internal stresses in the crystal lattice caused by the introduction of ytterbium. The graph shows that different doping or sample treatment methods (e.g., sputtering, diffusion) lead to different peak intensities, indicating differences in the structure and distribution of ytterbium in the silicon matrix.
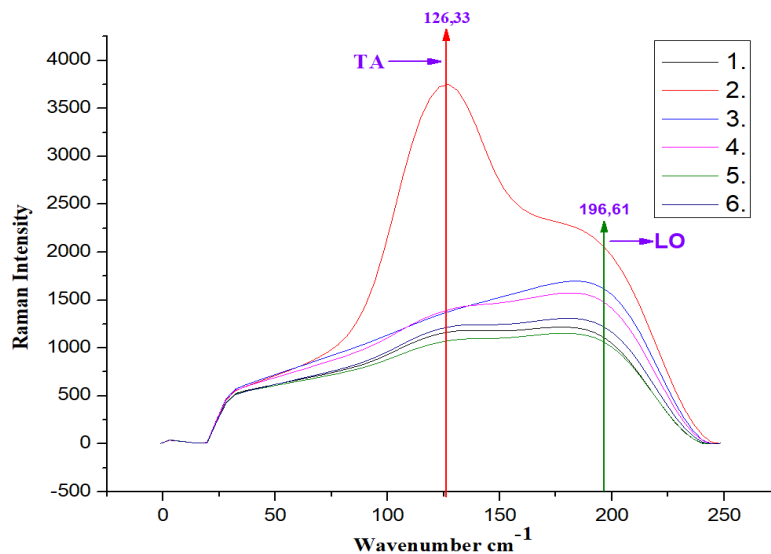
Figure 6. Raman spectrum:

1. p-Si original; **2.** p-Si<Yb> (thermal diffusion in the gas phase); **3.** p-Si<Yb> (thermal diffusion in the gas phase), after diffusion 2 μm of the surface were removed; **4.** p-Si<Yb> (Solid-phase thermal diffusion); **5.** p-Si<Yb> (Solid-phase thermal diffusion) after diffusion 2 μm of the surface were removed; **6.** Si control

The ytterbium-doped samples exhibit a noticeable increase in peak intensity compared to the control sample (Fig. 6). The maximum intensity of the TA peak at 126.33 cm⁻¹ significantly surpasses that of similar peaks in the other samples, suggesting a substantial influence of ytterbium on the silicon structure.

The LO peak (196.61 cm⁻¹) also shows an increase in intensity in the ytterbium sputtered sample, indicating possible formation of new phases or enhanced interatomic interactions in the doped samples.

The peak signals of the alloyed samples exhibit a broader shape compared to the control samples (Fig. 7). This suggests a potential increase in defects or stresses within the material's structure following alloying with ytterbium.
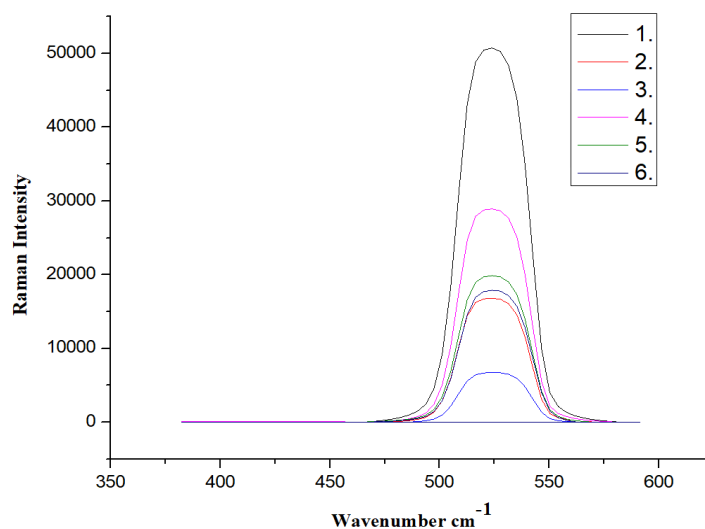
Figure 7. Raman spectrum
1. p-Si original; **2.** p-Si<Yb> (thermal diffusion in the gas phase); **3.** p-Si<Yb> (thermal diffusion in the gas phase), after diffusion 2 μm of the surface were removed; **4.** p-Si<Yb> (Solid-phase thermal diffusion); **5.** p-Si<Yb> (Solid-phase thermal diffusion) after diffusion 2 μm of the surface were removed; **6.** Si control.

A slight shift of the peaks towards shorter wavelengths in the doped samples (Fig. 8) may indicate changes in interatomic distances or the presence of internal stresses within the crystal lattice.

The difference in Raman phonon bands between crystallites and nanocrystallites mainly concerns their bandwidth, while the Raman frequencies are very close, this statement confirms the attribution of the calculated transition to internal stress [24-25].

The Raman spectrum of amorphous layers consists of several broad bands reflecting the single-phonon density of states. When the material is crystalline, the bands narrow and distinct peaks appear. In the case of Si-Yb, three first-order Raman bands associated with Si–Si appear, and vibrations of the Si-Yb and Yb–Yb bonds also appear. The peak position and intensity of these bands depend on the composition, as well as on other factors such as heating, etc., which in turn can contribute to a shift in the frequency of the peaks.

Figure 8. Raman spectrum:

1. p-Si original; **2.** p-Si<Yb> (thermal diffusion in the gas phase); **3.** p-Si<Yb> (thermal diffusion in the gas phase), after diffusion 2 μm of the surface were removed; **4.** p-Si<Yb> (Solid-phase thermal diffusion); **5.** p-Si<Yb> (Solid-phase thermal diffusion) after diffusion 2 μm of the surface were removed; **6.** Si control

The laser beam and temperature induce an ordered state (hereinafter referred to as LTIOS), which is monitored by the Raman spectrum. Further increase in temperature under the influence of light preserves the Raman signature of the nanocrystalline material.

As we have already mentioned, LTIOS appears under light exposure within a certain temperature range for different a-Si-Yb alloy compositions. LTIOS is observed at much lower laser power densities than those required for laser crystallization.

It was found that an increase in the number of defects causes broadening of the amorphous region. A similar relationship should exist for Si-Yb, although, to our knowledge, this has not been previously reported. We noted that the relative intensity of the three Raman scattering bands in Si-Yb systems in the LTIOS state changes. The relative intensity of the Si-Si bond decreases, which in turn indicates that dangling bonds are mainly formed due to Si-Si bond rupture.

CONCLUSIONS

The conducted studies demonstrated that doping silicon with ytterbium leads to significant changes in its structural and physicochemical properties. Observations indicate that doping causes a substantial increase in surface roughness, with the height of irregularities reaching up to 325 nm. This points to a complex microstructure resulting from the uneven distribution of ytterbium atoms, which is also associated with the formation of nanostructures and local stresses in the crystal lattice.

Doping also leads to a marked reduction in the concentration of optically active oxygen by 30-40%, indicating that ytterbium affects the chemical composition and interaction of silicon atoms with oxygen and carbon. The formation of new phases and nanocrystals in the doped samples is accompanied by shifts in the spectra and increased peak intensities, reflecting significant changes in interatomic interactions and the presence of internal stresses in the crystal lattice.

Moreover, the calculated diffusion coefficient of ytterbium in silicon shows a relatively low value, indicating a slow diffusion process typical for rare earth metals. Changes in the electrical characteristics of the material are evident through a reduction in surface state density at the $Si-SiO_2$ interface and the presence of deep levels with an ionization energy of $E_c-0.32$ eV.

Overall, the results demonstrate that ytterbium doping has a complex impact on the structure and properties of silicon. This makes the method promising for use in semiconductor electronics and optoelectronics. The obtained data open new opportunities for further research and optimization of technological processes in the development of new semiconductor materials with improved characteristics.

ORCID
Khodjakbar S. Daliev, https://orcid.org/0000-0002-2164-6797; **Sharifa B. Utamuradova**, https://orcid.org/0000-0002-1718-1122
Jonibek J. Khamdamov, https://orcid.org/0000-0003-2728-3832; **Shahriyor B. Norkulov**, https://orcid.org/0000-0002-2171-4884
Mansur B. Bekmuratov, https://orcid.org/0009-0006-3061-1568; **Ulugbek M. Yuldoshev**, https://orcid.org/0009-0003-7575-7497

REFERENCES

[1] L.T. Canham, "Silicon quantum wire array fabrication by electrochemical and chemical dissolution of wafers," Appl. Phys. Lett. **57**, 1046-1990. https://doi.org/10.1063/1.103561

[2] F. Huisken, H. Hofmeister, B. Kohn, M.A. Laguna, and V. Paillard, "Laser production and deposition of light-emitting silicon nanoparticles," Appl. Surf. Sci. **154–155**, 305 (2000). https://doi.org/10.1016/s0169-4332(99)00476-6

[3] V. Vinciguerra, G. Franzo, F. Priolo, F. Iacona, and C. Spinella, "Quantum confinement and recombination dynamics in silicon nanocrystals embedded in Si/SiO$_2$ superlattices,"J. Appl. Phys. **87**, 8165 (2000). https://doi.org/10.1063/1.373513

[4] F. Koch, and V. Petrova-Koch, "Light from Si-nanoparticle systems - a comprehensive view,"J. Non-Cryst. Solids, **198–200**, 840 (1996). https://doi.org/10.1016/0022-3093(96)00067-1

[5] Zh. Ma, X. Liao, J. He, W. Cheng, G. Yue, Y. Wang, and G. Kong, "Annealing behaviors of photoluminescence from SiO$_x$:H," J. Appl. Phys. **83**, 7934 (1998). https://doi.org/10.1063/1.367973

[6] M. Zaharias, H. Freistdt, F. Stolze, T.P. Drusedau, M. Rosenbauer, and M. Stutzmann, "Properties of sputtered a-SiO$_x$:H alloys with a visible luminescence," J. Non-Cryst. Solids, 164–166, 1089 (1993). https://doi.org/10.1016/0022-3093(93)91188-9

[7] U. Kahler, and H. Hofmeister, "Silicon nanocrystallites in buried SiO$_x$ layers via direct wafer bonding," Appl. Phys. Lett. **75**, 641 (1999). https://doi.org/10.1063/1.124467

[8] S. Zhang, W. Zhang, and J. Yuan, "The preparation of photoluminescent Si nanocrystal–SiO$_x$ films by reactive evaporation," Thin Solid Films, **326**, 92 (1998). https://doi.org/10.1016/S0040-6090(98)00532-X

[9] W. Li, G.S. Kaminski Schierle, B. Lei, Y. Liu, and C.F. Kaminski, „Fluorescent Nanoparticles for Super-Resolution Imaging," Chemical Reviews, **122**, 12495−12543 (2022). https://doi.org/10.1021/acs.chemrev.2c00050

[10] A.S. Zakirov, Sh.U. Yuldashev, H.D. Cho, J.C. Lee, T.W. Kang, J.J. Khamdamov, and A.T. Mamadalimov, "Functional Hybrid Materials Derived from Natural Cellulose," Journal of the Korean Physical Society, **60**(10), 1526-1530 (2012). https://doi.org/10.3938/jkps.60.1526

[11] A.S. Zakirov, Sh.U. Yuldashev, H.J. Wang, H.D. Cho, T.W. Kang, J.J. Khamdamov, and A.T. Mamadalimov, "Photoluminescence study of the surface modified and MEH-PPV coated cotton fibers," Journal of Luminescence, **131**(2), 301–305 (2011). https://doi.org/10.1016/j.jlumin.2010.10.019

[12] H. Richter, Z.P. Wang, and L. Ley, "The one phonon Raman spectrum in microcrystalline silicon," Solid State Commun. **39**, 625 (1981). https://doi.org/10.1016/0038-1098(81)90337-9

[13] Z. Iqbal, and S. Veprek, "Raman scattering from hydrogenated microcrystalline and amorphous silicon," J. Phys. C, **15**, 377 (1982). https://doi.org/10.1088/0022-3719/15/2/019

[14] J. Gonzales-Hernandez, G.H. Azarbayejani, R. Tsu, and F.H. Pollak, "Raman, transmission electron microscopy, and conductivity measurements in molecular beam deposited microcrystalline Si and Ge: A comparative study,"Appl. Phys. Lett. **47**, 1350 (1985). https://doi.org/10.1063/1.96277

[15] I.H. Campbell, and P.M. Fauchet, "The effects of microcrystal size and shape on the one phonon Raman spectra of crystalline semiconductors," Solid State Commun. **52**, 739 (1986). https://doi.org/10.1016/0038-1098(86)90513-2

[16] J. Zi, H. Buscher, C. Falter, W. Ludwig, K. Zhang, and X. Xie, "Raman shifts in Si nanocrystals," Appl. Phys. Lett. **69**, 200 (1996). https://doi.org/10.1063/1.117371

[17] D.R. dos Santos, and I.L. Torriany, "Crystallite size determination in μc-Ge films by x-ray diffraction and Raman line profile analysis," Solid State Commun. **85**, 307 (1993). https://doi.org/10.1016/0038-1098(93)90021-E

[18] Kh.S. Daliev, Z.E. Bahronkulov, and J.J. Hamdamov, "Investigation of the Magnetic Properties of Silicon Doped with Rare-Earth Elements," East Eur. J. Phys. **4**, 167 (2023). https://doi.org/10.26565/2312-4334-2023-4-18

[19] Kh.S. Daliev, Sh.B. Utamuradova, Z.E. Bahronkulov, A.Kh. Khaitbaev, and J.J. Hamdamov, "Structure Determination and Defect Analysis n-Si<Lu>, p-Si<Lu> Raman Spectrometer Methods," East Eur. J. Phys. (4), 193 (2023). https://doi.org/10.26565/2312-4334-2023-4-23

[20] P.A. Temple, and C.E. Hathaway, "Multiphonon Raman Spectrum of Silicon," Physical Review B, **7**(8), 3685–3697 (1973). https://doi.org/10.1103/PhysRevB.7.3685

[21] K.J. Kingma, and R.J. Hemley, "Raman spectroscopic study of microcrystalline silica," American Mineralogist, **79**(3-4), 269-273 (1994). https://pubs.geoscienceworld.org/msa/ammin/article-pdf/79/3-4/269/4209223/am79_269.pdf

[22] G.E. Walrafen, Y.C. Chu, and M.S. Hokmabadi, "Raman spectroscopic investigation of irreversibly compacted vitreous silica," The Journal of Chemical Physics, **92**(12), 6987–7002 (1990). https://doi.org/10.1063/1.458239

[23] B. Champagnon, C. Martinet, M. Boudeulle, D. Vouagner, C. Coussa, T. Deschamps, and L. Grosvalet, "High pressure elastic and plastic deformations of silica: in situ diamond anvil cell Raman experiments," Journal of Non-Crystalline Solids, **354**(2-9), 569–573 (2008). https://doi.org/10.1016/j.jnoncrysol.2007.07.079

[24] Sh.B. Utamuradova, H.J. Matchonov, Zh.J. Khamdamov, and H.Yu. Utemuratova, "X-ray diffraction study of the phase state of silicon single crystals doped with manganese," New Materials, Connections Oath Applications, **7**(2), 93-99 (2023). http://jomardpublishing.com/UploadFiles/Files/journals/NMCA/v7n2/Utamuradova_et_al.pdf

[25] Kh.S. Daliev, Sh.B. Utamuradova, J.J. Khamdamov, M.B. Bekmuratov, "Structural Properties of Silicon Doped Rare Earth Elements Ytterbium," East Eur. J. Phys. (1), 375-379 (2024). https://doi.org/10.26565/2312-4334-2024-1-37

ЗМІНИ СТРУКТУРИ ТА ВЛАСТИВОСТЕЙ КРЕМНІЮ ПІД ЧАС ЛЕГУВАННЯ ІТЕРБІЄМ: РЕЗУЛЬТАТИ КОМПЛЕКСНОГО АНАЛІЗУ

Ходжакбар С. Далієв, Шаріфа Б. Утамурадова, Джонібек Дж. Хамдамов,
Мансур Б. Бекмуратов, Шахрійор Б. Норкулов, Улугбек М. Юлдошев

Інститут фізики напівпровідників і мікроелектроніки Національного університету Узбекистану,
Ташкент, вул. Янгі Алмазара, 20, 100057, Узбекистан

У цій роботі проведено комплексне дослідження структурних, хімічних та електрофізичних властивостей монокристалічного кремнію (Si), легованого ітербієм (Yb). Легування проводили методом термодифузії при температурі 1473 К в умовах високого вакууму з подальшим швидким охолодженням. Для аналізу зразків використовували атомно-силову мікроскопію (АСМ), інфрачервону Фур'є-спектроскопію (FTIR), спектроскопію глибокого рівня (DLTS) і раманівську спектроскопію (RAMAN). АСМ-зображення легованих зразків продемонстрували суттєві зміни рельєфу поверхні. Середньоквадратична шорсткість зросла з менш ніж 10 нм до 60–80 нм, а максимальна висота нерівностей досягла 325 нм. Ці зміни зумовлені утворенням наноструктур внаслідок нерівномірного розподілу атомів ітербію у кристалічній решітці кремнію та виникненням внутрішніх напруг. ІЧ-Фур'є-спектроскопія виявила зниження концентрації оптично активного кисню (N_O^{opt}) на 30-40% після легування, що пов'язано з хімічною взаємодією ітербію з кремнієм. Спектри RAMAN виявили утворення нових фаз та нанокристалів, що свідчить про перебудову кристалічної решітки внаслідок введення ітербію. Коефіцієнт дифузії ітербію в кремнії становить $1,9 \times 10^{-15}$ см²/с, що свідчить про повільний процес дифузії, характерний для рідкоземельних металів. Це також сприяло зниженню густини поверхневих станів на межі Si-SiO$_2$ і появі глибоких рівнів з енергією іонізації E_c-0,32 еВ.

Ключові слова: *монокристалічний кремній; легування ітербієм; атомно-силова мікроскопія; раманівська спектроскопія; шорсткість поверхні; наноструктури; електричні властивості; MDS-структури; інтерфейс Si-SiO₂*

INVESTIGATION OF MORPHOLOGICAL AND OPTICAL PROPERTIES OF LiNbO₃ AND LiNbO₃:Fe 0.03 wt.% CRYSTALS

Murodjon A. Yuldoshev[a]*, Zakirjan T. Azamatov[b], Abror B. Bakhromov[b], Mira R. Bekchanova[c]

[a]University of business and science, Namangan, Uzbekistan
[b]Institute of Semiconductor Physics and Microelectronics, National University of Uzbekistan,
20 Yangi Almazor st., Tashkent, 100057, Uzbekistan
[c]University of Public Security of the Republic of Uzbekistan, Tashkent, Uzbekistan
*Corresponding Author e-mail: murod.yuldoshev1993@gmail.com
Received October 1, 2024; accepted November 20, 2024

This article is devoted to the morphological and optical properties of the photorefractive crystal LiNbO₃ and LiNbO₃:Fe 0.03 wt.%. According to it, the surface morphology of the samples was studied using an atomic force microscope (AFM). In addition, ordinary and extraordinary refractive indices of the LiNbO₃ crystal were calculated using empirical formulas. The results of the diffraction efficiency of the LiNbO₃:Fe 0.03 wt.% crystal for He-Ne and He-Cd lasers are presented.
Keywords: *Lithium niobate; AFM; Holography; Optical absorption*
PACS: 42.40.Eq, 42.40.Lx, 42.70.Mp

INTRODUCTION

Currently, the problem of the most efficient storage of information is particularly acute all over the world [1-4]. One of the effective ways to solve the problem of reliable and long-term storage of information with a high density of information carriers is the holographic method of storing information [1,5,13]. In recent years, comprehensive theoretical and practical research has been carried out in foreign countries to create high-capacity holographic storage devices that record information on various carriers [6-9]. It should be noted that holographic methods make it possible to record, store and restore wave fields, three-dimensional images and other types of information. Lithium niobate crystals, which have a wide band gap, are one of the promising materials used in the field of photonics, quantum electronics, optoelectronics and acoustoelectronics [1,10-13]. Optical properties such as electro-optical, piezoelectric, nonlinear effects, second harmonic generation and refractive index change under laser radiation allow the use of lithium niobate crystals for recording holograms [3,5,14-17].

Holograms created as a result of the photorefractive effect are based on orthogonal nonlinear processes and are also effective for long-wave and high-power lasers. The diffraction efficiency of holograms is practically independent of the intensity of the incident light and can reach 100% in most materials. Therefore, complex detectors and devices were not required. The main disadvantage of coding holograms based on the photorefractive effect is speed. Nonlinear effects become stationary, inversely proportional to intensity. The diffraction efficiency and information transfer rate for the above materials are 1 ms at 1 W/cm². However, the low speed of information processing in some materials was not recognized as a disadvantage.

EXPERIMENTAL PART

In holography, two coherent beams are required to form an interference pattern, one called the reference beam and the other called the object beam (the beam scattered from the object). The resulting interference pattern contains information about the amplitude and phase of the object beam. The intensity of the interference pattern can be recorded by placing an appropriate light-sensitive material (such as photographic film or a photorefractive crystal) in the interference region. This recorded fringe pattern or grating is called a hologram. The recorded hologram, when illuminated by the same reference beam, can scatter light in the direction of the object beam. The diffracted beam contains information about the phase and amplitude of the original object beam.

In experiments on studying optical recording in LiNbO₃:Fe 0.03 wt.% crystals, we used the scheme shown in Fig. 1.

The data were processed using helium-cadmium (He-Cd, l=440 nm) and helium-neon (He-Ne, l = 630 nm) lasers. The optical sensitivity of the crystal for this wavelength is very high. A virtual interference image in the form of light and dark lines is formed as a result of superradiance of two horizontal waves in the crystal. Double refraction of light occurs in the light lines. That is, a sinusoidal diffraction grating with a period equal to L is observed in the crystal:

$$L = \lambda_{re}[2\sin(\theta_{re}/2)], \tag{1}$$

where, λ_{re} – wavelength of the recording light; θ_{re} – angle between the recording beams. When reading volume holograms ($h \gg \lambda$ and $h \gg L$, where h is the thickness of the hologram) with radiation with a wavelength of λ_r, the angle between the incident and deflected beams is determined by the Wulff-Bragg conditions.

$$2\sin(\theta_r/2) = \lambda_r/\lambda, \tag{2}$$

where, $\theta_r/2$ – angle between the incident beam and the normal to the plate, the angles θ_{re} θ_r are related by the ratio.

$$\sin(\theta_{re}/2)\big/\sin(\theta_r/2) = \lambda_{re}\big/\lambda_r. \tag{3}$$

The diffraction efficiency of a sinusoidal grating when read by an extraordinary beam with a wavelength is determined by the Kogelnik formula [18]:

$$\eta = \sin^2\{\pi D \Delta n_e / \lambda \cos(\theta/2)\}, \tag{4}$$

where, Δn_e – modulation amplitude of the refractive index of the extraordinary ray, D is the thickness of the crystal, $\theta = \theta_{re}$.
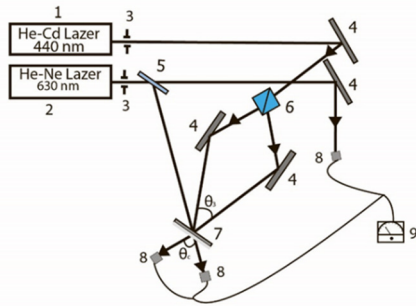
Figure 1. Scheme of the experimental setup: 1- recording laser (He-Cd) λ=440 nm and (He-Ne) λ=630 nm, 2- reading laser (He-Ne) λ = 630 nm, 3-diaphragm, 4-mirrors, 5-light filters, 6-Wollaston prism, 7-LiNbO₃:Fe 0.03 wt.% sample, 8-photodetector, 9-microammeter

Experimentally, the diffraction efficiency is defined as the ratio of the intensity of the diffracted reading beam to the intensity of the beam that has passed through the crystal when the hologram is not recorded in the crystal.

These crystals were grown by modified Czochralski grown technique with the use of Donetsk type growth set-up in air atmosphere in a platinum crucible [19].

The samples for research were made from nominally pure and iron-doped LiNbO₃ crystals and in the form of parallelepipeds with dimensions of 2×3×10 mm, the edges of which were oriented along the direction of the crystallographic axes. Absorption spectra were studied using a Shimadzu UV 3600 spectrometer. Measurements were carried out in the range of 320-1100 nm with a step of 1 nm. To study the surface morphology of LiNbO₃ and LiNbO₃:Fe crystals, an NT-MDT atomic force microscope was used. The spectra were processed using the Origin 8.1 software package.

RESULTS AND DISCUSSION

Figure 2 shows the absorption spectra of nominal pure lithium niobate and iron-doped lithium niobate LiNbO₃:Fe 0.03 wt.%, from which it is evident that the addition of the impurity significantly increases the absorption.
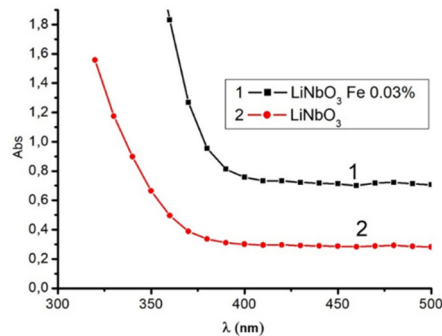
Figure 2. Absorption spectra of iron-doped LiNbO₃:Fe 0.03 wt.% and nominally pure lithium niobate

It is known that the use of transition metals as alloying additives is associated with their ability to reversibly donate d-electrons to the conduction band under the influence of radiation.

The resulting absorption spectrum in the decreasing linear part of the graph was approximated by a straight line until it intersected with the abscissa axis. The point where this line intersects the X-axis is the wavelength corresponding to the absorption edge of the crystal. The band gap was determined by the formula:

$$E_g = \frac{hc}{\lambda}, \tag{5}$$

where, λ– wavelength, corresponding to the absorption edge, h – Planck's constant, c – speed of light in vacuum.

One of the main quantities that determine the photorefractive properties of crystals is the refractive index. When determining the band gap width from the absorption spectra, the refractive index of LiNbO₃ and LiNbO₃:Fe 0.03 wt.% crystals was determined using the following empirical formula proposed by Ghosh [20]:

$$n^2 - 1 = \frac{A}{(E_g+B)^2}, \tag{6}$$

where, A = 25E$_g$ + 212, B = 0.21E$_g$ + 4.25 and (E$_g$ + B) refer to the corresponding band gap of the material.

The results obtained are respectively: LiNbO$_3$ (E$_g$=3.39 eV), LiNbO$_3$:Fe 0.03 wt.% (E$_g$=3,17 eV) and LiNbO$_3$ (n = 2.2922), LiNbO$_3$:Fe 0.03 wt.% (n = 2.3356).

The ordinary and extraordinary refractive indices of the LiNbO$_3$ crystal were calculated using the following formulas in the range λ = 400-5000 nm, the results obtained are presented in the Table.

$$n_o^2 - 1 = \frac{2.9804\lambda^2}{\lambda^2-0.01764} + \frac{1.229\lambda^2}{\lambda^2-0.05914} + \frac{12.614\lambda^2}{\lambda^2-474.6}, \tag{7a}$$

$$n_e^2 - 1 = \frac{2.4272\lambda^2}{\lambda^2-0.02047} + \frac{0.5981\lambda^2}{\lambda^2-0.0666} + \frac{8.9543\lambda^2}{\lambda^2-416.08}. \tag{7b}$$

Table. Ordinary and extraordinary refractive indices of LiNbO$_3$ crystal

λ., μm	n$_e$	n$_o$
0.4	2.191899762	2.509000635
0.5	2.110349304	2.410359464
0.6	2.073558512	2.365369563
0.7	2.052958976	2.340161846
0.8	2.039895099	2.324214431
0.9	2.030848757	2.313219856
1	2.024135933	2.30511079
1.1	2.01885865	2.298783645
1.2	2.014499216	2.293601912
1.3	2.010740815	2.289176022
1.4	2.007380114	2.285255981
1.5	2.004281412	2.281675003
1.6	2.001351109	2.278318112
1.7	1.998522787	2.27510379
1.8	1.995748124	2.271972796
1.9	1.992991166	2.268881124
2	1.990224609	2.265795427
2.1	1.987427319	2.262689961
2.2	1.984582637	2.259544508
2.3	1.981677201	2.256342924
2.4	1.978700112	2.253072109
2.5	1.975642324	2.249721263
2.6	1.972496205	2.246281348
2.7	1.96925521	2.242744676
2.8	1.965913629	2.239104611
2.9	1.962466401	2.235355334
3	1.958908964	2.231491665
3.1	1.95523715	2.227508926
3.2	1.951447084	2.223402828
3.3	1.947535121	2.219169388
3.4	1.943497786	2.214804858
3.5	1.939331726	2.210305664
3.6	1.935033671	2.205668366
3.7	1.930600404	2.200889618
3.8	1.926028732	2.195966131
3.9	1.921315461	2.190894654
4	1.916457381	2.185671942
4.1	1.911451244	2.180294744
4.2	1.906293747	2.17475978
4.3	1.900981523	2.169063724
4.4	1.895511121	2.163203196
4.5	1.889879	2.157174745
4.6	1.88408151	2.150974834
4.7	1.878114889	2.144599835
4.8	1.871975244	2.138046012
4.9	1.865658543	2.131309514
5	1.859160605	2.124386365

The results presented in the table show that the condition $n_o > n_e$ (negative crystal with one optical axis) is fulfilled in all wavelength ranges for the lithium niobate crystal.

The surface morphology of the obtained LiNbO$_3$ and LiNbO$_3$:Fe 0.03 wt.% samples was analyzed using AFM. The size of the study area was (10 mm÷10 mm) (Fig. 3 and 4).
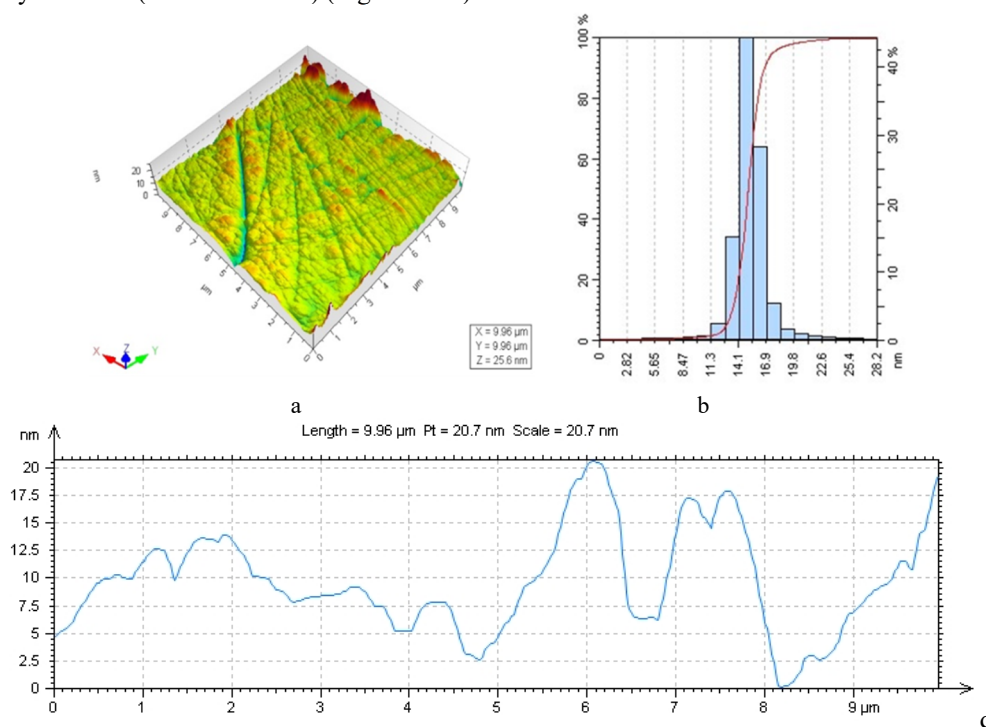
Figure 3. AFM images of the surface morphology of LiNbO$_3$ crystal: a) 3D phase image; b) surface histogram; d) surface relief
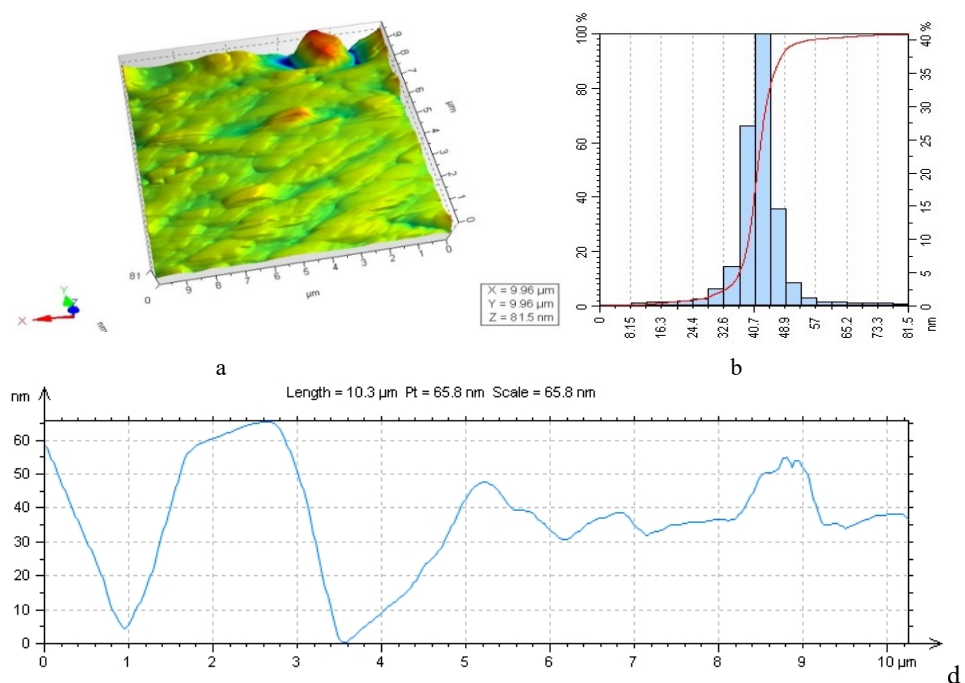
Figure 3. AFM images of the surface morphology of LiNbO$_3$:Fe 0.03 wt.% crystal: a) 3D phase image; b) surface histogram; d) surface relief

The obtained results show that various linear defects were formed on the surface of the LiNbO$_3$ crystal as a result of mechanical treatment (Fig. 3a). This, in turn, affects the distribution and relief of particles on the surface of the sample (Figs. 3b and 3d). The grains formed in the LiNbO$_3$ crystal are in the range (0÷20 nm), and it can be said that most of the surface consists of particles sized 14÷16 nm. In the LiNbO$_3$:Fe 0.03 wt.% samples, the surface morphology is relatively stable, linear defects are practically absent (Fig. 4a). The surface consists mainly of a rounded shape sized 35÷45 nm (Fig. 4b), which means that it is directly related to the influence of iron ions in the structure.

Figure 5 below shows the results of the study of the diffraction efficiency of holograms obtained by He-Ne (l = 630 nm) and He-Cd (l=440 nm) lasers on a LiNbO$_3$:Fe 0.03 wt.% crystal. The results show that the photosensitivity of the crystal increases significantly (2 times) with increasing laser beam power. It is evident that the maximum value of the diffraction efficiency is η=44% for a wavelength of λ=630 nm and η=55% for a wavelength of λ = 440 nm. The fact that the diffraction efficiency reaches a maximum point and then decreases again can be explained by the Chen model [21].
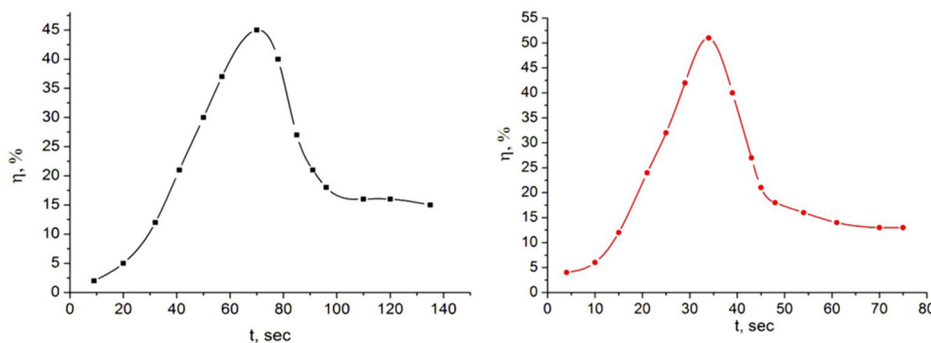
Figure 5. Experimental dependences of the diffraction efficiency of holograms on exposure: a) λ=630 nm; b) λ=440 nm

The interference images of two coherent laser beams are incident on the crystal and recorded as a hologram (Fig. 5). The charge carriers are mainly concentrated in thin layers and are then allowed to move until they recombine with drift and diffusion traps. Thus, the volume and charge are in the same phase as the interference image in the crystal. The electric field of this space charge moves due to the linear electrophoretic effect, and the size of the holographic grating creates the refractive index. Although this procedure depends on first- and second-order electrophoretic effects, it shows that the role of third-order nonlinear effects is significant for the incident beams.

CONCLUSIONS

The studies of photorefractive crystals LiNbO$_3$ and LiNbO$_3$:Fe 0.03 wt.% show that due to iron ions the optical absorption increases significantly (2.5÷3) and the change in the forbidden zone equal to ΔE_g=0.22 eV is established. It was found that the use of expressions 7a and 7b is suitable for the ordinary (n$_o$) refractive index in the near infrared region and for the extraordinary (n$_e$) refractive index in the visible and near infrared regions. Morphological analysis shows that iron ions make a significant contribution to the stability of the particle distribution on the surface. Holographically, when using LiNbO$_3$:Fe 0.03 wt.% samples as a memory element and increasing the power of laser beams, it was found that the time to achieve the maximum diffraction efficiency decreased by 2 times.

ORCID
Zakirjan T. Azamatov, https://orcid.org/0000-0001-7074-9437; **Abror B. Bakhromov,** https://orcid.org/0000-0001-8148-2467
Murodjon A. Yuldoshev, https://orcid.org/0000-0002-9722-9439

REFERENCES
[1]   V.A. Barachevsky, "The current status of the development of light-sensitive media for holography (a review)," Opt. Spectrosc. **124**, 373–407 (2018). http://dx.doi.org/10.1134/S0030400X18030062
[2]   Sh.B. Utamuradova, Z.T. Azamatov, M.A. Yuldoshev, N.N. Bazarbayev, A.B. Bakhromov, East Eur. J. Phys. (4), 147 (2023), https://doi.org/10.26565/2312-4334-2023-4-15
[3]   Sh.B. Utamuradova, Z.T. Azamatov, A.I. Popov, M.R. Bekchanova, M.A. Yuldoshev, A.B. Bakhromov, East Eur. J. Phys. (3), 278 (2024), https://doi.org/10.26565/2312-4334-2024-3-27
[4]   L. Dai, C. Tan, L. Wang, X. Han, C. Liu, and Y. Xu, "Investigation on nonvolatile holographic storage properties in Hf:Ru:Fe:LiNbO$_3$ crystals as a function of Li composition," Journal of Alloys and Compounds, **753**, 407 (2018). https://doi.org/10.1016/j.jallcom.2018.04.201
[5]   T. Volk, M. Wohlecke, "Lithium niobate," in: *Defects, Photorefraction and Ferroelectric Switching*, (Springer, Berlin, 2008).
[6]   M.H. Yükselici, D. Bulut, B.C. Ömür, A.A. Bozkurt, and C. Allahverdi, "Optical properties of iron-doped lithium niobate crystal depending on iron content and temperature," Phys. Status Solidi B, **251**, 1265–1269 (2014). http://dx.doi.org/10.1002/pssb.201451071
[7]   A.V. Syuy, N.V. Sidorov, M.N. Palatnikov, N.A. Teplyakova, D.S. Shtarev, and N.N. Prokopiv, "Optical properties of lithium niobate crystals," Optik, **156**, 239 (2018). https://doi.org/10.1016/j.ijleo.2017.10.136
[8]   N.V. Sidorov, L. A. Bobreva, N. Teplyakova, and G.M. Palatnikov, "Defect Complexes and Optical Properties of Doubly Doped Lithium Niobate Crystals," Inorganic Materials, **54**(10), 1009-1012 (2018). http://dx.doi.org/10.1134/S0020168518100151
[9]   E.M. de Miguel Sanz, M. Carrascosa, and L. Arizmendi. "Effect of the oxidation state and hydrogen concentration on the lifetime of thermally fixed holograms in LiNbO$_3$:Fe," Physical Review B, **65**(16), (2002). http://dx.doi.org/10.1103/PhysRevB.65.165101
[10] Sh.B. Utamuradova, Z.T. Azamatov, M.A. Yuldoshev, "Optical Properties of ZnO–LiNbO$_3$ and ZnO–LiNbO$_3$:Fe Structures," Russian Microelectronics, **52**(Suppl. 1), S99-S103 (2023). https://doi.org/110.1134/S106373972360022X
[11] Z.T. Azamatov, M.A. Yuldoshev, N.N. Bazarbayev, and A.B. Bakhromov, Physics AUC, **33**, 139 (2023). https://cis01.central.ucv.ro/pauc/vol/2023_33/13_PAUC_2023_139_145.pdf

[12] Z.T. Azamatov, Sh.B. Utamuradova, M.A. Yuldoshev, and N.N. Bazarbaev. "Some properties of semiconductor-ferroelectric structures," East Eur. J. Phys. (2), 187-190. (2023), https://doi.org/10.26565/2312-4334-2023-2-19

[13] Y.-Y. Li, H.-L. Chen, G.J. Chen, and W.-S. Hwang. "Investigation of the Defect Structure of Congruent and Fe-Doped LiNbO$_3$ Powders Synthesized by the Combustion Method," Materials, **10**(4), 380. (2017). http://dx.doi.org/10.3390/ma10040380

[14] R. Inoue, S. Takahashi, Y. Kitanaka, and T. Oguchi, "Enhanced photovoltaic currents in strained Fe-doped LiNbO$_3$ films," Physica Status Solidi (A) Applications and Materials, **212**(12), (2015). http://dx.doi.org/10.1002/pssa.201532398

[15] Y. Noguchi, R. Inoue, and M. Miyayama, "Electronic Origin of Defect States in Fe-Doped LiNbO$_3$ Ferroelectrics," Advances in Condensed Matter Physics, **2016**(4), 1-10. (2016). http://dx.doi.org/10.1155/2016/2943173

[16] A.S. Pritulenko, A.V. Yatsenko, and S.V. Yevdokimov, "Analysis of the nature of electrical conductivity in nominally undoped LiNbO$_3$ crystals," Crystallogr. Rep. **60**, 267–272 (2015). https://doi.org/10.1134/S1063774515020224

[17] Y.-Y. Li, H.-L. Chen, G.-J. Chen, C.-L. Kuo, P.-H. Hsieh, and W.-S. Hwang, "Investigation of the defect structure of congruent and Fe-doped LiNbO$_3$ powders synthesized by the combustion method," Materials, **10**(4), 380 (2017). https://doi.org/10.3390/ma10040380

[18] H. Kogelik, "Coupled wave theory for thick hologram grating," The Bell System Technical Journal, **48**(9), 2909-2947 (1969). http://users.ntua.gr/eglytsis/IO/Kogelnik_BSTJ_1969.pdf

[19] M.N. Palatnikov, O.V. Makarova, and N.V. Sidorov, "Growth and technological defects in lithium niobate crystals of various chemical compositions," Federal Research Center KSC RAS. pp. 89, (2018).

[20] D.K. Ghosh, L.K. Samanta, and G.C. Bhar, "A simple model for evaluation of refractive indices of some binary and ternary mixed crystals," Infrared Phys. **24**, 43–47 (1984). https://doi.org/10.1016/0020-0891(84)90046-0

[21] F.S. Chen, "Optically induced change of refractive indices in LiNbO$_3$," J. Appl. Phys. **40**, 3389-3393 (1969). https://doi.org/10.1063/1.1658195

**ДОСЛІДЖЕННЯ МОРФОЛОГІЧНИХ ТА ОПТИЧНИХ ВЛАСТИВОСТЕЙ КРИСТАЛІВ
LiNbO$_3$ ТА LiNbO$_3$:Fe 0,03 мас.%**
Муроджон А. Юлдошев[a], Закіржан Т. Азаматов[b], Аброр Б. Бахромов[b], Міра Р. Бекчанова[c]
[a]*Університет бізнесу та науки, Наманган, Узбекистан*
[b]*Інститут фізики напівпровідників та мікроелектроніки Національного університету Узбекистану. Ташкент, Узбекистан*
[c]*Університет громадської безпеки Республіки Узбекистан, Ташкент, Узбекистан*

Дана стаття присвячена морфологічним та оптичним властивостям фоторефрактивного кристала LiNbO$_3$ та LiNbO$_3$:Fe 0,03% мас. Відповідно до нього морфологію поверхні зразків вивчали за допомогою атомно-силового мікроскопа (АСМ). Крім того, за емпіричними формулами розраховано звичайний і надзвичайний показники заломлення кристала LiNbO$_3$. Наведено результати дифракційної ефективності кристала LiNbO$_3$:Fe 0,03 мас.% для He-Ne та He-Cd лазерів.
Ключові слова: *ніобат літію; АСМ; голографія; оптичне поглинання*

VOLT-AMPERE CHARACTERISTICS OF HETERO FILM PHOTOSENSITIVE STRUCTURE
Au-CdS-nSi-CdTe-Au

Sharifa B. Utamuradova[a], Khodjakbar S. Daliev[b], Shakhrukh Kh. Daliev[a],
Sultanpasha A. Muzafarova[a]*, Kakhramon M. Fayzullaev[a], Gulnoza A. Muzafarova[a]

*[a]Institute of Semiconductor Physics and Microelectronics, National University of Uzbekistan,
20 Yangi Almazor st., Tashkent, 100057, Uzbekistan*
*[b]Branch of the Federal State Budgetary Educational Institution of Higher Education "National Research University MPEI",
1 Yogdu st., Tashkent, Uzbekistan*
Corresponding Author e-mail: samusu@rambler.ru
Received July 5, 2024; revised September 2, 2024; accepted September 16, 2024

The results of studies of the current-voltage characteristics of a photodiode heterostructure are presented. Au-nCdS-nSi-pCdTe-Au, in forward and reverse directions. Photodiode heterostructures with an area of 29 mm^2 were created, which were obtained by vacuum evaporation in a quasi-closed volume by depositing layers of cadmium sulfide and cadmium telluride onto a single-crystalline silicon substrate with resistivity ρ = 607.47 Ohm·cm. A distinctive feature of the resulting photodiode Au-nCdS-nSi-pCdTe-Au structures is two-way sensitivity, where impurity complexes are formed. In the structures, the rate of recombination of nonequilibrium carriers at low excitation levels is determined by simple local centers in the boundary transition layers. The band diagram of a multilayer photodiode structure Au-nCdS-nSi-pCdTe-Au has been constructed.

Keywords: *Resistivity; Intensity; Current; Heterojunction; Photodiode; Structure; Junction; Microinterferometer; Vacuum; Capacitance; Band diagram*
PACS: 07.30.-t, 52.25.Mq, 61.72.jd, 61.72.uj, 66.70.Df

INTRODUCTION

In recent years, integrated circuits have almost reached the limit of the degree of integration of electronic components and speed. The use of optical interconnects to connect individual circuit elements will significantly increase the speed of signal transmission. For this purpose, the development of optoelectronic components necessary for the creation of photonic integrated circuits is actively underway for the purpose of efficient generation, modulation and detection of optical radiation [1-7]. The use of CdTe and CdS semiconductor compounds to create optoelectronic components operating in the near-IR wavelength range is a promising direction in the development of silicon optoelectronics and integrated photonics. However, the number of photonic components on modern integrated circuits is only approaching the ten thousand marks. Optical systems for transmitting and receiving information, being an alternative to cable transmission, are beginning to become widely used. Their important elements are receiving optical modules, the functions of which include converting the optical signal received by the photodetector into an electrical one, which is processed by electronic devices. At the same time, the photodetector is required to capture even a very weak optical signal, low inertia and noise [7-9]. Phototransistors and photodiodes without charge accumulation meet these requirements to a certain extent. However, the time constant of a phototransistor is longer than that of a photodiode, which limits its application in communication systems [1,8]. The above problem can be solved by creating structures with two Schottky barriers based on silicon. The appeal to silicon is due to the fact that it is the most technologically proven, well-developed material, however, photodiode structures with two barriers and based on it remain poorly studied. In a photodiode structure, the creation of a second or third barrier helps to reduce its capacitance, enhance the primary photocurrent and increase the frequency range and speed of operation [10-13].

This article presents the results of a study of the current-voltage characteristics of MSM photodiode structures with silicon-based potential barriers in the forward and reverse directions at 300 K.

EXPERIMENTAL PART

The heterojunction photodiode structure Au-nCdS-nSi-pCdTe-Au was obtained in a quasi-closed volume by vacuum thermal evaporation of CdS and CdTe powders onto a single-crystalline n-type silicon substrate with film thickness d = 0.55 μm, determined with an MII-4 microinterferometer.

The substrate is single-crystal n-type silicon of the KEF-600 brand according to TU 48-4-295-82 with a thickness d = 130 μm and a diameter D = 42 mm with a resistivity of 607.47 Ohm·cm, oriented in the crystallographic direction (111) and concentration of the main carriers' component N_n = 7·10^{12} cm^{-3}.

Using the method of vacuum evaporation in a quasi-closed volume [14] makes it possible to obtain layers with thicknesses ranging from several hundred angstroms to several tens of microns. At the same time, homogeneity and maximum frequency of the material are achieved, and film growth conditions are easily controlled.

N-type CdS powder with a particle size of 120 μm and a purity of 99.99 % was used as the starting material to obtain the Au-nCdS-nSi-pCdTe-Au photodiode structure. 60 μm p-type CdTe with 99.999% purity from Advanced materials (China). The resistivity of CdTe is $\rho \approx 10^4 \div 10^6$ Ohm·cm, and the resistivity of CdS $\rho \approx 10^2$ Ohm·cm. The concentration of the main carriers of CdTe is $N \approx 10^{12} \div 10^{14}$ cm^{-3}, CdS = 10^{18} cm^{-3} [15]. CdS and CdTe films were deposited by vacuum evaporation on the silicon surface of an AVP-05 unit, at a pressure in the chamber P = 1.8·10^{-5} mmHg.

When depositing CdS films on the surface of a silicon substrate, the evaporator temperature was varied in the range T_e=750÷800 °C, necessary for congruent evaporation of CdS particles, in which the temperature of the silicon substrate was simultaneously maintained in the range T_e=200÷250 °C. At a low temperature of the silicon substrate, fine-grained and randomly oriented grains are formed in the polycrystalline film. CdTe films were deposited on the back side of the substrate at an evaporator temperature T_e= 550°C.

During the deposition of CdTe films, the substrate temperature was T_s = 270÷290°C. The film growth time is t = 5 minutes at a rate of υ = 16.7 Å/s, at which the thickness of each film is 0.55 μm. The thickness of the films was measured with a Linnik MII-4 microinterferometer. The data obtained when studying the surface using a MII-4 microscope showed that a thin layer of CdS deposited on the surface of the n Si substrate consists of columnar crystallites, misoriented in azimuth and oriented in the direction of film growth [16].

To obtain a rectifying contact on the surface of the film layers of the heterostructure, metal-semiconductor transitions obtained by sputtering gold (Au) with a thickness d = 100 Å in a VUP-4 vacuum station at a temperature t = 435°C. Next, the resulting heterojunction structure Au-nCdS-nSi-pCdTe-Au scribed into discrete samples with an area of 29 mm^2 (Fig. 1)

Figure 1. Cross section of a photosensitive multilayer double heterostructure Au-nCdS-nSi-pCdTe-Au

RESULTS AND DISCUSSION

Studying the current-voltage characteristics of heterostructures solves two problems at once:

- first, is directly related to the determination of the most important characteristics of semiconductor devices;

- second, performs in the role of feedback in further increasing the efficiency of the structures under consideration, allowing, if necessary, to adjust the parameters of the formation of heterostructures in the event of observing degradation of the electrical characteristics of diodes based on them.

Au-nCdS-nSi-pCdTe-Au heterojunction photodiode structure was obtained by sequential vacuum thermal evaporation of CdS and CdTe powders onto a substrate - the surface of a monocrystalline n-type silicon wafer.

In Fig. 2 the direct (I) and reverse (II) branches of the current-voltage characteristics (CV characteristics) of the heterojunction are presented Au-nCdS-nSi-pCdTe-Ag structures, which were measured at room temperature and plotted on a log-log scale.
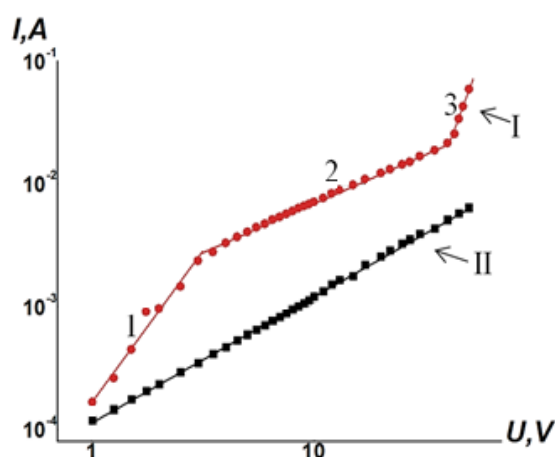
Figure 2. Current-voltage characteristic Au-nCdS-nSi-pCdTe-Au heterostructures in the voltage range from zero to 3 V $- J \propto V^{2.44}$ (1), in the range from 5 to 40 V $- J \propto V^{0.78}$ (2), in the range from 43 to 50 V $- J \propto V^{5.55}$ (3)

The direct branch of the current-voltage characteristics of Au-nCdS-nSi-pCdTe-Au structures (Fig. 2) is well described by power-law dependences of the type $-I = AV^\alpha$ with different values of the exponent α. Analysis of the direct branch of the current-voltage characteristic shows that at room temperature there are three pronounced sections in the voltage range from zero to 3 V - $J \propto V^{2.44}$ (1), in the range from 5 to 40 V $- J \propto V^{0.78}$ (2), in the range from 43 to 50 V $- J \propto V^{5.55}$ (3).

According to theory [5], diode structures have a power-law dependence of current on voltage of the type $J \propto V^\alpha$, ($\alpha \geq 2$), including a region of sharp increase in current when complex defect-impurity complexes are involved in recombination processes along with point defects, within which electron exchange occurs [17].

$$U = N_R \frac{c_n c_p (pn - n_i^2)}{c_n(n+n_1) + c_p(p+p_1) + a\tau_i pn},$$ (1)

where N_R is the concentration of recombination centers (complexes), n, p are the concentrations of electrons and holes, n_i is the intrinsic concentration in the semiconductor, c_n, c_p are the capture coefficients of electrons and holes, n_1, p_1 are the equilibrium concentrations of electrons and holes under conditions, when the Fermi level coincides with the impurity level (the so-called static Shockley-Read factors), τ_i is the time that takes into account certain processes of electron exchange within the recombination complex, a is a coefficient that depends on the specific type of impurity or defect-impurity complexes.

The nCdS-nSi-pCdTe structure under study may contain point defects - vacancies of both cadmium (Cd) atoms and sulfur (S) or tellurium (Te) atoms.

In the sublattice of cadmium atoms, their singly and doubly charged vacancies V_{Cd}^-, V_{Cd}^{2-} are easily formed. Doubly charged vacancies of cadmium atoms in most cases form complexes with positively charged impurities of the type $(V_{Cd}^{2-} D^+)^{-1}$ and neutral sulfur atoms of the type $(V_{Cd}^{2-} S^*)^{-2}$[10]. In addition to these complexes, there is a high probability of the formation of such defect-impurity complexes as - "negatively charged acceptor + positively charged interstitial ion" or "positively charged donor + negatively charged vacancy" [18], which play a decisive role in recombination processes.

Despite the difference in the type of complexes, one general pattern can be traced in them - the recombination of nonequilibrium electrons and holes in nCdS-nSi-pCdTe occurs with a delay, and taking into account the inertia of electron exchange inside the recombination complex causes the appearance of the last term in the denominator of formula (1), which, when sufficiently a high level of arousal can become decisive. In this case, the current-voltage characteristic has the following analytical expression in the voltage range from 0 to 4 V:

$$V = A + B\sqrt{J} - \frac{D}{\sqrt{J}},$$ (2)

where A, B and D are constants depending on the properties of the material. The value of the coefficients A = 2,464 V, B = 11.4 V A$^{-1/2}$ and D = 4.4 10^{-4} V·A$^{-1/2}$.

Dependence (2) allows us to describe any value of the slope of the current-voltage characteristic of the type $J \propto V^\alpha$, including for sections with a sharp increase in current. As the voltage increases, we can very clearly see the sublinear nature of the dependence of the current on the voltage, which clearly indicates that an injection depletion effect is observed. It is known that the appearance of a sublinear section is usually associated with the imperfection of one of the transitions in the npn or p - n - n$^+$ structure. In our case, in the Au-nCdS-nSi-pCdTe-Au structure, since it does not limit the current through the np junction.

In the forward bias direction near the pCdTe-Au-contact, electrons, as well as holes, are accumulated to maintain electrical neutrality due to a high potential barrier of the order of 0.843 eV, which promotes the accumulation of nonequilibrium charge carriers and the appearance of a positive gradient $dn / dx > 0$. As a result, the diffusion and drift flows of carriers are directed towards each other and, starting from a certain value of the bias voltage (5V), these flows are mutually compensated, increasing the base resistance and forming a sublinear dependence [20].

According to the theory given in [18,19] in structures with developed accumulation, a sublinear part of the current-voltage characteristic appears when the conditions $Ja\ d \geq 2$ are met. This shows that for samples of structures based on CdTe-Si-CdS the value $Jad = 3$, at T = 300 K.

This section of the current-voltage characteristic can be well described within the framework of the above theory of the effect injection depletion:

$$V = V_0 \exp(aJd),$$ (3)

where $a = \frac{1}{2kT\mu_n N_t}$ is a parameter that depends only on the mobility of the majority carriers - electrons (μ_n) and the concentration of deep impurities - N_t. Using expression (3), you can determine the value of the parameter "a" directly from the sublinear section of the current-voltage characteristic, as shown in Fig. 2.
Au-nCdS-nSi-pCdTe-Au with forward and reverse bias on a logarithmic scale:

$$a = \frac{S \cdot \ln(V_2/V_1)}{(I_2 - I_1) \cdot d}.$$ (4)

The value of the parameter "a" in expression (4), determined on the basis of experimental data on the current-voltage characteristics of the Au-nCdS-nSi-pCdTe-Ag structure was at room temperature $a = 5.22 \cdot 10^4$ cm/A then, accordingly μ_n - $N_t = 2.31 \cdot 10^{15} V^{-1} \cdot cm^{-1} \cdot s^{-1}$. The mobility of the majority carriers was $\mu_n \approx 500$ cm^2/Vs, and minority carriers $\mu_p \approx 60$ cm^2/Vs, therefore, the concentration of deep impurities leading to the injection depletion effect is $N_t \approx 4.62 \cdot 10^{12}$ cm^{-3}.

With further increase in voltage, as can be seen from Fig. 1. starting from U = 43 V, a sharp increase in current is observed, and the exponent $\alpha \approx 5.55$. This section is called pre-breakdown. In this case, the third term in the denominator of expression (1) becomes significant and the recombination rate no longer obeys the Shockley–Reed statistics. In this case, according to [19], the current-voltage characteristics of the system under consideration take the form:

$$J = \frac{q^2(b+1)^2 N_r d^3}{\varepsilon \tau_i^2 c_p (V_0 - V)}. \tag{5}$$

Where, ε is the dielectric constant and

$$V_0 = \sqrt{\frac{q(b+1)N_r d^4}{2\varepsilon \tau_i \mu_p}} = const. \tag{6}$$

From (5) it is clear that the denominator decreases with increasing voltage, i.e. the increase in current in the voltage range (43÷50) V is described by a dependence like (5). First-principles calculations of band electronic structure based on density functional theory [16,18]. In accordance with the original material data given in Table 4.3 of the multilayer heterojunction Au-nCdS-nSi-pCdTe-Au - structures can be constructed with a high-quality energy band diagram in an equilibrium state.

Table 1. Data on the physical parameters of the studied multilayer heterofilm photosensitive Au-nCdS-nSi-pCdTe-Ag structure

No	Name of parameters		Heterofilm layers		Substrate
			nCdS	pCdTe	nSi
1	Material thickness, W (μm)		0.55	0.55	130
2	Band gap, E_g (eV)		2.42	1.45	1.12
3	Dielectric constant, $\varepsilon/\varepsilon_0$		9.0	9.4	12
4	Resistivity, ρ (Ohm·cm)		$2 \cdot 10^2$	10^5	600
5	conductivity, σ(Ohm·cm)$^{-1}$		$0.5 \cdot 10^{-2}$	10^{-5}	$0.83 \cdot 10^{-3}$
6	electron affinity, χ(eV)		4.5	4.28	4.01
7	Mobility, cm^2/(V·s)	μ_c	350	500	1200
		μ_p	50	60	500
8	Own concentration of charge carriers, N (cm^{-3})		$1.1 \cdot 10^{18}$	$2.0 \cdot 10^{14}$	$3.6 \cdot 10^{12}$
9	Charge carrier concentration, (cm^{-3})	N_c	$1.8 \cdot 10^{19}$	$7.5 \cdot 10^{17}$	
		N_v	$2.4 \cdot 10^{18}$	$1.8 \cdot 10^{18}$	

Based on the data calculated from the experimental results, a band diagram was constructed Au-nCdS-nSi-p CdTe-Au heterostructure, which is shown in Fig. 3. From the band diagram of the heterostructure it is clear that forward and reverse currents are limited by the resistance of the space charge layer at the interface of the nCdS-n Si and n Si-pCdTe heterojunction. This space charge consists of negatively charged mobile and immobile donor centers, which are located in the nCdS and – p CdTe layer adjacent to silicon, respectively, since the donor concentration in nSi is ten orders of magnitude greater than the carrier concentration in these layers.

In this structure, the contact between Si and nCdS also gives a contact potential difference of U=1.1 eV, however, an enriched layer of space charge appears at the interface of the Si and nCdS layer, since the work function of the metal (Au) present in large quantities in n CdS layer is less than the work function of the semiconductor - Si.
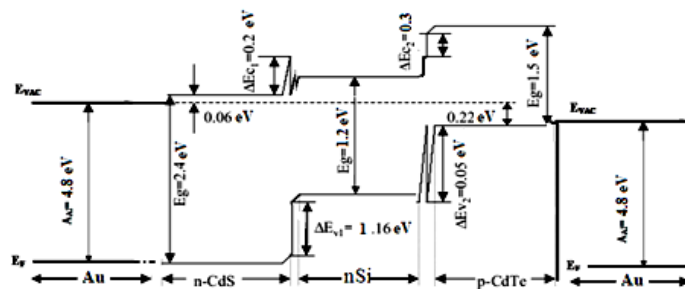
Figure 1. Energy band diagram of the Au-nCdS-nSi-pCdTe-Au structure in the equilibrium state

When illuminated from Au-nCdS-nSi-p CdTe-Au heterojunctions from the rear sides, photogeneration of film carriers of chalcogenide compounds nCdT e and pCdS occurs. The main current carriers diffuse into the n-layer of silicon, where they are separated by the transition field with further acceleration of the carriers by the applied external field, sufficient for impact ionization of Si atoms, which leads to the development of the avalanche process.

It is obvious that the introduction of films of chalcogenide compounds CdT e and CdS into the active region of the diode leads to the following results: firstly, there is an expansion of the spectral range of photosensitivity into the near-IR region below the optical absorption edge of silicon to 1.4 μm, which corresponds to the optical band gap for films of chalcogenide compounds CdT e and CdS at room temperature 300 K [16]; secondly, the photo response in this region has increased by more than two orders of magnitude, including at wavelengths corresponding to the transparency windows of quartz optical fibers, which are used for telecommunications; thirdly, there is an almost tenfold increase in sensitivity near and above the band gap of Si in the region λ = (1.0÷1.4) μm, which is also associated with the contribution to photon absorption and carrier generation in films of chalcogenide compounds CdTe and CdS .

Therefore, the external potential applied to the structure, including the contact potential difference, mainly falls on the space charge layer of the structure boundaries. Moreover, surface states (N_{SS}) at the interface of contacting semiconductors - cadmium sulfide and silicon, can affect the height of the potential barrier. The nature of these surface states is associated with the difference in the crystal lattice constants n CdS and n Si, as well as p CdTe and n Si. The properties of the multilayer diode structure of Au-n CdS-nSi-pCdTe-Au heterojunctions depend on the technological parameters and method conditions.

CONCLUSIONS

The conducted studies show that the current-voltage characteristic of Au-nCdS-nSi-pCdTe-Au structures has three sections: power-law - $I \propto V^{2.44}$, sublinear $V \propto \exp(Jad)$, and prebreakdown dependence – $I \propto V^{5.55}$, arising in nCdS-nSi-pCdTe layers with a change in current density at a constant temperature due to a change in the type of recombination processes. Recombination of nonequilibrium carriers at low current densities occurs through point local centers (defects), and at high current densities, complex complexes are responsible for the recombination processes, within which electron exchange occurs.

Based on the data obtained, it was established that in the layers nCdS-nSi-pCdTe photosensitive Au-nCdS-nSi-pCdTe-Au structure, impurity complexes (defects) are formed, in which the rate of recombination of nonequilibrium carriers at low excitation levels is determined by simple local centers in the boundary transition layers. A band diagram of a multilayer photodiode structure Au-nCdS-nSi-pCdTe-Au has been constructed, which can be schematically described as Au-nCdS-nCdS-nSi-nSi-pCdTe+pCdTe-Au.

ORCID
◉**Sharifa B. Utamuradova**, https://orcid.org/0000-0002-1718-1122, ◉**Khodjakbar S. Daliev,** https://orcid.org/0000-0002-2164-6797
◉**Shakhrukh Kh. Daliev,** https://orcid.org/0000-0001-7853-2777; ◉**Sultanpasha A. Muzafarova,** https://orcid.org/0000-0001-5491-7699
◉**Kakhramon M. Fayzullaev,** https://orcid.org/0000-0001-7362-1439; ◉**Gulnoza A. Muzafarova,** https://orcid.org/0009-0002-1773-920X

REFERENCES
[1]   M. Bass, *et al*., editors, *Handbook of optics*, Vol. 2. (New York, McGraw-Hill, 1995).
[2]   Z.T. Azamatov, M.A. Yuldoshev, N.N. Bazarbayev, and A.B. Bakhromov, "Investigation of Optical Characteristics of Photochromic Materials," Physics AUC, **33**, 139-145 (2023). https://cis01.central.ucv.ro/pauc/vol/2023_33/13_PAUC_2023_139_145.pdf
[3]   K.S. Daliev, Sh.B. Utamuradova, J.J. Khamdamov, and M.B. Bekmuratov, "Structural properties of silicon doped rare earth elements ytterbium," East European Journal of Physics, (1), 375–379 (2024). https://doi.org/10.26565/2312-4334-2024-1-37
[4]   Z.T. Azamatov, Sh.B. Utamuradova, M.A. Yuldoshev, and N.N. Bazarbaev, "Some Properties of Semiconductor-Ferroelectric Structures," East Eur. J. Phys. (2), 187-190 (2023). https://doi.org/10.26565/2312-4334-2023-2-19
[5]   N.A. Sultanov, Z.X. Mirzajonov, F.T. Yusupov, and T.I. Rakhmonov, "Nanocrystalline ZnO Films on Various Substrates: A Study on Their Structural, Optical, and Electrical Characteristics," East Eur. J. Phys. (2), 309-314 (2024), https://doi.org/10.26565/2312-4334-2024-2-35
[6]   A. Heintz, B. Ilahi, A. Pofelski, G. Botton, G. Patriarche, A. Barzaghi, and A. Boucherif, "Defect free strain relaxation of microcrystals on mesoporous patterned silicon," Nature Communications, **13**(1), 6624 (2022). https://doi.org/10.1038/s41467-022-34288-4
[7]   Z.L. Wang, Y. Liu, and Z. Zhang, *Handbook of nanophase and nanostructured materials II*, (Kluwer Academic Plenum, 2003).
[8]   H.S. Nalwa, *Photodetectors and Fiber Optics*, (Academic Press, 2001).
[9]   Sh.B. Utamuradova, A.V. Stanchik, K.M. Fayzullaev, and B.A. Bakirov, "Raman scattering of light by silicon single crystals doped with chromium atoms," Applied Physics, (2), 33–38 (2022).
[10] Y. Liu, Y. Li, Y. Wu, G. Yang, L. Mazzarella, P. Procel-Moya, A.C. Tamboli, *et al.*, "High-efficiency silicon heterojunction solar cells: materials, devices and applications," Materials Science and Engineering: R: Reports, **142**, 100579 (2020), https://doi.org/10.1016/j.mser.2020.100579
[11] Sh.B. Utamuradova, and D.A. Rakhmanov, "Effect of Holmium Impurity on the Processes of Radiation Defect Formation in n-Si<Pt>," Annals of the University of Craiova, Physics, **32**, 132–136 (2022). https://cis01.central.ucv.ro/pauc/vol/2022_32/15_PAUC_2022_132_136.pdf
[12] M.H. Abdullal, R.A. Jaseen, and A.H. Resan, "Annealing effect on the optical energy gap of (CdTe) thin films," J. Pure Sciences, **7**(3), 205-213 (2011), https://www.iasj.net/iasj/pdf/ccf116d82c221e01
[13] Sh.B. Utamuradova, D.A. Rakhmanov, A.S. Doroshkevich, Z. Slavkova, and M.N. Ilyina, "Impedance spectroscopy of p-Si<Pt>, p-Si<Cr> irradiated with protons," Advanced Physical Research, **5**(1), 5–11 (2023). http://jomardpublishing.com/UploadFiles/Files/journals/APR/V5N1/Utamuradova_et_al.pdf
[14] T.M. Razikov, S.A. Muzafarova, R.T. Yuldoshov, Z.M. Khusanov, M.K. Khusanova, Z.S. Kenzhaeva, and B.V. Ibragimova, East Eur. J. Phys. (1), 370-374 (2024). https://doi.org/10.26565/2312-4334-2024-1-36

[15] A.J. Mawat, M.H. Al-Timimi, W.H. Albanda, and M.Z. Abdullah, "Morphological and optical properties of $Mg_{1-x}CdS_x$ nanostructured thin films," AIP Conference Proceedings, **2475**(1), 090019 (2023). https://doi.org/10.1063/5.0103955

[16] F.A. Giyasova, "Study of the spectral and temporal characteristics of a heterofilm photosensitive Au-nCdS-nSi-pCdTe-Au structure," Scientific journal "Physics of Semiconductors and Microelectronics", **4**(1), 42-50 (2022).

[17] Sh. B. Utamuradova, A.S. Achilov, R.R. Kabulov, and S.A. Muzafarova, "Effect of temperature on the current transfer mechanism in the reverse I-V characteristics of the n-CdS/i-$CdS_x Te_{1-X}$/ p-CdTe heterostructure," Modern Physics Letters B, **37**(33), 2350162 (2023). https://doi.org/10.1142/S0217984923501622

[18] A.S. Saidov, K.A. Amonov, and A.Yu. Leiderman, "Study of the dependence of the current-voltage characteristic p-Si–n–$(Si_2)_{1-x-y}(Ge_2)_x(ZnSe)_y$-structures on temperature," Computational nanotechnology, **6**(3), 16-20 (2019). (in Russian)

[19] Sh.B. Utamuradova, S.Kh. Daliev, S.A. Muzafarova, and K.M. Fayzullaev, "Effect of the Diffusion of Copper Atoms in Polycrystalline CdTe Films Doped with Pb Atoms," East Eur. J. Phys. (3), 385 (2023). https://doi.org/10.26565/2312-4334-2023-3-41

[20] A.H.H. Asal, and S.N.T. Al-Rashid, "Effects of Quantum Confinement Energy on the Transmittance of Cadmium Telluride (CdTe) Within the Near Infrared Region (700-2500nm)," East. Eur. J. Phys. (3), 329 (2023), https://doi.org/10.26565/2312-4334-2023-3-33

ВОЛЬТ-АМПЕРНА ХАРАКТЕРИСТИКА ФОТОЧУТЛИВОЇ ГЕТЕРОПЛІВКОВОЇ СТРУКТУРИ Au-CdS-nSi-CdTe-Au

Шаріфа Б. Утамурадова[a], Ходжакбар С. Далієв[b], Шахрух Х. Далієв[a], Султанпаша А. Музафарова[a], Кахрамон М. Файзуллаев[a], Гульноза А. Музафарова[a]

[a]Інститут фізики напівпровідників і мікроелектроніки Національного університету Узбекистану,
100057, Узбекистан, Ташкент, вул. Янги Алмазор, 20
[b]Філія ФДБУ «Національний дослідницький університет МПЕІ», Йогду, 1, Ташкент, Узбекистан

Наведено результати досліджень вольт-амперних характеристик фотодіодної гетероструктури. Au-nCdS-nSi-pCdTe-Au, в прямому і зворотному напрямках. Створено фотодіодні гетероструктури площею 29 мм², отримані методом вакуумного напарювання у квазізамкнутому об'ємі шляхом нанесення шарів сульфіду кадмію та телуриду кадмію на підкладку монокристалічного кремнію. з питомим опором ρ=607,47 Ом·см. Відмінною особливістю отриманих фотодіодних структур Au-nCdS-nSi-pCdTe-Au є двостороння чутливість, де утворюються домішкові комплекси. У структурах швидкість рекомбінації нерівноважних носіїв на низьких рівнях збудження визначається простими локальними центрами в граничних перехідних шарах. Побудовано зонну діаграму багатошарової фотодіодної структури Au-nCdS-nSi-pCdTe-Au.

Ключові слова: *питомий опір; інтенсивність; струм; гетероперехід; фотодіод; структура; перехід; мікроінтерферометр; вакуум; ємність; смугова діаграма*

EXPLORING THE ELASTIC, MAGNETIC, THERMODYNAMIC AND ELECTRONIC PROPERTIES OF XNNi3 (X: Cd,In)CUBIC ANTI-PEROVSKITES

Jounayd Bentounes[a], Amal Abbad[b], Wissam Benstaali[b,*], Kheira Bahnes[b], Noureddine Saidi[b]

[a]*Faculty of Exact Sciences and Computer Sciences, Abdelhamid Ibn Badis University, Mostaganem (27000) Algeria*
[b]*Laboratory of Technology and Solids Properties, Faculty of Sciences and Technology, BP227,*
Abdelhamid Ibn Badis University, Mostaganem (27000) Algeria
*Corresponding Author e-mail: ben_wissam@yahoo.fr

Density functional theory is used to investigate the structural, electronic, thermodynamic and magnetic properties of the cubic anti-perovskites $InNNi_3$ and $CdNNi_3$. Elastic and electronic properties were determined using generalized gradient approximation (GGA) and local spin density approximation (LSDA) approaches. The quasi-harmonic Debye model, using a set of total energy versus volume calculations is applied to study the thermal and vibrational effects. The results show that the two compounds are strong ductile and satisfy the Born-Huang criteria, so they are mechanically stable at normal conditions. Electronic properties show that the two compounds studied are metallic and non-magnetic. The thermal effect on the bulk modulus, heat capacity, thermal expansion and Debye temperature was predicted.
Keywords: *Anti-Perovskites; Electronic band structure; Elastic constants; First-principles calculations; Thermodynamic properties*
PACS: 61.50.Ah; 71.20.Nr; 62.20.Dc; 71.15.Mb; 65.40.Ba

1. INTRODUCTION

In recent years, the anti-perovskite carbides, nitrides and borides compounds have gained considerable attention because they have an extensive range of interesting physical and chemical properties. Their attractive physical properties derived from the association of magnetic phase transition and crystal lattice, such as nearly zero temperature coefficient of resistivity, magnetostriction, negative thermal expansion, giant magnetoresistance (GMR), and superconductivity at high temperature [1-7].

The ternary nitrides or carbides have the cubic anti-perovskite structure of the general formula XAM3(X are elements of (III–V) group, A is carbon or nitrogen, and M are transition metals) [8]. The cubic anti-perovskite type is an ordinary cubic perovskite where the metal atoms have exchanged positions with the non-metal atoms within the unit cell. The M metal atoms are positioned at the face-centered positions, the X metal atoms are positioned at the cube corner sites, and the non-metal atoms are positioned at the body-centered positions [9]. Because of the exceptional properties of several binary nitrides, ternary and higher nitrides have gained much attention during the last years, also, theoretical investigations of the physical properties of the anti-perovskite nitrides with alkali-earth metals have involved many interest [10–23]. Compared to the other member of these large family, the physical properties of the Ni-based cubic anti-perovskite compounds with a general composition MNNi3 (M = Cd and In) are less investigated. A more complete understanding of the physical properties of $CdNNi_3$ and InNNi3 is needed to ultimate technological applications of these compounds.

First-principles calculations offer one of the greatest tools for carrying out theoretical studies of significant number of physical and chemical properties of many materials with big accuracy. Nowadays it is possible to make clear and calculate properties of many solids which were in the past difficult to get with experiments.

Motivated by the above mentioned reasons and considering the lack of high order elastic constants for most anti-perovskite materials, we report in this paper a systematic study of the structural, elastic, thermodynamic and electronic properties for the two cubic anti-perovskite compounds $InNNi_3$ and $CdNNi_3$ using the full-potential linearized augmented plane wave (FPLAPW) method based on the density functional theory (DFT) within the generalized-gradient approximation (GGA) and the local spin density approximation (LSDA) approximations. The objective of the present paper is to theoretically predict and give a wide comprehension of the elastic, electronic and thermodynamic properties of the two compounds.

2. CALCULATION

In the present work Kohn–Sham equations [24] are solved to calculate the structural, electronic and magnetic properties of the cubic anti-perovskite $CdNNi_3$ and InNNi3using the WIEN2K code [25, 26]. It is based on the full-potential linearized augmented plane wave method (FPLAPW) [27]. The two anti-perovskites are assumed to have an ideal cubic structure (space group is Pm3m (221) [28]). Basis functions were expanded as combinations of spherical harmonic functions inside non-overlapping spheres around the atomic sites (MT spheres) and in Fourier series in the interstitial region. The valence wave functions, inside the spheres are expanded up to $l_{max}=10$, the calculation gives

84 K-points corresponding to a mesh (12×12×12) which is equivalent to 2000 K-points in the Brillouin zone (BZ). The wave functions in the interstitial region were expanded in plane waves with a cutoff of $k_{max}=7/R_{MT}$ (where R_{MT} is the average radius of the MT spheres). The muffin-tin radius R_{MT} is based on two conditions: (i) no core charge leaks out of MT spheres and (ii) no overlapping is permitted between spheres. The muffin–tin radii of the cubic $CdNNi_3$ anti-perovskite are taken to be 2.43, 1.62, and 1.82 atomic units (a.u.) for Cd, N and Ni respectively. The muffin–tin radii of the cubic $InNNi_3$ anti-perovskite are taken to be 2.24, 1.6, and 1.8 atomic units (a.u.) for In, N and Ni respectively. The lattice constants and bulk modulus are calculated by fitting the total energy versus volume according to the Murnaghan's equation of state [29]. For the exchange correlation functional, we have used the GGA [30] as well as the local spin density approximation (LSDA) [31].

3. RESULTS AND DISCUSSIONS
3.1. Structural and Elastic properties

In order to calculate the ground-state properties of $InNNi_3$ and $CdNNi_33$ antiperovskites, we performed the structural optimization by minimizing the total energy with respect to the cell parameters and the atomic positions. The equilibrium lattice parameters of both of the compounds are obtained by performing structural optimization and the calculated energy volume data is fitted to Murnaghan's equation of state.

To determine the magnetic ground state, both spin-polarized (ferromagnetic Fig. 1 (a) and (b)) and spin-unpolarized (non-magnetic Fig.1 (c) and (d)) calculations are also performed, for the magnetic and non-magnetic states as a function of volume (see Table 1), which is clearly indicating that the non-magnetic state has the lower energy as compared to the magnetic state for the two compounds, and therefore, the non-magnetic state is more favorable.
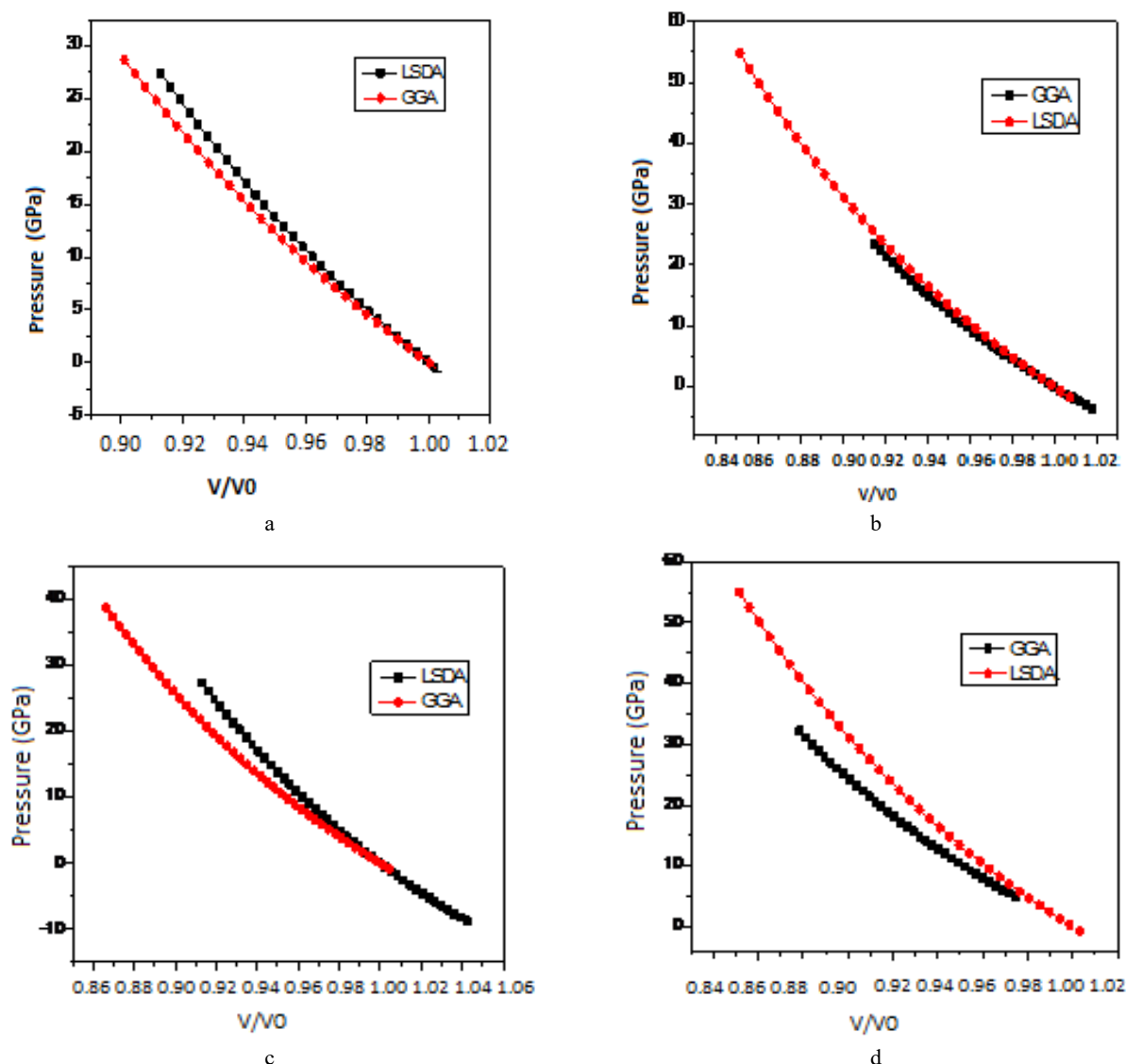
Figure 1. The variation of pressure (Gpa) as a function of v/v0 using LSDA and GGA approximations. (a) CdNNi₃ in ferromagnetic state. (b) InNNi₃ in ferromagnetic state. (a) CdNNi₃ in non-magnetic state. (a) InNNi₃ in non-magnetic state

Table 1. Calculated equilibrium lattice constant (a, in Å), bulk modulus (B, in GPa) and its pressure derivative (B₀), cell volumes (V, in bhor^3) and the minimum total energy (E, in Ry) in ferromagnetic (FM) and non-magnetic (NM) phases, for cubic anti-perovskites $CdNNi_3$ and $InNNi_3$ obtained with GGA and LSDA. Available experimental and theoretical results are quoted for comparison

Anti-perovskite	Parameters	LSDA	GGA	Exp	Other theoretical results
$CdNNi_3$	a [Å]	3.761(FM) 3.762 (NM)	3.807(FM) 3.857 (NM)	3.852[33]	-
	V	358.67(FM) 359.30 (NM)	372.369(FM) 387.4 (NM)	-	-
	B	234.49(FM) 235.85 (NM)	212.8(FM) 194.71 (NM)	-	-
	B₀	5.26(FM) 5.1 (NM)	5.26(FM) 5.1 (NM)	-	-
	E	-20401.22(FM) -20401.229 (NM)	-20422.36(FM) -20426.55 (NM)	-	-
$InNNi_3$	a [Å]	3.782(FM) 3.782 (NM)	3.826(FM) 3.879 (NM)	3.844[32] 3.862[33]	3.784(LDA) [34] 3.882(GGA)[34]
	V	365.119(FM) 365.142 (NM)	378.164(FM) 393.924 (NM)	-	-
	B	233.33(FM) 231.66 (NM)	210.81(FM) 176.77 (NM)	-	226.91(LDA) [34] 179.93(GGA)[34]
	B₀	4.758(FM) 4.6 (NM)	5.639(FM) 4.9 (NM)	-	4.761(LDA) [34] 4.281(GGA)[34]
	E	-20975.497(FM) -20975.499 (NM)	-20997.04(FM) -21001.12(NM)	-	-

The calculated bulk moduli B_0, the pressure derivatives of bulk modulus B' and the equilibrium lattice parameter a_0 using GGA and LSDA, are given in Table 01 with the available experimental and theoretical data for comparison [32-34]. Our calculated equilibrium lattice constant a_0 is in good agreement with the experimental data. We can see that, the use of the LSDA slightly underestimates the lattice constants comparing to GGA approximation which gives better theoretical results.

The elastic constants are elemental and very important for describing the mechanical properties of materials. They have significant information which can be obtained from ground state total energy calculations [35, 36]. The elastic constants are connected to a number of fundamental properties such as equation of state, interatomic potential, specific heat, phonon spectra, Debye temperature and melting point. They also provide information about the mechanical, dynamical behavior and the nature of forces operating in solids. The study of elasticity defines the properties of material that undergoes stress, deforms, and then recovers and returns to its original shape after stress stops.

To study the stability of cubic $CdNNi_3$ and $InNNi_3$ anti-perovskites, we have calculated the elastic constants at equilibrium lattice parameter within GGA and LSDA approaches, we have used the numerical first-principle calculation by computing the components of the stress tensor δ for small stains, by means of the method developed by Charpin and integrated in WIEN2K code which has been applied successfully in previous works [37–39]. In the case of cubic system, there are three independent elastic constants, namely C_{11}, C_{12}, and C_{44} to totally characterize the mechanical properties, the mechanical stability criteria for a cubic crystal are, its three independent elastic constants should satisfy the following relations given by Born and Huang [40]; $(C_{11}-C_{12}) > 0$, $C_{12} > 0$, $C_{44} > 0$ and $C_{11} + C_{12} > 0$

The bulk modulus B is calculated using the following formula;

$$B = \frac{(C_{11}-2C_{12})}{3} \tag{1}$$

After that, the most important mechanical parameters for cubic anti-perovskites, namely shear modulus G, Young's modulus E, Poisson's ratio σ and Lamé's coefficients μ and λ, the anisotropy factor A, which are the main elastic moduli for applications, are calculated from the elastic constants of the single crystals using the following relations:

$$G = \frac{C11-C12+3C44}{5}, \tag{2}$$

$$E = \frac{9BG}{3B+G}, \tag{3}$$

$$\sigma = \frac{3B-E}{6B}, \tag{4}$$

$$\mu = \frac{E}{2(1+\sigma)}, \tag{5}$$

$$\lambda = \frac{\sigma E}{(1+\sigma)(1-\sigma)}, \tag{6}$$

$$A = \frac{2C_{44}}{(C_{11}-C_{12})}. \tag{7}$$

The computed values of the elastic constants for CdNNi$_3$ and InNNi$_3$ are given in Table 2. Till date, no experimental or theoretical data for CdNNi$_3$ are available to be compared with our computed results. We remark that C$_{11}$, C$_{12}$ and C$_{44}$ calculated using LSDA are higher than those calculated using GGA. Referring to Table 2, the values of B0 obtained from EOS fitting and elastic constants (B$_0$= (C$_{11}$+2C$_{12}$)/3) are nearly same, which ensures that the computed elastic constants for CdNNi$_3$ and InNNi$_3$ are consistent. Moreover, this may be an approximation of the accuracy of our calculated elastic constants. Also from Table 2, we can compare our results against the Born-Huang criteria for stability, so our two compounds satisfy the Born-Huang criteria, so they are mechanically stable at normal conditions. The elastic constants for InNNi$_3$ are compared with theoretical study done by Z.F. Hou [34] and we can note that our results are in good agreement.

Table 2. Calculated elastic constants (C$_{11}$, C$_{12}$, C$_{44}$ (GPa)), bulk modulus B$_0$ (GPa), Young's modulus E(GPa), Shear modulus G(GPa), Poisson's ratio σ, and Lamé's coefficients (λ and μ, in GPa) and anisotropy factor A for cubic anti-perovskites CdNNi$_3$ and InNNi$_3$ obtained with GGA and LSDA. Available theoretical results are quoted for comparison.

	CdNNi$_3$		InNNi$_3$	
	LSDA	GGA	LSDA	GGA
B$_0$	235.85[a] ,236.45[b]	190.47[a], 184.61[b]	231.66[a],232.8[b]	176.77[a],182.97[b]
C$_{11}$	399.42	258.60	412.60(356.77[c])	310.97(274.08[c])
C$_{12}$	157.47	147.62	142.89(164.23[c])	116.97(131.20[c])
C$_{44}$	84.94	41.49	61.72(69.06[c])	71.71(60.01[c])
G	97.89	46.61	84.89 (79.24[c])	80.61(64.35[c])
E	391.56	186.47	339.58(212.94[c])	322.44(172.37[c])
σ	0.22	0.33	0.25(0.34[c])	0.20(0.33[c])
λ	194.50	244.61	225.49	136.60
μ	239.63	124.16	213.41	194.48
A	0.70	0.74	0.4577	0.74

[a]From Birch– Murnaghan's equation of state.
[b]FromB$_0$= (C$_{11}$ +2C$_{12}$)/3.
[c]From ref. [34]

The elastic anisotropy of crystals A has a significant interest in materials science in view of the fact that it is well correlated with the possibility to induce micro cracks in the materials. Isotropic crystal has an anisotropy factor equal to the unity, while any deviated value from 1 indicates anisotropy and this deviation is a measure of the degree of elastic anisotropy possessed by the crystal. The obtained values A are 0.45 for LSDA and 0.74 for GGA for CdNNi$_3$ and 0.36 for LSDA and 0.53 for GGA for InNNi$_3$, which are smaller than 1, which indicates a strong elastic anisotropy of the two compounds. The anisotropy is strong within LSDA compared to GGA, so the anisotropy factor is sensitive to the potential exchange.

Two other parameters are important for technological and engineering applications: Young's modulus E and Poisson's ratio σ. Young's modulus is defined as the ratio of tensile stress to tensile strain. It is frequently used to give a measure of rigidity of a solid, i.e., the larger is the value of Young's modulus, the rigid is the material. The calculated values for CdNNi$_3$ for LSDA and GGA are 391 and 186 respectively, so the material is stiffest using LSDA than GGA.

The value of Poisson's ratio σ is related with the volume change throughout uniaxial deformation. It presents information about the characteristics of the bonding forces. The σ = 0.25 and 0.5 are the lower and upper limit for the central forces in solids, respectively [41]. The values of Poisson's ratio σ obtained, suggest a considerable ionic contribution in intra-atomic bonding for these compounds.

The shear modulus G represents the resistance to reversible deformation, while the bulk modulus B gives the resistance to fracture. Pugh's index of ductility (B/G) allows us to know the ductile/brittle nature of a given material. The B/G critical value which separates ductile and brittle material is around 1.75 [42]. Our results show that the B/Gratio is 2.41 for LSDA and 3.91 for GGA for CdNNi$_3$ and 2.74 for LSDA and 2.26 for GGA for InNNi$_3$, which means that the two compounds are strong ductile.

The calculated density ρ, longitudinal, transverse and average sound velocity y$_l$, y$_t$ and y$_m$ and Debye temperature θ$_D$ for the InNNi$_3$ and CdNNi$_3$ anti-perovskites using LSDA and GGA, are listed in Table 3. CdNNi$_3$ shows lower velocities and Debye temperature in the GGA scheme comparing to LSDA approximation.

Table 3. Calculated density ρ (in g/cm3), longitudinal, transverse and average sound velocity (V_l, V_t and V_m, respectively, in m/s) calculated from polycrystalline elastic moduli, and Debye temperature (θ_D in K), calculated from the average sound velocity, for $CdNNi_3$ and $InNNi_3$ anti-perovskites

		ρ	V_m	V_t	V_l	Θ_D
$CdNNi_3$	GGA	2.45	5059	4358	10028	255.62
	LSDA	2.66	7098.5	6055.3	11724	368.85
$InNNi_3$	GGA	2.42	6764.3	5761.5	10936	339.85
	LSDA	2.61	6653.9	5692.5	11492	342.87

3.2. Electronic properties

In order to explore the electronic properties of $CdNNi_3$ and $InNNi_3$ cubic anti-perovskites at equilibrium volume, spin-polarized calculations have been performed. We have studied the electronic properties of these two materials by the GGA and LSDA in order to compare between them. We have shown the electronic properties including band structure and density of states. The spin-polarized band structures of $CdNNi_3$ and $InNNi_3$ are plotted in Figs. 2 and 3, at the equilibrium lattice parameter for LSDA and GGA approximations. As can be seen, the two compounds studied are metallic. There is not much different from the DOSs using GGA or LSDA.
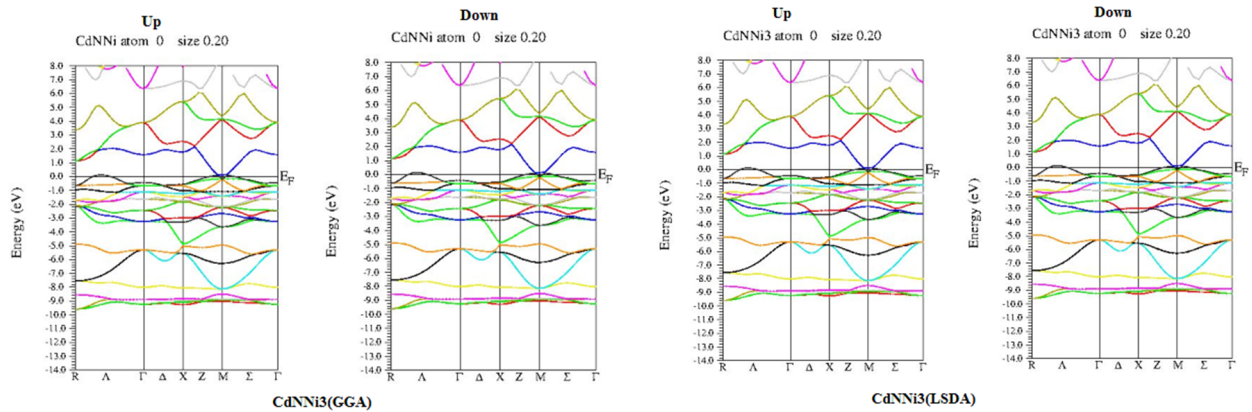
Figure 2. Spin-polarized band structures of $CdNNi_3$ using LSDA and GGA approximations
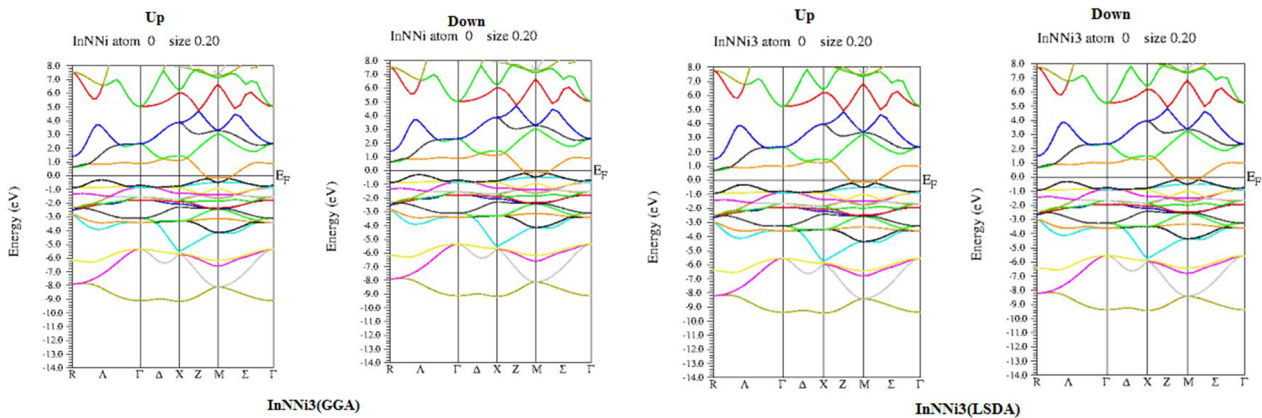
Figure 3. Spin-polarized band structures of $InNNi_3$ using LSDA and GGA approximations

There is a total hybridization between the valence band and the conduction one; hence there is no band gap in the two materials. The nonexistence of the gap is a good indication of the presence of ionic bonding. This comes to confirm results obtained by elastic study.

The spin polarization total and partial density of states (DOS), using LSDA and GGA, are calculated and plotted in Figs. 4 and 5. The perfect symmetry of the states of spin "up" and the states of spin "down" is due to the fact that the Cd, In, N and Ni atoms are non-magnetic. For $CdNNi_3$ and for the two approaches LSDA and GGA, the bands between -9.5 eV and -8.5 eV are mainly due to the contribution of Cd 4d states, the second region between -8.1 eV and -5 eV is hybridization between N 2p and Ni 3d orbitals. The same contribution is observed in the region between -4.3 eV and 4 eV, and no contribution of Cd 4d states is seen in these two regions. This hybridization around Fermi level is responsible for the metallic behaviour observed in $CdNNi_3$. For $InNNi_3$, a different tendency can be noticed. The bandwidth in the lower part of the valence band (between -9 eV and -5.4 eV) is composed essentially from In 3d orbitals and N 2p states where the remaining part comes mostly from Ni 3d and some In 5p and N 2p states.
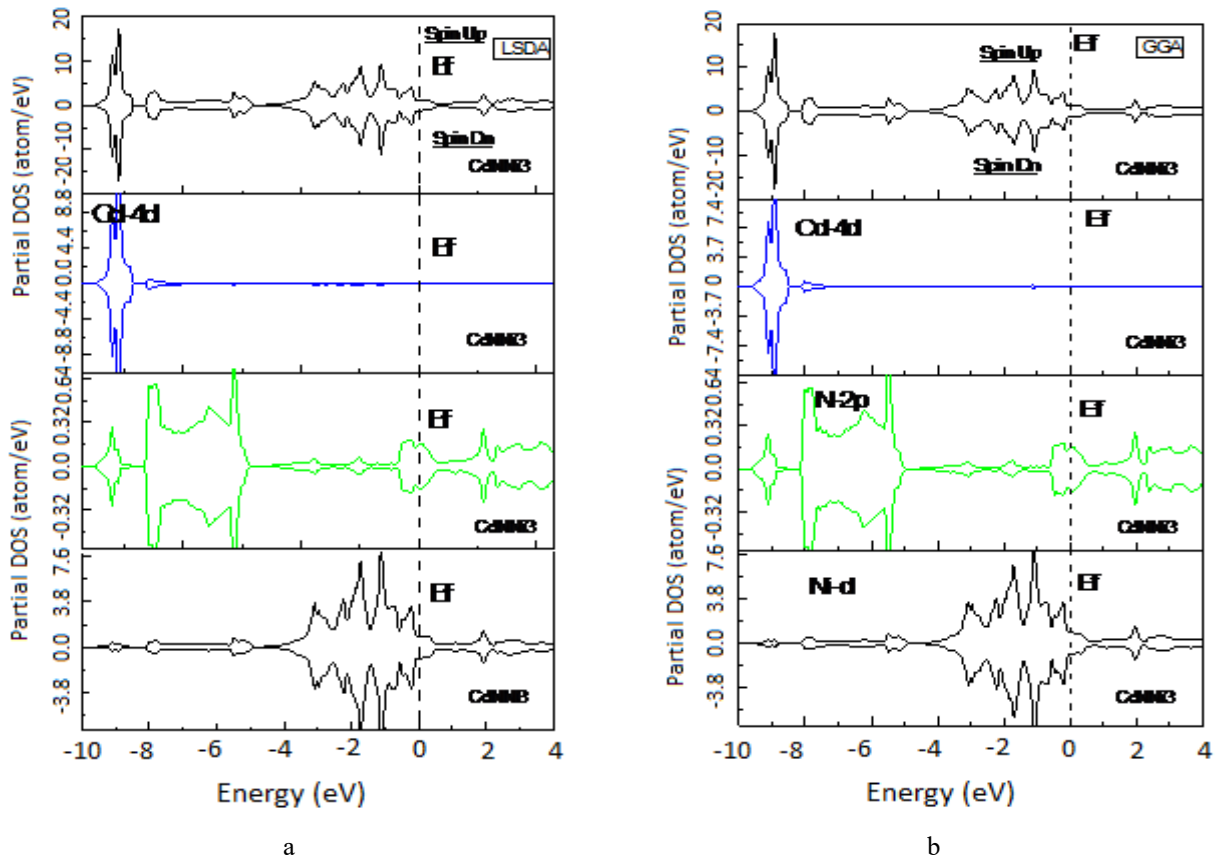
Figure 4. Total and partial density of States of CdNNi₃ anti-perovskite. (a) LSDA approximation. (b) GGA approximation. Fermi level is set to zero
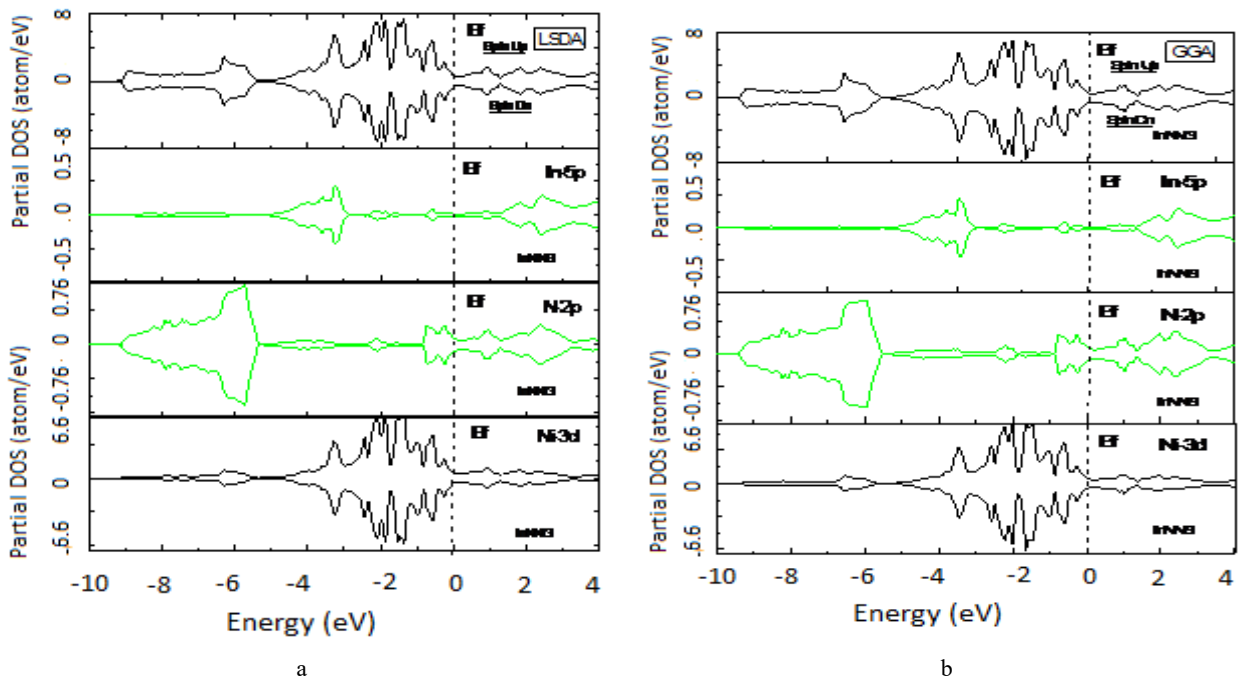
Figure 5. Total and partial density of States of InNNi₃ anti-perovskite. (a) LSDA approximation. (b) GGA approximation. Fermi level is set to zero

3.1 Thermodynamic properties

Exploration on the thermodynamic properties of solids is of great practical importance in engineering applications. In order to understand the thermodynamic properties of CdNNi₃ and InNNi₃ anti-perovskites under different temperatures and pressures, the quasi-harmonic Debye model as implemented in the Gibbs program [54] is applied.

The non-equilibrium Gibbs function G*(V, P, T) is giving by [43]:

$$G^*(V; P, T) = E(V) + PV + A_{vib}[\theta_D(V), T]. \tag{8}$$

Where $E(V)$ is the total energy per unit cell of the crystal. *PV is* the constant hydrostatic pressure condition, θ_D *(V)* the Debye temperature and A_{vib} is the vibrational Helmholtz free energy, which can be written as [44, 45]:

$$A_{vib}(\theta_D, T) = nK_B T[\frac{9\theta_D}{8T} + 3\ln\left(1 - e^{\frac{-\theta_D}{T}}° - D\left(\frac{\theta_D}{T}\right)\right]. \tag{9}$$

Where n is the number of atoms per formula unit, KB is the Boltzmann's constant and $D\left(\frac{\theta_D}{T}\right)$ is the Debye integral. The Debye temperature θ_D for an isotropic solid is given as [45]:

$$\theta_D = \frac{\hbar}{\theta_D}\left[6\pi^2 V^{\frac{1}{2}} n\right]^{\frac{1}{3}} f(\sigma)\sqrt{\frac{B_s}{M}}. \tag{10}$$

Where M is the molecular mass per unit cell and BS is the adiabatic bulk modulus, which is approximately given by the static compressibility;

$$B_s \cong B(V) = V\frac{d^2 E(V)}{dV^2}. \tag{11}$$

$f(\sigma)$ is given by Refs. [46, 47] and σ is the Poisson ratio. The non-equilibrium Gibbs function G* can be minimized with respect to the volume V as:

$$\left[\frac{\partial G(V,P,T)}{\partial V}\right]_{P,T} = 0. \tag{12}$$

By solving equation (12) we obtain the thermal equation of state (EOS) *V (P, T)*. Thermodynamic quantities such as the heat capacities Cv (at constant volume), Cp (at constant pressure) and thermal expansion coefficient α, have been calculated by using the following relations [48];

$$C_V = 3nk\left[4D(\frac{\theta}{T}) - \frac{3\theta/T}{e^{\frac{\theta}{T}-1}}\right], \tag{13}$$

$$C_p = C_V(1 + \alpha\gamma T), \tag{14}$$

$$\alpha = \frac{\gamma C_V}{B_T V}. \tag{15}$$

B_T and γ are respectively the isothermal expansion coefficient and the Grüneisen parameter. Their formulas are given in reference [44].

Figures 6 (a) and (b) show the evolution of bulk modulus in terms of temperature of CdNNi3 and InNNi3 for different values of pressure using GGA approximation. From this figure, we can see that the bulk modulus decreases slowly at low temperature and then rapidly and linearly above 170 K linearly with increasing temperature at a given pressure. However, and at a given temperature, B increases with pressure. For T = 0K, B is minimal for 0 GPa and maximal for 30 GPa, it is evident that the impact of temperature and pressure on the bulk modulus of material are inverse. We can also notice that CdNNi3 is hardest than InNNi3. Also, in Figure 6 (c) and (d), we report the variation of bulk modulus versus pressure at different temperatures for the two compounds, we can see that B increase linearly with pressures.

In Figure 7 (a) and (b), we give the variation of the lattice constant a0 as a function of temperatures for different pressures. We can notice that it stills constant until 170 K, after it increases linearly with temperature, however, a0 decreases with increasing pressure (Fig. 7 (c) and (d)). The tendencies are the same for the two compounds.

The thermal expansion coefficient α was calculated to reflect the temperature dependence of the volume. The calculated thermal expansion coefficient of CdNNi3 and InNNi3 as a function of temperature and pressure is shown in Fig. 8 (a) and (b). It is clear that the thermal expansion coefficient α rapidly increases with Tup to 500 K and then it gradually tends to a linear increase for higher temperatures, this means that the temperature dependence of α is very small at high temperature. The increase of α with T becomes smaller as pressure increases (Fig. 8 (c) and (d)). The thermal expansion coefficients of the two anti-perovskites exhibit similar tendency but it is larger for InNNi3 comparing with CdNNi3. In conclusion, we have found that the effects of T and P on α are opposite

The heat capacity Cv can be used to analyze vibrational properties of solids and can serve as a connection between microscopic structure and macroscopic thermodynamics property. Appropriately, the specific heat is the change in the internal energy per unit of temperature change. When we provide heat to a material, it will automatically cause an increase of temperature. This latter parameter provides us an insight into its vibrational properties' mandatory for many applications.
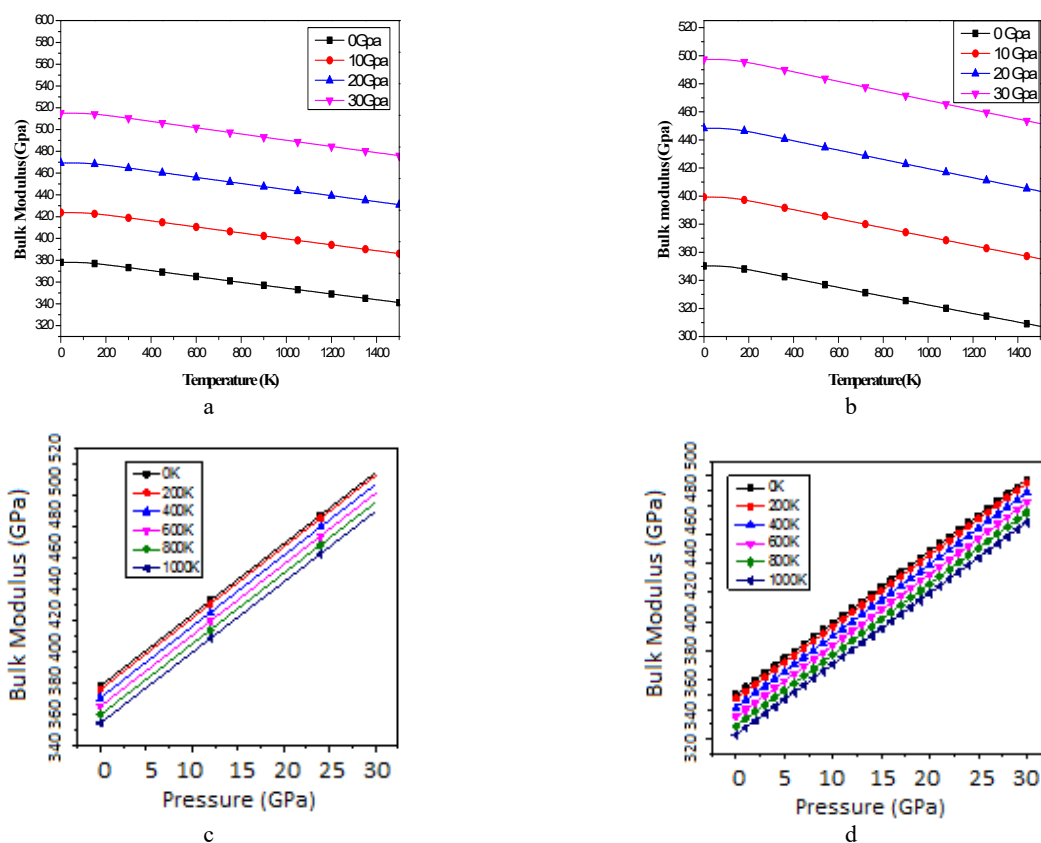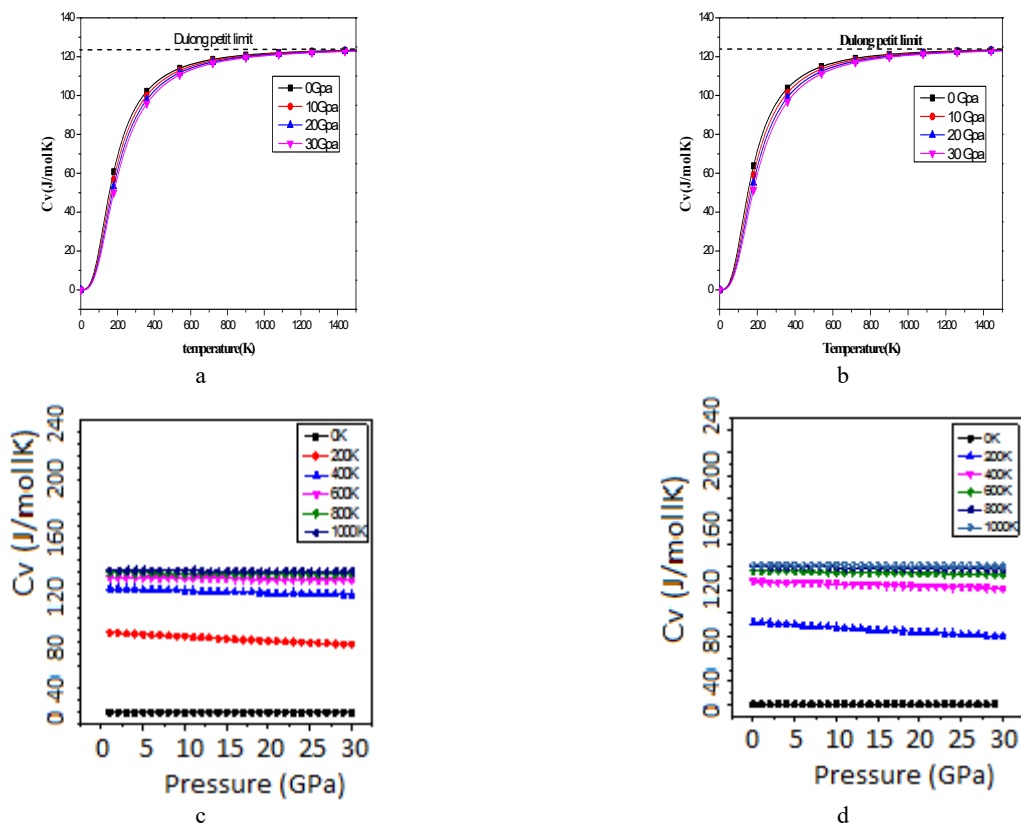
Figure 6. The variation of the bulk modulus. (a) As function of temperature at different pressures for CdNNi$_3$. (b) As function of temperature at different pressures for InNNi$_3$. (c) As function of pressure at different temperatures for CdNNi$_3$. (d) As function of pressure at different temperatures for InNNi$_3$
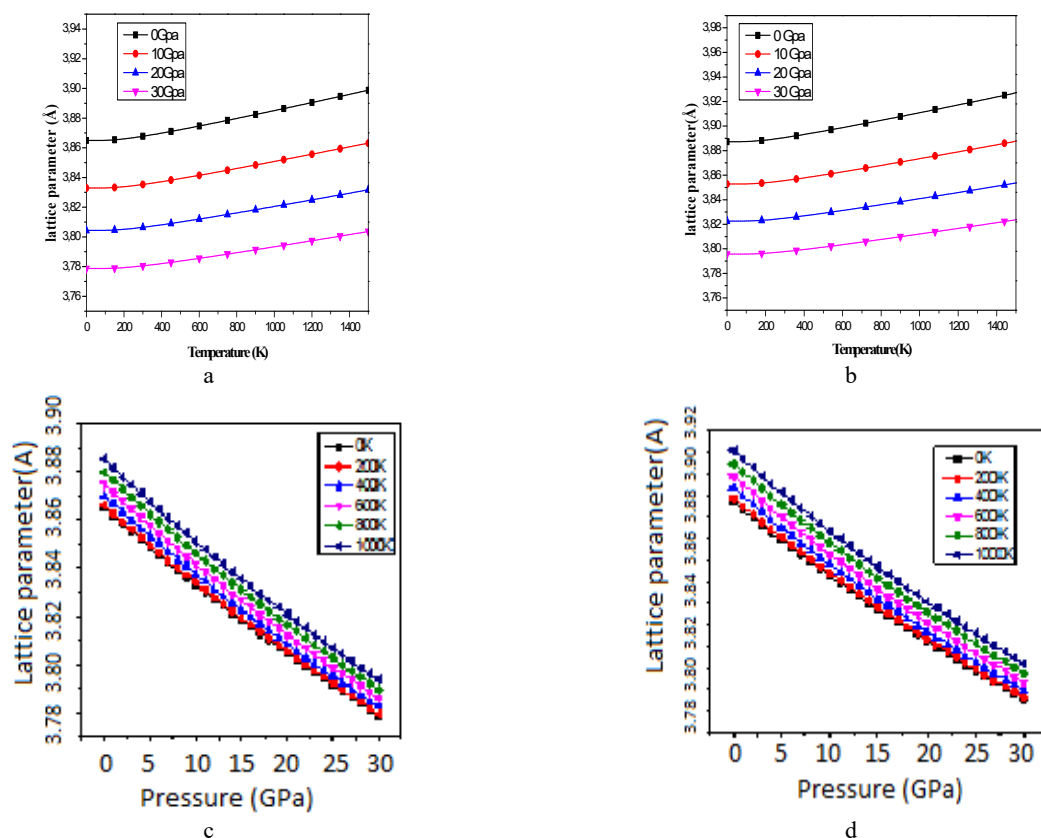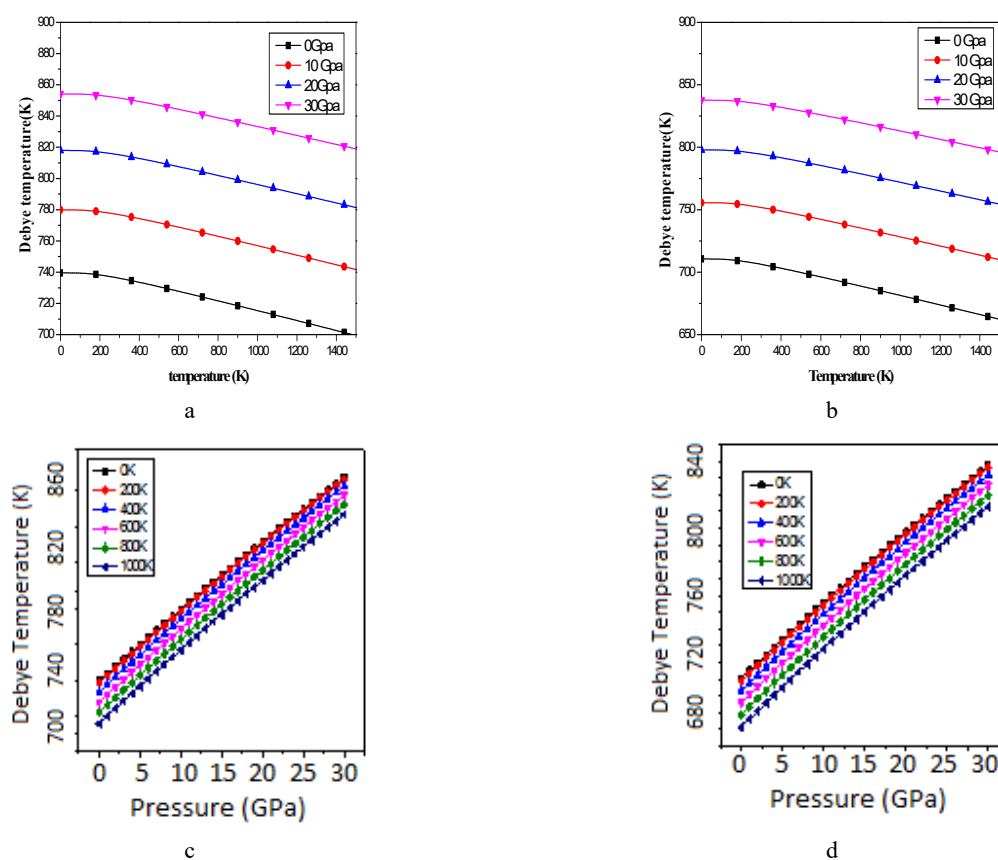

Figure 7. The variation of lattice parameter. (a) as function of temperature at different pressures for CdNNi$_3$. (b) as function of temperature at different pressures for InNNi$_3$. (c) as function of pressure at different temperatures for CdNNi$_3$. (d) as function of pressure at different temperatures for InNNi$_3$
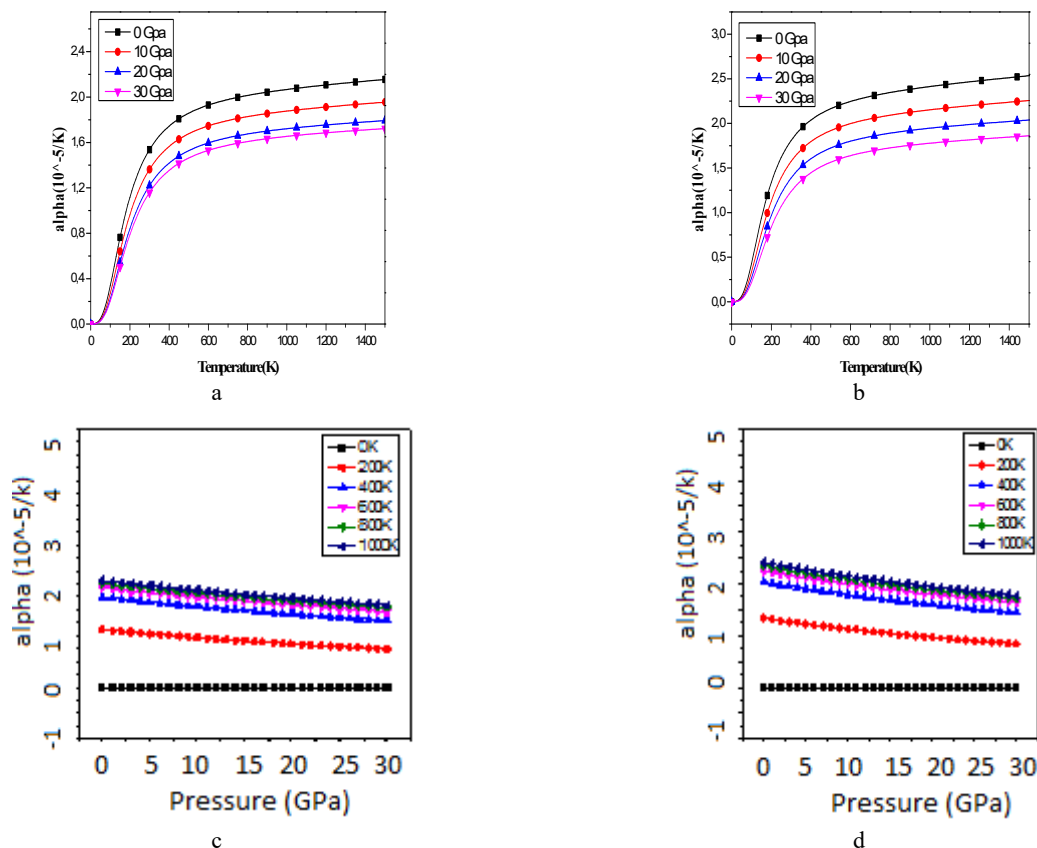
Figure 8. The variation of thermal expansion. (a) as function of temperature at different pressures for CdNNi₃. (b) as function of temperature at different pressures for InNNi₃. (c) as function of pressure at different temperatures for CdNNi₃. (d) as function of pressure at different temperatures for InNNi₃

Figure 9. The variation of heat capacity. (a) as function of temperature at different pressures for CdNNi₃. (b) as function of temperature at different pressures for InNNi₃. (c) as function of pressure at different temperatures for CdNNi₃. (d) as function of pressure at different temperatures for InNNi₃

We present in Fig. 9 (a) and (b), the variation of the heat capacity C_V at constant volume versus temperature at 0, 10, 20 and 30 GPa. The variation of C_V for the investigated compound exhibits similar features for the two anti-perovskites. It can be seen that C_V shows a quick increase up to around 500 K, which is due to the anharmonic approximation. At higher temperature (>500 K), the anharmonic effect on Cv is suppressed, and Cv is close to the so-called Dulong-Petit limit [49] at high temperature, which is reasonable to all solids at high temperature, signifying that the thermal energy at high temperature excites all phonon modes. In addition, Fig. 08 indicates that the heat capacity is not affected by the variation of the pressure since the curves are superposed. The two compounds CdNNi₃ and InNNi₃ have similar values of heat capacity.

The Debye temperature θ_D is an important parameter since it determines the thermal characteristics of materials. A higher θ_D implies a higher thermal conductivity and melting temperature. Fig. 10 (a) and (b) display the dependence of the Debye temperature θ_D on temperature at several fixed pressures using GGA approach. CdNNi₃ has high Debye temperatures comparing to InNNi₃. θ_D is almost constant from 0 to 200 K and decreases linearly with increasing temperature especially. The Debye temperature increases with the enhancement of pressure. Our calculated θ_D is 739 K for CdNNi₃ and 710 K for InNNi₃ at T= 0 K and P= 0 GPa.

Figure 10. Variations of Debye temperature. (a) as function of temperature at different pressures for CdNNi₃. (b) as function of temperature at different pressures for InNNi₃. (c) as function of pressure at different temperatures for CdNNi₃. (d) as function of pressure at different temperatures for InNNi₃

3. CONCLUSIONS

In summary, we have performed first principles calculations based on the FPLAPW method within the GGA and LSDA to calculate the structural, electronic and thermodynamic properties of CdNNi₃ and InNNi₃ cubic anti-perovskites. The calculated equilibrium lattice constants of these compounds are in reasonable agreement with the available experimental data. We can see that our compounds are characterized by a high bulk modulus and show high stiffness, which make its very important for technological applications. In addition, the two compounds studied are metallic and non-magnetic which is in good agreement with experimental studies. Using the quasi-harmonic Debye model, we have obtained the pressure and temperature dependence of the bulk modulus, the heat capacity, Debye temperature, and thermal expansion coefficient of CdNNi₃ and InNNi₃. The two compounds CdNNi₃ and InNNi₃ have similar values of heat capacity and CdNNi₃ has high Debye temperatures comparing to InNNi₃.

ORCID
Jounayd Bentounes, https://orcid.org/0000-0003-2660-7102; **Amal Abbad,** https://orcid.org/0009-0006-1622-5564
Wissam Benstaali, https://orcid.org/0000-0003-4634-6210; **Kheira Bahnes,** https://orcid.org/0009-0007-3676-1126
Noureddine Saidi, https://orcid.org/0009-0004-5343-8572

REFERENCES

[1] C. Shang, X. Xiao, and Q. Xu", Coordination chemistry in modulating electronic structures of perovskite-type oxide nanocrystals for oxygen evolution catalysis," Coordination Chemistry Reviews, **485**, 215109(2023). https://doi.org/10.1016/j.ccr.2023.215109

[2] Z.-Y. Chen, N.-Y. Huang, and Q. Xu "Metal halide perovskite materials in photocatalysis: Design strategies and applications," Coordination Chemistry Reviews, **481**, 215031 (2023). https://doi.org/10.1016/j.ccr.2023.215031

[3] C. Ana, C. Dutra, and J.A. Dawson, "Computational Design of Antiperovskite Solid Electrolytes," J. Phys. Chem. C, **127**, 18256-18270(2023). https://doi.org/10.1021/acs.jpcc.3c04953

[4] X. Li, Y. Zhang, W. Kang, Z. Yan, Y. Shen, and J. Huo, "Anti-perovskite nitrides and oxides: Properties and preparation," Computational Materials Science, **225**, 112188 (2023). https://doi.org/10.1016/j.commatsci.2023.112188

[5] H.M.T. Farid, A. Mera, T.I. Al-Muhimeed, A.A. Al-Obaid, H. Albalawi, H.H. Hegazy, S.R. Ejaz, *et al.*, "Optoelectronic and thermoelectric properties of A3AsN (A = Mg, Ca, Sr and Ba) in cubic and orthorhombic phase," Journal of Materials Research and Technology, **13**, 1495 (2021). https://doi.org/10.1016/j.jmrt.2021.05.032

[6] S.O. Volkova, S.P.S. Berdonosov, I.K. Shamova, B. Rahaman, A. Iqbal, T.S. Dasgupta, and A.N. Vasiliev, "Thermal and magnetic properties of $Cu_4O(SeO_3)_3$composed by ferrimagnetic O_2Cu_6units of edge-sharing OCu_4tetrahedra," Journal of Alloys and Compounds, **956**, 170346 (2023). https://doi.org/10.1016/j.jallcom.2023.170346

[7] M. Zhang, Z. Zhang, H. Cao, T. Zhang, H. Yu, J. Du, Y. Shen, *et al.*, "Recent progress in inorganic tin perovskite solar cells," Mater. Today Energy, **23**, 100891 (2022). https://doi.org/10.1016/j.mtener.2021.100891

[8] J.B. Goodenough, W. Gräper, F. Holtzberg, D.L. Huber, R.A. Lefever, J.M. Longo, T.R. McGuire, and S. Methfessel, *Magnetic and other properties of oxides and related compounds*, Landolt–Bornstein, New Series, Group III, vol. 4a, (Springer, Berlin, 1970), pp. 126–275.

[9] K. Haddadi, A. Bouhemadoub, and L. Louail, "Ab initio investigation of the structural, elastic and electronic properties of the anti-perovskite $TlNCa_3$," Solid State Communications, **150**, 932 (2010).https://doi.org/10.1016/j.ssc.2010.02.024

[10] I.R. Shein, and A.L. Ivanovskii, "Electronic band structure and chemical bonding in the new antiperovskites $AsNMg_3$ and $SbNMg_3$", J. Solid State Chem. **177**, 61(2004). https://doi.org/10.1016/S0022-4596(03)00309-8

[11] M. Moakafi, R. Khenata, A. Bouhemadou, F. Semari, A. Reshak, and M. Rabah, "Elastic, Electronic and Optical Properties of Cubic Antiperovskites $SbNCa_3$ and $BiNCa_3$", Comput. Mater. Sci. **46**(4), 1051-1057 (2009). https://doi.org/10.1016/j.commatsci.2009.05.011

[12] A. Bouhemadou, R. Khenata, M. Chegaar, and S. Maabed, "First-principles calculations of structural, elastic, electronic and optical properties of the antiperovskite $AsNMg_3$," Phys. Lett. A, **371**, 337 (2007). https://doi.org/10.1016/j.physleta.2007.06.030

[13] C.M.I. Okoye, "First-principles optical calculations of $AsNMg_3$ and $SbNMg_3$," Mater. Sci. Eng. B,**130**, 101-107 (2006). https://doi.org/10.1016/j.mseb.2006.02.066

[14] F. Gabler, M. Kirchner, W. Schnelle, U. Schwarz, M. Schmitt, H. Rosner, R. Niewa, and Z. Anorg,"$(Sr_3N)E$ and $(Ba_3N)E$ (E = Sb, Bi): Synthesis, Crystal Structures, and Physical Properties," Allg. Chem. **630**, 2292 (2004).https://doi.org/10.1002/zaac.200400256

[15] D.A. Papaconstantopoulos, and W.E. Pickett, "Ternary nitrides BiNCa3 and PbNCa3: Unusual ionic bonding in the antiperovskite structure," Phys. Rev. B, **45**, 4008 (1992). https://doi.org/10.1103/PhysRevB.45.4008

[16] P.R. Vansant, P.E. Van Camp, V.E. Van Doren, and J.L. Martins, "Variable-cell-shape-based structural optimization applied to calcium nitrides", Phys. Rev. B, **57**, 7615 (1998). https://doi.org/10.1103/PhysRevB.57.7615

[17] P.R. Vansant, P.E. Van Camp, V.E. Van Doren, and J.L. Martins, "Electronic Structure and Pressure Dependence for Some Ternary Calcium Nitrides," Phys. Status Solidi (b), **198**, 87 (1996). https://doi.org/10.1002/pssb.2221980112

[18] P.R. Vansant, P.E. Van Camp, V.E. Van Doren, and J.L. Martins, "AsNCa3 at high pressure", Comput. Mater. Sci, **10**, 298 (1998).

[19] B.V. Beznosikov, "Predicted nitrides with an antiperovskite structure", J. Struct. Chem. **44**, 885-888 (2003). https://doi.org/10.1023/B:JORY.0000029831.93738.b1

[20] K. Haddadi, A. Bouhemadou, L. Louail, S. Maabed, and D. Maouche, "Structural and elastic properties under pressure effect of the cubic antiperovskite compounds ANCa 3(A = P, As, Sb, and Bi)," Phys. Lett. A, **373**, 1777-1781 (2009). https://doi.org/10.1016/j.physleta.2009.03.016

[21] K. Haddadi, A. Bouhemadou, L. Louail, and Y. Medkour, "Structural, elastic and electronic properties of XNCa3 (X = Ge, Sn and Pb) compounds," Solid State Commun. **149**, 619 (2009). https://doi.org/10.1016/j.ssc.2009.01.025

[22] I. Ahmad, S.J. Asadabadi, A. Bouhemadou, M. Bilal, R. Ahmad, "Electronic Properties of Antiperovskite Materials from State-of-the-Art Density Functional Theory," Journal of Chemistry, **2**, 1(2015). https://doi.org/10.1155/2015/495131

[23] K. Haddadi, A. Bouhemadou, L. Louail, F. Rahal, and S. Maabed, "Prediction study of the structural, elastic and electronic properties of ANSr3 (A= As, Sb and Bi)," Comput. Mater. Sci.46, 881-886 (2009). https://doi.org/10.1016/j.commatsci.2009.04.028

[24] W. Kohn, and L.S. Sham, "Self-Consistent Equations Including Exchange and Correlation Effects," Phys. Rev. A, **140**, 1133 (1965). https://doi.org/10.1103/PhysRev.140.A1133

[25] K. Schwarz, and P. Blaha, "Solid state calculations using WIEN2k", Computational Materials Science, **28**, 259-273 (2003). https://doi.org/10.1016/S0927-0256(03)00112-5

[26] P. Blaha, K. Schwarz, G.K.H. Madsen, D. Kvasnicka, and J. Luitz, *WIEN2K-An Augmented plane wave & Local Orbital Program for Calculating Crystal Properties*, (Techn. Universitat Wien, Austria, 2001).

[27] O.K. Andersen, "Linear methods in band theory," Phys. Rev. B, **12**, 3060 (1975). https://doi.org/10.1103/PhysRevB.12.3060

[28] C.J. Howard, B. J. Kennedy, and B.C. Chakoumakos, "Neutron powder diffraction study of rhombohedral rare-earth aluminates and the rhombohedral to cubic phase transition," Journal of Physics-Condensed Matter, **12**, 349 (2000). https://doi.org/10.1088/0953-8984/12/4/301

[29] F.D. Murnaghan, "The Compressibility of Media under Extreme Pressures," Proc. Natl. Acad. Sci. USA, **30**, 5390 (1944). https://www.ncbi.nlm.nih.gov/pmc/articles/PMC1078704/pdf/pnas01666-0028.pdf

[30] J.P. Perdew, A. Ruzsinszky, G.I. Csonka, O.A. Vydrov, G.E. Scuseria, L.A. Constantin, X. Zhou, and K. Burke, "Restoring the Density-Gradient Expansion for Exchange in Solids and Surfaces," Phys. Rev. Lett. **100**, 136406 (2008). https://doi.org/10.1103/PhysRevLett.100.136406

[31] U. Von Barth, and L. Hedin, "A local exchange-correlation potential for the spin polarized case," J. Phys C: Solid State Phys. **5**, 1629 (1972). https://doi.org/10.1088/0022-3719/5/13/012

[32] W.H. Cao, B. He, C.Z. Liao, L.H. Yang, L.M. Zeng, and C. Dong, "Preparation and properties of antiperovskite-type nitrides: InNNi₃ and InNCo3," J. Solid State Chem. **182**, 3353-3357 (2009). https://doi.org/10.1016/j.jssc.2009.10.002

[33] M. Uehara, A. Uehara, K. Kozawa, T. Yamazaki, and Y. Kimishima, "New antiperovskite superconductor ZnNNi3, and related compounds CdNNi₃ and InNNi₃," Physica C, **470**, 688 (2010). https://doi.org/10.1016/j.physc.2009.11.131

[34] Z.F. Hou, "Elastic properties and electronic structures of antiperovskite-type InNCo3 and IInNNi₃," Solid State Communications **150**, 1874-1879 (2010). https://doi.org/10.1016/j.ssc.2010.07.047

[35] V. Kanchana, G. Vaitheeswaran, A. Svane, and A. Delin, "First-principles study of elastic properties of CeO2, ThO2 and PoO2", J. Phys. Condens. Matter, **18**, 9615 (2006). https://doi.org/10.1088/0953-8984/18/42/008

[36] B. Ghebouli, M.A. Ghebouli, A. Bouhemadou, M. Fatmi, R. Khenata, D. Rached, T. Ouahrani, and S. Bin-Omran, "Theoretical prediction of the structural, elastic, electronic, optical and thermal properties of the cubic perovskites CsXF3 (X = Ca, Sr and Hg) under pressure effect," Solid State Sciences, **14**, 903-913 (2012). https://doi.org/10.1016/j.solidstatesciences.2012.04.019

[37] F. El Haj Hassan, and H. Akbarzadeh, "Ground state properties and structural phase transition of beryllium chalcogenides," Comput. Mater. Sci. **35**, 423 (2006). https://doi.org/10.1016/j.commatsci.2005.02.010

[38] R. Khenata, A. Bouhemadou, M. Sahnoun, Ali.H. Reshak, H. Baltache, and M. Rabah, "Elastic, electronic and optical properties of ZnS, ZnSe and ZnTe under pressure", Comput. Mater. Sci. **38**, 29 (2006). https://doi.org/10.1016/j.commatsci.2006.01.013

[39] A. Bouhemadou, R. Khenata, M. Kharoubi, T. Seddik, A.H. Reshak, and Y. Al-Douri, "FP-APW + lo calculations of the elastic properties in zinc-blende III-P compounds under pressure effects," Comput. Mater. Sci. **45**, 474 (2009). https://doi.org/10.1016/j.commatsci.2008.11.013

[40] M. Born, and K. Huang, *Dynamical Theory of Crystal Lattices*, (Clarendon, Oxford, 1956).

[41] J.P. Watt, and L. Peselnick, "Clarification of the Hashin-Shtrikman bounds on the effective elastic moduli of polycrystals with hexagonal, trigonal, and tetragonal symmetries," J. Appl. Phys. **51**, 1525(1980).

[42] S.F. Pugh, "Relations between the elastic moduli and the plastic properties of polycrystalline pure metals," Philos. Mag. **45**, 823-843 (1954). https://doi.org/10.1080/14786440808520496

[43] M.A. Blanco, E. Francisco, and V. Luaña, "GIBBS: isothermal-isobaric thermodynamics of solids from energy curves using a quasi-harmonic Debye model," Comput. Phys. Commun. **158**, 57 (2004). https://doi.org/10.1016/j.comphy.2003.12.001

[44] M.A. Blanco, A.M. Pendás, E. Francisco, J. M. Recio, and R. Franco, "Thermodynamical properties of solids from microscopic theory: applications to MgF₂ and Al₂O₃," J. Mol. Struct. Theochem. **368**, 245 (1996). https://doi.org/10.1016/S0166-1280(96)90571-0

[45] M. Flórez, J.M. Recio, E. Francisco, M.A. Blanco, and A.M. Pendás, "First-principles study of the rocksalt–cesium chloride relative phase stability in alkali halides,", Phys. Rev. B, **66**, 144112 (2002). https://doi.org/10.1103/PhysRevB.66.144112

[46] E. Francisco, J.M. Recio, M.A. Blanco, A. Martín Pendás, and A. Costalesm, "Quantum-Mechanical Study of Thermodynamic and Bonding Properties of MgF2," J. Phys. Chem. A, **102**, 1595-1601 (1998). https://doi.org/10.1021/jp972516j

[47] E. Francisco, M.A. Blanco, and G. Sanjurjo, "Atomistic simulation of SrF2 polymorphs," Phys. Rev. B, **63**, 094107 (2001). https://doi.org/10.1103/PhysRevB.63.094107

[48] R. Hill, "The Elastic Behaviour of a Crystalline Aggregate," Proc. Phys. Soc. London A, **65**, 349 (1952). https://doi.org/10.1088/0370-1298/65/5/307

[49] A.T. Petit, and P.L. Dulong, "Recherches de la Theorie de la Chaleur," Ann. Chim. Phys. **10**, 395 (1819).

ДОСЛІДЖЕННЯ ПРУЖНИХ, МАГНІТНИХ, ТЕРМОДИНАМІЧНИХ ТА ЕЛЕКТРОННИХ ВЛАСТИВОСТЕЙ КУБІЧНИХ АНТИПЕРОВСКІТІВ XNNi3 (X: Cd, In)

Жонаід Бентунес[a], Амал Аббад[b], Віссам Бенстаалі[b], Хейра Бахнес[b], Нуреддін Саїді[b]

[a]Факультет точних наук і комп'ютерних наук, Університет Абдельхаміда Ібн Бадіса, Мостаганем (27000), Алжир
[b]Лабораторія технології та властивостей твердих тіл, факультет природничих наук і технологій, BP227, Університет Абдельхаміда Ібн Бадіса, Мостаганем (27000), Алжир

Теорія функціонала густини використовується для дослідження структурних, електронних, термодинамічних і магнітних властивостей кубічних антиперовскітів InNNi₃ і CdNNi₃. Пружні та електронні властивості були визначені за допомогою підходів узагальненої градієнтної апроксимації (GGA) та локальної спінової апроксимації (LSDA). Для вивчення теплових і вібраційних ефектів використовується квазігармонічна модель Дебая з використанням набору розрахунків повної енергії та об'єму. Результати показують, що дві сполуки є міцними пластичними та задовольняють критерії Борна-Хуанга, тому вони механічно стабільні за нормальних умов. Електронні властивості показують, що дві досліджувані сполуки є металевими та немагнітними. Було передбачено тепловий вплив на об'ємний модуль, теплоємність, теплове розширення та температуру Дебая.

Ключові слова: *антиперовскіти; структура електронної смуги; пружні константи; розрахунки перших принципів; термодинамічні властивості*

STRUCTURAL, DIELECTRIC AND MAGNETIC PROPERTIES OF EPITAXIAL GROWN YMn$_{0.5}$Cr$_{0.5}$O$_3$ THIN FILMS

⊙A. Rambabu[a]*, ⊙G. Jeevana Mounika[b], K. Jayadev[c], B. Sridhar[d]

[a]*Department of Basic Sciences and Humanities, GMR Institute of Technology, Rajam, Andhra Pradesh, India-532127*
[b]*Department of Physics, Government Degree College, Chintalapudi, Eluru, Andhra Pradesh, India-534460*
[c]*Department of Physics, P. R Government College (A), Kakinada, Andhra Pradesh, India-533003*
[d]*Department of Physics, RGUKT Srikakulam, Andhra Pradesh, India-521202*
Corresponding Author e-mail: rambabu.a@gmrit.edu.in

YCr$_{(1-x)}$Mn$_x$O$_3$ is an intriguing member of the perovskite family, attracting significant interest due to its versatile properties and potential applications in various fields. Epitaxial orthorhombic YMn$_{0.5}$Cr$_{0.5}$O$_3$ films are grown on STO substrates by pulsed laser deposition method. Well crystalline with (0 ℓ 0) orientation of YMn$_{0.5}$Cr$_{0.5}$O$_3$ films are identified by X-ray diffraction. Field emission scanning electron microscopy used to capture the morphological behavior of crystalline YMn$_{0.5}$Cr$_{0.5}$O$_3$ films. Temperature dependent dielectric properties are analyzed thoroughly. The magnetic properties of YMn$_{0.5}$Cr$_{0.5}$O$_3$ films are characterized using physical property measurement system. There is a clear magnetic transition observed around 60K for three YMn$_{0.5}$Cr$_{0.5}$O$_3$ films. Films deposited at 600ºC exhibited high dielectric and magnetic properties.

Keywords: *Thin films; Multiferroics; Dielectric properties; Magnetic properties*
PACS: 61.05.-a, 77.22.-d, 78.66.-w

INTRODUCTION

Multiferroics are the materials which exhibits both the ferroelectric and ferromagnetic properties together, have gained much interest due to possibility of significant applications such as sensors, telecommunications, and non-volatile memory devices etc. From past few years, the extensive work has been going on different material compounds (BiFeO$_3$, YMnO$_3$ and GaFeO$_3$) in order to explore the multiferroics properties [1-3]. In addition to these materials, recently, rare-earth chromites (RCrO$_3$, R = Y, Ho, Er, Yb) have found to exhibit the multiferroic properties due to antiferromagnetic nature and local non-centrosymmetric behavior [4-6]. These multiferroic properties are extracted from the interaction between rare-earths (R^{3+}) and chromium (Cr^{3+}) cations. Among the rare-earth orthochromites YCr$_{(1-x)}$Mn$_x$O$_{3,}$ have exhibited the temperature dependence of magnetic, ferroelectric and dielectric properties due to spin-phonon coupling. YCr$_{(1-x)}$Mn$_x$O$_3$, a derivative of the well-known perovskite YCrO$_3$, has emerged as a fascinating material in the field of materials science due to its diverse and tunable properties [7-8]. The broad spectrum of potential applications and the ability to fine-tune the properties of YCr$_{(1-x)}$Mn$_x$O$_3$ by adjusting the Mn concentration underscore its significance. As researchers continue to develop into its complexities, this material stands out as a promising candidate for next-generation technologies. Its adaptability and multifunctionality position of YCr$_{(1-x)}$Mn$_x$O$_3$ at the forefront of materials science, promising exciting developments in both fundamental research and practical applications. Studies have been carried out with YCr$_{(1-x)}$Mn$_x$O$_3$ in bulk ceramic form, Sinha *et al* studied the electric and optical properties of YCr$_{(1-x)}$Mn$_x$O$_3$ nanoparticles [9]. Zhang et.al, explored the effect of Mn content on electric properties and activation energy [10]. Rajeswaran et.al, studied the ferroelectric and ferromagnetic properties [11]. However there haven't been many studies on thin film form of YCr$_{(1-x)}$Mn$_x$O$_3$. Properties in thin film form are strongly related to microstructural and thickness. For example, BiFeO$_3$ exhibits the ferroelectric behavior in thin films rather than to bulk form. Hence it important to study YCr$_{(1-x)}$Mn$_x$O$_3$ in thin film form in order to explore multiferroic behavior in detail. There are different methods, such as physical vapor deposition methods (RF sputtering, pulsed laser deposition, evaporation etc,), chemical vapor deposition techniques (sol-gel, hydrothermal, combustion synthesis etc.). Pulsed laser deposition is the most suitable technique among all the others for compounds deposition to obtain stoichiometrically balanced thin films. This manuscript discusses the temperature dependence of dielectric and magnetic characteristics, as well as morphological studies, and describes fabrication single phase epitaxial YCr$_{(1-x)}$Mn$_x$O$_3$ thin films.

EXPERIMENTAL

Polycrystalline YCr$_{0.5}$Mn$_{0.5}$O$_3$ bulk powder samples were synthesized by solid state method with help of the stoichiometric compounds such as Y$_2$O$_3$, Cr$_3$O$_3$ and Mn$_2$O$_3$ at 1400 ºC about 40 h with grinding at different interval of time. X-ray diffraction technique used to confirm the phase purity of final powder samples. These crystalline YCr$_{0.5}$Mn$_{0.5}$O$_3$ powders were pressed and sintered at various temperatures in order to get good densification for the sputtering target compound. Highly densified (95%) target was used to deposit the thin films. The pulsed laser deposition method was used to deposit YCr$_{0.5}$Mn$_{0.5}$O$_3$ thin films on STO substrates at different temperatures. Prior to deposition,

high vacuum (10x^{-5} Torr) was created using turbo molecular pump in order to avoid the impurities in the films. Mixture of oxygen; argon atmosphere was maintained during the thin film deposition. Thin film deposition optimized condition is tabulated in Table 1. Deposited thin films crystalline nature and phase purity was examined by X-ray diffractometer (Bruker D8 advanced diffractometer). Grain size, shape and surface morphology studies were obtained from FE-SEM (Car Zeiss, Ultra 55). QD-PPMS-6600 was used to study the magnetic measurements of YCr$_{0.5}$Mn$_{0.5}$O$_3$ thin films. LCR meter and electrometer was used to study the dielectric properties of YCr$_{0.5}$Mn$_{0.5}$O$_3$ thin films.

Table 1. Dielectric constant and loss tangent at various deposition temperatures.

S.No	Deposition temperature	Dielectric constant	Loss tangent
1	500 °C	161	1.2
2	600 °C	183	0.8
3	700 °C	165	0.85

RESULTS AND DISCUSSION
Structural properties

Figure 1(a-c) shows the X-ray diffraction pattern of the YCr$_{0.5}$Mn$_{0.5}$O$_3$ thin films deposited at various temperatures (500–700°C) on STO (0 ℓ 0) oriented substrates.
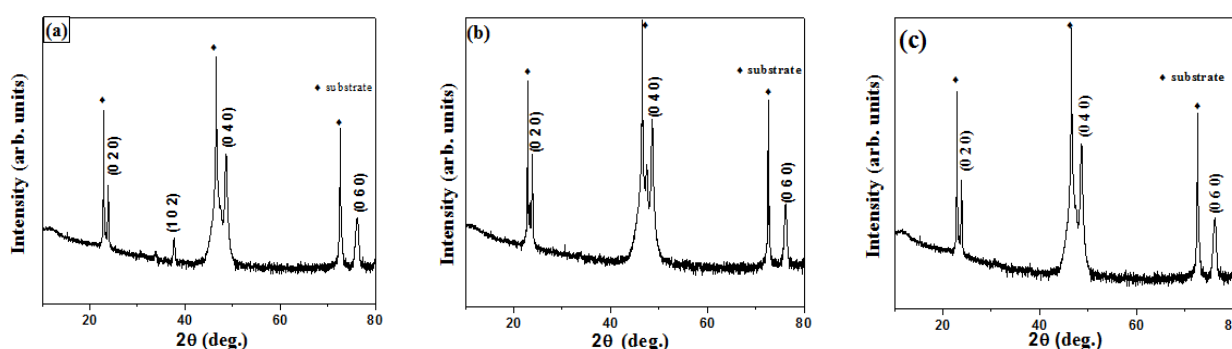
Figure 1. X-ray diffraction pattern of YCr$_{0.5}$Mn$_{0.5}$O$_3$ thin films deposited at (a) 500°C (b) 600°C (c) 700°C

As it was observed from Figure 1, all the films were crystallized into orthorhombic structure (*pnma*) with (0 ℓ 0) orientation which indicates that the epitaxial nature of the films. Films deposited at 500°C exhibited crystalline nature and epitaxial grown along with other peaks from (1 0 2) reflections due to low annealing temperature. Films deposited at 600°C and above exhibited good crystalline nature and perfect epitaxial growth without any other peaks. The X-ray diffraction patterns demonstrates that the films exhibited crystalline nature and phase purity without any secondary phases. The lattice parameters of YCr$_{0.5}$Mn$_{0.5}$O$_3$ thin films and STO substrates are nearly same which results in films were grown in (0 2 0) (0 4 0) and (0 6 0) orientations.

$$D = \frac{k\,\lambda}{\beta cos\theta}. \qquad (1)$$

Scherer's equation was used to calculate the crystallite size of the thin films. Formula description was provided by A Rambabu et.al [12]. The crystallite values are estimated for films deposited at 500°C, 600°C and 700°C are 25, 33 and 45 nm respectively.

Morphological studies

Figure 2(a-c) showed the surface morphology images of the YCr$_{0.5}$Mn$_{0.5}$O$_3$ thin films deposited at different temperature (500–700°C) obtained from field emission scanning electron microscopy. Films deposited at 500°C shows relatively uniform distribution of grains with smooth spherical morphology and closely packed. However, grain size is around 80 nm due low annealing temperature. Films deposited at 600°C exhibits the grain size is around 110 nm with good packing density. On other hand, films deposited at 700°C morphology has less dense and separation between the grains is more due to high temperature treatment during thin film deposition.
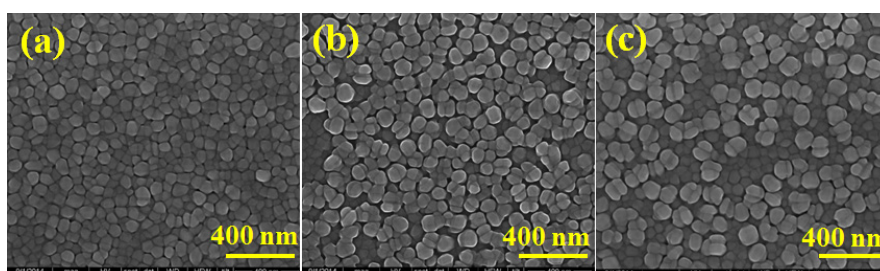
Figure 2(a-c). Surface morphology images of YCr$_{0.5}$Mn$_{0.5}$O$_3$ thin films deposited at (a) 500°C (b) 600°C and (c) 700°C

Dielectric properties

Temperature dependent dielectric properties of $YCr_{0.5}Mn_{0.5}O_3$ thin films deposited at various temperatures are shown in Figure 3(a-f). These dielectric measurements were carried out at different frequencies (50 KHz, 100 KHz, 500 KHz and 1 MHz) for all three $YCr_{0.5}Mn_{0.5}O_3$ films. Dielectric properties revealed that the $YCr_{0.5}Mn_{0.5}O_3$ thin films are invariable dependent on temperature as well as frequency. The dielectric constant increases with temperature, peaking at around 300K temperature and then slowly decreases. On other hand, as the frequency increases, dielectric constant decreases as it noticeable significance in multiferroic/dielectric materials. This behavior was consistent across all the frequencies and for all the thin films. There is clear temperature dependent relaxation was observed around 300K for all $YCr_{0.5}Mn_{0.5}O_3$ thin films due to a Maxwell-Wagner like effect with dielectric anomaly at 300K. The relaxation (peak broadening) in dielectric constant behavior at 300K is the noteworthy characteristic of typical relaxor behavior of the bulk ceramic samples, which have reported by many authors [13-15]. Similar effect was observed in case of dielectric losses as well. The presence of dielectric anomaly at T_N, indicates that the magneto dielectric effect. It is surprising to see this magneto dielectric effect in $YCr_{0.5}Mn_{0.5}O_3$ thin films, which was not observed even in $YFeO_3$ and $YCrO_3$ compounds. Films deposited at 600°C exhibited the highest dielectric properties compared to films deposited at 500 and 700°C. These results are well supporting to structural and morphological studies. The dielectric constant and loss tangent values for three $YCr_{0.5}Mn_{0.5}O_3$ thin films are tabulated in table 1 for the frequency at 50 KHz. Films deposited at 500°C exhibited the less dielectric properties due to less crystallization nature. Similarly, films deposited at 700°C showed the less dielectric properties to due to poor densification and oxygen losses at high temperatures. Overall, films deposited at 600°C showed good dielectric properties which are favorable to device applications.
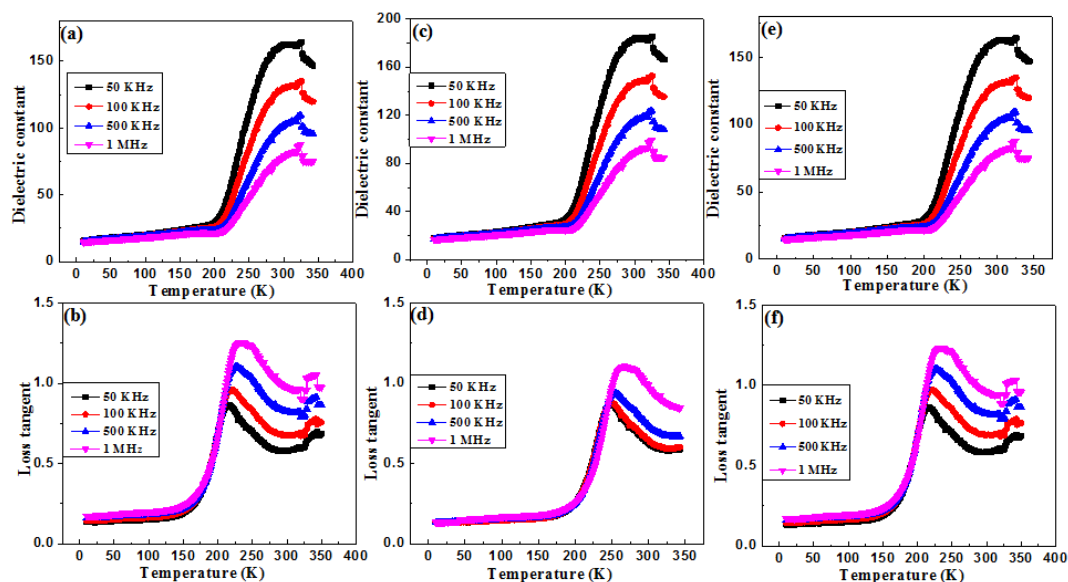
Figure 3 (a-b). Dielectric constant and loss tangent of $YCr_{0.5}Mn_{0.5}O_3$ thin films deposited at 500°C (c-d) Dielectric constant and loss tangent of $YCr_{0.5}Mn_{0.5}O_3$ thin films deposited at 600°C (e-f) Dielectric constant and loss tangent of $YCr_{0.5}Mn_{0.5}O_3$ thin films deposited at 700°C

Magnetic properties

Magnetic properties of $YCr_{0.5}Mn_{0.5}O_3$ thin films are shown in Figure 4 (a-f). Figure 4(a) indicates the magnetization of hysteresis curve in the range of ±5T magnetic field. The hysteresis curve showed inferred loop with well symmetric along the field axis and exhibited no proper saturation. This indicates that films deposited at 500°C exhibits the weak ferromagnetism. Figure 4(c) shows the hysteresis curve for the films deposited at 600°C. It's clear from the curve that the magnetization properties of $YCr_{0.5}Mn_{0.5}O_3$ thin films are enhanced with well saturation. This indicates that anti-ferromagnetism behavior decreases and exhibits the strong ferromagnetic behavior [16-17]. However, films deposited at 700 °C exhibited weak anti-ferromagnetism and ferromagnetism due to pores created at high fabrication temperature, which supports the structural and morphological studies. Overall, films deposited at 600°C, exhibited superior magnetic properties compared with films deposited at 500°C and 700°C. Figure 4 (b, d, f) displays the temperature dependent field cooled magnetization of $YCr_{0.5}Mn_{0.5}O_3$ thin films at an applied field of 100 Oe in a temperature range from 0 – 400°K. The clear magnetization transition was observed for the $YCr_{0.5}Mn_{0.5}O_3$ thin films deposited at different temperatures. The transition exhibited at 67,55 and 59 K for films deposited at 500°C, 600°C and 700°C respectively. It's surprising to observe the transition temperature decreased compared to pristine $YCrO_3$. This is attributed due to double exchange interaction between Mn^{4+}/Cr^{3+} and Mn^{3+} ions [18-19]. This kind of mechanism reveals that the weakening of antiferromagnetic interaction among Cr^{3+} ions and develops the ferromagnetic behavior which results in decrease in Neel temperature [20]. Properties of the films deposited at 600°C exhibited the favorable ferromagnetic behavior with low Neel temperature.
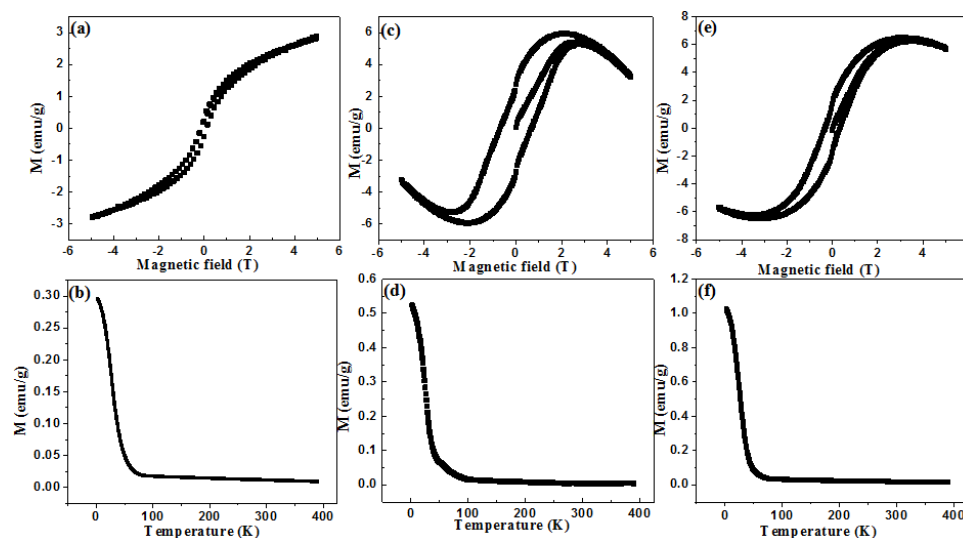
Figure 4 (a-f). Magnetic moment of YCr$_{0.5}$Mn$_{0.5}$O$_3$ thin films deposited at 500°C with respect to:
(a) magnetic field (b) temperature; magnetic moment of YCr$_{0.5}$Mn$_{0.5}$O$_3$ thin films deposited at 600°C with respect to (c) magnetic field (d) temperature; magnetic moment of YCr$_{0.5}$Mn$_{0.5}$O$_3$ thin films deposited at 700°C with respect to (e) magnetic field (f) temperature (measured temperature 2K)

CONCLUSIONS

In summary, we have successfully fabricated the epitaxial grown YCr$_{0.5}$Mn$_{0.5}$O$_3$ thin films on STO substrates using pulsed laser deposition. Dielectric and magnetic properties of YCr$_{0.5}$Mn$_{0.5}$O$_3$ thin films at low temperatures were studied. Films deposited at 600°C exhibited superior dielectric properties with relaxer behavior. Substitution of Mn$^{4+/3+}$ ions result in weakening of antiferromagnetic nature and strengthening of ferromagnetic behavior. These results indicates that the careful optimized YCr$_{0.5}$Mn$_{0.5}$O$_3$ thin film are favorable for fabrication of multistate memory and spintronic devices.

Declaration of Competing Interest
The authors declare that they have no known competing financial interests or personal relationships that could have appeared to influence the work reported in this paper

ORCID
A. Rambabu, https://orcid.org/0000-0001-5562-3334, **G. Jeevana Mounika,** https://orcid.org/0009-0002-1854-5941

REFERENCES
[1] Y. Zhua, K. Suna, S. Wub, P. Zhoua, Y. Fua, J. Xiaa, and H.-F. Lia, "A comprehensive review on the ferroelectric orthochromates: Synthesis, property, and application," Coordination Chemistry Reviews, **475**, 214873 (2023). https://doi.org/10.1016/j.ccr.2022.214873.
[2] T. Choi, Y. Horibe, H.T. Yi, Y.J. Choi, W. Wu, and S.-W. Cheong, "Insulating interlocked ferroelectric and structural antiphase domain walls in multiferroic YMnO₃," Nat. Mater. **9**, 253–258 (2010). https://doi.org/10.1038/nmat2632
[3] S. Mukherjee, A. Roy, S. Auluck, R. Prasad, R. Gupta, and A. Garg, "Room Temperature Nanoscale Ferroelectricity in Magnetoelectric GaFeO3 Epitaxial Thin Films," Phys. Rev. Lett. **111**, 87601 (2013). https://doi.org/10.1103/PhysRevLett.111.087601
[4] N. Panwar, S. Kumar, I. Coondoo, M. Vasundhara, and N. Kumar, "Low temperature magnetic and magnetocaloric studies in YCr₀.₈₅Mn₀.₁₅O₃ ceramic," Physica B: Physics of Condensed Matter, **545**, 352-357 (2018). https://doi.org/10.1016/j.physb.2018.06.038
[5] S. Kumar, I. Coondoo, A. Rao, B.-H. Lu, Y.-K. Kuo, A.L. Kholkin, and N. Panwar, "Impact of low-level praseodymium substitution on the magnetic properties of YCrO₃ orthochromites," Phys. B Condens. Matter, **510**, 104–108 (2017). http://dx.doi.org/10.1016/j.physb.2017.01.003
[6] G.N.P. Oliveira, P. MacHado, A.L. Pires, A.M. Pereira, J.P. Araujo, and A.M.L. Lopes, "Magnetocaloric effect and refrigerant capacity in polycrystalline YCrO₃," J. Phys.Chem. Solids, **91**, 182–188 (2016). https://doi.org/10.1016/j.jpcs.2015.12.012
[7] S. Yin, T. Sauyet, M.S. Seehra, and M. Jain, "Particle size dependence of the magnetic and magneto-caloric properties of HoCrO₃," J. Appl. Phys. **121**, 63902 (2017). https://doi.org/10.1063/1.4975405
[8] H. Wang, X. Liu, K. Sun, X. Ma, H. Guo, I. Bobrikov, Y. Sui, *et al.*, "Competition of ferromagnetism and anti-ferromagnetism in Mn-doped orthorhombic YCrO₃," Journal of Magnetism and Magnetic Materials, **535**, 168022 (2021). https://doi.org/10.1016/j.ccr.2022.214873
[9] R. Sinha, S. Basu, and A.K. Meikap, "Investigation of dielectric and electrical behavior of Mn doped YCrO₃ nanoparticles synthesized by the sol gel method," Phys. E Low-Dimensional Syst. Nanostructures, **69**, 47–55 (2015). https://doi.org/10.1016/j.physe.2015.01.010

[10] B. Zhang, Q. Zhao, A. Chang, Y. Li, Y. Liu, and Y. Wu, "Electrical conductivity anomaly and X-ray photoelectron spectroscopy investigation of $YCr_{1-x}Mn_xO_3$ negative temperature coefficient ceramics," Appl. Phys. Lett. **104**, 102109 (2014). https://doi.org/10.1063/1.4868435

[11] B. Rajeswaran, D.I. Khomskii, A.K. Zvezdin, C.N.R. Rao, and A. Sundaresan, "Fieldinduced polar order at the Néel temperature of chromium in rare-earth orthochromites: Interplay of rare-earth and Cr magnetism," Phys. Rev. B, **86**, 214409 (2012). https://doi.org/10.1103/PhysRevB.86.214409

[12] A. Rambabu, K.C.J. Raju, "The crystalline nature and samarium substitution improves the nanomechanical and microwave dielectric properties of SBTi thin films," Physica B: Condensed Matter, **626**, 413557 (2022). https://doi.org/10.1016/j.physb.2021.413557

[13] K.S. Cole, and R.H. Cole, "Dispersion and Absorption in Dielectrics I. Alternating Current Characteristics," J. Chem. Phys. **9**, 341–351 (1941). https://doi.org/10.1063/1.1750906

[14] A.K. Jonscher, The "universal" dielectric response, Nature. **267**, 673–679 (1977). https://doi.org/10.1038/267673a0

[15] A. Rambabu, and K.C.J. Raju, "Impact of Sm-substitution and microwave sintering on dielectric and mechanical properties of $SrBi_4Ti_4O_{15}$ ceramics," J Mater Sci: Mater Electron, **31**, 19698–19712 (2020). https://doi.org/10.1007/s10854-020-04496-z

[16] A. Durn, A.M. Arvalo-Lpez, E. Castillo-Martnez, M. Garca-Guaderrama, E. Moran, M.P. Cruz, F. Fernndez, and M.A. Alario-Franco, "Magneto-thermal and dielectric properties of biferroic $YCrO_3$ prepared by combustion synthesis," J. Solid State Chem. **183**, 1863–1871 (2010). https://doi.org/10.1016/j.jssc.2010.06.001

[17] Y. Sharma, S. Sahoo, W. Perez, S. Mukherjee, R. Gupta, A. Garg, R. Chatterjee, and R.S. Katiyar, "Phonons and magnetic excitation correlations in weak ferromagnetic $YCrO_3$," J. Appl. Phys. **115**, 0–9 (2014). https://doi.org/10.1063/1.4875099

[18] S. Kumar, I. Coondoo, M. Vasundhara, A.K. Patra, A.L. Kholkin, and N. Panwar, "Magnetization reversal behavior and magnetocaloric effect in $SmCr_{0.85}Mn_{0.15}O_3$ chromites," J. Appl. Phys. **121**, 43907 (2017). https://doi.org/10.1063/1.4974737

[19] C.L. Li, S. Huang, X.X. Li, C. M. Zhu, G. Zerihun, C.Y. Yin, C.L. Lu, and S.L. Yuan, "Negative magnetization induced by Mn doping in $YCrO_3$," J. Magn. Magn. Mater. **432**, 77–81 (2017). https://doi.org/10.1007/s10854-023-10196-1

[20] S. Kumar, I. Coondoo, M. Vasundhara, V.S. Puli, and N. Panwar, "Observation of magnetization reversal and magnetocaloric effect in manganese modified $EuCrO_3$ orthochromites," Phys. B Condens. Matter, **519**, 69–75 (2017). https://doi.org/10.1016/j.physb.2017.05.050

СТРУКТУРНІ, ДІЕЛЕКТРИЧНІ ТА МАГНІТНІ ВЛАСТИВОСТІ ЕПІТАКСІАЛЬНОГО НАРОЩЕННЯ ТОНКИХ ПЛІВОК $YMn_{0,5}Cr_{0,5}O_3$

А. Рамбабу[a], Г. Дживана Муніка[b], К. Джаядев[c], Б. Шрідхар[d]
[a]Відділ фундаментальних та гуманітарних наук, Технологічний інститут GMR, Раджам, Андхра-Прадеш, Індія
[b]Факультет фізики, державний коледж, Чінталапуді, Елуру, Андхра-Прадеш, Індія
[c]Департамент фізики, П.Р. державний коледж (А), Какінада, Андхра-Прадеш, Індія
[d]Департамент фізики, RGUKT Шрикакулам, Андхра-Прадеш, India

$YCr_{(1-x)}Mn_xO_3$ є інтригуючим членом сімейства перовскітів, який привертає значний інтерес завдяки своїм універсальним властивостям і потенційним застосуванням у різних областях. Епітаксіальні орторомбічні плівки $YMn_{0.5}Cr_{0.5}O_3$ вирощені на підкладках STO методом імпульсного лазерного осадження. Добре кристалічні з орієнтацією (0 ℓ 0) плівки $YMn_{0.5}Cr_{0.5}O_3$ ідентифіковані за допомогою рентгенівської дифракції. Полеемісійна скануюча електронна мікроскопія використовується для фіксації морфологічної поведінки кристалічних плівок $YMn_{0.5}Cr_{0.5}O_3$. Температурно залежні діелектричні властивості ретельно аналізуються. Магнітні властивості плівок $YMn_{0.5}Cr_{0.5}O_3$ охарактеризовано за допомогою системи вимірювання фізичних властивостей. Існує чіткий магнітний перехід, який спостерігається близько 60 K для трьох плівок $YMn_{0.5}Cr_{0.5}O_3$. Плівки, нанесені при 600°C, показали високі діелектричні та магнітні властивості.
Ключові слова: *тонкі плівки; мультифероїки; діелектричні властивості; магнітні властивості*

MECHANISM OF CURRENT PERFORMANCE IN THIN-FILM HETEROJUNCTIONS n-CdS/p-Sb₂Se₃ OBTAINED BY THE CMBD METHOD

ⓘT.M. Razykov[a], ⓘK.M. Kuchkarov[a], ⓘA.A. Nasirov[b], ⓘM.P. Pirimmatov[a]*, ⓘR.R. Khurramov[a], ⓘR.T. Yuldashev[a], ⓘD.Z. Isakov[a], M.A. Makhmudov[a], ⓘSh.M. Bobomuradov[a], ⓘK.F. Shakhriyev[a,b]

[a]*Physical and Technical Institute of the Academy of Sciences of the Republic of Uzbekistan, st. Chingiza Aitmatova, 2B, 100084, Tashkent, Uzbekistan*
[b]*National University of Uzbekistan, University named after Mirzo Ulugbek, st. Universitet, 4, 100174, Tashkent, Uzbekistan*
*Corresponding Author e-mail: mpirimmatov@gmail.com

In this work, we analyzed the temperature dependence of the current-voltage characteristics of the structure of glass/Mo/p-Sb₂Se₃/n-CdS/In. From an analysis of the temperature dependences of the direct branches of the I-V characteristic of the heterojunction, it was established that the dominant mechanism of current transfer at low biases ($3kT/e<V<0.8V$) is multi-stage tunneling-recombination processes involving surface states at the Sb₂Se₃/CdS interface. At V>0.8 V, the dominant current transfer mechanism is Newman tunneling. In the case of reverse bias ($3kT/e<V<1.0$ eV), the main mechanism of charge carrier transfer through a heterojunction is tunneling through a potential barrier involving a deep energy level. At higher reverse voltages, a soft breakdown occurs.

Keywords: *Sb₂Se₃ SCR; CMBO; Thin films; Heterostructure; Heterojunction*
PACS: 73.61.Le

INTRODUCTION

Currently, researchers are paying special attention to chalcogenide binary compounds such as Sb₂Se₃, Sb₂S₃, and their solid solutions Sb₂(Sₓ,Se₁₋ₓ)₃ (chemical formula Sb₂X₃) as absorbing layers for solar cells [1]. This interest is due to their favorable physical properties, including p-type conductivity, a band gap (E_g) of 1.1 to 1.8 eV, a high absorption coefficient ($\alpha > 10^5$ cm⁻¹ in the visible region of solar radiation), a low melting point (Sb₂Se₃: 823 K, Sb₂S₃: 885 K), and high partial pressure, which are very similar to the properties of Cu(In,Ga)(Se,S) [2]. Additionally, the constituent elements of these materials are relatively inexpensive, abundant in nature, stable under external influences, and non-toxic [3]. These characteristics make it possible to produce environmentally friendly and efficient solar modules, paving the way for their large-scale industrial production.

At present, the efficiency of thin-film solar cells using Sb₂X₃ compounds ranges from 3% to 10.57% [4]. Although these efficiencies are low for large-scale industrial applications, similar to CdTe and Cu(In,Ga)Se-based solar cells, the theoretical maximum efficiency of Sb₂Se₃ solar cells is approximately 32.23% (Shockley-Queisser limit) [5]. Therefore, there is significant potential to improve the efficiency of these solar cells, which have not yet reached their theoretical maximum. The calculated limit values for open-circuit voltage (U_{OC}), short-circuit current (I_{SC}), and fill factor (FF) for Sb₂Se₃ solar cells are $U_{OC} = 0.935$ V, $I_{SC} = 39.99$ mA/cm², and FF(%) ≤ 87.7%, respectively [5]. To date, the parameters for Sb₂Se₃ solar cells have achieved the following values: $U_{OC} = 0.467$ V, $I_{SC} = 33.52$ mA/cm², and FF(%) ≤ 67% [6]. Over the past six years, there has been a slight increase in open-circuit voltage and fill factor values. Further improvements in solar cell efficiency can be achieved by increasing these parameters.

In our previous studies, we examined the structural and morphological properties of Sb₂Se₃ films obtained by chemical molecular beam deposition (CMBD) from Sb₂Se₃ powders at different substrate temperatures. The results showed that all films were enriched in antimony, exhibited an orthorhombic structure with predominant orientations (120) and (221), and had crystallite sizes ranging from 200 to 300 nm [7–9].

This study investigates the charge transfer mechanism in thin-film Sb₂Se₃/CdS heterostructures, which primarily determines critical solar cell parameters such as short-circuit current and open-circuit voltage.

EXPERIMENTAL PART

Using the method of chemical molecular beam deposition (CMBD), Sb₂Se₃ films (2–3 μm thick) were obtained on glass substrates with a molybdenum coating. The process of obtaining Sb₂Se₃ solid solution films by the CMBD method is described in detail in [10–12]. Subsequently, thin CdS films (80–100 nm thick) were deposited onto the surfaces of the glass and glass/Mo/ substrates using vacuum deposition. These structures were used to fabricate thin-film glass/Mo/Sb₂Se₃/CdS/In heterostructures.

To enhance the electrical and photovoltaic properties, heat treatments were performed on the glass/Mo/Sb₂Se₃/CdS/In thin-film heterostructures in pure argon at a temperature of approximately 200°C for 30 minutes.

Indium contacts were then deposited on the front side of the glass/Mo/Sb$_2$Se$_3$/CdS/In heterostructures via vacuum deposition. To further improve the front contacts, additional thermal annealing was conducted at a temperature of approximately 200°C for 20 minutes in argon.

The current-voltage characteristics of the glass/Mo/Sb$_2$Se$_3$/CdS/In heterostructures were measured using a Keithley SM2460 device. Additionally, the temperature dependences of the current-voltage characteristics at low temperatures (80–300 K) were measured using the van der Pauw method.

RESULTS AND DISCUSSION

Figure 1 shows the forward I-V characteristics of the anisotype p-Sb$_2$Se$_3$/n-CdS heterojunction measured at different temperatures. By extrapolating the linear sections of the I-V characteristic to the intersection with the voltage axis, the potential barrier height of the heterojunction at different temperatures was determined (see inset in Fig. 1). It was found that the temperature dependence of the potential barrier height of the p- Sb$_2$Se$_3$/n-CdS heterostructure is well described by the equation:

$$\varphi_0(T) = \varphi_0(0) - \beta_\varphi(T)T \,, \qquad (1)$$

where $\beta_\varphi = 5.5 \times 10^{-2} \, eV \cdot K^{-1}$ is the temperature coefficient of the potential barrier height, and $\varphi_0(0) = 2.71 \, eV$ is the potential barrier height of the heterostructure at absolute zero temperature (Fig. 2).

It is worth noting that the potential barrier height of the p-Sb$_2$Se$_3$/n-CdS heterojunction at room temperature ($\varphi_k = eV_{bi} = 0.84 \, eV$, where V_{bi} is the built-in potential) significantly exceeds the similar parameter for heterojunctions using the semiconductor p-Sb$_2$Se$_3$/n-CdS or n-type conductivity ($\varphi_k = 0.3 - 0.4 \, eV$) [13, 14]. The higher potential barrier height of the p-Sb$_2$Se$_3$/n-CdS heterojunction is due to the different types of conductivity of the glass and base materials.

The series resistance R_s of the p-Sb$_2$Se$_3$/n-CdS heterostructure can be determined from the slope of the forward branch of the I-V characteristic [15]. It can be seen that in the voltage range greater than the height of the potential barrier, the *(I=f(V))* curves (Fig. 1) transform from an exponential dependence to a linear one. This indicates that the voltage across the barrier regions of the heterojunction ceases to change, i.e., the barrier is practically open, and the current through the heterojunction is limited by its series resistance R_s.
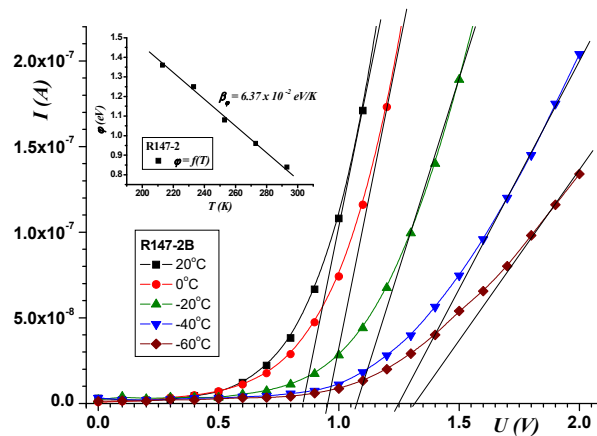
Figure 1. Forward current-voltage (I-V) characteristics of the p-Sb$_2$Se$_3$/n-CdS heterostructure at different temperatures (T). The inset shows the temperature dependence of the potential barrier height (φ_0)
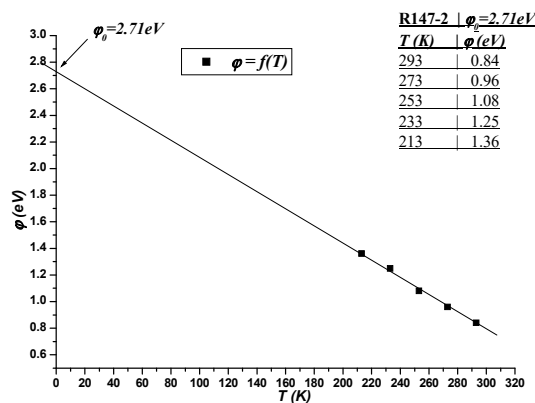
Figure 2. Temperature dependence of the potential barrier height.

To determine the mechanism of current flow, the temperature dependence of the current-voltage (I-V) characteristics of the p-Sb$_2$Se$_3$/n-CdS heterostructure was studied. The temperature dependence of the forward branch of the dark I-V characteristic on a semi-logarithmic scale in the voltage range ($kT/e<V<V_D$) is shown in Fig. 3. The I-V characteristic is described by the equation:

$$I = I_{0_1} \exp(eV/A_1\, kT) + I_{0_2} \exp(eV/A_2\, kT). \tag{2}$$

In the first region, at low voltages $kT/e < V < 0.1\div0.7V$, the exponent of the first exponential is A = 2.21, and in the second region, at higher voltages $0,1\div0,7B \leq V < V_D$ $A_2=1\div1.85.$ ranges from 1 to 1.85. Moreover, the value of the saturation current I_0 decreases with temperature. Therefore, equation (2) can be written as:

$$I = I_0(T)\exp(S_1V) + I_{0_2}(T)\exp(S_2V). \tag{3}$$

Figure 3 shows the dependence of the forward current on temperature at various voltages on a semi-logarithmic scale. It can be seen that the slope of this dependence dI_{np}/dT does not depend on voltage.
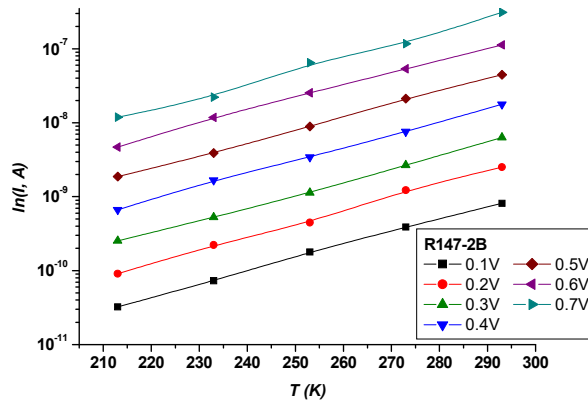
Figure 3. Temperature dependence of the forward current of the p-Sb$_2$Se$_3$/n-CdS heterostructure at various biases of 0.1–0.7 V
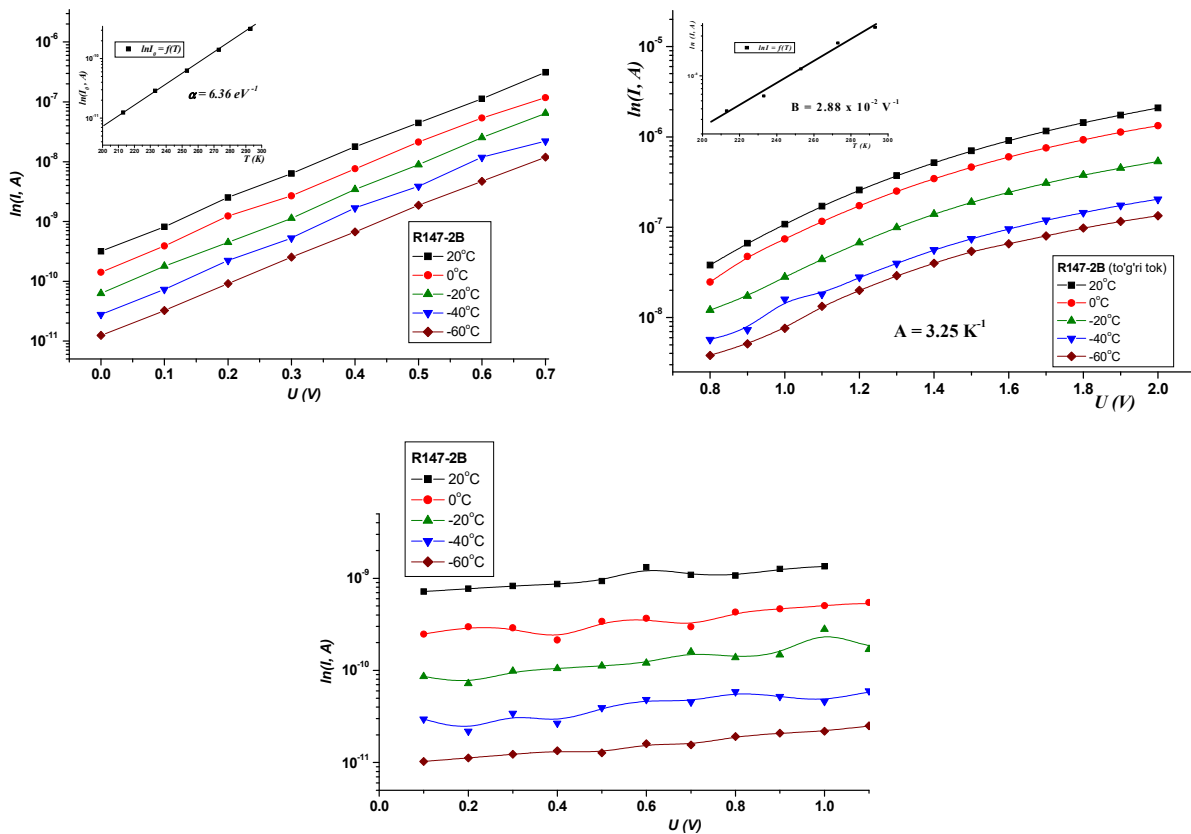
Figure 4. Dark current-voltage characteristics of glass/Mo/p-Sb2Se3/n-CdS/In heterostructures: (a, b) forward current-voltage characteristic, (c) reverse current-voltage characteristic.

Figure 4a shows the forward branches of the current-voltage characteristics of the heterojunction in semi-logarithmic coordinates at different temperatures. In the region of forward biases *V>3kT/e,* straight sections are observed, indicating an exponential dependence of the current on the voltage.

It is worth noting that the slope of the straight sections *(3kT/e<V<0,7B) Δln(I)/ΔV* does not depend on temperature. This circumstance excludes the possibility of analyzing current transfer mechanisms based on generation-recombination processes in the space charge region (SCR), since for this case the temperature dependence of the slope of the rectilinear sections of the current-voltage characteristics should be observed in semi-logarithmic coordinates *Δln(I)/ΔV=e/nkT,* where n is the non-ideality coefficient [16]. The constant slope of the *ln(I)=f(V)* dependences at different temperatures can be considered as evidence of the tunneling nature of the current transfer mechanism [17, 18].

Straight-line sections of the current-voltage characteristic with identical slopes begin at small displacements, at which the SCR is not yet narrow enough for direct tunneling, which is described by the Newman formula [19]. Therefore, the only physically substantiated current transfer mechanism can be considered multi-stage tunneling-recombination processes involving surface states at the p-Sb$_2$Se$_3$/n-CdS interface. In this case, the forward bias current is determined by the following expression [11]:

$$I = B \exp\left(-\alpha(\varphi_0(T) - eV)\right), \tag{4}$$

where B is a quantity that weakly depends on temperature and voltage, and φ_0 is the height of the potential barrier. Rewriting expression (4) in another form:

$$I = B \exp\left(-\alpha(\varphi_0(T)\right) \exp(\alpha eV) = I_0 \exp(\alpha eV), \tag{5}$$

where $I_0 = B \exp\left(-\alpha(\varphi_0(T)\right)$ is the cutoff current, which does not depend on the applied voltage. From expression (4) it is clear that the slope *Δln(I)/ΔV* of the initial sections of the forward branches of the current-voltage characteristic, shown in Fig. 4a, determines the coefficient α, which takes a value of 3.6 eV^{-1}.

From the current-voltage characteristics presented in Fig. 4b, we can qualitatively conclude that the predominant mechanism of carrier transfer in the studied heterostructure is tunneling, and it is described by the empirical formula:

$$I = I_0 \exp(AT + BV), \tag{6}$$

where A and B are experimentally determined quantities that are typical for the tunnel-recombination mechanism of current passage in the heterostructure. Based on the calculation results, it was determined that *A=3,25 K^{-1}* and *B=2.88×10^{-2} B^{-1}.*

The mechanism of current passage at reverse biases *kT/e<V<1.0* is due to the thermal generation of charge carriers in the SCR (Fig. 4c). At higher reverse biases *1<V<5 V,* the tunnel charge transfer mechanism predominates.

CONCLUSION

Thin-film heterostructures based on Sb$_2$Se$_3$ films on borosilicate substrates coated with a molybdenum layer using the CMBD method were obtained. The results of measuring the current-voltage characteristics of the heterostructures showed that after heat treatment, the main parameters (k, φ$_0$, R$_s$) of thin-film glass/Mo/Sb$_2$Se$_3$/CdS heterostructures improved and had the following values: *k≈1·10$^{2÷3}$, R$_s$=80 Ω, α=6.36 eV^{-1}, A=3.25 K^{-1} and B=2.88×10^{-2} V^{-1}, β$_\varphi$=5.7·10^{-2} eV/K, φ≈0.84÷0.95 eV, φ$_0$=2.71 eV, φ=0.4÷0.45 eV,* which will make it possible to produce efficient solar cells based on them.

From an analysis of the temperature dependences of the direct branches of the I-V characteristic of the heterojunction, it was established that the dominant mechanism of current transfer at low biases (*3kT/e<V<0.8V*) is multi-stage tunneling-recombination processes involving surface states at the Sb$_x$Se$_y$/CdS interface. At *V > 0.8B*, the dominant current transfer mechanism is Newman tunneling. In the case of reverse bias (*3kT/e <V < 1.0 eV*), the main mechanism of charge carrier transfer through a heterojunction is tunneling through a potential barrier involving a deep energy level.

ORCID
Takhirdjon. M. Razykov, https://orcid.org/0000-0001-9738-3308; **Kudrat M. Kuchkarov,** https://orcid.org/0000-0002-2238-7205
Abdumanap A. Nasirov, https://orcid.org/0000-0002-7683-5667; **Ruhiddin T. Yuldoshov,** https://orcid.org/0000-0002-7886-1607
Muhammad M. Pirimmatov, https://orcid.org/0009-0000-4829-7817; **Diyorbek Z. Isakov,** https://orcid.org/0000-0003-4314-5683;
Ramozan R. Khurramov, https://orcid.org/0009-0008-1038-0138; **Sherzod M. Bobomuradov,** https://orcid.org/0009-0001-1338-3202
Kuvonchbek F. Shakhriyev, https://orcid.org/0009-0005-4153-9293

REFERENCES
[1] X. Wang, R. Tang, and C. Wu, "Development of antimony sulfide–selenide Sb$_2$(S, Se)$_3$ -based solar cells," Journal of Energy Chemistry, **27**, 713–721 (2018). https://doi.org/10.1016/j.jechem.2017.09.031
[2] N. Selmane, A. Cheknane, F. Khemloul, M.H.S. Helal, and H.S. Hilal, "Cost-saving and performance-enhancement of CuInGaSe solar cells by adding CuZnSnSe as a second absorber," Solar Energy, **234**, 64-80 (2022). https://doi.org/10.1016/j.solener.2022.01.072

[3]   A. Mavlonov, T. Razykov, F. Raziq, *et al*., "A review of Sb$_2$Se$_3$ photovoltaic absorber materials and thin-film solar cells," Solar Energy, **201**, 227-246 (2020). https://doi.org/10.1016/j.solener.2020.03.009

[4]   L. Zhang, C. Wu, W. Liang, and T. Chen, "Low-dimensional antimony selenosulfide as an emerging material for solar cell applications," Energy Lab. **1**, 220016 (2023). https://doi.org/10.54227/elab.20220016

[5]   Mamta, Y. Singh, K.K. Maurya, *et al*., "A review on properties, applications, and deposition techniques of antimony selenide," Solar Energy Materials & Solar Cells, **230**, 111223 (2021). https://doi.org/10.1016/j.solmat.2021.111223

[6]   Y. Zhao, S. Wang, C. Li, *et al*., "Regulating deposition kinetics via a novel additive-assisted chemical bath deposition technology enables fabrication of 10.57%-efficiency Sb$_2$Se$_3$ solar cells," Energy Environ. Sci. **15**, 5118–5128 (2022). https://doi.org/10.1039/D2EE02261C

[7]   T.M. Razykov, K.M. Kuchkarov, M.S. Tivanov, D.S. Bayko, L.S. Lyashenko, B.A. Ergashev, A.A. Mavlonov, *et al*., "Characteristics of thin Sb$_2$Se$_3$ films obtained by the chemical molecular beam deposition method for thin-film solar cells," Thin Solid Films, **774**, 139844 (2023). https://doi.org/10.1016/j.tsf.2023.139844

[8]   M.S. Tivanov, T.M. Razykov, K.M. Kuchkarov, D.S. Bayko, I.A. Kaputskaya, R.T. Yuldoshov, and M.P. Pirimmetov, "Effect of the Sb/Se Ratio on the Structural and Electrical Properties of Sb$_x$Se$_y$ Films," Applied Solar Energy, **59**(5), 595–603 (2023). https://doi.org/10.3103/S0003701X23600959

[9]   T.M. Razykov, K.M. Kuchkarov, B.A. Ergashev, O.M. Tursunkulov, A. Olimov, D. Isakov, M. Makhmudov, and M. Pirimmatov, "Microstructural, Optical, and Electrical Properties of Sb$_2$Se$_3$ Films Fabricated by the CMBD Method for Solar Cells," Applied Solar Energy, **58**(1), 21–27 (2022). https://doi.org/10.3103/S0003701X22010157

[10] T.M. Razykov, J. Bekmirzoev, A. Bosio, B.A. Ergashev, D. Isakov, R. Khurramov, K.M. Kouchkarov, *et al*., "Structural and optical properties of Sb$_x$Se$_y$ thin films obtained by chemical molecular beam deposition method from Sb and Se precursors," Solar Energy, **254**, 67–72 (2023). https://doi.org/10.1016/j.solener.2023.03.010

[11] T.M. Razykov, K.M. Kuchkarova, M.S. Tivanov, B.A. Ergashev, R. Khurramov, D.Z. Isakov, A. Olimov, *et al*., "Structural Properties of Sb$_x$Se$_y$ Thin Films Obtained by CMBD for Solar Cells," Applied Solar Energy, **58**(4), 461–465 (2022). https://doi.org/10.3103/S0003701X22040132

[12] T.M. Razykov, M.S. Tivanov, K.M. Kuchkarova, R.T. Yuldoshov, R. Khurramov, S. Muzafarova, and D. S. Bayko, "Structural and Optical Properties of Thin Sb$_x$Se$_y$ Films Obtained at a Substrate Temperature of 400°C," https://doi.org/10.3103/S0003701X23601552

[13] L.A. Kosyachenko, Yu.S. Paranchich, V.N. Makogonenko, V.M. Sklyarchuk, E.F. Sklyarchuk, and I.I. German, "Electrical properties of surface-barrier photodiode structure based on HgInTe," J. Tech. Phys. **73**, 126 (2003). (in Russian)

[14] L.A. Kosyachenko, I.M. Rarenko, O.F. Sklyarchuk, I.I. German, and Weiguo Sun, "Electrical characteristics of ITO/HgInTe photodiodes," Physics and technology of semiconductors, **40**(5), 568 (2006). (in Russian)

[15] M.N. Solovan, G.O. Andrushchak, A.I. Mostovyi, *et al*., "Graphite/p-SiC Schottky Diodes Prepared by Transferring Drawn Graphite Films onto SiC," Semiconductors, **52**, 236–241 (2018). https://doi.org/10.1134/S1063782618020185

[16] V.V. Brus, M.I. Ilashchuk, Z.D. Kovalyuk, P.D. Maryanchuk, and K.S. Ulyanytsky, "Electrical and photoelectrical properties of photosensitive heterojunctions n-TiO$_2$/p-CdTe," Semicond. Sci. Technol. **26**, 125006 (2011). https://doi.org/10.1088/0268-1242/26/12/125006

[17] V.V. Brus, "On impedance spectroscopy analysis of nonideal heterojunctions," Semicond. Sci. Technol. **27**, 035024 (2012). https://doi.org/10.1088/0268-1242/27/3/035024

[18] V.V. Brus, M.I. Ilashchuk, Z.D. Kovalyuk, P.D. Maryanchuk, and O.A. Parfenyuk, "The effect of interface state continuum on the impedance spectroscopy of semiconductor heterojunctions," Semicond. Sci. Technol. **28**, 025013 (2013). https://doi.org/10.1088/0268-1242/28/2/025013

[19] A.L. Fahrenbruch, and R.H. Bube, *Fundamentals of solar cells. Photovoltaic solar energy conversion*, (N.Y., 1983)].

МЕХАНІЗМ ПРОТІКАННЯ СТРУМУ В ТОНКОПЛІВКОВИХ ГЕТЕРОПЕРЕХОДАХ n-CdS/p-Sb$_2$Se$_3$, ОТРИМАНИХ МЕТОДОМ CMBD

Т.М. Разиков[a], К.М. Кучкаров[a], А.А. Насіров[b], М.П. Пірімматов[a], Р.Р. Хуррамов[a], Р.Т. Юлдашев[a], Д.З. Ісаков[a], М.А. Махмудов[a], Ш.М. Бобомурадов[a], К.Ф. Шахрієв[a,b]

[a]*Фізико-технічний інститут Академії наук Республіки Узбекистан, вул. Чингіза Айтматова, 2Б, Ташкент, Узбекистан*
[b]*Національний університет Узбекистану Університет імені Мірзо Улугбека, вул. Університетська, 4, Ташкент, Узбекистан*

У даній роботі проаналізовано температурну залежність вольт-амперної характеристики структури скло/Mo/p-Sb$_2$Se$_3$/n-CdS/In. З аналізу температурних залежностей прямих гілок ВАХ гетеропереходу встановлено, що домінуючим механізмом передачі струму при малих зміщеннях (3kT/e<V<0,8V) є багатоступінчасті тунельно-рекомбінаційні процеси. за участю поверхневих станів на межі розділу Sb$_2$Se$_3$/CdS. При V>0,8 В домінуючим механізмом передачі струму є тунелювання Ньюмена. У випадку зворотного зсуву (3kT/e<V<1,0 eV) основним механізмом перенесення носія заряду через гетероперехід є тунелювання через потенційний бар'єр із залученням глибокого рівня енергії. При більш високих зворотних напругах відбувається м'який пробій.

Ключові слова: *Sb$_2$Se$_3$ SCR; CMBO; тонкі плівки; гетероструктура; гетероперехід*

IMPACT OF SULFUR CONCENTRATION ON THE MAGNETIC AND ELECTRICAL CHARACTERISTICS OF ZnMnO THIN FILMS

 Azamat O. Arslanov[a]*, Shavkat U. Yuldashev[a,b], Younghae Kwon[c], Ahn Il-Ho[c]

[a]National University of Uzbekistan named after Mirzo Ulugbek, Tashkent, Uzbekistan
[b]Center of Nanotechnology Development, National university of Uzbekistan, Tashkent, Uzbekistan
[c]Dongguk University, Seoul, South Korea
*Corresponding Author e-mail: azamat20296@gmail.com

Influence of the sulfur doping on the structural, optical, electrical and magnetic properties of ZnMnO thin films fabricated using the ultrasonic spray pyrolis technique was investigated. Our study reveals that increasing sulfur content leads to a noticeable shift in the band gap energy towards the red spectrum, an indicator of altered electronic states and potential for enhanced spintronic functionalities. The strong reduction in the band gap for the sulfur doped ZnMnO alloys is the result of the upward shift of the valence-band edge. As a result, the room temperature bandgap of $ZnMnO_{1-x}S_x$ alloys can be tuned from 3.2 eV to 2.97 eV for $x \leq 0.2$. The observed large bowing in the composition dependence of the energy bandgap arises from the anticrossing interactions between the valence-band of ZnO and the localized sulfur level above the ZnMnO valence-band maximum. The doping process significantly modifies the ferromagnetic properties, with an observed increase in Curie temperature correlating with higher sulfur concentrations. These changes are attributed to the increased free holes concentration, which facilitates a more robust exchange interaction between the magnetic ions. Additionally, the structural assessments via scanning electron microscopy confirm the uniform integration of sulfur into the ZnMnO matrix, resulting in distinct nanocrystalline formations. This study contributes to the understanding of doping mechanisms in semiconductor materials, especially for highly mismatched alloys, where the anions are partially substituted with isovalent atoms of considerably different size and/or electronegativity, offering insights into the tunability of their magnetic and electronic properties for potential future applications in spintronic devices.

Keywords: *Diluted magnetic semiconductors; Mn-doped p-type ZnO; Isovalent anion alloying; ZnO-ZnS alloy; Sulfur-doped ZnMnO; Resistivity anomaly; Valence band (VB) offset bowing; Defined hysteresis loop; Critical point; Curie temperature*
PACS: 61.72.uj

INTRODUCTION

Diluted magnetic semiconductors (DMSs) have attracted increasing attention in last 20 years [1]. The exchange effect between magnetic ions and carriers in semiconductors gives DMSs novel magneto-electric and magneto-optical properties. In addition, DMSs take advantage of both the charge and spin properties of electrons, making them potentially widely useful in spin field effect transistors (spin-FETs), high-density nonvolatile memory and spin qubits for quantum computers [2]. There are two main factors that limit the practical application of DMSs in equipment. The first is that the Curie temperature of DMS material is lower than room temperature, and the second is whether the ferromagnetism in DMS material is intrinsic, that is, mediated by free carriers, or purely from the local secondary phase of magnetic dopants, such as clusters or precipitates. If ferromagnetism is not mediated by free carriers, spin polarization cannot be carried by them.

In the seminal paper by T. Dietl et al. [3] it was theoretically predicted a room temperature ferromagnetism (RTFM) in at 5% Mn-doped *p*-type GaN and ZnO, with free holes concentration about $10^{20} cm^{-3}$. ZnO suffer from a low concentration of free holes and isovalent anion alloying can improve this problem. ZnO and ZnS alloy exhibits a very strong valence band (VB) offset bowing as a function of sulfur content [4]. The VB-bowing can be utilized to enhance *p*-type doping with lower formation energy and shallower acceptor state in the ZnO-ZnS alloy.

In this work, structural, optical and magnetic properties of $Zn_{1-x}Mn_xO_{1-y}S_y$, additionally doped with nitrogen, thin films grown by ultrasonic spray pyrolysis system are reported.

EXPERIMENTAL PART

Sulfur-doped ZnMnO thin films were deposited on Si [100] substrates using the ultrasonic spray pyrolysis method (USP). Aqueous chemicals were utilized during the solution preparation. Zinc acetate dihydrate ($Zn(C_2H_3O_2)_2\ 2H_2O$) and manganese acetate tetrahydrate ($Mn(C_2H_3O_2)_2\ 4H_2O$) were used as sources of zinc and manganese, respectively. Thiourea ($SC(NH_2)_2$) and ammonium acetate ($C_2H_7NO_2$) were added in appropriate quantities for the sulfur and nitrogen doping. The substrate was cleaned for 10 *min* in hydrofluoric acid, acetone, ethanol and D.I. water to remove impurities and organic solvents. Molar ratio of zinc acetate dihydrate was 0.3 *mol/l* while manganese concentration was kept same 5% of Zn for all samples. We employed an ultrasonic nebulizer with 2.4 M*Hz* frequency for atomizing prepared solution. The substrate temperature was set 400 ºC while growing thin film. All samples were annealed after grows at 500^0C for 15 minutes. Thickness of the samples was approximately 500 *nm*.

The morphology was studied with the scanning electron microscope (SEM). The crystallographic properties of the films were analyzed by Rigaku Miniflex X-ray diffractometer (XRD) using the CuKa radiation. The optical properties of the films were measured with a UV/VIS spectrometer. The magnetic properties were measured by using the superconducting quantum interference device (SQUID) magnetometer (Quantum design MP MS XL).

RESULTS AND DISCUSSION

Figure 1 shows SEM images (a) top and (b) side views of hexagonal-shaped nanocrystals, whose sizes were estimated between 150-200 *nm*. From the side view, thickness of sample could be seen around 500 *nm*.
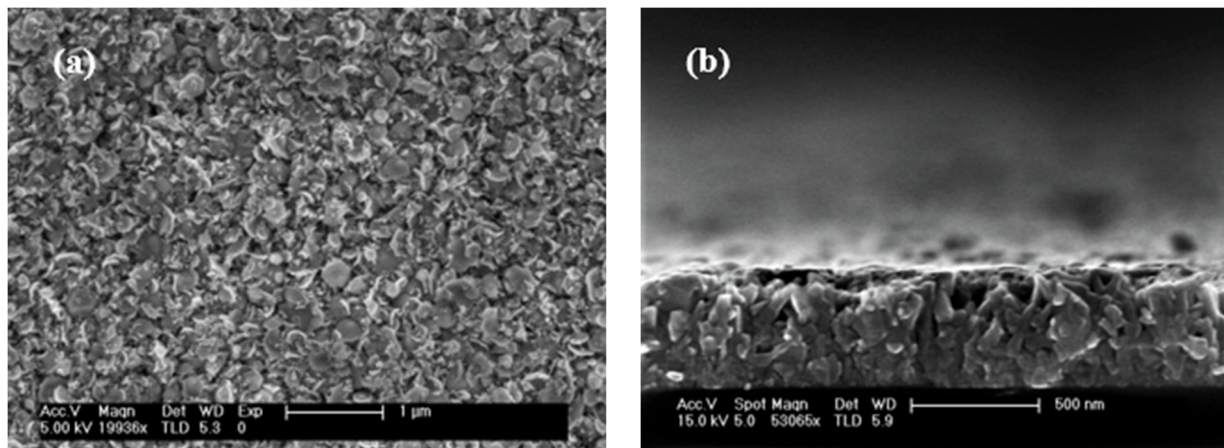
Figure 1. SEM images (a) top and (b) side views of the nitrogen doped $Zn_{0.95}Mn_{0.05}O_{0.90}S_{0.1}$ thin film

Figure 2 shows the XRD patterns for the pure ZnO and the $Zn_{1-x}Mn_xO_{1-y}S_y$, with 5% of Mn and different concentrations of S thin films grown on a silicon substrate by using the USP method. A dominant diffraction peak for (002) indicates a high degree of orientation with the *c*-axis vertical to the substrate surface. The shift of the (002) diffraction peak to the lower angle demonstrates a successful incorporation of the sulfur into ZnO lattice since the lattice constant $c = 6.26$ Å for ZnS is larger than 5.21 Å for ZnO [5]. It is also seen from Fig. 2, that the (002) peak is widening with increasing of the sulfur concentration which is due to the decreasing of the average size of crystal grains and the alloying effect. The diffraction peaks shown in Fig. 2 by star symbol demonstrate the existence of the Mn_2O_3 precipitates, even so the concentration of Mn in the samples was limited to the 5 %.
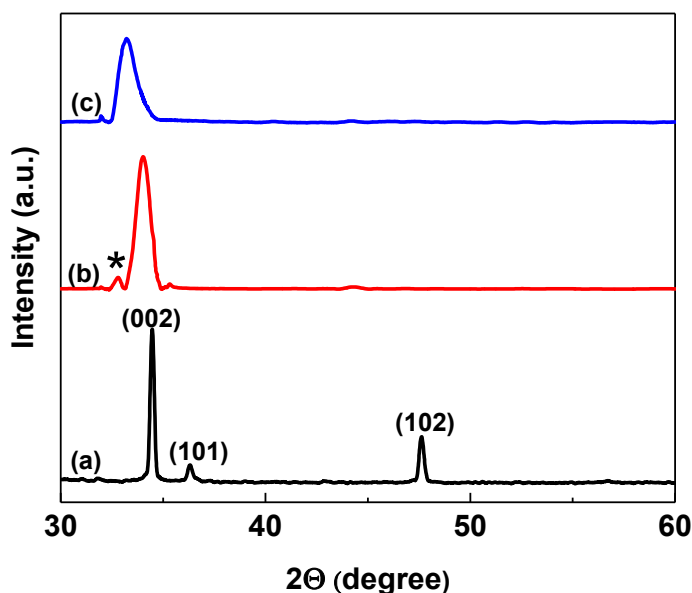
Figure 2. X-ray diffraction spectra of a) pure ZnO, b) $Zn_{0.95}Mn_{0.05}O_{0.9}S_{0.1}$, and c) $Zn_{0.95}Mn_{0.05}O_{0.80}S_{0.20}$ thin films, respectively. The diffraction peak of Mn_2O_3 shown by star symbol

The band gap energy of ZnMnO, 10% and 20% sulfur doped ZnMnOS can be determined from the Tauc plot ($\alpha hv = A(hv-E_g)^{1/2}$) equation [6]. Figure 3 shows $(\alpha hv)^2$ vs. phonon energy and each extrapolation represent the band gap energy of the thin film grown on Si substrates. Results show successfully incorporation of sulfur into ZnMnO films.

Band gap energy is decreasing with sulfur concentration increasing. The $Zn_{0.95}Mn_{0.05}O_{0.8}S_{0.2}$ sample has the band gap of 2.97 *eV*, while $Zn_{0.95}Mn_{0.05}O$ thin film remains almost 3.2 *eV* as same as pure zinc oxide. So, overall red shift was

observed in band gap energy. This directly reduced activation energy of the nitrogen acceptors. And, the Hall measurements show 5.1×10^{16} cm^{-3} and 4.85×10^{17} cm^{-3} of the free holes' concentrations in 10% and 20% of sulfur doped samples, respectively. $ZnO_{1-x}S_x$ alloys are classified as highly mismatched alloys (HMAs), semiconductor compounds where the anions are partially substituted with isovalent atoms of considerably different size and/or electronegativity.
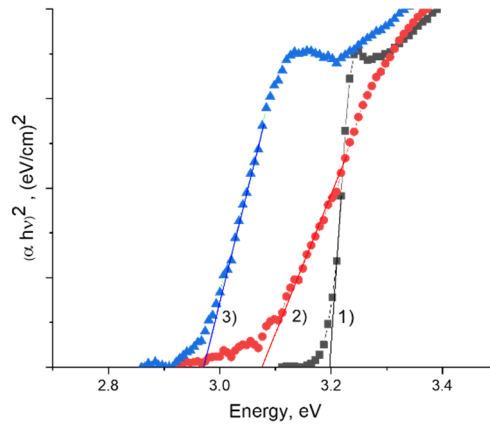
Figure 3. Tauc plots of the $Zn_{0.95}Mn_{0.05}O_{1-x}S_xN$ for 1) 0%, 2) 10% and 20 % of the sulfur concentrations, respectively.

Due to the high mismatch, the bandgap of these materials cannot be easily predicted with the virtual crystal approximation (VCA) model or modified VCA models [7]. The bandgap of HMA drastically decreases by the substitution of a small fraction (few percent) of anions with an isovalent element. The electronic band structure of HMAs is well described by the band anticrossing (BAC) model that considers an interaction between localized states introduced by the minority anions and the extended states of the host conduction/valence band in the dilute alloy composition limit [7].

Applying external magnetic field to the 10% and 20% sulfur doped samples at 10 K shows well-defined hysteresis loop for both samples (Fig. 4). Results represent both sample are ferromagnetic at 10 K. The magnetization completely saturated at ±1000 Oe (Oersted). It is obvious that sulfur is not a magnetic element, but 20% sulfur doped sample represent higher saturation magnetization value than that of 10% sulfur doped thin film. This could be explained by increase in the concentration of free holes. Because, the exchange interaction between magnetic ions is mediated by free holes, which are increased by adding more sulfur into ZnMnON thin film.
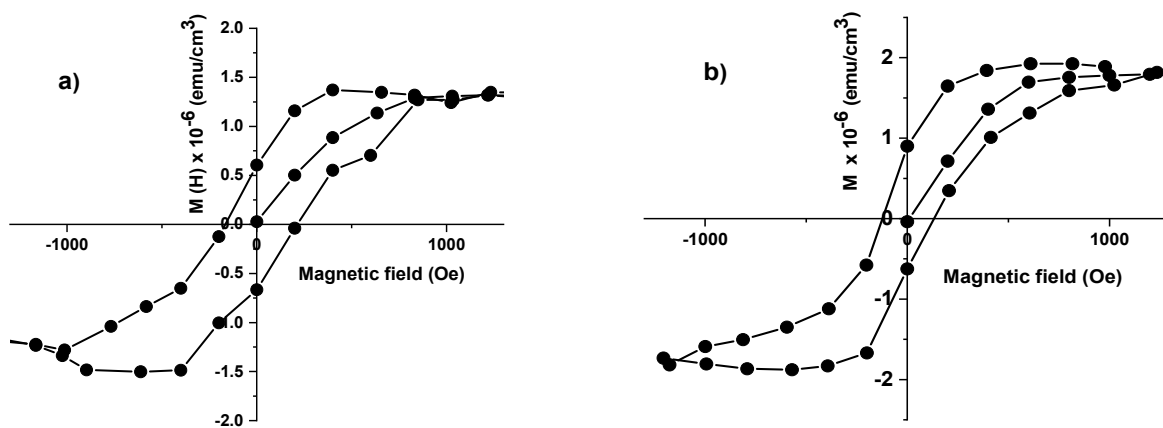
Figure 4. Magnetic field dependence of the magnetization (Hysteresis loop) at 10 K for
a) $Zn_{0.95}Mn_{0.05}O_{0.9}S_{0.1}$ and b) $Zn_{0.95}Mn_{0.05}O_{0.8}S_{0.2}$ thin films.

Figure 5 shows the magnetization dependence on temperature for a) $Zn_{0.95}Mn_{0.05}O_{0.9}S_{0.1}$ and b) $Zn_{0.95}Mn_{0.05}O_{0.8}S_{0.2}$ thin films in the temperature range from 10 K to 300 K. Results show that the value of magnetization for the $Zn_{0.95}Mn_{0.05}O_{0.9}S_{0.1}$ and $Zn_{0.95}Mn_{0.05}O_{0.8}S_{0.2}$ samples is higher than zero until temperature reached 170 K and 200 K, respectively. These measurements demonstrate the increasing the sulfur concentration in ZnMnO causes some increase in the Curie temperature. In the low temperature region < 50 K, the magnetization value is significantly high.

This could be explained by existing of the manganese oxide precipitates. Because of the low growing temperature, Mn_3O_4 ferromagnetic phase of the manganese oxide was formed, with Curie temperature near 47 K [8]. So that reason, the magnetization value enhances below 50 K.

In the ferromagnetic state (below T_C), the spins of magnetic ions become aligned, resulting in less scattering of the spin polarized charge carriers and low resistivity. As the temperature approaches the critical point, the most disordered

state of spins is formed. For ferromagnets with a small concentration of free carriers the T_C is attributed to the maximum of resistivity as it follows from the theory of the resistivity anomaly at T_C in ferromagnets given by de Gennes and Fridel [9].
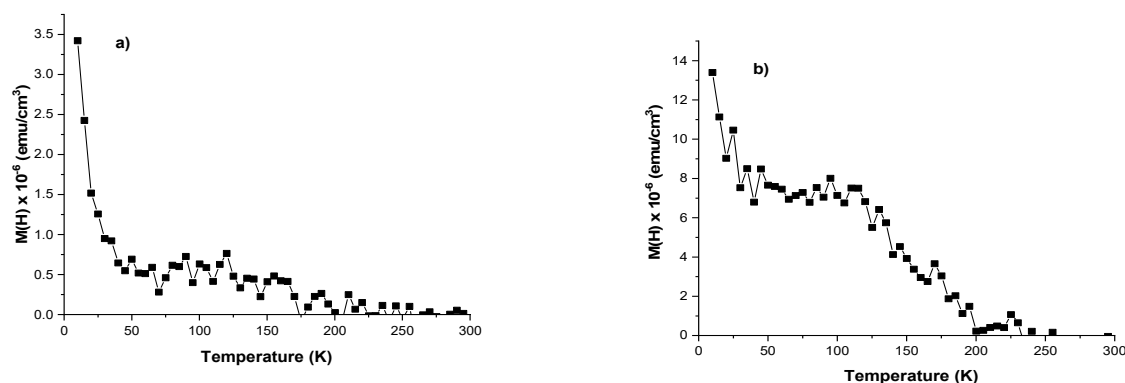
Figure 5. Magnetization dependence on temperature
a) $Zn_{0.95}Mn_{0.05}O_{0.9}S_{0.1}$ and b) $Zn_{0.95}Mn_{0.05}O_{0.8}S_{0.2}$ thin films in temperature range from 10 K to 300 K

Figure 6 shows the resistivity peaks near 170 K and 200 K for 10% and 20% sulfur-doped ZnMnO, respectively.
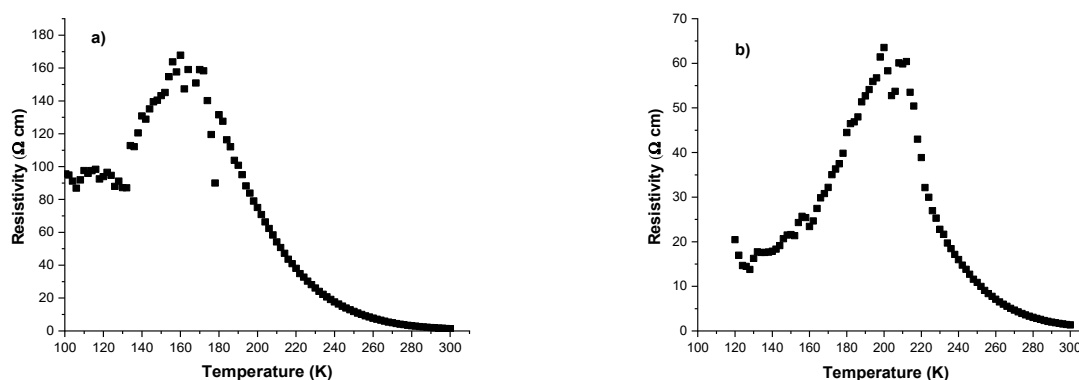
Figure 6. Temperature dependence of the resistivity
a) $Zn_{0.95}Mn_{0.05}O_{0.9}S_{0.1}$ and b) $Zn_{0.95}Mn_{0.05}O_{0.8}S_{0.2}$ thin films, respectively

From these results the ferromagnetic to paramagnetic phase transition can be observed, and the Curie temperature also can be determined by finding the highest resistivity point. These critical temperatures values determined from the resistivity peaks coincide well with critical temperatures found by the magnetization measurements presented above in Fig.4. When temperature is higher than T_C, resistivity decreases again as the material loses its magnetic ordering.

CONCLUSIONS

This study systematically explores the impact of sulfur doping on the properties of ZnMnO thin films, synthesized using ultrasonic spray pyrolysis. Our findings confirm that sulfur doping effectively shifts the band gap energy towards the longer wavelengths, thereby enhancing the magnetic properties of the films. We observed a notable increase in Curie temperature as the sulfur concentration increased. The enhanced hole concentrations facilitate stronger exchange interactions between magnetic ions.

The Curie temperature was determined for both 10% and 20% sulfur-doped ZnMnON by magnetization measurements, with hysteresis loops observed at 10 K. Near the Curie temperature, resistivity peaks were observed. The critical point, marking the ferromagnetic to paramagnetic phase transition temperature, was determined from the resistivity peak.

ORCID

Arslanov O. Azamat, https://orcid.org/0009-0000-4817-8770; **Yuldashev U. Shavkat,** https://orcid.org/0000-0002-2187-5960

REFERENCES

[1] H. Kalita, M. Bhushan, and L.R. Singh, Materials Science and Engineering: B, **288**, 116201 (2023). https://doi.org/10.1016/j.mseb.2022.116201

[2] S.J. Pearton, C.R. Abernathy, M.E. Overberg, G.T. Thaler, D.P. Norton, N. Theodoropoulou, A.F. Hebard, *et al.*, Journal of Applied Physics, **93**, 1 (2003). https://doi.org/10/1063/1.1517164

[3] T. Dietl, H. Ohno, F. Matsukura, J. Cibert, and D. Ferrand, Science, **287**, 1019 (2000). https://doi.org/10.1126/science.287.5455.10

[4] C. Persson, C. Platzer-Björkman, J. Malmström, T. Törndahl, and M. Edoff, Phys. Rev. Lett. **97**, 146403 (2006). https://doi.org/10.1103/PhysRevLett.97.146403

[5] O. Madelung, *Semiconductor basic data,* (Springer-Verlag, Berlin, 1996).

[6] J. Tauc, Materials Research Bulletin, **3**, 37 (1968). https://doi.org/ 10.1016/0025-5408(68)90023-8

[7] J. Wu, W. Shan, and W. Walukiewicz, Semiconductor Science and Technology, **17**, 860 (2002). https://doi.org 10.1088/0268-1242/17/8/315

[8] L.W. Guo, *et al.*, Journal of Magnetism and Magnetic materials, **123**, 321 (2000). https://doi.org/10.1016/S0304-8853(00)00008-1

[9] P.G. de Gennes, and J. Friedel, J. Phys. Chem. Solids, **4**, (1958). https://doi.org/10.1016/0022-3697(58)90196-3

ВПЛИВ КОНЦЕНТРАЦІЇ СІРКИ НА МАГНІТНІ ТА ЕЛЕКТРИЧНІ ХАРАКТЕРИСТИКИ ТОНКІХ ПЛІВОК ZnMnO

Азамат О. Арсланов[a], Шавкат У. Юлдашев[a,b], Йонгхе Квон[c], Ан Іль-Хо[c]
[a]Національний університет Узбекистану імені Мірзо Улугбека, Ташкент, Узбекистан
[b]Центр розвитку нанотехнологій, Національний університет Узбекистану, Ташкент, Узбекистан
[c]Університет Донгук, Сеул, Південна Корея

Досліджено вплив легування сіркою на структурні, оптичні, електричні та магнітні властивості тонких плівок ZnMnO, виготовлених методом ультразвукового розпилювального піролізу. Наше дослідження показує, що збільшення вмісту сірки призводить до помітного зміщення енергії забороненої зони в бік червоного спектру, індикатора змінених електронних станів і потенціалу для покращених функцій спінтроніки. Сильне зменшення забороненої зони для легованих сіркою сплавів ZnMnO є результатом зсуву вгору краю валентної зони. У результаті ширина забороненої зони при кімнатній температурі сплавів $ZnMnO_{1-x}S_x$ може бути налаштована від 3,2 еВ до 2,97 еВ для $x \leq 0,2$. Спостережуване велике викривлення в залежності від складу забороненої зони виникає через антикросингові взаємодії між валентною зоною ZnO та локалізованим рівнем сірки вище максимуму валентної зони ZnMnO. Процес легування суттєво змінює феромагнітні властивості, спостерігаючи підвищення температури Кюрі, що корелює з вищими концентраціями сірки. Ці зміни пояснюються збільшенням концентрації вільних дірок, що сприяє більш міцній обмінній взаємодії між магнітними іонами. Крім того, структурні оцінки за допомогою скануючої електронної мікроскопії підтверджують рівномірну інтеграцію сірки в матрицю ZnMnO, що призводить до чітких нанокристалічних утворень. Це дослідження сприяє розумінню механізмів допування в напівпровідникових матеріалах, особливо для сплавів із сильною неузгодженістю, де аніони частково заміщені ізовалентними атомами значно різного розміру та/або електронегативності, пропонуючи розуміння регульованості їхніх магнітних та електронних властивостей для потенціалу. майбутні застосування в спінтронних пристроях.

Ключові слова: *розчинені магнітні напівпровідники; Mn-легований ZnO p-типу; легування ізовалентним аніоном; сплав ZnO-ZnS; легований сіркою ZnMnO; аномалія питомого опору; зсув валентної зони (VB); визначена петля гістерезису; критична точка; температура Кюрі*

INFLUENCE OF BORON DIFFUSION ON PHOTOVOLTAIC PARAMETERS OF n^+-p-p^+ SILICONE STRUCTURES AND BASED PHOTODETECTORS

⊙**Mykola S. Kukurudziak[a,b*]**, ⊙**Eduard V. Maistruk [b]**, ⊙**Ivan P. Koziarskyi [b]**

[a]Rhythm Optoelectronics Shareholding Company, Holovna str. 244, 58032, Chernivtsi, Ukraine
[b]Yuriy Fedkovych Chernivtsi National University, Kotsyubyns'kogo str. 2, 58012, Chernivtsi, Ukraine
*Corresponding Author e-mail: mykola.kukurudzyak@gmail.com

The paper investigates the photovoltaic properties of the silicon n^+-p-p^+-structures and photodiodes made on their basis. It was found that boron diffusion to the reverse side of the substrate, in addition to creating an ohmic contact, generates generation-recombination centers, which allows to reduce the dark current of photodiodes and increase their responsivity. It was also found that chemical dynamic polishing of the back side of the substrates before boron diffusion allows to eliminate a significant number of defects and improve the final parameters of the products. In samples without a p^+-layer and samples not polished from the back side, a breakdown of the p-n junction is observed on the back side, which is caused by the expansion of the space charge region to the entire thickness of the substrate and the achievement of a defective back side of the crystal.
Keywords: *Silicon; Photodetectors; Avalanche Photodiode; Dark Curren; Isovalent Impurity; Sensitivity*
PACS: 61.72. Ji, 61.72. Lk, 85.60. Dw

In recent decades, semiconductor photodetectors with one or more p-n junctions have been widely used in optoelectronics, radioelectronics, automation, telemechanics, and other areas of electronics. The interest in photodetectors has especially increased due to the emergence and improvement of various types of coherent and incoherent radiation sources [1, 2]. The development of injection semiconductor LEDs and new types of semiconductor photodetectors based on one or more p-n junctions in miniature and micro-miniature designs has contributed to the rapid development of the field of electronic engineering - optoelectronics, which combines two methods of transmitting and processing information - optical and electrical.

Photodetectors, or photodiodes (PD) with a single p-n junction, are conventional semiconductor diodes with a reverse-biased p-n junction and the ability to irradiate it with a light flux. This class of solid-state electronics devices operates on the basis of the internal photoelectric effect: when radiation is absorbed in the p-n junction or in areas at a distance of the diffusion length of charge carriers from it, nonequilibrium charge carriers are generated, which drift to the p-n junction under the influence of an external electric field, crossing it to increase the photodiode reverse current - the photocurrent [3].

Increased photosensitivity and high-speed performance, as well as a wider spectral and frequency range, are possible with the use of n^+-p-p^+ structures, which form the class of p-i-n PDs. In the p-i-n structure, the i-region is located between two regions of the opposite type of conductivity and has a resistivity 10^6-10^7 times higher than the doped n^+- and p^+-regions. At sufficiently high reverse biases, a strong electric field, the space charge region (SCR), stretches across the entire high-resistance i-region. The photogenerated holes and electrons are quickly separated by the SCR field. In this type of photodetectors, the diffusion of charge carriers (as in p-n photodetectors) is replaced by their drift in the electric field, which creates the basis for a fast, highly sensitive photodetectors [4, 5].

While active n^+-regions are usually formed by the diffusion of impurities of elements of Group V (P, As, Sb, Bi) [6,7], the variability of the formation of an ohmic p^+-layer is much wider: it includes epitaxial growth of a low-resistivity silicon layer [8], grinding or structuring [9], and diffusion of acceptor elements (atoms of Group III - B, Al, Ga, In) [10,11]. Epitaxial growth of the silicon layer, grinding or structuring of the back side of the substrate can cause a decrease in the reflection coefficient from the Au-mirror on the back side, which provides double passage of radiation through the crystal thickness and an increase in the number of photogenerated charge carriers [12]. As for the acceptor impurities, boron diffusion has become widely used [13-15]. Boron diffusion is also used as one of the methods of silicon substrates doping in the process of manufacturing photovoltaic elements [16, 17]. Also, [18] reports on the fabrication of a highly sensitive silicon p^+-n-n^+ PD in the range of λ=200-1000 nm based on black silicon, where the active regions were doped with boron. In [19], silicon PDs for use as low-energy electron detectors have been fabricated using pure-boron technology to form the p^+-anode region. In [20], the technology of a UV avalanche photodiode based on a silicon p^+-in structure with a nanoscale boron doping profile of the responsive regions is described.

It should be noted that the references mainly describe the cases of fabrication and study of detectors with boron-doped photosensitive regions based on n-type Si, and there are very few studies of the effect of boron diffusion to the back side of p-type substrates (as a gettering or ohmic layer) as an isotypic impurity, and, accordingly, the effect of this operation on the parameters of photodetectors has not been studied sufficiently.

We are also actively studying boron diffusion and its effect on the parameters of *p-i-n* PDs based on *p*-Si. In particular, in [11], we studied the effect of the concentration of doped boron from solid-state planar sources on the efficiency of gettering and the improvement of the dark current and photodiode responsivity. In [11] we investigated the effect of boron concentration on the collection coefficient of nonequilibrium carriers by studying the optical properties of p^+-layers of PDs too. This article describes some of the effects of p^+-layer formation on the photovoltaic properties of n^+-p-p^+-structures and PDs based on them, in particular, the effect of the surface treatment of the back side before diffusion on the final parameters of photodetectors. The study of the photovoltaic properties of these structures is the aim of this work.

EXPERIMENTAL

The research was carried out on the example of silicon four-element *p-i-n* PDs with guard ring (GR) using single-crystal dislocation-free *p*-type FZ-Si with orientation [111], resistivity at $\rho \approx 16$-17 kΩ·cm. The structures were prepared using diffusion planar technology in a single process cycle under the same conditions. Three types of structures were produced: n^+-p-structures (PD_{n+-p}) (Fig. 1a), n^+-p-p^+-structures (without polishing the back side of the substrate, $PD'_{n+-p-p+}$), and n^+-p-p^+-structures (with polishing the back side of the substrate, $PD_{n+-p-p+}$) (Fig. 1b). The samples of type PD_{n+-p} were made according to the following technological route: silicon wafers were oxidized; windows in SiO$_2$ were opened by photolithography for two-stage phosphorus diffusion [7] and formation of n^+-layers (R_S=2.7-2.9 Ω/□), phosphorus-doped layers formed responsive elements (REs) and GR; the masking oxide was etched from the back side of the structures; Cr-Au contacts to the front and back sides were formed by thermal evaporation in vacuum; and to form the final *p-i-n* PDs, the crystals were separated by a diamond disk with an external cutting edge and encased. The $PD'_{n+-p-p+}$ were fabricated according to the same route, but after phosphorus diffusion, boron was diffused to the back side of the substrate from solid-state boron sources according to the methodology described in [11] (R_S=34-40 Ω/□). $PD_{n+-p-p+}$ was manufactured according to the same route as $PD'_{n+-p-p+}$, but before boron diffusion, a chemical dynamic polishing (CDP) operation was performed according to the procedure described in [21] The thickness of the PD_{n+-p} and $PD'_{n+-p-p+}$ crystals was about 510-515 μm, and that of $PD_{n+-p-p+}$ was 495-500 μm. The parameters and photovoltaic properties of the obtained structures were compared.

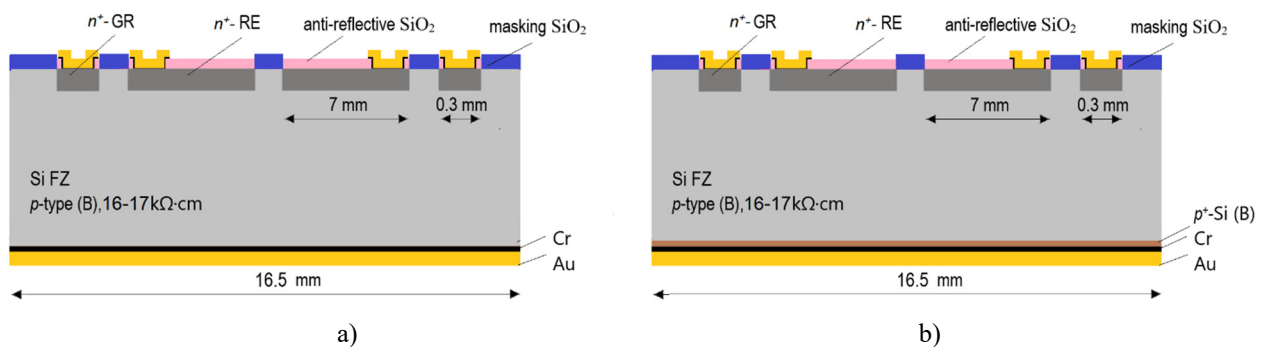**Figure. 1.** Schematic cross-section of PD_{n+-p} (a) and $PD'_{n+-p-p+}$ /$PD_{n+-p-p+}$ (b).

The *IV*-characteristics of PDs (dark current (I_d), photocurrent (I_{ph})) were measured using a hardware-software complex implemented on the basis of the Arduino platform, an Agilent 34410A digital multimeter and a Siglent SPD3303X programmable power source, which were controlled by a personal computer using software created by the authors in the LabView environment.

Monitoring of current monochromatic pulse responsivity (S_{pulse}) was carried out by method of comparing responsivity of the investigated PD with a reference photodiode certified by the respective metrological service of the company. Measurements were performed when illuminating the PD with a radiation flux of a power of not over $1 \cdot 10^{-3}$ W; at the reverse bias voltages of $|U_{bias}|$ = 2-270 V and pulse duration τ_i = 500 ns, λ=1064 nm. Measurements of current monochromatic (λ=1064 nm) responsivity on modulated flow ($S_{I\lambda}$) were performed under illumination of the PD with a modulated radiation flux of f_{mod} = 20 kHz and a power of below $1 \cdot 10^{-3}$ W. Load resistance of the responsive element was R_L = 10 kΩ and operating voltage $|U_{bias}|$ = 1-15 V. The spectral characteristics of photodiode responsivity are also obtained. The measurement was carried out using the KSVU-23 automated spectral complex.

After oxidation and each subsequent thermal operation, the high-frequency volt-farad (*CV*) characteristics of the metal-oxide-semiconductor-structures (MOS) were measured at a frequency of 30 kHz and a probe diameter 1 mm, which made it possible to predict the final parameters of the products.

The capacitance of REs (C_{RE}) was determined at a $|U_{bias}|$ =2-120 V.

RESULTS OF THE RESEARCH AND THEIR DISCUSSION
A) Study of the dark currents

When measuring the *IV*-characteristics of the obtained structures, we observed some differences in the values of the I_d: the PD_{n+-p} had the highest dark currents, and the $PD_{n+-p-p+}$ had the lowest (Fig. 2a). The dark current of $PD_{n+-p-p+}$ at $|U_{bias}|$ =140-160 V reached saturation (Fig. 2b), which indicated the expansion of the SCR to the entire thickness of the

crystal, since the volume generation component of the dark current is directly proportional to the width of the SCR [22]. Samples of $PD'_{n+-p-p+}$ had a significant spread of dark currents along the RE: in three REs in the range of $|U_{bias}|$ =180-200 V, the *p-n* junction breakdown was observed, and the dark current of RE_2 in the range of $|U_{bias}|$ =190-200 V reached saturation (Fig. 2c). As for the PD_{n+-p}, their *IV*-characteristics in the range of $|U_{bias}|$ =2-230 V acquired a linear character, and at $|U_{bias}|$ = 30-260 V, a breakdown of the *p-n* junction was observed in all REs (Fig. 2d).
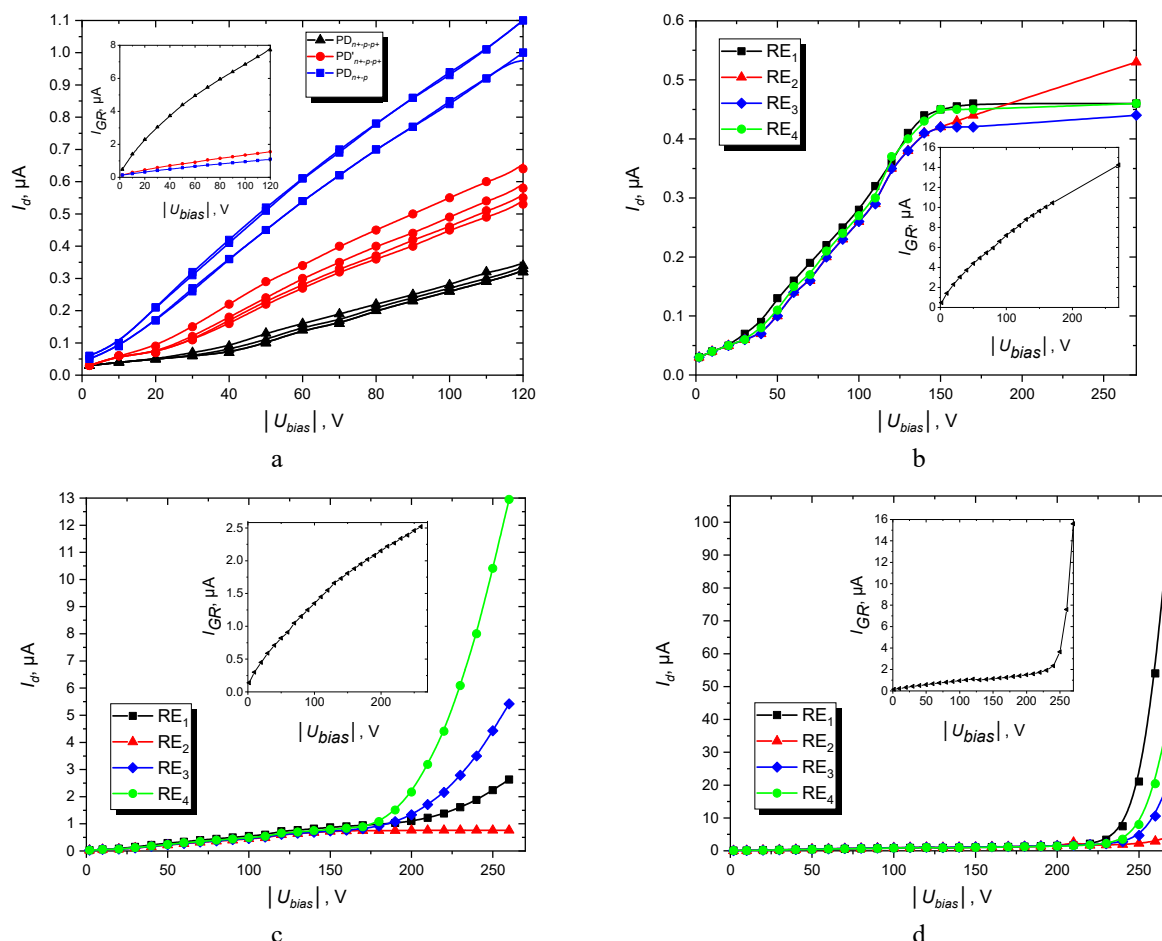
Figure. 2. Reverse dark *I–V*-characteristics of PDs REs and GRs: a) all investigated PDs at $|U_{bias}|$ =2-120 V; b) $PD_{n+-p-p+}$; c) $PD'_{n+-p-p+}$; d) PD_{n+-p}; inserts - *IV*-characteristics of GRs

The difference in the values of the dark currents indicates a different number of generation-recombination centers (GRCs) in the volume of the PD crystals and a different degree of their gettering in the process of manufacturing photodetectors. In the case of PD_{n+-p}, the gettering operations were the predeposition and drive-in of phosphorus into the front side of the PDs, but this gettering process is effective only in the crystal region adjacent to the n^+-layer, and the back side of the and the crystal volume close to it remained saturated with recombination centers, in particular, atoms of uncontrolled impurities and crystallographic defects introduced or created during high-temperature thermal operations. Accordingly, these GRCs make a significant contribution to the level of dark currents of the PDs, and at a high reverse bias voltage (and, accordingly, a high electric field intensity) and when the SCR reaches to the back side of the crystal with defects, the latter provoke an avalanche breakdown [23-25]. It is also known that the breakdown voltage near the surface is lower than in the crystal volume, which also explains the avalanche breakdown when the space charge region of the back side of the crystal is reached [26].

A similar situation applies to the $PD'_{n+-p-p+}$, although the backside boron gettering operation is present in the manufacturing route of these PDs, but still, boron gettering is not so effective as to completely eliminate the GRC of the crystal region near the backside of the crystal. Therefore, for the same reasons as in the previous case, breakdown of the *p-n* junction is possible, and a decrease in the breakdown voltage is possible due to the achievement of the SCR of the defective backside of PDs at a lower bias voltage.

It should be noted that this thermal operation of boron diffusion is also an annealing for more efficient gettering by the n^+-layer of the front side of the substrate, which allows diffusion of the deepest uncontrolled impurities to the getter zone. An increase in the annealing time improves the efficiency of GRC elimination. It is worth noting that in [11] we

described a method of effective additional doping of the back side of the substrate by simultaneous diffusion of phosphorus into the front and back sides of the crystal, followed by etching the back n^+-layer before boron diffusion.

The minimum spread and value of I_d were observed in the PD'$_{n+\text{-}p\text{-}p+}$. This was achieved by etching by CDP method the silicon layer of the back side of the substrate saturated with GRC.

It should be noted that the dark currents of the GR (I_{GR}) also had different values and did not reach saturation (Fig. 2 inserts). The I_{GR} depend on the density of surface states and the presence of inversion layers at the interface of Si-SiO$_2$ at the periphery of the crystal, since with increasing voltage the SCR of GR shift expands not only into the crystal thickness but also towards the periphery.

The samples of PD'$_{n+\text{-}p\text{-}p+}$ and PD$_{n+\text{-}p\text{-}p+}$ had slightly higher values of the I_{GR}, which indicates a higher density of surface states than in PD$_{n+\text{-}p}$. This is also confirmed by the measurement of the insulation resistance between the GR and the REs R_{con}, since this parameter characterizes the presence of conductive inversion channels at the interface of Si-SiO$_2$ between the active elements: PD$_{n+\text{-}p\text{-}p+}$ -R_{con}=1.4 MΩ, PD'$_{n+\text{-}p\text{-}p+}$ -R_{con}=6.2 MΩ, PD$_{n+\text{-}p}$ -R_{con}=8.7 MΩ. The increase in the conductivity of inversion channels in the case of PD'$_{n+\text{-}p\text{-}p+}$ and PD$_{n+\text{-}p\text{-}p+}$ is caused by the presence of a larger number of thermal operations, unlike PD$_{n+\text{-}p}$, since during the initial thermal operations, atoms of uncontrolled impurities (it can be phosphorus too) diffuse into the surface of silicon oxide, which, during further heat treatments, diffuse to the oxide-silicon interface, and with a significant total duration of heat treatments, can cause a deterioration in the insulation resistance between the active elements and an increase in I_{GR} [27]. The presence of inversion layers can also be assessed by measuring the *CV*-characteristics of MOS structures (Fig. 3), where the curves of PD'$_{n+\text{-}p\text{-}p+}$ and PD$_{n+\text{-}p\text{-}p+}$, which have a longer total duration of thermal operations, can invert.
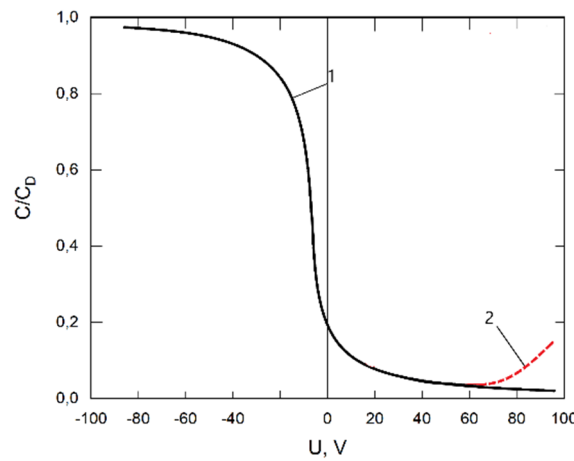
Figure 3. *CV*-characteristics of MOS structures: 1- n^+-p-structure
2 — n^+-n-p^+--structure

B) **Study of the responsivity and photocurrent of PDs**

When studying the pulse current monochromatic responsivity, it was seen that the photosensitivity of PD$_{n+\text{-}p\text{-}p+}$ reaches saturation at approximately the same bias voltage as its dark current (Fig. 4, Fig. 5a). This is due to the same reason - the achievement of the maximum width of the SCR, at which further growth of the charge carrier collection coefficient, and, accordingly, responsivity, is impossible (1) [28]. As for the PD'$_{n+\text{-}p\text{-}p+}$, the responsivity of all REs reached saturation around the $|U_{bias}|$ = 180-200 V, as well as the dark current of RE$_2$, which did not show breakdown. It should be noted that all REs of PD'$_{n+\text{-}p\text{-}p+}$ behaved typically during the responsivity measurement, although some REs showed breakdown at the *IV*-characteristic. The saturation of the samples at different reverse bias voltages indicates the expansion of the SCR to the entire thickness of the crystal at different bias voltages, and, accordingly, the difference in the final resistivity of the *i*-region of the structures (2) [29].

$$S_\lambda = (1 - R)TQ \sum \gamma \frac{\lambda_{op}}{1.24} \qquad (1)$$

where T is the transmission coefficient of the input window or optical filter; Q is the quantum output of the internal photoeffect, R is the reflection coefficient, γ is the charge carrier collection coefficient.

$$W_i = \left(\frac{2\varepsilon\varepsilon_0 (\phi_c - U_{bias})}{eN_A}\right)^{\frac{1}{2}}. \qquad (2)$$

where ε, ε_0 are dielectric constants for silicon and vacuum, respectively; φ_c is contact potential difference, N_A is the concentration of acceptors in *i*-region, e is the electron charge.

A different picture was observed when measuring the responsivity of n^+-p-structures: at a $|U_{bias}|$ = 120 V, a jump-like increase in responsivity was observed (Fig. 4), although according to Fig. 2, the breakdown of the *p-n* junction of these

PDs was observed at a voltage of -230-260 V. The S_{pulse} of PD_{n+-p} did not reach saturation, but increased rapidly with increasing bias voltage (Fig. 5b-f) and the responsivity reached the theoretically possible value (3) [28] at $\left| U_{bias} \right| \approx 230$-250 V. Such an increase in responsivity is caused by avalanche breakdown and a significant increase in nonequilibrium charge carriers, similar to an avalanche photodiode. Note that formula (3) is valid for photodetectors without amplifiers or optical concentrators, as well as avalanche photodiodes.

$$S_{\lambda max} = \frac{\lambda}{1.24}$$ (3)
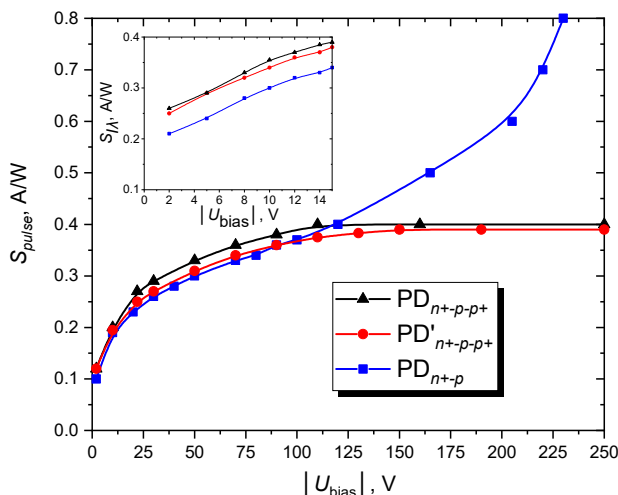
Figure 4. Dependence of the S_{puse} of PDs on the reverse bias voltage (insert $S_{I\lambda}$).
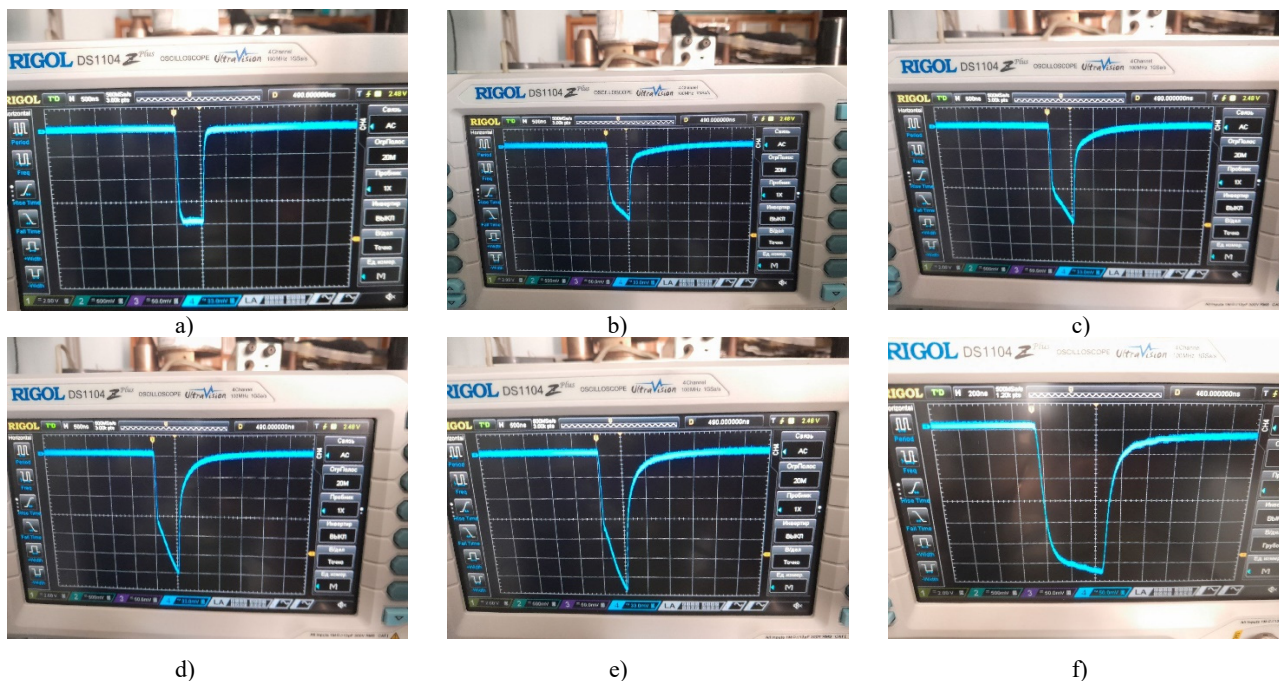
Figure 5. Photodiode pulse waveform: a) $PD_{n+-p-p+}$: $\left| U_{bias} \right|$ =160 V, S_{pulse}=0.4 A/W; b) a) PD_{n+-p}: $\left| U_{bias} \right|$ =120 V, S_{pulse}=0.4 A/W; c) PD_{n+-p}: $\left| U_{bias} \right|$ =165 V, S_{pulse}=0.5 A/W; d) PD_{n+-p}: $\left| U_{bias} \right|$ =205 V, S_{pulse}=0.6 A/W; e) PD_{n+-p}: $\left| U_{bias} \right|$ =220 V, S_{pulse}=0.7 A/W; f) PD_{n+-p}: $\left| U_{bias} \right|$ =240 V, S_{pulse}=0.86 A/W (different scale).

It is worth noting that $PD'_{n+-p-p+}$ and $PD_{n+-p-p+}$ had a slightly higher low-voltage $S_{I\lambda}$ than PD_{n+-p} (Fig. 4 insert). This indicates that $PD'_{n+-p-p+}$ and $PD_{n+-p-p+}$ had a longer diffusion length of minority charge carriers due to more efficient gettering than PD_{n+-p}, and also indicates that at the same voltage, the SCR of PDs with higher responsivity is greater than that of the PD with lower responivity due to lower ρ of i-region.

The behavior of light IV-characteristics in the visible wavelength range was also studied. It was found that in PD_{n+-p} around a voltage of $\left| U_{bias} \right|$ = 120-130 V, a jump-like increase in photocurrent is observed when illuminated with a white light-emitting diode of different illumination (Fig. 6). In the same voltage range, an increase in photocurrent and

sensitivity at a wavelength of 1064 nm is observed. Taking into account the described avalanche-like growth of photocurrent and sensitivity in PD$_{n+-p}$, it is possible that such a structure of photodetectors can be used for avalanche photodiodes [30]. It should be noted that there was no abrupt increase in photocurrent, similar to breakdown, in PD'$_{n+-p-p+}$ and PD$_{n+-p-p+}$ (PD'$_{n+-p-p+}$ was measured by RE without breakdown) (Fig. 8, 9).
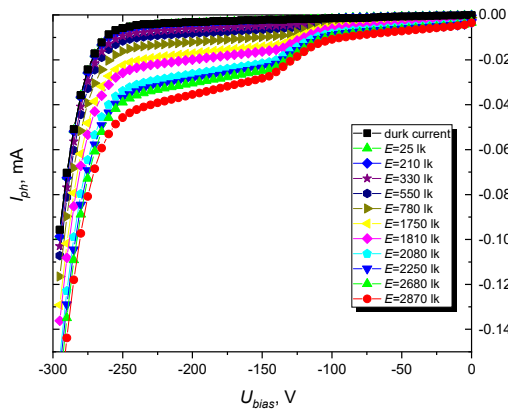

Figure 6. Light *IV*-characteristics of PD$_{n+-p}$ illuminated with a white light-emitting diode of different illumination
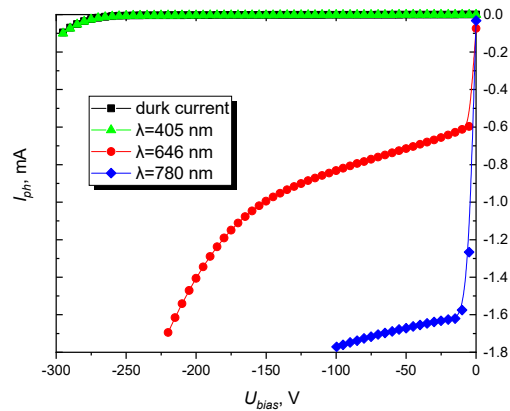
Figure 7. Light *IV*-characteristics of PD$_{n+-p}$ when illuminated with lasers of different wavelengths (*P*=5 mW)
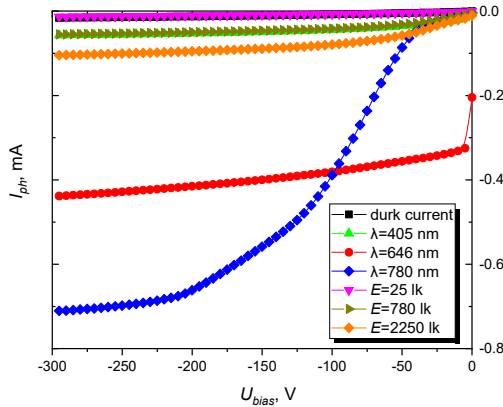
Figure 8. Light *IV*-characteristics of PD$_{n+-p-p+}$ illuminated with a white light-emitting diode of different illumination illuminated with lasers of different wavelengths (*P*=5 mW)
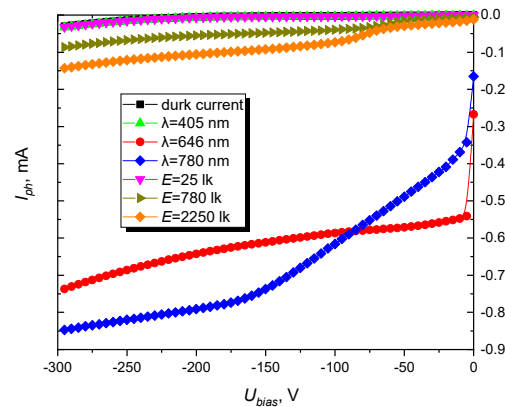
Figure 9. Light *IV*-characteristics of PD'$_{n+-p-p+}$ illuminated with a white light-emitting diode of different illumination illuminated with lasers of different wavelengths (*P*=5 mW)
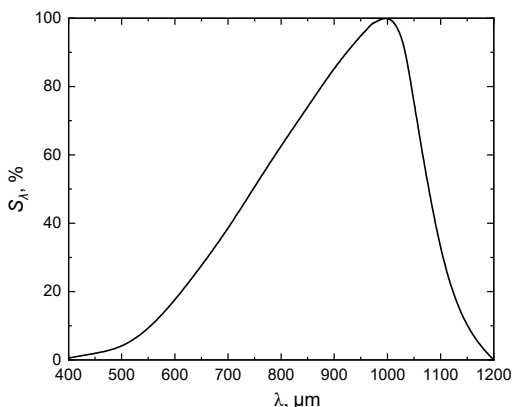
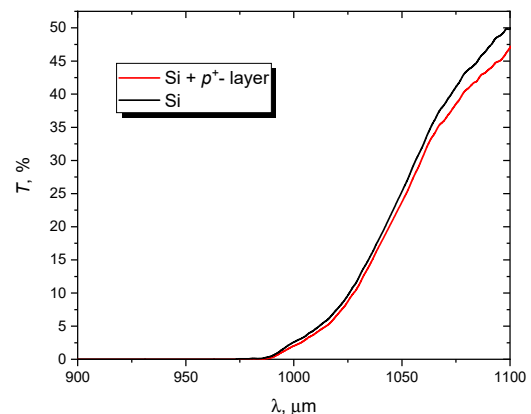**Figure 10.** Typical spectral characteristics of the studied PDs

Figure 11. Transmittance spectrum of a silicon substrate and a substrate with a *p*⁺-layer

When studying the light *IV*-characteristics with illumination with lasers of different wavelengths (Fig. 7-9), it was found that the photocurrent at λ=405 nm is virtually the same as the dark current, and with increasing wavelengths, the photocurrent increases sharply . This is due to the fact that the studied photodiodes are sensitive in the range of λ = 400-1200 nm, with a maximum of about λ = 1000 nm, respectively, at λ = 405 nm the responstivity is minimal (Fig. 10).

It should be noted that the formation of a p^+-layer in the visible wavelength range does not affect the value of the charge carrier collection coefficient and responsivity, since in this case there is no reflection of radiation from the gold mirror on the back side of the substrate due to absorption in the near-surface layers of the substrate. At λ = 1064 nm, the p^+-layer absorbs about 2% of the radiation in one pass, with increasing λ, the absorption of the p^+-layer increases (Fig. 11), but the described photodetectors are not used to detect longer wavelengths.

C) Study of the barrier capacity of structures and final electrophysical characteristics of the base material

When measuring the dependence of the capacitance (C_{RE}) of the REs on the reverse voltage, it was found that PD$_{n+-p-p+}$ had the lowest capacitance values, and PD$_{n+-p}$ had the highest (Fig. 12). The difference in values is caused by the difference in the final ρ of the i-region (or N_A), since C_{RE}~1/ρ and C_{RE}~N_A (4) [29]. Accordingly, the capacitance measurements also indicate the most effective crystal gettering in the case of PD$_{n+-p-p+}$, and the least effective in case of PD$_{n+-p}$.

$$C_{RE} = A_{RE}\left(\frac{\varepsilon\varepsilon_0 eN_A}{2(\phi_c - U_{bias})}\right)^{\frac{1}{2}} \tag{4}$$

where A_{RE} is the area of REs.

If we also determine the resistivity and the diffusion length (L_n) of the minority charge carriers according to the methodology given in [31] (Table 1), we obtain:

Table 1. Values of ρ and L_n of PDs

Parameter	PD$_{n+-p-p+}$	PD`$_{n+-p-p+}$	PD$_{n+-p}$
ρ, kΩ	14.7-15.7	11-11.6	8.5-9.5
L_n, μm	70-80	50-55	-

Note: the voltage at which the SCR reached the entire thickness of the crystal of PD$_{n+-p}$ was chosen as the breakdown voltage of $|U_{bias}|$ = 230 V.
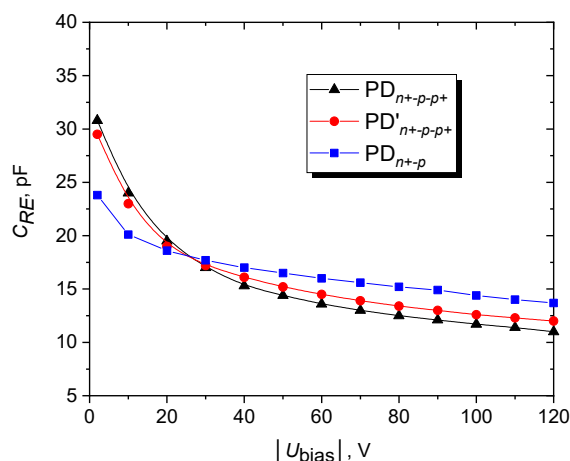
Figure 12. The dependence of the C_{RE} on the reverse voltage.

The data from Table 1 show that PD$_{n+-p-p+}$ have the lowest degree of degradation of the electrophysical characteristics of silicon in the process of manufacturing photodiodes, respectively, the technological route with CDP on the back side of the substrate before boron diffusion allows to obtain the most efficient PDs with the lowest values of dark currents and capacitance, as well as the highest resposivity among the studied variants of structures.

CONCLUSIONS

The photovoltaic properties of silicon n^+-p-p^+-structures and p-i-n photodiodes fabricated on their basis have been investigated. The following conclusions have been made:

1. Boron doping of the back side of the photodetector substrate significantly improves their parameters. During the boron diffusion operation, the n^+-layer also functions as a getter too.

2. Chemical dynamic polishing of the back side of the wafers before boron diffusion reduces the dark currents of photodetectors and improves the final electrophysical characteristics of silicon, in particular, the resistivity of the i-region and the diffusion length of minority charge carriers.

3. Photodiodes made without an p^+-layer are characterized by a breakdown of the p-n junction in the reverse voltage range of 230-260 V, which significantly increases their sensitivity and photocurrent. Presumably, such structures can be considered as possible for avalanche photodiodes.

ORCID

Ⓘ**Mykola S. Kukurudziak,** https://orcid.org/0000-0002-0059-1387; Ⓘ**Eduard V. Maistruk**, https://orcid.org/0000-0002-9025-6485
Ⓘ**Ivan P. Koziarskyi,** https://orcid.org/0000-0002-4984-4349

REFERENCES

[1]   K. K. Samarkhanov, Applied Radiation and Isotopes, 111503 (2024). https://doi.org/10.1016/j.apradiso.2024.111503
[2]   S. Khan, Instrumentation and Science Applications, 51-81 (2020). https://doi.org/10.1007/978-3-030-23201-6_5
[3]   Y. Xu, & Q. Lin, Applied Physics Reviews, **7**(1) (2020). https://doi.org/10.1063/1.5144840
[4]   K. Schneider-Hornstein, B. Goll, & H. Zimmermann, IEEE Photonics Journal, **15**(3), 1-9 (2023). https://doi.org/10.1109/JPHOT.2023.3279935
[5]   M.S. Kukurudziak, and E.V. Maistruk, Semicond. Sci. Technol. 38, 085007 (2023). https://doi.org/10.1088/1361-6641/acdf14
[6]   S. Meng-Ju, and E. G. Hemme, Semicond. Sci.Technol. 38, 033001 (2023). https://doi.org/10.1088/1361-6641/acb16b
[7]   M.S. Kukurudziak, Semiconductor Physics, Quantum Electronics & Optoelectronics, **25**(4), 385 (2022). https://doi.org/10.15407/spqeo25.04.385
[8]   R. Maeda et al., Appl. Phys. Express, **17**, 011006 (2024). https://doi.org/10.35848/1882-0786/ad16ae
[9]   P. N. Vinod, Semicond. Sci. Technol., **20**, 966 (2005). https://doi.org/10.1088/0268-1242/20/9/014
[10] Tuck, B. Atomic diffusion in III-V semiconductors (CRC Press. 236, 2021)
[11] M.S. Kukurudziak, and E.V. Maistruk, in: 2022 IEEE 3rd KhPI Week on Advanced Technology (KhPIWeek) (IEEE, Kharkiv, 2022), pp. 1-6. https://doi.org/10.1109/KhPIWeek57572.2022.9916420
[12] M.S. Kukurudziak and E.V. Maistruk, in: Fifteenth International Conference on Correlation Optics, 121261V (SPIE, Chernivtsi, 2021). https://doi.org/10.1117/12.2616170
[13] D. Yan, et al., Solar Energy Materials and Solar Cells, **152**, 73-79 (2016). https://doi.org/10.1016/j.solmat.2016.03.033
[14] De. Salvador et al., B—Condensed Matter and Materials Physics, **81**(4), 045209 (2010). https://doi.org/10.1103/PhysRevB.81.045209
[15] S. Mirabella, et al. Journal of Applied Physics, **113**(3) (2013). https://doi.org/10.1063/1.4763353
[16] A. Y. Liu, et al. Solar Energy Materials and Solar Cells, **234**, 111447 (2022). https://doi.org/10.1016/j.solmat.2021.111447
[17] Q. Zhang, et al., RSC advances, **14**(8), 5207-5215 (2024). https://doi.org/10.1039/D3RA08772G
[18] O. E. Setälä, et al., ACS photonics, **10**(6), 1735-1741 (2023).
[19] A, Šakić, et al., Solid-state electronics, **65**, 38-44 (2011). https://doi.org/10.1016/j.sse.2011.06.042
[20] Z. Xia, et al., Applied Physics Letters, **111**(8) (2017). https://doi.org/10.1063/1.4985591
[21] M.S. Kukurudziak, Him. Fiz. Tehnol. Poverhni, **14**(1), 42 (2023). https://doi.org/10.15407/hftp14.01.042 (in Ukrainian)
[22] K.V. Ravi, Imperfections and impurities in semiconductor silicon, (Wiley, New York, 1981).
[23] J. Bauer, et al., Progress in Photovoltaics: Research and Applications, **21**(7), 1444-1453 (2013). https://doi.org/10.1002/pip.2220
[24] N. Rouger, COMPEL: The International Journal for Computation and Mathematics in Electrical and Electronic Engineering, **35**(1), 137-156 (2016). https://doi.org/10.1108/COMPEL-12-2014-0330
[25] O. Breitenstein, IEEE Transactions on Electron Devices, **57**(9), 2227-2234 (2010). https://doi.org/10.1109/TED.2010.2053866
[26] B. J. Baliga, Fundamentals of Power Semiconductor Devices, 89-170 (2019). https://doi.org/10.1007/978-3-319-93988-9_3
[27] M.S. Kukurudziak, East Eur. J. Phys. **2**, 289 (2023), https://doi.org/10.26565/2312-4334-2023-2-33
[28] A.V. Fedorenko, Technology and design in electronic equipment, **17**(3–4), 17 (2020). https://doi.org/10.15222/ TKEA2020.3-4.17 (in Ukrainian)
[29] N.M. Tugov, B.A. Glebov, and N.A. Charykov, Semiconductor devices: Textbook for universities, edited by V.A. Labuntsov, (Energoatomizdat, Moscow, 1990). (in Russian)
[30] J. C. Campbell, Journal of Lightwave Technology, **34**(2), 278-285 (2015). https://doi.org/10.1109/JLT.2015.2453092
[31] M.S. Kukurudziak, East Eur. J. Phys. **2**, 345 (2024). https://doi.org/10.26565/2312-4334-2024-0-41

ВПЛИВ ДИФУЗІЇ БОРУ НА ФОТОЕЛЕКТРИЧНІ ПАРАМЕТРИ n^+-p-p^+-КРЕМНІЄВИХ СТРУКТУР ТА ФОТОПРИЙМАЧІВ НА ЇХ ОСНОВІ

Микола С. Кукурудзяк[a,b], Едуард В. Майструк[b], Іван П. Козярський[b]

[a]АТ «Центральне конструкторське бюро Ритм», 58032, м. Чернівці, вул. Головна, 244, Україна

[b]Чернівецький національний університет імені Юрія Федьковича, 58002, м. Чернівці, вул. Коцюбинського, 2, Україна

У статті досліджено фотоелектричні властивості кремнієвих n^+-p-p^+-структур та фотодіодів виготовлених на їх основі. Встановлено, що проведення дифузії бору в зворотну сторону підкладки крім створення омічного контакту гетерує генераційно-рекомбінаційні центри, що дозволяє знизити темновий струм фотодіодів та підвищити їх чутливість. Також встановлено, що хіміко-динамічне полірування зворотної сторони підкладок власне перед дифузією бору дозволяє ліквідувати значну кількість дефектів та покращити кінцеві параметри виробів. В зразків без p^+-шару та зразків не полірованих зі зворотної сторони спостерігається пробій p-n переходу, що спричинено розширенням області просторого заряду на всю товщу підкладки та його досягненням дефектної зворотної сторони кристала.

Ключові слова: *кремній; фотоприймачі; лавинні фотодіоди; темновий струм; ізовалентна домішка; чутливість*

THE SURFACE LAYER MORPHOLOGY OF Si<Cr> SAMPLES

M.Sh. Isaev[a], A.I. Khudayberdieva[b], M.N. Mamatkulov[b], U.T. Asatov[b], S.R. Kodirov[c]

[a]*National University of Uzbekistan, Tashkent, Uzbekistan*
[b]*Tashkent Institute of Chemical Technology, Tashkent, Uzbekistan*
[c]*Urgench State University, Urgench, Uzbekistan*
Corresponding Author e-mail: isayevmahmud02@gmail.com

In this work, the electrical and photoelectric properties of the near-surface and surface layers of silicon doped by diffusion with chromium atoms were investigated. The formation of an anomalous concentration of charge carriers in these regions, as well as an anomalously low mobility, was revealed. The specific conductivity of the near-surface layer with a thickness of $1 \div 5$ µm turned out to be equal to $(1.6 \div 9.9) \cdot 10^3$ Ohm^{-1}·cm^{-1}. The inhomogeneity of the crystal under study was determined by the light probe method.
Keywords: *Silicon; Chromium; Surface; Subsurface; Conductivity; Hall mobilty; Inhomogeneity; Silicide*
PACS: 32.30.Ea, 33.20.Fb.

INTRODUCTION

Modern world scientific and technical progress is largely determined by the development of microelectronics and nanoelectronics, the achievements of which directly depend on the successes of fundamental sciences, primarily solid state physics and semiconductor physics. The latest achievements in these areas are related to the physics of doped semiconductors and the creation of technologies for obtaining micro- and nanostructures with fundamentally new functional capabilities for computer and measuring equipment, communications, etc. In this regard, studies of physical processes occurring both in the volume and on the surface, and in the near-surface layers of a single-crystal semiconductor, in particular, silicon in the process of diffusion doping with impurities, creating deep levels and obtaining compensated materials with specified electrophysical, tensoelectric, photoelectric and optical properties are urgent tasks of today [1-6].

The observed increased interest in the development of new materials with improved thermoelectric properties is due to the ever-expanding needs for the use of such materials in the national economy as thermal sensors and active elements [7-8].

Traditional materials used as effective thermoelectric converters of thermal energy, in particular solar energy, into electrical energy are various compounds of bismuth and lead with tellurium and selenium, as well as binary compounds in the form of alloys and solutions based on isovalent elements of germanium and silicon [9-11]. Along with the existing materials listed above, manganese silicide can also find an equally important application as a base material for creating highly effective thermoelectric power sensors.

The thermoelectric properties of a number of silicides have been considered in sufficient detail [12, 13], where, in particular, the possibility of creating a thermoelectric generator with a semiconductor nature of electrical conductivity based on manganese silicide was demonstrated. Thermoelectric properties were studied on samples of manganese silicide obtained by the method [14].

At the global level, the use of diffusion-doped monocrystalline silicon to obtain compensated materials with specified electrophysical, photoelectric and optical properties in modern microelectronics is an urgent task. Well-developed technology for growing monocrystalline silicon, planar technology for creating integrated devices based on it, a fundamentally new technology for creating low-dimensional objects in silicon, modification of properties by various methods, as well as the discovery of new physical phenomena that are not characteristic of bulk silicon, attracts the close attention of researchers as an active material for the needs of micro- and nanotechnology [15].

Currently, transition metal silicides are becoming the base material for new, promising technological schemes of future generations due to their resistance to aggressive environments and high-temperature treatments. Therefore, a comprehensive study of the mechanism of impurity entry into the crystal volume and their interaction with both the matrix atoms of the crystal and technological impurities is relevant. From this point of view, the study of the formation of silicides in the surface region of silicon during diffusion doping and the development of new semiconductor devices based on them is of particular scientific importance in the context of creating new materials for micro- and nanoelectronics.

The purpose of this work is to study the heterogeneity of the near-surface and surface layer within the formation of chromium silicides of diffusion-doped silicon with chromium atoms.

EXPERIMENTAL METHODS

Chromium has a high diffusion coefficient in silicon, so we used the diffusion alloying method. This method has a number of other advantages: 1) relative simplicity of the technology; 2) the ability to study the effect of annealing

temperature on the initial parameters of the crystal; 3) the ability to regulate the concentration of electrically active chromium atoms by changing the temperature.

For alloying silicon with chromium, we used ingots of both *p*-type KDB-10 and *n*-type KEF-20 silicon monocrystals grown by the Czochralski method. Their initial parameters are as follows: for n-type silicon, the resistivity is $\rho = 20$ Ohm·cm, the electron mobility is $\mu_n = 1430$ cm^2/V s, the electron concentration is $n = 2.2 \cdot 10^{14}$ cm^{-3}; for *p*-type silicon, the resistivity is $\rho = 10$ Ohm·cm, the hole mobility is $\mu_p = 430$ cm^2/V s, the hole concentration is $p = 1.5 \cdot 10^{15}$ cm^{-3}, the oxygen concentration is $1 \cdot 10^{17}$ cm^{-3}.

Parallelepiped-shaped samples measuring $(1 \div 2) \times (2 \div 5) \times (10 \div 30)$ mm^3 were cut out from silicon single-crystal ingots using a diamond disk. The samples were ground using silicon carbide micropowder M-5, M-10. In order to remove the surface layer damaged during grinding, the samples were degreased in toluene at a temperature of 40-50°C and chemically etched in a 1HF:5HNO$_3$ solution for $1 \div 2$ minutes, washed in deionized water and dried at a temperature of no more than 100°C. Silicon samples were placed in a quantity of 3 pcs. in quartz ampoules, pre-washed in a solution of HNO$_3 \div 3$HCl and boiled in distilled water.

The mass of the alloying metal atoms was determined from the Mendeleev-Clapeyron equation: $pV = mRT\mu^{-1}$. Hence $m = pV\mu R^{-1}T^{-1}$, where p is the metal vapor pressure in the ampoule, which is equal to $1 \cdot 10^{-2} \div 2 \cdot 10^{-5}$ mm Hg at T=1000÷1250°C. The mass of the metal determined in this way was 3 mg. The mass of the metal is not limited upwards, i.e. not less than 3 mg is used. Metal powder of 99.999 purity was placed in the ampoule in an amount of $3 \div 5$ mg. The ampoules with samples and diffusant were pumped out to a vacuum of ~10^{-3} mmHg ($1.33 \div 10^{-1}$ Pa) and sealed. Then the ampoules were placed in a horizontal furnace and annealed at a temperature of $950 \div 1070$ °C for 20 minutes to 2 hours. Temperature fluctuations in the working area of the furnace did not exceed ±5 °C. After annealing, the samples were quenched by cooling at a rate of 100-150 deg/s by dropping the ampoules into water and kept until the crystal temperature T=15-20°C. After opening the ampoules, the surface of the samples had p-type conductivity [14,16,17].

Since the samples had a highly conductive surface layer, to eliminate its shunting effect, the samples were ground on three sides to a depth of about 40-50 μm. Electrical contacts were connected to two opposite unground ends, and measurements were taken on the unground surface lying between them with successive removal of thin layers. It turned out that the conductivity profiles have two sections - a near-surface section with increased conductivity and a volume section with conductivity close to the intrinsic one. Parallel measurements of conductivity and the Hall effect at temperatures T = -196÷27°C showed that the surface layer has *p*-type conductivity with a carrier concentration of ~$10^{20} \div 10^{21}$ cm^{-3} and a Hall mobility of $\mu_H = 2 - 6 cm^2/V \cdot s$, while the bulk layer has *i*-type conductivity with a carrier concentration of $10^{10} \div 10^{12}$ cm^{-3} and a mobility of $\mu_H = 300 - 700$ cm^2/V·s. The same conductivity distribution (*p*-type with a concentration of $p \approx 10^{20} \div 10^{21}$ cm^{-3}) was obtained in the surface layer also when doping the initial n-type silicon with chromium. However, the bulk carrier concentration in the bulk of the sample remained almost unchanged (relative to the initial silicon).

The measurement results showed that the near-surface anomalous layer has a current carrier concentration of ~$10^{20} \div 10^{21}$ cm^{-3} and a Hall mobility of $1 \div 17$ cm^2/V·s. Calculations showed that the near-surface Si<Cr> layers with a thickness of $1 \div 5$ μm have a specific conductivity of ~$(1.6 \div 9.9) \times 10^3$ Ohm$^{-1} \times$cm^{-1}.

RESULT AND DISCUSSION

To analyze the obtained thermoelectric properties of samples with higher chromium silicides (HCS), we will use generally accepted criteria.
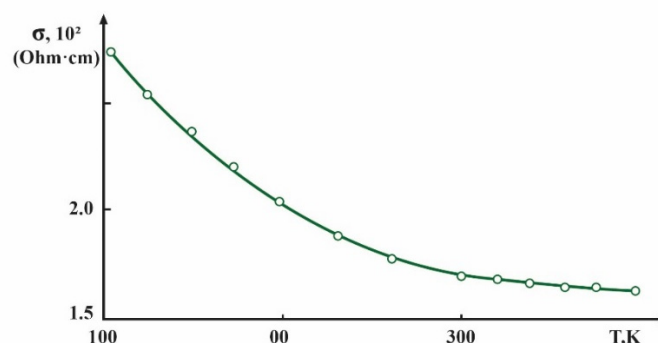

Figure 1. Temperature dependence of conductivity of HCS

It is known that the total efficiency of the Carnot cycle is determined by the thermoelectric figure of merit, the value of which for a particular material is determined as [18]

$$Z = \frac{\alpha^2 \sigma}{\varkappa} \qquad (1)$$

where α, σ and $\varkappa$ —electrical conductivity, differential thermoEMF, thermal conductivity, respectively.

The figure of merit is the only parameter that determines the characteristics of a thermoelectric device, and therefore it is desirable to have a material with the maximum value of α and, accordingly, the minimum ρ and $\varkappa$. The parameters that determine the thermoelectric figure of merit are interdependent and, in addition, they depend on the temperature, since $\varkappa$ and ρ depend on the concentration and mobility of carriers. With some degree of assumption, it can be assumed that the thermal conductivity of semiconductors $\varkappa = \varkappa e + \varkappa p$, where $\varkappa e$ is the electron component, and $\varkappa p$ is the phonon component of thermal conductivity.

Photoconductivity and photo-EMF measurements were performed at room temperature on Si<Cr> samples in which the bulk part of the crystal was overcompensated, i.e. *n*-type. The sample sizes were as follows: after doping with metal atoms – $0.3 \times 0.4 \times 0.5$ cm^3 and $0.4 \times 1.6 \times 1.6$ cm^3, after cutting for photo-EMF studies – $0.15 \times 0.13 \times 0.5$ cm^3 and $0.3 \times 1.5 \times 1.6$ cm^3.

Fig. 2 shows the results of light scanning for typical Si<Cr> samples, irradiated with light of wavelength 0.63 μm, after removing a layer 3-5 μm thick from the surface. It is evident from the figures that the photo signal does not change monotonically from point to point.
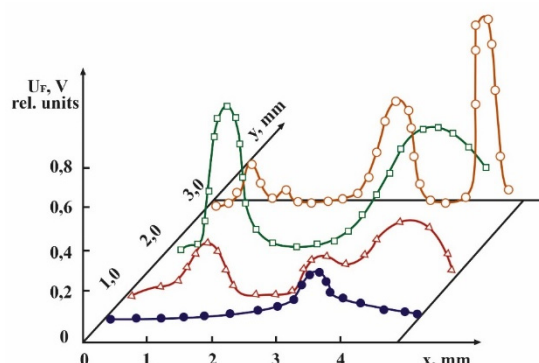
Figure 2. Results of light scanning for one n-Si<Cr> sample under irradiation with light with λ = 0.63 μm

It was found that the density of the photo-EMF spectrum decreases with increasing thickness of the layer being removed. The results of the study show that a new phase is formed on the surface of silicon diffusion-doped with chromium in the high-temperature process. Such a phase grows on the orienting substrate taking into account its atoms and regularly continues the crystal lattice of the substrate.

The formation of chromium mono- and disilicides was proven by X-ray diffraction [7].

Measurements showed that the areas of the photo-EMF spectra depend on the wavelength of light, and the shifts in the areas and their shape are apparently related to the depth of light penetration depending on λ. This shows that when using infrared radiation in the region of ~0.6 – 3.4 μm, it is possible to determine inhomogeneities inside the crystal.

A study of the dependence of the photo-EMF value on the thickness of the surface layer revealed that the photo-EMF signal increases as the layer is removed to a depth of ~25 μm, and then saturates in a narrow region and gradually decreases from ~30 μm and completely disappears after removal of more than 45÷50 μm [8].

To determine the internal electric field of a non-uniform region of a crystal, an external electric field of polarity E_e, opposite to the internal electric field E_i, was applied to it.

Research has shown that at E_e=0.9-1.2 V/cm, the volume photo-EMF current is zero when illuminated with modulated light. In this case, E_i can be determined according to the expression [19]:

$$E_i = \frac{1+b}{2} \cdot \frac{i}{s} \cdot p \qquad (2)$$

where s is the cross-section of the crystal, b is the ratio of the electron and hole mobilities, i is the compensating direct current, p is the specific resistance of the crystal.

When substituting the values $b = \mu_n/\mu_p = 3, p = 1.3 \cdot 10^4$ Ohm $\cdot$ cm, $i = 1.39 \cdot 10^{-6} A, s = 2 \cdot 10^{-2}$ cm^2, the value $E_i = 1.8$ V/cm was obtained.

A model of the structure of the near-surface region of diffusion-doped silicon with chromium is proposed. The near-surface region of compensated silicon is a large number of Schottky diodes (pairs) connected in opposite directions, with a layer of silicon metal atoms compensated between them, connected in parallel and series. Such a model is determined by the island character of the second-phase inclusions located at a depth of ~3-45 μm from the surface. This is confirmed by the maximum photo-EMF value at a depth of ~25-30 μm, where there is apparently an optimal ratio between the number of islands (inclusions) and their surface, giving the maximum total surface of the silicon-second-phase inclusions boundary.

CONCLUSIONS

1. The local photo-EMF method was used to study inhomogeneities in the initial, heat-treated, and control silicon crystals and chromium-diffusion-doped silicon crystals. It was found that in the initial and control silicon samples of both n-type and p-type conductivity, inhomogeneous areas in photoconductivity and photo-EMF along the crystal and in depth

were not detected, while in chromium-doped *n*-type and *p*-type silicon crystals, photo-EMF and photo-conductivity signals were detected.

2. It was found that photo-conductivity and photo-EMF signals in chromium-diffusion-doped silicon samples are detected in the near-surface region with a depth of 3÷50 μm. It was shown that in these samples, photo-conductivity and photo-EMF signals are not detected in the near-surface region up to ~3 μm thick and in the bulk region more than ~50 μm from the surface.

3. It is shown that the photo signal in the inhomogeneous region of doped crystals changes from point to point non-monotonically. Measurements of layer-by-layer removal of layers have established that the sizes of the second-phase inclusions decrease deep into the crystal in the form of a cone.

ORCID
Makhmudkhodja Sh. Isaev, https://orcid.org/0009-0007-9559-5834

REFERENCES
[1] Kh.S. Daliev, and A.A. Lebedev, *Properties of doped semiconductor materials,* (Moscow, Nauka, 1990). (in Russian)
[2] Sh.B. Utamuradova, Kh.S. Daliev, Sh.Kh. Daliev, abd K.M. Fayzullaev, Applied Physics, (6), 90–95 (2019). (In Russian)
[3] F.Y. Wang, *Impurity Doping Processes in Silicon*, (North Holland Publishing, North Holland, 2013).
[4] A.A. Lebedev, "Deep level centers in silicon carbide: A review," Semiconductors, **33(2),** 107-130 (1999). https://doi.org/10.1134/1.1187657
[5] K.P. Abdurakhmanov, Sh.B. Utamuradova, Kh.S. Daliev, S.G. Tadjy-Aglaeva, and R.M. Érgashev, "Defect-formation processes in silicon doped with manganese and germanium," Semiconductors, **32**(6), 606–607 (1998). https://doi.org/10.1134/1.1187448
[6] U.O. Kutliev, M.K. Karimov, F.O. Kuryozov, and K.U. Otabaeva, Journal of Physics: Conference Series, **1889**(2), 022063 (2021). https://doi.org/10.15330/pcss.22.4.742-745
[7] M.K. Karimov, U.O. Kutliev, S.B. Bobojonova, and K.U. Otabaeva. Physics and Chemistry of Solid State, **22**(4), 742–745 (2021). https://doi.org/10.1088/1742-6596/1889/2/022063
[8] Kh.S. Daliev, Sh.B. Utamuradova, O.A. Bozorova, and Sh.Kh. Daliev, "Joint effect of Ni and Gf impurity atoms on the silicon solar cell photosensitivity," Applied Solar Energy (English translation of Geliotekhnika), **41**(1), 80–81 (2005). https://www.researchgate.net/publication/294234192_Joint_effect_of_Ni_and_Gf_impurity_atoms_on_the_silicon_solar_cell_photosensitivity
[9] K.S. Daliev, S.B. Utamuradova, J.J. Khamdamov, and M.B. Bekmuratov, "Structural properties of silicon doped rare earth elements ytterbium," East Eur. J. Phys. (1), 375–379 (2024). https://doi.org/10.26565/2312-4334-2024-1-37
[10] S.B. Utamuradova, S.Kh. Daliev, E.M. Naurzalieva, and X.Yu. Utemuratova, "Investigation of defect formation in silicon doped with silver and gadolinium impurities by raman scattering spectroscopy," East European Journal of Physics, (3), 430-433 (2023). https://doi.org/10.26565/2312-4334-2023-3-47
[11] Kh.S. Daliev, Sh.B. Utamuradova, O.A. Bozorova, and Sh.Kh. Daliev, "Joint influence of impurity atoms of nickel and hafnium on photosensitivity of silicon solar cells," Applied Solar Energy (English translation of Geliotekhnika), **1,** 85–87 (2005).   https://www.researchgate.net/publication/294234192_Joint_effect_of_Ni_and_Gf_impurity_atoms_on_-the_silicon_solar_cell_photosensitivity
[12] M.Sh. Isaev, I.T. Bozarov, and A.I. Tursunov, "Investigation of thermally stimulated conductivity of cobalt silicide," E3S Web of Conferences, **402,** 14019 (2023). https://doi.org/10.1051/e3sconf/202340214019
[13] M.Sh. Isaev, T.U. Atamirzaev, M.N. Mamatkulov, U.T. Asatov, and M.A. Tulametov, "Study of the mobility and electrical conductivity of chromium silicide," East European Journal of Physics, (4), 189–192 (2023). https://doi.org/10.26565/2312-4334-2023-4-22
[14] Sh.B. Utamuradova, Sh.Kh. Daliyev, J.J. Khamdamov, Kh.J. Matchonov, and Kh.Y. Utemuratova, "Research of the Impact of Silicon Doping with Holmium on its Structure and Properties Using Raman Scattering Spectroscopy Methods," East Eur. J. Phys. (2), 274 (2024), https://doi.org/10.26565/2312-4334-2024-2-28.
[15] A.A. Rakhmankulov. E3S Web Conf. **411**, 01022 (2023). https://doi.org/10.1051/e3sconf/202341101022
[16] A.T. Mamadalimov, M.Sh. Isaev, T.U. Atamirzaev, S.N. Ernazarov, and M.K. Karimov, "CVC Structure of PtSi - Si<Pt>-M in a Wide Range of Temperatures," East Eur. J. Phys. (2), 358–361 (2024). https://doi.org/10.26565/2312-4334-2024-2-43
[17] A.T. Mamadalimov, M.Sh. Isaev, I.T. Bozarov, A.E. Rajabov, and S.K. Vakhabova, "Study of the Thermoelectric Properties of Chrome Silicides," East Eur. J. Phys. (2), 362–365 (2024). https://doi.org/10.26565/2312-4334-2024-2-44
[18] A.A. Snarsky, A.K. Sarychev, I.V. Bezsudnov, and A.N. Lagarkov, "Thermoelectric figure of merit of bulk nanostructured composites with distributed parameters," Semiconductors, **46**(5), 677-683 (2012). http://journals.ioffe.ru/articles/viewPDF/7707 (in Russian)
[19] *Semiconductor and Semiconductor Devices Workshop*, edited by K.V. Shalimova, (Vyschsz shkola, Moscow, 1968). (in Russian).

МОРФОЛОГІЯ ПОВЕРХНЕВОГО ШАРУ ЗРАЗКІВ Si<Cr>
М.Ш. Ісаєв[a], А.І. Худайбердієва[b], М.Н. Маматкулов[b], У.Т. Асатов[b], С.Р. Кодиров[c]
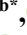*[a]Національний університет Узбекистану, Ташкент, Узбекистан*
[b]Ташкентський хіміко-технологічний інститут, Ташкент, Узбекистан
[c]Ургенчський державний університет, Ургенч, Узбекистан
У роботі досліджено електричні та фотоелектричні властивості приповерхневого та поверхневого шарів кремнію, легованого дифузією атомів хрому. Виявлено формування аномальної концентрації носіїв заряду в цих областях, а також аномально низьку рухливість. Питома електропровідність приповерхневого шару товщиною 1÷5 мкм виявилася рівною $(1{,}6{÷}9{,}9){\cdot}10^3{\cdot}$Ом$^{-1}{\cdot}$см$^{-1}$. Методом світлового зонду визначали неоднорідність досліджуваного кристала.
Ключові слова: *кремній; хром; поверхня; підповерхневий; провідність; Hall мобільність; неоднорідність; силицид*

DEFECT FORMATION IN MIS STRUCTURES BASED ON SILICON WITH AN IMPURITY OF YTTERBIUM

Khodjakbar S. Daliev[a], Sharifa B. Utamuradova[b], Jonibek J. Khamdamov[b],
Mansur B. Bekmuratov[b*], Oralbay N. Yusupov[c], Shahriyor B. Norkulov[b],
Khusniddin J. Matchonov[b]

[a]*Branch of the Federal State Budgetary Educational Institution of Higher Education "National Research University MPEI",*
1 Yogdu st., Tashkent, Uzbekistan
[b]*Institute of Semiconductor Physics and Microelectronics at the National University of Uzbekistan,*
20 Yangi Almazar st., Tashkent, 100057, Uzbekistan
[c]*Nukus State Pedagogical Institute named after Ajiniyaz, Nukus, Uzbekistan*
*Corresponding Author e-mail: mans-bek@mail.ru

The characteristics of silicon MIS structures with ytterbium impurity are studied using non-stationary capacitance spectroscopy of deep levels. It is established that the presence of ytterbium atoms in the bulk of the silicon substrate leads to a shift in the capacitance-voltage characteristics towards positive bias voltages and a decrease in the density N_{ss} of the surface states of the MIS structures. It is shown that this effect depends on the concentration of ytterbium atoms in the silicon substrate of the studied structures. In MIS structures based on $Si<Yb>$, one deep level with an ionization energy E_c-0.32 eV is detected.

Key words: *Silicon; Substrate; Impurity; Rare Earth element; Diffusion; Doping; Ytterbium; MIS structure*
PACS: 33.20.Ea, 33.20.Fb

INTRODUCTION

Currently, solid-state electronics devices are used in almost all areas of science and technology throughout the world. The scope of application of solid-state devices is constantly expanding, fundamentally new devices are created, stimulating the development of industry in new directions, which requires a significant increase in the perfection of the silicon structure - the main material of modern solid-state semiconductor electronics. Therefore, research aimed at studying the processes of defect formation in silicon doped with various impurities and establishing controlled methods for stabilizing the parameters of semiconductor devices are one of the important problems [1-10]. In connection with the search for semiconductor materials with special properties (increased thermal stability, radiation resistance, etc.), interest in silicon doped with rare earth elements has recently increased [5-13]. These specially introduced impurities enter into various interactions with structural defects and various uncontrolled impurities during technological processing, which is accompanied by almost any method of manufacturing semiconductor devices. Among all the rare earth elements in silicon, ytterbium is the least studied.

Analysis of the trends in the development of microelectronics worldwide today shows that in the future, the majority of manufactured microcircuits will be digital logic integrated circuits, the basic element of which is MIS (metal-insulator-semiconductor) structures. Charge-coupled devices (CCDs) are already widely used in digital and analog signal processing devices, and photosensitive CCDs, which are also based on MIS structures, are used as solid-state photodetectors [12-16].

However, with an increase in the degree of integration of microcircuits, when creating large and very large integrated circuits, surface and volume defects in multilayer silicon structures have an increasing impact on the operation of devices. This necessitates a more in-depth study of defects near the semiconductor-insulator boundary and in the volume of the semiconductor and determining their contribution to changes in the parameters of manufactured devices. The study of the interaction between impurity particles and defects in the semiconductor structure, the influence of the heterogeneity of the structure of the MIS structure on the redistribution of impurities opens up the possibility of increasing the stability of the operating parameters of microcircuits based on MIS structures [14-20].

It should be noted that the influence of various impurity atoms on the properties of MIS structures was studied using CV methods in [15-22], and the role of these impurities in the formation of the characteristics of multilayer structures was determined. The use of the *CC-DLTS* method allows scanning the DL both in the bulk of *Si* and *SiO₂* and at the *Si-SiO₂* interface and studying in detail the properties of each defect separately. There are no data in the literature on the influence of rare-earth element atoms introduced into the silicon substrate on the parameters of MIS structures. Therefore, this paper attempts to fill this gap and study in detail the properties of silicon MIS structures with impurities of rare-earth (non-traditional) elements.

EXPERIMENTAL PART

The aim of this work is to study the processes of defect formation in MIS structures with a silicon substrate doped with ytterbium impurity.

To study the effect of ytterbium atoms on the properties of the bulk and the interface of *Si-SiO₂*, we carried out complex studies using *CC-DLTS* and high-frequency capacitance-voltage characteristics (HF CV-characteristics). Doping of silicon with *Yb* was carried out by the diffusion method in the temperature range of 900÷1250°C for 5÷20 hours from a layer of metallic ytterbium deposited on

the Si surface with different cooling rates of the samples after diffusion. Silicon wafers doped with ytterbium impurity during growth from the melt were also used. The method for fabricating MIS structures is described in our work [15]. After doping on Si plates with a specific resistance of ρ=15 Ω×cm, a layer of SiO_2 with a thickness of 650-700 Å was grown thermally at 900°C in an atmosphere of humid oxygen with the addition of trichloroethylene. Metallic electrodes on SiO_2 with an area of A=0.03 cm^2 and a thickness of 7000 Å were created by thermal spraying of aluminum.

The *CC-DLTS* spectra were measured in the temperature range of 77 - 300 K at different values of E_{FS} in the state of electron emission from the PS, where E_{FS} is the energy of the quasi-Fermi level for electrons on the Si surface, measured from the lower edge of the conduction band downwards [19]. E_{FS} is determined from the value of the constant capacitance C of the structure during emission and the position of the Fermi level in the neutral semiconductor depending on the temperature. The HF CV characteristics were measured at T = 280 K and a frequency of 150 kHz.

Measurements of the capacitance-voltage characteristics of MIS structures based on *Si<Yb>* showed that in the samples where the silicon substrate is doped with ytterbium during the Si growth process (Fig. 1, curve 2), they are shifted towards positive bias voltages compared to the control samples (Fig. 1, curve 1).
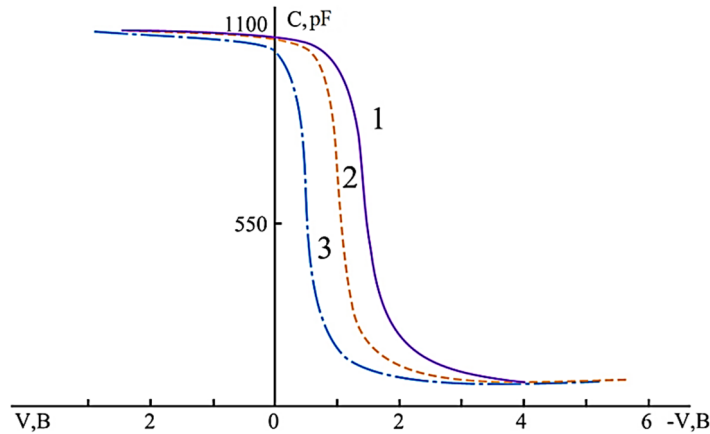

Figure 1. High-frequency capacitance-voltage characteristics of control MIS structures (1) and MIS structures based on *Si* with *Yb* (2 and 3)

Such a shift in the capacitance-voltage characteristics indicates that the presence of ytterbium impurity in the bulk of silicon leads to a decrease in the density of surface states of MIS structures and a decrease in the value of the positive charge at the *Si-SiO$_2$* interface (relative to the control samples).

Analysis of the capacitance-voltage characteristics of MIS structures, where the silicon substrate is doped with ytterbium by the diffusion method (Fig. 1, curve 3) showed that an even greater shift towards positive bias voltages is observed compared to structures whose substrate is doped with ytterbium during melt growth (Fig. 1, curve 2).

Measurements of the *CC-DLTS* spectra in MIS structures based on *Si<Yb>* (Fig. 2, curve 2) and control MIS structures (Fig. 2, curve 1) showed that their spectra differ somewhat, since the value of N_{ss} decreases when ytterbium is introduced into the silicon substrate of the MIS structures. Analysis of the *CC-DLTS* spectra showed that this effect depends on the method of introducing the ytterbium impurity into the silicon substrate of the studied structures (by diffusion or during the growth process. A peak with a maximum at T=165 K is observed in the *CC-DLTS* spectra of MIS structures with a silicon substrate doped with ytterbium impurity by the diffusion method.
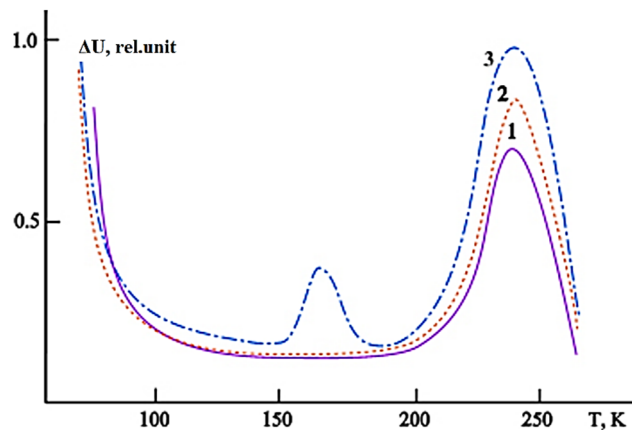
Figure 2. *CC-DLTS* spectra in control MIS structures (1) and MIS structures based on *Si<Yb>*, where *Yb* is introduced during growth (2) and diffusion (3)

Figure 2 shows the *CC-DLTS* spectra of the control MIS structures (curve 1) and MIS structures based on Si doped with *Yb* during growth (curve 2), measured at a depletion capacitance such that the quasi-Fermi level for electrons on the silicon surface EFS is approximately in the middle of the silicon band gap and a filling pulse U_f=10 V with a duration t_f=1 ms, delay times t_1=10 ms, t_2=20 ms. The maximum at T=280 K (peak B) is associated with the recharging of surface states by minority current carriers, which we observed earlier [15]. Measurements of the *CC-DLTS* spectra of MIS structures based on Si diffusion-doped with *Yb* (Fig. 2, curve 3) showed that another peak with a maximum at a temperature of T_{max}=165 K (peak A) is observed in the spectra of the doped samples.

To determine the energy parameters of this defect caused by the ytterbium impurity in the studied MIS structures, the oxide layer was removed and Schottky barriers were fabricated on them. Measurements of the *CC-DLTS* spectra on the obtained barriers showed that in these samples, a recharge of one deep level in the upper half of the Si band gap with an ionization energy of E_c-0.32 eV is observed. The concentration of this level depends on the technological diffusion modes: the higher the diffusion temperature and the cooling rate of the samples after diffusion, the higher the concentration of the detected level E_c-0.32 eV. Analysis of the obtained results allows us to conclude that this level is caused by the introduction of an ytterbium impurity.

CONCLUSIONS

Thus, it has been established that the presence of ytterbium atoms in the bulk of the silicon substrate leads to a shift in the capacitance-voltage characteristics towards positive bias voltages and a decrease in the density of surface states N_{ss} of MIS structures.

Analysis of the *CC-DLTS* spectra showed that this effect depends on the method of introducing the ytterbium impurity into the silicon substrate of the studied structures (by diffusion or during the growth process).

From measurements of the CC-DLTS spectra on *Si<Yb>*-based Schottky barriers, it has been established that peak A at 165 K is due to a deep level in with an ionization energy of Ec-0.32 eV.

ORCID

Khodjakbar S. Daliev, https://orcid.org/0000-0002-2164-6797; **Sharifa B. Utamuradova**, https://orcid.org/0000-0002-1718-1122
Jonibek J. Khamdamov, https://orcid.org/0000-0003-2728-3832; **Mansur B. Bekmuratov**, https://orcid.org/0009-0006-3061-1568
Shahriyor B. Norkulov, https://orcid.org/0000-0002-2171-4884; **Khusniddin J. Matchonov,** https://orcid.org/0000-0002-8697-5591
Oralbay N. Yusupov, https://orcid.org/0009-0005-8419-2293

REFERENCES

[1] V.G. Litovchenko, and A.P. Gorban, *Fundamentals of Physics of Microelectronic Metal-Semiconductor Systems*, (Kyiv, 1978). (in Russian)

[2] S.B. Utamuradova, S.Kh. Daliev, E.M. Naurzalieva, and X.Yu. Utemuratova, "Investigation of Defect Formation in Silicon Doped with Silver and Gadolinium Impurities by Raman Scattering Spectroscopy," East Eur. J. Phys. (3), 430 (2023), https://doi.org/10.26565/2312-4334-2023-3-47

[3] V.F. Kiselov, and S.N. Kozlov, *Fundamentals of solid surface physics*, (Mir, Moscow, 1999). (in Russian)

[4] Sh.B. Utamuradova, Kh.J. Matchonov, J.J. Khamdamov, and Kh.Y. Utemuratova, "X-ray diffraction study of the phase state of silicon single crystals doped with manganese," New Materials, Compounds and Applications, **7**(2), 93-99 (2023). http://jomardpublishing.com/UploadFiles/Files/journals/NMCA/v7n2/Utamuradova_et_al.pdf

[5] Sh.B. Utamuradova, Sh.Kh. Daliyev, K.M. Fayzullayev, D.A. Rakhmanov, and J.Sh. Zarifbayev, "Raman spectroscopy of defects in silicon doped with chromium atoms," New Materials, Compounds and Applications, **7**(1), 37-43 (2023). http://jomardpublishing.com/UploadFiles/Files/journals/NMCA/V7N1/Utamuradova_et_al.pdf

[6] Y. Nishioka, E. F. Da Silva, Jr., Y. Wang, and T.-P. Ma, "Dramatic Improvement of Hot-Electron-Induced Interface Degradation in MOS Structures Containing F or CI in SiO$_2$," IEEE Electron Device Letters, **9**(1), 38–40 (1988). https://doi.org/10.1109/55.20406

[7] K.S. Daliev, S.B. Utamuradova, J.J. Khamdamov, and M.B. Bekmuratov, "Structural properties of silicon doped rare earth elements ytterbium," East Eur. J. Phys. (1), 375–379 (2024). https://doi.org/10.26565/2312-4334-2024-1-37

[8] K.S. Daliev, S.B. Utamuradova, A. Khaitbaev, J.J. Khamdamov, S.B. Norkulov, and M.B. Bekmuratov, "Defective Structure of Silicon Doped with Dysprosium," East Eur. J. Phys. (2), 283-287 (2024). https://doi.org/10.26565/2312-4334-2024-2-30

[9] S.B. Utamuradova, S.K. Daliev, A.K. Khaitbaev, J.J. Khamdamov, K.J. Matchonov, and X.Y. Utemuratova, "Research of the Impact of Silicon Doping with Holmium on its Structure and Properties Using Raman Scattering Spectroscopy Methods," East Eur. J. Phys. (2), 274-278 (2024). https://doi.org/10.26565/2312-4334-2024-2-28

[10] S.B. Utamuradova, K.S. Daliev, A.I. Khaitbaev, J.J. Khamdamov, J.S. Zarifbayev, and B.S. Alikulov, "Defect Structure of Silicon Doped with Erbium," East Eur. J. Phys. (2), 288-292 (2024). https://doi.org/10.26565/2312-4334-2024-2-31

[11] K.S. Daliev, S.B. Utamuradova, J.J. Khamdamov, and Z.E. Bahronkulov, "Morphology of the Surface of Silicon Doped with Lutetium," East Eur. J. Phys. (2), 304-308 (2024). https://doi.org/10.26565/2312-4334-2024-2-34

[12] V.V. Emtsev, V.V. Emtsev (Jr.), D.S. Poloskin, N.A. Sobolev, E.I. Shek, J. Mikhel, and L.S. Kimerling, "Impurity centers in silicon doped with rare-earth impurities dysprosium, holmium, erbium and ytterbium," FTP, **33**(6), 649-651 (1999). https://journals.ioffe.ru/articles/viewPDF/3576. (in Russian)

[13] C. Xiao, J. Blundell, F. Hagelberg, and W.A. Lester Jr. "Silicon clusters doped with an yttrium metal atom impurity," International Journal of Quantum Chemistry, **96**(4), 416–425 (2004). https://doi.org/10.1002/qua.10735

[14] Y.B. Andree, G.G. Bondarenko, A.A. Stolyarov, D.S. Basyutin, and A.M. Mikhal'ko, "Influence of High_Field Electron Injection Regimes on Modification of Dielectric Films of MOS DeYb ice," Inorganic Materials: Applied Research, **1**(2), 105–109 (2010).

[15] *Charge-Coupled Devices (Topics in Applied Physics)*, edited by D.F. Barb, (Springer-Verlag, 1980).

[16] S. Gomes, and J. Ziane, "Investigation of electrical degradation of a metal-oxide-silicon structure by scanning thermal microscopy," Solid-State Electronics, **47**, 919-922 (2003). https://doi.org/10.1016/S0038-1101(02)00451-3

[17] Y. Khlifi, K. Kassmi, A. Aziz, F. Olivie, G. Sarrabayrouse, and A. Martinez, "Ionizing Radiation Effect on the Electrical Properties of Metal/Oxide/Semiconductor Structures," M. J. Condensed Matter, **6**(1), 20-26 (2005). https://doi.org/10.34874/PRSM.mjcm-vol6iss0.132

[18] H.S. Daliev, A.A. Lebedev, and V. Ekke, "Effect of heat treatment on the density of radiation defects in the dielectric and on the surface of the semiconductor of silicon MIS structures," FTP, **21**(5), 836-841 (1987).

[19] H.S. Daliev, A.A. Lebedev, and V. Ekke, "Study of electrophysical properties of silicon MIS structures irradiated with γ-quanta in the presence of an electric field in the dielectric," FTP, **21**(1), 23-29 (1987).

[20] K.P. Abdurakhmanov, Kh.S. Daliev, Sh.B. Utamuradova, and N.Kh. Ochilova, "On defect formation in silicon with impuritiesof manganese and zinc," Applied Solar Energy (English translation of Geliotekhnika), **34**(2), 73–75 (1998).

[21] Sh.B. Utamuradova, Sh.Kh. Daliev, A.V. Stanchik, and D.A. Rakhmanov, "Raman spectroscopy of silicon, doped with platinum and irradiated by protons", E3S Web of Conferences, **402**, 14014 (2023). https://doi.org/10.1051/e3sconf/202340214014

[22] A.S. Zakirov, Sh.U. Yuldashev, H.D. Cho, J.C. Lee, T.W. Kang, J.J. Khamdamov, and A.T. Mamadalimov, "Functional Hybrid Materials Derived from Natural Cellulose," Journal of the Korean Physical Society, **60**(10), 1526-1530 (2012). https://doi.org/10.3938/jkps.60.1526

ДЕФЕКТОУТВОРЕННЯ В МДП СТРУКТУРАХ НА ОСНОВІ КРЕМНІЮ З ДОМІШКОЮ ІТЕРБІЮ

Ходжакбар С. Далієв[a], Шаріфа Б. Утамурадова[b], Джонібек Дж. Хамдамов[b], Мансур Б. Бекmuratов[b], Оралбай Н. Юсупов[c], Шахрійор Б. Норкулов[b], Хусніддін Дж. Матчонов[b]

[a]Філія ФДБУ «Національний дослідницький університет МПЕІ», Йогду, 1, Ташкент, Узбекистан
[b]Інститут фізики напівпровідників та мікроелектроніки Національного університету Узбекистану, Ташкент,
вул. Янгі Алмазара, 20, Узбекистан
[c]Нукуський державний педагогічний інститут імені Аджиніяза, Нукус, Узбекистан

Методами нестаціонарної ємнісної спектроскопії глибоких рівнів досліджено характеристики кремнієвих МДП-структур з домішкою ітербію. Встановлено, що присутність атомів ітербію в об'ємі кремнієвої підкладки призводить до зсуву вольт-фарадних характеристик у бік позитивних напруг зміщення та зменшення густини N_{ss} поверхневих станів МДП-структур. Показано, що цей ефект залежить від концентрації атомів ітербію в кремнієвій підкладці досліджуваних структур. У МДП-структурах на основі Si<Yb> виявляється один глибокий рівень з енергією іонізації E_c-0,32 еВ.

Ключові слова: *кремній; підкладка; домішка; рідкоземельний елемент; дифузія; допінг; ітербій; МДП структура*